

# **Preparation and characterization of rhombohedral metal-oxide thin films on *c*-plane $\alpha$ -Al<sub>2</sub>O<sub>3</sub> substrates**

zur Erlangung des akademischen Grades

**Doktor der Ingenieurwissenschaften**

von der KIT-Fakultät für Maschinenbau  
des Karlsruher Instituts für Technologie (KIT)

Genehmigte

**Dissertation**

von

**M. Sc. Yin Gao**

aus Shanxi, China

Tag der mündlichen Prüfung: 29.11.2019

Hauptreferent: apl. Prof. Dr. Sven Ulrich

Korreferent: Prof. Dr. Michael J. Hoffmann



# Acknowledgement

I would like to express my sincere gratitude and appreciation to Prof. Dr. H. J. Seifert for giving me the opportunity to do my Ph.D. thesis at the Institute of Applied Materials (IAM-AWP) of the Karlsruhe Institute of Technology (KIT). Many thanks to apl. Prof. Dr. S. Ulrich, Dr. H. Leiste, and Dr. M. Stüber who offered me this interesting research theme, and for helpful suggestions, discussions and many help. I benefited a lot from their guidance during my doctoral study.

I gratefully acknowledge the financial support by China Scholarship Council (File No. 201304910212).

I would like to give my thanks to my colleagues: Dr. J. Ye for meaningful discussion and suggestions; Mr. K. Erbes for help on the EPMA measurements; Mrs. B. Rabsch for SEM measurements and preparation the samples for TEM measurements; Mr. S. Heißler from the Institute of Functional Interfaces (IFG) at KIT for the help on the optical measurements (IR and VIS spectroscopy) and helpful discussion; Mr. T. Weingärtner for the help on the AES measurements; Mr. S. Mumbauer and Mr. S. Zils for their technical support, great tricks and many good suggestions to solve the problems during the experiments; Dr. M. Rinke for the support in Raman spectroscopy measurements; Dr. K. Seemann for the help on the electrical measurements; and Mr. H. Besser for providing the sapphire substrates by laser cutting.

Many thanks to Mr. C. C. Tang, Dr. K. Krüger, Dr. J. Fischer, Dr. S. Spitz, Mr. M. Strafela, Mr. S. Beirle, Mr. F. Seifried and Mr. C. Poltorak for their kind cooperation, especially Dr. S. Spitz gave me many advices about my work and told me a lot about the culture of Germany so that I could adapt the new environment fast.

Additionally, I especially would like show my thanks to Mrs. J. Howell, Mrs. C. Schuler and Mrs. P. Severloh for their kind support.

Special thanks are dedicated to my family. They always encouraged and supported me during my doctoral study. Especially I herewith thank my mother who did all the house

work and took care of me and my baby during the time when I was writing my doctoral dissertation.

Beijing, in February 2019

Yin Gao

# Abstract

In this work, the growth of nanocrystalline (0001) oriented thin oxide films with corundum structure on the (0001) oriented *c*-plane  $\alpha$ -Al<sub>2</sub>O<sub>3</sub> substrates was studied. The thin films development was realized by magnetron sputtering with ceramic oxide targets at low substrate temperatures. In order to realize an epitaxial film growth, increasing the deposition temperature and decreasing the deposition rate are the common methods. We developed iso-structural epitaxial films of binary Cr<sub>2</sub>O<sub>3</sub>, V<sub>2</sub>O<sub>3</sub> and ternary phases in the systems of Al-Cr-O, V-Al-O and V-Cr-O grown on the  $\alpha$ -Al<sub>2</sub>O<sub>3</sub> substrates at low temperatures by physical vapor deposition (PVD) successfully. Furthermore, growth characterization of the films was investigated.

First of all, considering the structural isomorphism of Cr<sub>2</sub>O<sub>3</sub>, V<sub>2</sub>O<sub>3</sub> and  $\alpha$ -Al<sub>2</sub>O<sub>3</sub> even with relatively high lattice parameter mismatch of around 4 % for *a*-axis and 4 % - 8 % for *c*-axis, pure binary Cr<sub>2</sub>O<sub>3</sub> and V<sub>2</sub>O<sub>3</sub> films on the  $\alpha$ -Al<sub>2</sub>O<sub>3</sub> substrates were obtained. Then we extended our research to nano-crystalline coatings with corundum structure in the ternary Al-Cr-O, V-Al-O and V-Cr-O systems. Segmented targets were used to deposit films with different compositions in one single PVD process in order to realize combinatorial thin materials approach. Various analytical methods were used to characterize the composition, microstructure and properties of the films. The stoichiometric composition of the films was determined by electron probe micro-analysis (EPMA) and Auger electron spectroscopy (AES). The crystallization behaviors of the thin films were characterized by detailed X-ray diffraction (XRD) analyses (i.e. XRD in Bragg-Brentano geometry, rocking curves ( $\omega$ -scans), pole figures, and reciprocal space mapping (RSM)). Transmission electron microscopy (TEM) was carried out to study the microstructure and describe the orientation and epitaxial relationship between the films and the substrates. Further, Raman spectroscopy and infrared reflection-absorption spectroscopy (IRRAS) were carried out, and ultraviolet-visible (UV-VIS) spectroscopy was used to get the film band gap.

To investigate the microstructure and properties of  $\text{Cr}_2\text{O}_3$  and  $\text{V}_2\text{O}_3$  coatings with corundum structure, we realized thin film deposited on the sapphire substrates at the temperatures below  $400\text{ }^\circ\text{C}$  in the laboratory scale coater. The influence of the film thickness and the deposition temperature on the film microstructure and the film properties was discussed comprehensively. Nano-crystalline locally epitaxial film growth could be realized at lower deposition temperatures in the case of  $\text{V}_2\text{O}_3$  films in comparison to  $\text{Cr}_2\text{O}_3$  thin films. In addition, the crystalline quality and properties of the films deposited on the substrates with and without plasma-etching process before coating were compared and discussed.

The growth characteristics of nano-crystalline, ternary, chromium-rich, epitaxial grown thin films in the system Cr-Al-O films with composition variation and deposition temperature variation were elucidated. Further, the microstructure and optical property of ternary coatings in the systems V-Al-O and V-Cr-O with different composition deposited at  $400\text{ }^\circ\text{C}$  were investigated.

It could be shown that the films with different compositions were grown with locally epitaxy. (0001) orientation of stoichiometric  $\text{Cr}_2\text{O}_3$ ,  $\text{V}_2\text{O}_3$ , and solid solution  $\alpha\text{-(Cr}_{1-x}\text{Al}_x)_{\delta+2}\text{O}_3$ ,  $\alpha\text{-(V}_{1-x}\text{Al}_x)_{\delta+2}\text{O}_3$  and  $\alpha\text{-(V}_{1-x}\text{Cr}_x)_{\delta+2}\text{O}_3$  thin films were grown on (0001) *c*-plane  $\alpha\text{-Al}_2\text{O}_3$  single crystal substrates. The epitaxial relationship of  $(0001)_{\text{film}} // (0001)_{\text{substrate}}$  and  $(10\bar{1}0)_{\text{film}} // (10\bar{1}0)_{\text{substrate}}$  could be identified. Individual columnar grains grow in *c*-axis direction of the substrates. Plasma-etching process on the substrate could cause the stacking faults during the film growth. Raman spectra show a significant shift of phonon frequency with lattice parameters caused by thickness variation, composition variation, and deposition temperature variation.

# Kurzfassung

Diese Arbeit beschreibt die Herstellung nanokristalliner (0001)-texturierter Dünnschichten in Korundstruktur auf (0001)-orientierten  $\alpha$ -Al<sub>2</sub>O<sub>3</sub>-Substraten. Die Entwicklung der Dünnschichten wurde durch Magnetron-Zerstäuben mit keramischen Oxid-Targets bei niedriger Substrattemperatur realisiert. Generell sind die Erhöhung der Abscheidetemperatur und die Verringerung der Aufwachsrate gängige Verfahren, um ein epitaktisches Schichtwachstum zu realisieren. Im Rahmen dieser Arbeit wurden erfolgreich PVD-Prozessparameter erarbeitet, mit denen binäre Cr<sub>2</sub>O<sub>3</sub>- und V<sub>2</sub>O<sub>3</sub>-Schichten sowie ternäre Schichten in den Systemen Al-Cr-O, V-Al-O und V-Cr-O bei möglichst tiefen Temperaturen synthetisiert werden konnten. Des Weiteren wurde das

Schichtwachstum dieser Schichten umfassend untersucht. In Anbetracht des strukturellen Isomorphismus von Cr<sub>2</sub>O<sub>3</sub>, V<sub>2</sub>O<sub>3</sub> und  $\alpha$ -Al<sub>2</sub>O<sub>3</sub> erhalten wir reine binäre Cr<sub>2</sub>O<sub>3</sub>- und V<sub>2</sub>O<sub>3</sub>-Schichten auf den  $\alpha$ -Al<sub>2</sub>O<sub>3</sub>-Einkristall-Substraten mit (0001) Textur selbst bei einer relativ hohen Gitterparameterfehlpassung (4 % für *a*-Achse und 4 % - 8 % für *c*-Achse). Danach wurden die Forschungsaktivitäten innerhalb dieser Dissertation auf kristalline ternäre Al-Cr-O-, V-Al-O- und V-Cr-O-Systeme vom Korundtyp. Es wurden segmentierte Targets verwendet, um Schichten mit verschiedenen Zusammensetzungen in einem einzigen PVD-Prozess und um einen smarten materialkombinatorischen Ansatz zu realisieren. Die stöchiometrische Zusammensetzung der Schichten wurde durch Elektronensondenmikroanalyse (EPMA) und Auger-Elektronenspektroskopie (AES) bestimmt. Das Kristallisationsverhalten der charakterisierten dünnen Schichten wurde durch detaillierte Röntgenbeugungsanalysen (XRD) (d.h. XRD in Bragg-Brentano-Geometrie,  $\omega$ -kurve ( $\omega$ -Scans), Polfiguren, reziproke Raumabbildung (RSM)) analysiert. Es wurden Transmissionselektronische Untersuchungen (TEM) durchgeführt, um die Mikrostruktur zu bestimmen und die Orientierung und epitaktische Beziehung zwischen den Filmen und den Substraten zu beschreiben. Weiterhin wurden die Raman-Spektroskopie und Infrarot-Reflexionsabsorptionsspektroskopie (IRRAS) eingesetzt, um Informationen über die Bindungszustände zu erhalten, und die Bandlücke mittels optischer Transmissionsspektroskopie im ultravioletten und sichtbaren (UV-VIS) Spektroskopie wurde verwendet, um die Bandlücke zu erhalten. Die binären Cr<sub>2</sub>O<sub>3</sub>- und V<sub>2</sub>O<sub>3</sub>-Schichten mit Korund-Struktur

können erfolgreich bei Depositionstemperaturen unter 400 °C im Labormaßstab hergestellt und hinsichtlich ihrer Mikrostruktur und ihrer Schichteigenschaften umfassend charakterisiert werden. Bei der Schichtentwicklung wurde insbesondere der Einfluss der Schichtdicke und der Abscheideparameter auf die Schichtkonstitution systematisch untersucht. Die Mindesttemperatur, bei der noch ein lokales epitaktisches Wachstum möglich war lag bei den  $V_2O_3$ -Schichten bei 150 °C und bei den  $Cr_2O_3$  bei 320 °C. Zusätzlich wurde der Einfluss einer Plasmavorbereitung der Substrate auf das Schichtwachstum untersucht und optimiert.

Des Weiteren wurde das Wachstum von chromreichen, epitaktisch gewachsenen Dünnschichten im System Cr-Al-O in Abhängigkeit der elementaren Zusammensetzung. Die Mikrostruktur wurde durch Glühen weiter optimiert. Außerdem wurden die Mikrostruktur und die optischen Eigenschaften von ternären V-Al-O (V-reich) und V-Cr-O (V-reich) Filmen mit unterschiedlicher Zusammensetzung bei 400 °C untersucht.

Es konnte gezeigt werden, dass Schichten mit unterschiedlicher Zusammensetzung mit ein lokales epitaktisches Wachstum aufweisen können. Prozessparameter für die Abscheidung von Schichten mit einer (0001) Orientierung konnten für  $Cr_2O_3$ ,  $V_2O_3$ ,  $\alpha-(Cr_{1-x}Al_x)_{\delta+2}O_3$ ,  $\alpha-(V_{1-x}Al_x)_{\delta+2}O_3$  und  $\alpha-(V_{1-x}Cr_x)_{\delta+2}O_3$  erfolgreich erarbeitet werden. Die epitaktische Beziehung von (0001) Schicht // (0001) Substrat und  $(10\bar{1}0)$  Schicht //  $(10\bar{1}0)$  Substrat konnte ebenfalls identifiziert werden. Einzelne säulenförmige Körner wachsen in die Richtung der *c*-Achse der Substrate. Eine etwasige Plasmavorbereitung der Substrate kann während des Filmwachstums zu Stapelfehlern führen. Raman-Spektren zeigen eine signifikante Verschiebung der Phononfrequenz, wobei Gitterparameter durch Dickenchwankung, Zusammensetzungsänderung und Abscheidungstemperaturänderung verursacht werden statt werden.

# Contents

<b>Acknowledgement</b> .....	<b>i</b>
<b>Abstract</b> .....	<b>i</b>
<b>Kurzfassung</b> .....	<b>iii</b>
<b>Contents</b> .....	<b>v</b>
<b>List of figures</b> .....	<b>ix</b>
<b>List of tables</b> .....	<b>xxv</b>
<b>Symbols and abbreviations</b> .....	<b>xxvii</b>
<b>1 Introduction, Motivation and Objectives</b> .....	<b>1</b>
1.1 Introduction .....	1
1.2 Motivation and objectives .....	4
<b>2 Material systems and state of the art</b> .....	<b>7</b>
2.1 Crystal structure.....	7
2.1.1 Definition of a crystal .....	7
2.1.2 Hexagonal close-packed crystal structure.....	8
2.1.3 Corundum-type crystal structure.....	10
2.2 Aluminium oxide, Al <sub>2</sub> O <sub>3</sub> .....	13
2.2.1 Structure, properties and applications .....	14
2.2.2 Methods for Al <sub>2</sub> O <sub>3</sub> thin film deposition.....	16
2.3 Chromium oxide, Cr <sub>2</sub> O <sub>3</sub> .....	17
2.3.1 Structure, properties and applications .....	17
2.3.2 Methods for Cr <sub>2</sub> O <sub>3</sub> thin film deposition.....	20
2.4 Vanadium sesqui-oxide, V <sub>2</sub> O <sub>3</sub> .....	21
2.4.1 Structure, properties and applications .....	21
2.4.2 Methods for V <sub>2</sub> O <sub>3</sub> thin film deposition.....	24
2.5 Materials in the ternary system of Al-Cr-O.....	25
2.6 Materials in the ternary system of V-Al-O.....	28
2.7 Materials in the ternary system of V-Cr-O.....	30

2.8	Additional corundum-type crystalizing systems.....	32
<b>3</b>	<b>Experimental details.....</b>	<b>35</b>
3.1	Thin film deposition.....	35
3.1.1	Radio-frequency (RF) magnetron sputtering process.....	35
3.1.2	Experimental materials .....	42
3.2	Thin film characterization.....	44
3.2.1	Electron probe micro-analysis .....	45
3.2.2	Auger electron spectroscopy .....	47
3.2.3	X-ray diffraction .....	49
3.2.4	Raman Spectroscopy .....	59
3.2.5	Infrared reflection-absorption spectroscopy.....	62
3.2.6	Ultraviolet-visible-near infrared spectroscopy .....	64
3.2.7	Transmission electron microscopy .....	66
3.2.8	Film thickness and deposition rate .....	68
<b>4</b>	<b>Results.....</b>	<b>71</b>
4.1	Cr <sub>2</sub> O <sub>3</sub> films deposited on <i>c</i> -plane $\alpha$ -Al <sub>2</sub> O <sub>3</sub> substrates .....	71
4.1.1	Compositional and structural analysis.....	71
4.1.2	Raman spectroscopy analysis .....	81
4.1.3	Optical properties characterization.....	84
4.1.4	Influence of the plasma-etching process on the crystal growth.....	85
4.2	V <sub>2</sub> O <sub>3</sub> films deposited on <i>c</i> -plane $\alpha$ -Al <sub>2</sub> O <sub>3</sub> substrates .....	93
4.2.1	Compositional and structural analysis.....	93
4.2.2	Raman spectroscopy analysis .....	102
4.2.3	Optical properties characterization.....	104
4.2.4	Influence of the plasma-etching process on the crystal growth.....	105
4.3	$\alpha$ -(Cr <sub>1-x</sub> Al <sub>x</sub> ) <sub>2</sub> O <sub>3</sub> solid solution thin films grown on <i>c</i> -plane $\alpha$ -Al <sub>2</sub> O <sub>3</sub> substrates	113
4.3.1	Chemical composition .....	113
4.3.2	Structural analysis.....	116
4.3.3	Raman spectroscopy analysis .....	128
4.3.4	Infrared absorption spectroscopy analysis.....	130
4.3.5	Optical properties characterization.....	135
4.4	$\alpha$ -(V <sub>1-x</sub> Al <sub>x</sub> ) <sub>2</sub> O <sub>3</sub> solid solution thin films grown on <i>c</i> -plane $\alpha$ -Al <sub>2</sub> O <sub>3</sub> substrates.	136
4.4.1	Chemical composition .....	137
4.4.2	Structural analysis.....	139

4.4.3 Raman spectroscopy analysis.....	148
4.4.4 Infrared absorption spectroscopy analysis .....	149
4.4.5 Optical properties characterization .....	150
4.5 $\alpha$ -(V <sub>1-x</sub> Cr <sub>x</sub> ) <sub>2</sub> O <sub>3</sub> solid solution thin films grown on <i>c</i> -plane $\alpha$ -Al <sub>2</sub> O <sub>3</sub> substrates	152
4.5.1 Chemical composition.....	152
4.5.2 Structural analysis .....	153
4.5.3 Raman spectroscopy analysis.....	161
4.5.4 Infrared absorption spectroscopy analysis .....	162
4.5.5 Optical properties characterization .....	162
<b>5 Summary discussion .....</b>	<b>165</b>
<b>6 Summary.....</b>	<b>177</b>
<b>References.....</b>	<b>179</b>
<b>Publications and Conferences.....</b>	<b>209</b>



# List of figures

Fig. 1 Stacking sequences of the hcp layers of atoms. “a” are the atoms in the first layer, and “b” are the atoms in the second layer. ....	10
Fig. 2 A hcp structure where $a = b \neq c$ , and $\alpha = \beta = 90^\circ$ , $\gamma = 120^\circ$ [53]. ....	10
Fig. 3 (a) The corundum structure in ideal hexagonal description. The oxygen atoms (red-filled circles) form an hcp array. The metal atoms (blue-filled circles) occupy two-thirds of the octahedral interstices between two oxygen layers. $c$ is the lattice parameter. The metal layers stack as .... <i>ABCABC</i> .... (b) (c) and (d) show the stacking model. The top views of the (b) A layer, (c) B layer and (d) C layer show that the oxygen-sublattice exhibits 6-fold symmetry while the metal sublattice exhibits only 3-fold symmetry. ....	12
Fig. 4 Al-O Phase diagram [83,84]. ....	15
Fig. 5 Cr-O phase diagram [95,96]. ....	19
Fig. 6 V-O Phase diagram (Condensed System, 0.1 MPa) according to H.A. Wriedt (ref. [136]). (V), $\alpha'$ , $\beta$ , $\beta'$ , $\delta$ , $\delta'$ , $\gamma$ indicate the various solid phases of V-O system, and the structure and composition of the phases are shown in Table 4. “L” indicates “liquid”.....	22
Fig. 7 Binary section $\text{Al}_2\text{O}_3\text{-Cr}_2\text{O}_3$ of the Al-Cr-O phase diagram according to [74]. “SS” is short for “solid solution”. ....	28
Fig. 8 Phase diagram in the $\text{Al}_2\text{O}_3\text{-V}_2\text{O}_3$ system [176]. ....	29
Fig. 9 Phase diagram in the $\text{V}_2\text{O}_3\text{-Cr}_2\text{O}_3$ system according to ref. [158]. ....	31
Fig. 10 Phase diagram for the metal-insulator transition in $(\text{Cr}_x\text{V}_{1-x})_2\text{O}_3$ as a function of temperature (extracted from ref. [186]) AFI is short for antiferromagnetic insulator; PM is short for paramagnetic metal; PI is short for paramagnetic insulator. ....	31
Fig. 11 Plasma formation in a magnetron sputtering system with a cylindrical magnetron. ....	36
Fig. 12 Structure-zone-model of Thornton for the films deposited by magnetron sputtering [208] ( $T$ is the substrate temperature during deposition; $T_m$ is the melting point of material.). ....	37

Fig. 13 A schematic representation of the different growth modes [209].	38
Fig. 14 The setup of the Leybold Z 550 PVD coater used in this thesis. The system is equipped with (a) a RF power supply connected with the sputtering target, (b) a multi-gas controller, (c) a DC power supply, (d) a RF power supply used for the plasma plasma-etching of the substrate, (e) the control panel of the system, (f) a RF matching unit, (g) supply of process gases and pressure gauge, (h) the vacuum chamber, (i) a mechanical prevacuum pump, (j) an oil condenser of the prevacuum pump, (k) the gas mass flow controllers, (l) a target holder with water cooling and connection to the RF power supply, and (m) the substrate table with an integrated heater, water cooling and with RF-bias / RF-plasma-etching line below the vacuum chamber.	39
Fig. 15 Schematic experimental setup for the non-reactive RF magnetron sputtering processes used in this thesis: (a) with a circular ceramic target, and, (b) with a segmented ceramic target (one half plate is the material A, and the other half plate is the material B). $\oplus$ indicates $\text{Ar}^+$ , $\ominus$ indicates electron, $\textcircled{N}$ indicates neutral atom.	40
Fig. 16 The relationship between the substrate temperature and the DC voltage applied on the substrate heater when 100 W of RF power is applied to the sputtering target in Ar. The red line is a fitting line.	40
Fig. 17 Sputtering targets and the substrate positions during thin film deposition in relation to the targets in this thesis: (a) a pure $\text{Cr}_2\text{O}_3$ target was used for depositing the pure $\text{Cr}_2\text{O}_3$ film; (b) a pure $\text{V}_2\text{O}_3$ target was used for depositing the pure $\text{V}_2\text{O}_3$ thin film; (c) for the deposition of Cr-Al-O thin films, a segmented target was used; it consists of two half plates; one half plate is a compound of a mixture of $\text{Cr}_2\text{O}_3$ (80 at. %) and $\text{Al}_2\text{O}_3$ (20 at. %), and the other half plate is pure $\text{Cr}_2\text{O}_3$ ; (d) for the deposition of V-Al-O thin films, a similar segmented target was used; one half plate is a compound of a mixture of $\text{V}_2\text{O}_3$ (80 at. %) and $\text{Al}_2\text{O}_3$ (20 at. %), and the other half plate is pure $\text{V}_2\text{O}_3$ ; (e) for the deposition of V-Cr-O thin films, a different segmented target was used, consisting of one half plate of pure $\text{Cr}_2\text{O}_3$ , and another half plate of pure $\text{V}_2\text{O}_3$ . In case of the deposition of pure $\text{Cr}_2\text{O}_3$ and $\text{V}_2\text{O}_3$ thin films, substrates were located below the “race track” erosion zone of	

the targets; in case of deposition of the ternary thin films, the substrate positions were projected in the target plane and marked as Pos. 1 - Pos. 5 in the above images. ....	44
Fig. 18 Schematic drawing of the basic components of the electron probe micro-analyzer. The dashed square shows that the electron beam focuses on the sample surface and characteristic X-rays are generated from beneath the surface and collected by the spectrometer. The shaded area represents the excited volume, from which the chemical information can be obtained [214–216]. ....	46
Fig. 19 Signals generated when high-energy incident electrons interact with a thin sample [217]. The typical analysis depth of AES and EPMA is 0.4 nm - 5 nm and $1\ \mu\text{m} - 2\ \mu\text{m}$ respectively. ....	47
Fig. 20 Schematic representation of (a) the characteristic X-rays emission in EPMA and (b) Auger electron emission in AES [218]. K, L <sub>1</sub> , L <sub>2</sub> , L <sub>3</sub> , M <sub>1</sub> , M <sub>2</sub> ...indicate the various electron energy levels. ....	48
Fig. 21 Schematic drawing of X-rays incident into and reflected from parallel lattice planes and the illustration of the Bragg's law. $d$ is the interplanar spacing and $\theta$ is the scattering angle of the X-rays. ....	51
Fig. 22 Schematic representation of XRD in Bragg-Brentano geometry. The incident angle $\omega$ is defined as the angle between the X-ray source and the sample, and the diffracted angle $2\theta$ is the angle between the incident beam and the detector. ....	51
Fig. 23 A schematic drawing of rocking curves of the films grown on the substrates (a) with nearly perfect epitaxial growth and (b) with strong tilt. ....	52
Fig. 24 (a) schematic representation of texture measurements configuration in pole figures analyses. (b) Pole figure measured at $\omega = 36.472^\circ$ and $2\theta = 72.944^\circ$ from a $(10\bar{1}10)$ oriented $\text{Cr}_2\text{O}_3$ film deposited on $c$ -plane $\alpha\text{-Al}_2\text{O}_3$ substrate deposited at $320\ ^\circ\text{C}$ . $\varphi$ and $\psi$ are azimuth and tilt angles, respectively. ....	54
Fig. 25 schematic representation of RSM configuration (a) symmetrical diffraction geometry, (b) and (c) asymmetrical diffraction geometry. $\omega$ is the angle between the incident beam and the sample surface; $2\theta$ is the angle between the scattered beam and the incident beam; and $\chi$ is the angle between the scattering plane tilted to the in-plane of the sample surface. ....	56

Fig. 26 A section through the reciprocal space for an [0001]-oriented Al <sub>2</sub> O <sub>3</sub> substrate. Regions of reciprocal space in gray could not be detected by RSM. ....	57
Fig. 27 Two examples of RSMs measured in asymmetric geometry of (a) fully strained film and (b) fully relaxed film grown on the substrate. The schematic representations below the RSM results indicate the relationship of the in-plane lattice constant <i>a</i> between the film and the substrate. ....	58
Fig. 28 Energy-level diagram for light scattering (Stokes Raman scattering, Rayleigh scattering, and anti-Stokes Raman scattering) and the infrared absorption according to [226] and [227]. The incident laser radiation energy is $h\nu_0$ , and the vibrational energy is $h\nu_{vibration}$ . ....	60
Fig. 29 Vibrational modes in corundum structured crystals. Me is metal and O is oxygen. (a), (b), (c), (d), (e) and (f) indicate the vibrational modes of $A_{1g}$ , $E_g$ , $A_{1u}$ , $E_u$ , $A_{2g}$ , $A_{2u}$ , respectively. ....	62
Fig. 30 IRRAS optical configuration: $\theta_0$ is the incident angle ( $\theta_0 = 80^\circ$ in this thesis); $R_0$ and $R_r$ are incident and reflected infrared in p-polarization, respectively; $n_0$ is the refractive index of the incident medium (air); $n_1$ and $n_2$ are the complex refractive index of the film and the substrate, respectively; $d$ is the film thickness. ....	63
Fig. 31 Interactions of light with a solid. ....	65
Fig. 32 Schematic representation of imaging and diffraction modes in the TEM [238]. In the imaging mode, an objective aperture is inserted in the back focal plane to select one or more beams that contribute to the final image (BF mode, DF mode, or HRTEM). In the SAED mode, a selected area aperture in the plane of the first intermediate image is inserted to define the diffraction region to be obtained. ....	68
Fig. 33 Schematic representation of film thickness determination by surface profiler. (a) the top view and (b) cross-section of Si substrate covered by a Si stripe; (c) after the plasma-etching process, $t_e$ denotes the plasma-etching depth of the Si substrate; (d) after etching, deposition and removing the covered Si stripe, $t_m$ denotes the measured thickness by the surface profiler, $d$ is the film thickness. $d = t_m + t_e$ . ....	69
Fig. 34 (a) $\theta - 2\theta$ XRD patterns of the Cr <sub>2</sub> O <sub>3</sub> films with different thickness (30 nm, 75 nm, 105 nm, 188 nm, and 407 nm) deposited on the $\alpha$ -Al <sub>2</sub> O <sub>3</sub> substrates at the	

substrate temperature of 400 °C. The film thickness is marked on the corresponding line. The (0006) and (00012) reflections of the films are observed at lower diffraction angles of the corresponding reflections from substrates. The dashed vertical lines show the theoretical positions of the (0006) and (00012) reflections of Cr<sub>2</sub>O<sub>3</sub> according to PDF card No. 38-1479 from the ICDD-database. (b) shows the (0006) reflections of the films in more detail for a narrow range of the diffraction angle. .... 74

Fig. 35 Dependence of the lattice plane distance  $d_{0006}$  on the film thickness for Cr<sub>2</sub>O<sub>3</sub> films deposited at 400 °C. The dashed line indicates the theoretical value of  $d_{0006}$  of Cr<sub>2</sub>O<sub>3</sub> according to PDF card No. 38-1479 from the ICDD-database. .... 74

Fig. 36 Dependence of the FWHM values of (0006) reflections on film thickness for the films deposited at 400 °C. .... 75

Fig. 37 XRD rocking curves ( $\omega$ -scans) of the (0006) reflection of the Cr<sub>2</sub>O<sub>3</sub> films with the thickness of 105 nm, 188 nm, and 407 nm. The FWHM is 1.32°, 1.24°, and 1.07°, respectively. .... 75

Fig. 38 Reciprocal space mapping (RSM) results of the samples with the film thickness of 188 nm and 407 nm. (a) and (b) are the symmetric (0006) reflection and the asymmetric (10 $\bar{1}$ 10) reflection of the  $\alpha$ -Al<sub>2</sub>O<sub>3</sub> substrate upon which the Cr<sub>2</sub>O<sub>3</sub> thin film thickness is 188 nm respectively. (c) and (d) are the symmetric (0006) reflection and the asymmetric (10 $\bar{1}$ 10) reflection of the  $\alpha$ -Al<sub>2</sub>O<sub>3</sub> substrate upon which the Cr<sub>2</sub>O<sub>3</sub> thin film thickness is 407 nm respectively. .... 77

Fig. 39 X-ray pole figures taken from (a) the (0006) peak and (b) the (10 $\bar{1}$ 10) peak of the Cr<sub>2</sub>O<sub>3</sub> film with the thickness of 188 nm deposited on  $\alpha$ -Al<sub>2</sub>O<sub>3</sub> (0001) substrates at 400 °C. .... 78

Fig. 40  $\varphi$ -scan of the (10 $\bar{1}$ 10) reflex of the Cr<sub>2</sub>O<sub>3</sub> film (black line) and  $\alpha$ -Al<sub>2</sub>O<sub>3</sub> substrate (red line). .... 79

Fig. 41 Schematic drawing illustrating the pole figure of the (10 $\bar{1}$ 10) reflection of the Cr<sub>2</sub>O<sub>3</sub> film with the thickness of 188 nm on the  $\alpha$ -Al<sub>2</sub>O<sub>3</sub> substrate: (a) the top view of the structure in real space from the direction  $\langle 0001 \rangle$  (b) pole figure from the (10 $\bar{1}$ 10) peak of the  $\alpha$ -Al<sub>2</sub>O<sub>3</sub> substrate and the Cr<sub>2</sub>O<sub>3</sub> film with two different

domains of orientation. ● Al <sup>3+</sup> ; ● Cr <sup>3+</sup> of the first domain; ● Cr <sup>3+</sup> of the second domain rotated by 60°. .....	79
Fig. 42 TEM results of the Cr <sub>2</sub> O <sub>3</sub> film with the thickness of 188 nm grown on $\alpha$ -Al <sub>2</sub> O <sub>3</sub> substrate at 400 °C: (a) BF image showing a cross sectional view, (b) the SAED pattern revealing a partially epitaxial orientation relationship between the film and the substrate, (c) a HRTEM image of the film and (d) a high resolution TEM image of the interface between the film and the substrate. ....	80
Fig. 43 Raman spectra of the Cr <sub>2</sub> O <sub>3</sub> films with different thickness (30 nm, 75 nm, 105 nm, 188 nm, and 407 nm) deposited on $\alpha$ -Al <sub>2</sub> O <sub>3</sub> substrates and of a Cr <sub>2</sub> O <sub>3</sub> single crystal (supplied by EVOCHEM Advanced Materials GmbH) from bottom to top. The film thickness is marked on the corresponding line. “s” indicates reflexes corresponding to the $\alpha$ -Al <sub>2</sub> O <sub>3</sub> substrates. The gray areas refer to the areas of the Raman shift of the Raman active modes of pure Cr <sub>2</sub> O <sub>3</sub> according to ref. [230,242–244]. ....	82
Fig. 44 Correlation of the Raman shift of the A <sub>1g</sub> mode on the film thickness with a corresponding lattice plane distance $d_{0006}$ obtained from $\theta - 2\theta$ XRD measurements. The inset is the A <sub>1g</sub> vibrational mode [227]. ....	83
Fig. 45 UV-VIS-NIR spectra of Cr <sub>2</sub> O <sub>3</sub> films with different thickness. ....	84
Fig. 46 Plots of $(ah\nu)^2$ vs. $h\nu$ for the Cr <sub>2</sub> O <sub>3</sub> films with different thickness. ....	85
Fig. 47 $\theta - 2\theta$ XRD patterns of the Cr <sub>2</sub> O <sub>3</sub> films with thickness of 320 nm deposited on the $c$ -plane $\alpha$ -Al <sub>2</sub> O <sub>3</sub> substrates. The black curve corresponds to the film grown without plasma-etching process before deposition. The red curve corresponds to the film grown after plasma-etching before deposition. The dashed lines indicate the theoretical (0006) and (00012) reflection positions of Cr <sub>2</sub> O <sub>3</sub> according to the PDF card No. 38-1479 from the ICDD-database. The inset shows the magnification of the (0006) reflections of the film and the substrate. ....	86
Fig. 48 XRD rocking curves ( $\omega$ -scans) of the (0006) reflections of the Cr <sub>2</sub> O <sub>3</sub> films with thickness of 320 nm deposited on the $c$ -plane $\alpha$ -Al <sub>2</sub> O <sub>3</sub> substrates. The black curve corresponds to the film grown without plasma-etching process before deposition. The red curve corresponds to the film grown after plasma-etching before deposition. ....	87

- Fig. 49 RAMAN spectra of the Cr<sub>2</sub>O<sub>3</sub> films with thickness of 320 nm deposited on the *c*-plane  $\alpha$ -Al<sub>2</sub>O<sub>3</sub> substrates. The black curve corresponds to the film grown without plasma-etching process before deposition. The red curve corresponds to the film grown after plasma plasma-etching before deposition. “s” indicates reflexes corresponding to the  $\alpha$ -Al<sub>2</sub>O<sub>3</sub> substrate. The gray areas refer to the Raman active modes of pure Cr<sub>2</sub>O<sub>3</sub> cited from ref. [230,242–244]. The inset shows the magnification of the Raman signal in the wavenumber area characteristic of the *A*<sub>1g</sub> mode of bulk Cr<sub>2</sub>O<sub>3</sub>. ..... 88
- Fig. 50 The IRRAS spectra of the Cr<sub>2</sub>O<sub>3</sub> films with thickness of 320 nm deposited on the *c*-plane  $\alpha$ -Al<sub>2</sub>O<sub>3</sub> substrates. The black curve corresponds to the film grown without plasma-etching process before deposition. The red curve corresponds to the film grown after plasma-etching. The dashed line is the position of *A*<sub>2u</sub> mode of single crystalline Cr<sub>2</sub>O<sub>3</sub> according to ref. [207]..... 89
- Fig. 51 X-ray pole figures taken from (a) the (0006) reflection and (b) the (10 $\bar{1}$ 10) reflection of the Cr<sub>2</sub>O<sub>3</sub> films with the thickness of 320 nm deposited on the *c*-plane  $\alpha$ -Al<sub>2</sub>O<sub>3</sub> substrates without plasma-etching process before coating. .... 89
- Fig. 52 TEM analysis of the Cr<sub>2</sub>O<sub>3</sub> films (320 nm) deposited on the *c*-plane  $\alpha$ -Al<sub>2</sub>O<sub>3</sub> substrates: (a), (c) and (e): the film grown on the  $\alpha$ -Al<sub>2</sub>O<sub>3</sub> substrate without plasma-etching process before deposition. (b), (d) and (f): the film grown on the  $\alpha$ -Al<sub>2</sub>O<sub>3</sub> substrate after plasma-etching. (a) and (b): SAED patterns showing the epitaxial relationship between the film and the substrate. (c) and (d): HRTEM images after FFT and IFFT process. (e) and (f): the partial enlargement for the red square in (c) and (d) respectively. .... 92
- Fig. 53 (a)  $\theta - 2\theta$  XRD results of the V<sub>2</sub>O<sub>3</sub> films deposited on the  $\alpha$ -Al<sub>2</sub>O<sub>3</sub> substrates at different substrate temperatures. The substrate temperatures are marked on the corresponding lines. The (0006) and (00012) reflections of the films are at lower diffraction angles of the corresponding reflections from substrates. The dashed vertical line is the theoretical positions of the (0006) and (00012) reflections of V<sub>2</sub>O<sub>3</sub> according to PDF card No. 34-187 from the ICDD-database. (b) shows the (0006) reflections of the films in more detail for a narrow range of the diffraction angle. .... 95

Fig. 54 Dependence of the relative (0006) intensity ratio of the intensity of the (0006) reflections of the V <sub>2</sub> O <sub>3</sub> films and the substrate on the substrate temperature. ....	96
Fig. 55 Dependence of the FWHM of the (0006) reflections of the V <sub>2</sub> O <sub>3</sub> films on the substrate temperature. ....	96
Fig. 56 Dependence of the lattice distance $d_{0006}$ values of the V <sub>2</sub> O <sub>3</sub> films on the substrate temperature. The dashed line shows the theoretical $d_{0006}$ value of V <sub>2</sub> O <sub>3</sub> according to PDF card No. 34-187 from the ICDD-database. ....	97
Fig. 57 XRD rocking curves ( $\omega$ -scans) of the (0006) reflections of the V <sub>2</sub> O <sub>3</sub> films deposited at 150 °C, 200 °C, 320 °C, 400 °C. The insert shows the enlargement of the mosaic spreading of the film deposited at 150 °C. ....	98
Fig. 58 The FWHM values of the mosaic spreading of (0006) reflections in Fig. 57 (9.49°, 3.44°, 0.99°, and 0.75° for films grown at 150 °C, 200 °C, 320 °C, and 400 °C, respectively). ....	98
Fig. 59 X-ray pole figures taken from the reflections of the V <sub>2</sub> O <sub>3</sub> film grown at (a) (b) 150 °C and (c) (d) 400 °C on the $\alpha$ -Al <sub>2</sub> O <sub>3</sub> (0001) substrate which was plasma-etched before deposition. (a) and (c) are taken from the (0006) reflections, and (b) and (d) are taken from the (10 $\bar{1}$ 10) reflections. ....	99
Fig. 60 RSM results of V <sub>2</sub> O <sub>3</sub> films grown at 320 °C and 400 °C. (a) is the symmetric (0006) reflection of the $\alpha$ -Al <sub>2</sub> O <sub>3</sub> substrate upon which the V <sub>2</sub> O <sub>3</sub> film is grown at 320 °C; (b) is the asymmetric (10 $\bar{1}$ 10) reflection of the $\alpha$ -Al <sub>2</sub> O <sub>3</sub> substrate upon which the V <sub>2</sub> O <sub>3</sub> film is grown at 320 °C; (c) is the symmetric (0006) reflection of the $\alpha$ -Al <sub>2</sub> O <sub>3</sub> substrate upon which the V <sub>2</sub> O <sub>3</sub> film is grown at 400 °C; (d) is the asymmetric (10 $\bar{1}$ 10) reflection of the $\alpha$ -Al <sub>2</sub> O <sub>3</sub> substrate upon which the V <sub>2</sub> O <sub>3</sub> film is grown at 400 °C. ....	100
Fig. 61 TEM results of a V <sub>2</sub> O <sub>3</sub> film with thickness of 50 nm grown on $\alpha$ -Al <sub>2</sub> O <sub>3</sub> substrate after plasma-etching before deposition at 400 °C. (a) BF image showing a cross sectional view, (b) the SAED pattern revealing a partially epitaxial orientation relationship between the film and the substrate, (c) a high resolution TEM (HRTEM) image of the film and, (d) a high resolution TEM image of the interface between the film and the substrate. ....	101

Fig. 62 Raman spectra of the $V_2O_3$ films grown on $\alpha$ - $Al_2O_3$ substrates at different temperatures. The gray areas refer to the Raman active modes of pure $V_2O_3$ according to ref. [247–249,251].....	103
Fig. 63 Correlation of the Raman shift of the $E_g$ mode of the $V_2O_3$ films grown at different substrate temperatures with the corresponding lattice plane distance $d_{0006}$ obtained from $\theta$ - $2\theta$ XRD measurements. The curve is fitted by an exponential function. The inset schematically represents the $E_g$ vibrational mode of $V_2O_3$ [227]. .....	104
Fig. 64 UV-VIS-NIR spectroscopy data from 200 nm to 1200 nm of a $V_2O_3$ film deposited at 150 °C (black curve) and 400 °C (red curve).....	105
Fig. 65 Plots of $(ah\nu)^2$ vs. $h\nu$ for the $V_2O_3$ films grown at 150 °C (black curve) and 400 °C (red curve). .....	105
Fig. 66 $\theta$ - $2\theta$ XRD patterns of the $V_2O_3$ films with 60 nm thickness grown on the $c$ -plane $\alpha$ - $Al_2O_3$ substrates at 400 °C. The black curve corresponds to the film grown without plasma-etching process before deposition. The red curve corresponds to the film grown after plasma-etching for 50 nm before deposition. The dashed lines indicate the theoretical positions of the (0006) and (00012) reflections of $V_2O_3$ according to the PDF card No. 34-187 from the ICDD-database. ....	106
Fig. 67 XRD rocking curves ( $\omega$ -scans) of the (0006) reflections of the $V_2O_3$ films with a thickness of 60 nm grown on the $c$ -plane $\alpha$ - $Al_2O_3$ substrates at 400 °C. The black curve corresponds to the film grown without plasma-etching process before deposition. The red curve corresponds to the film grown after plasma-etching for 50 nm before deposition. ....	107
Fig. 68 X-ray pole figures taken from (a) the (0006) reflections and (b) the $(10\bar{1}10)$ reflections of a $V_2O_3$ film with a thickness of 60 nm grown on an $\alpha$ - $Al_2O_3$ (0001) substrate without plasma-etching before deposition at 400 °C. ....	108
Fig. 69 RSM results of the $V_2O_3$ films (60 nm thickness) grown on the $\alpha$ - $Al_2O_3$ substrates at 400 °C. (a) is the symmetric (0006) reflection of the substrates without plasma-etching before deposition; (b) is the asymmetric $(10\bar{1}10)$ reflection of the substrates without plasma-etching before deposition; (c) is the symmetric (0006) reflection of the substrates after plasma-etching of 50 nm	

depth before deposition; (d) is the asymmetric (10 $\bar{1}$ 10) reflection of the substrates after plasma-etching of 50 nm depth before deposition. ....	109
Fig. 70 Raman spectra of the V <sub>2</sub> O <sub>3</sub> films (60 nm thick) grown on $\alpha$ -Al <sub>2</sub> O <sub>3</sub> substrates without (black curve) and after (red curve) plasma-etching. The areas marked in gray refer to the Raman active modes of pure V <sub>2</sub> O <sub>3</sub> according to refs. [247–249,251]. “s” indicates the Raman signals attributed to the substrates. ....	110
Fig. 71 TEM analysis of the V <sub>2</sub> O <sub>3</sub> films with thickness of 60 nm grown on the <i>c</i> -plane $\alpha$ -Al <sub>2</sub> O <sub>3</sub> substrates. (a) and (c): the film grown on the $\alpha$ -Al <sub>2</sub> O <sub>3</sub> substrate without plasma-etching process before deposition. (b) and (d): the film grown on the $\alpha$ -Al <sub>2</sub> O <sub>3</sub> substrate which was plasma-etched for 50 nm before deposition. (a) and (b): the SAED patterns showing the epitaxial relationship between the films and the substrates. (c) and (d): HRTEM images of cross sections of these samples. ...	112
Fig. 72 The chemical composition of the Al-Cr-O films deposited on the substrates in different positions related to the target. ....	114
Fig. 73 AES depth profile of the Cr-Al-O film deposited on the $\alpha$ -Al <sub>2</sub> O <sub>3</sub> substrate in Pos. 2 according to Fig. 15 (b).....	115
Fig. 74 $\theta - 2\theta$ XRD patterns of the $\alpha$ -(Cr <sub>1-x</sub> Al <sub>x</sub> ) <sub>2</sub> O <sub>3</sub> films with different Al concentration of $x = 0.08$ (curves on top of the diagrams), $0.13$ (curves in the mid of the diagrams), and $0.16$ (curves at the bottom of the diagrams) deposited on the $\alpha$ -Al <sub>2</sub> O <sub>3</sub> substrates without heating (black curves), at $320\text{ }^{\circ}\text{C}$ (red curves), and $400\text{ }^{\circ}\text{C}$ (blue curves). The dashed lines indicate the theoretical position of the (0006) reflection of Cr <sub>2</sub> O <sub>3</sub> according to the PDF card No. 38-1479 from the ICDD-database. (a) $\theta - 2\theta$ XRD patterns in large range of the diffraction angle. (b) the (0006) reflections of the films and the substrates in more detail for a narrow range of the diffraction angle. The (0006) reflections of the films are shifted significantly to lower diffraction angles compared to reflections of the substrates (indicated by the (0006) reflections of Al <sub>2</sub> O <sub>3</sub> ) and are shifted to higher diffraction angles in comparison to those of the pure Cr <sub>2</sub> O <sub>3</sub> . ....	118
Fig. 75 Dependence of the FWHM of the (0006) reflections of the Cr-Al-O films on the Al concentration. The red and blue points correspond to the films deposited at $320\text{ }^{\circ}\text{C}$ and $400\text{ }^{\circ}\text{C}$ , respectively. ....	119

- Fig. 76  $\theta - 2\theta$  XRD patterns of  $\alpha$ -(Cr<sub>1-x</sub>Al<sub>x</sub>)<sub>2</sub>O<sub>3</sub> films with different composition ( $x = 0.08, 0.10, 0.13, 0.15, \text{ and } 0.16$ ) deposited on the  $\alpha$ -Al<sub>2</sub>O<sub>3</sub> substrates at 400 °C. The dashed line indicates the theoretical position of the (0006) reflection of Cr<sub>2</sub>O<sub>3</sub> according to the PDF card No. 38-1479 from the ICDD-database. .... 120
- Fig. 77 Dependence of the lattice plane distance  $d_{0006}$  on the Al concentration of the films (the abscissa is the coefficient  $x$  in  $\alpha$ -(Cr<sub>1-x</sub>Al<sub>x</sub>)<sub>2</sub>O<sub>3</sub>). The dashed horizontal line represents the theoretical  $d_{0006}$  value of Cr<sub>2</sub>O<sub>3</sub> according to the PDF card No. 38-1479 from the ICDD-database ( $d_{0006}(\text{Cr}_2\text{O}_3) = 0.2266 \text{ nm}$ ). .... 121
- Fig. 78 (a) The lattice constants  $a$  and (b)  $c$  of the films versus the Al concentration (the abscissa is the coefficient  $x$  in  $\alpha$ -(Cr<sub>1-x</sub>Al<sub>x</sub>)<sub>2</sub>O<sub>3</sub>). ● (red solid circles) show the measured lattice constants calculated from asymmetric RSM. ■ (black solid squares) show the theoretical lattice constants calculated using data from PDF cards No. 38-1479 and No. 42-1468 (the ICDD-database) according to Vegard's law. .... 122
- Fig. 79 XRD rocking curves ( $\omega$ -scans) of the (0006) reflections of the  $\alpha$ -(Cr<sub>1-x</sub>Al<sub>x</sub>)<sub>2</sub>O<sub>3</sub> films with  $x = 0.08, 0.10, 0.13, 0.15$  and  $0.16$  deposited on the  $\alpha$ -Al<sub>2</sub>O<sub>3</sub> substrates at 400°C. The FWHM values of these mosaic spreading reflections are 1.23°, 1.08°, 1.07°, 1.10° and 1.43°, respectively. .... 124
- Fig. 80 TEM images of the  $\alpha$ -(Cr<sub>1-x</sub>Al<sub>x</sub>)<sub>2</sub>O<sub>3</sub> films with (a) (c) (e):  $x = 0.16$  and (b) (d) (f):  $x = 0.13$  deposited at 400 °C on the  $\alpha$ -Al<sub>2</sub>O<sub>3</sub> substrates. (a) and (b): BF image showing a cross sectional view of the films grown on the  $\alpha$ -Al<sub>2</sub>O<sub>3</sub> substrates. (c) and (d): SAED patterns revealing a partially epitaxial orientation relationship between the films and the substrates. (e) and (f): HRTEM images of the films, with the insets showing the FFT images of the HRTEM images, indicating the same lattice planes as shown in (c) and (d). The dashed lines indicate the boundaries of the individual grains. The arrows in (e) and (f) show the film growth direction of  $\langle 0001 \rangle$ . .... 127
- Fig. 81 Raman spectra of the  $\alpha$ -(Cr<sub>1-x</sub>Al<sub>x</sub>)<sub>2</sub>O<sub>3</sub> films with different Al concentration of  $x = 0.08$  (curves in the upper part),  $0.13$  (curves in the middle part), and  $0.16$  (curves in the bottom part) deposited on the  $\alpha$ -Al<sub>2</sub>O<sub>3</sub> substrates at different temperatures. "s" indicates the reflexes corresponding to the substrates. The gray

areas refer to the Raman active modes of pure Cr <sub>2</sub> O <sub>3</sub> cited from ref. [230,242–244].	128
Fig. 82 Dependence of the Raman shift of the <i>A</i> <sub>1g</sub> mode on the Al concentration <i>x</i> ( $0.08 \leq x \leq 0.16$ ) of the $\alpha$ -(Cr <sub>1-x</sub> Al <sub>x</sub> ) <sub>2</sub> O <sub>3</sub> films deposited at 320 °C and 400 °C. The <i>A</i> <sub>1g</sub> mode of the Cr <sub>2</sub> O <sub>3</sub> single crystal is located at 552.0 cm <sup>-1</sup> .	129
Fig. 83 Correlation of the Raman shift of the <i>A</i> <sub>1g</sub> mode of $\alpha$ -(Cr <sub>1-x</sub> Al <sub>x</sub> ) <sub>2</sub> O <sub>3</sub> films with various Al concentration ( <i>x</i> = 0.16, 0.15, 0.13, 0.10, 0.08) and deposited at 400 °C with the corresponding lattice constant <i>c</i> of the films ( <i>c</i> has been calculated from results of $\theta$ - $2\theta$ XRD measurements). The black curve is fitted by an exponential function.	130
Fig. 84 The IRRAS spectra of the Cr <sub>2</sub> O <sub>3</sub> and $\alpha$ -(Cr <sub>1-x</sub> Al <sub>x</sub> ) <sub>2</sub> O <sub>3</sub> films with different composition ( <i>x</i> = 0.08, 0.10, 0.13, 0.15, and 0.16) deposited on $\alpha$ -Al <sub>2</sub> O <sub>3</sub> substrates at 400 °C. The spectra of $\alpha$ -(Cr <sub>1-x</sub> Al <sub>x</sub> ) <sub>2</sub> O <sub>3</sub> films can be fitted to two peaks ( <i>A</i> <sub>2u</sub> mode and <i>E</i> <sub>u</sub> mode) by Gaussian functions. The red dashed lines represent the longitudinal optical phonon frequency of the <i>A</i> <sub>2u</sub> and <i>E</i> <sub>u</sub> mode of single crystal Cr <sub>2</sub> O <sub>3</sub> according to ref. [207].	131
Fig. 85 Dependence of the band position of the <i>E</i> <sub>u</sub> mode of the $\alpha$ -(Cr <sub>1-x</sub> Al <sub>x</sub> ) <sub>2</sub> O <sub>3</sub> ( $0.08 \leq x \leq 0.16$ ) films deposited at 400 °C and the pure Cr <sub>2</sub> O <sub>3</sub> ( <i>x</i> = 0) cited from ref. [207] on Al concentration.	132
Fig. 86 The IRRAS spectra of the $\alpha$ -(Cr <sub>1-x</sub> Al <sub>x</sub> ) <sub>2</sub> O <sub>3</sub> films with different concentration ( <i>x</i> = 0.08, blue curves; <i>x</i> = 0.13, red curves; <i>x</i> = 0.16, black curves) deposited at different substrate temperatures. The absolute length of the vertical axis in (a) (b) and (c) are the same. The blue curves are fitted by Gaussian function.	133
Fig. 87 Dependence of the <i>E</i> <sub>u</sub> mode position of the $\alpha$ -(Cr <sub>1-x</sub> Al <sub>x</sub> ) <sub>2</sub> O <sub>3</sub> ( $0.08 \leq x \leq 0.16$ ) films deposited at 320 °C and 400 °C on the Al concentration.	134
Fig. 88 Plots of $(\alpha h\nu)^2$ vs. $h\nu$ for the $\alpha$ -(Cr <sub>1-x</sub> Al <sub>x</sub> ) <sub>2</sub> O <sub>3</sub> ( <i>x</i> = 0.16, 0.13, 0.08) deposited at (a) without substrate heating (135 °C) (b) 320 °C and (c) 400 °C. (d) Dependence of the experimental band gap of $\alpha$ -(Cr <sub>1-x</sub> Al <sub>x</sub> ) <sub>2</sub> O <sub>3</sub> films on the Al concentration <i>x</i> and substrate temperature.	135
Fig. 89 The atomic concentration of the elements in the V-Al-O films (left-sided Y-axis) and the atomic concentration ratio of metal to oxygen concentration (right-	

sided Y-axis, data shown in hollow circles) dependent on different sample positions in relation to the target.....	138
Fig. 90 $\theta - 2\theta$ XRD patterns of $\alpha$ -(V <sub>1-x</sub> Al <sub>x</sub> ) <sub>2</sub> O <sub>3</sub> thin films deposited on the $\alpha$ -Al <sub>2</sub> O <sub>3</sub> substrates at different positions as shown in Fig. 17 (d). The reflections of the films are observed at lower $2\theta$ positions in relation to the substrates. The dashed line indicates the theoretical position of the (0006) reflection of V <sub>2</sub> O <sub>3</sub> according to the PDF card No. 34-187 from the ICDD-database. (a) $\theta - 2\theta$ XRD patterns in large range of the diffraction angle. (b) the (0006) reflections of the films and the substrates in more detail for a narrow range of the diffraction angle. ....	139
Fig. 91 Dependence of the (0006) lattice plane distance ( $d_{0006}$ ) on the sample position during deposition. The theoretical $d_{0006}$ values of the V <sub>2</sub> O <sub>3</sub> and Al <sub>2</sub> O <sub>3</sub> are marked in this graph. The dashed line is a fitting curve. ....	141
Fig. 92 Dependence of the (0006) lattice plane distance ( $d_{0006}$ ) on the concentration of Al. The dashed line is a fitting curve. ....	141
Fig. 93 The XRD rocking curves ( $\omega$ -scans) of the (0006) reflections of the V-Al-O films deposited at different positions, from Pos. 1 to Pos. 5 (in black, red, green, blue, and magenta color, respectively).....	142
Fig. 94 Dependence of the FWHM values of the mosaic spreadings of the (0006) reflections on the Al concentration (From Pos. 1 to Pos. 5: 0.36°, 0.34°, 0.27°, 0.31° and 0.31°, respectively). ....	142
Fig. 95 RSM results of the $\alpha$ -(V <sub>1-x</sub> Al <sub>x</sub> ) <sub>δ+2</sub> O <sub>3</sub> films deposited on $\alpha$ -Al <sub>2</sub> O <sub>3</sub> substrates in different positions related to the target: (a) and (b) in Pos. 1; (c) and (d) in Pos. 3; (e) and (f) in Pos. 5. (a), (c) and (e) are the symmetric (0006) reflections and (b), (d) and (f) are the asymmetric (10 $\bar{1}$ 10) reflections.....	144
Fig. 96 The lattice constants $a$ (below) and $c$ (above) versus the sample positions during deposition. ● (red solid circles) show the real lattice constants calculated from RSM; ■ (black solid squares) show the theoretical lattice constants calculated using data from PDF card No. 34-187 and No. 42-1468 (the ICDD-database) according to Vegard's law. ....	145
Fig. 97 X-ray pole figures taken from (a) the (0006) reflections and (b) the (10 $\bar{1}$ 10) reflections of the $\alpha$ -(V <sub>1-x</sub> Al <sub>x</sub> ) <sub>2</sub> O <sub>3</sub> film deposited on the substrate without plasma-etching process. ....	146

- Fig. 98 TEM images of the  $\alpha$ -(V<sub>1-x</sub>Al<sub>x</sub>)<sub>2</sub>O<sub>3</sub> film deposited in Pos. 3. (a) BF image showing a cross sectional view of the film grown on the  $\alpha$ -Al<sub>2</sub>O<sub>3</sub> substrate. (b) SAED patterns revealing a partially epitaxial orientation relationship between the film and the substrate. (c) IFFT image of the HRTEM image shown in the inset which shows the interface between the substrate and the film. (d) IFFT image of the HRTEM image shown in the inset which shows the film. .... 147
- Fig. 99 Raman spectra of the  $\alpha$ -(V<sub>1-x</sub>Al<sub>x</sub>)<sub>2</sub>O<sub>3</sub> thin films deposited on the  $\alpha$ -Al<sub>2</sub>O<sub>3</sub> substrates in different positions related to the target. “s” indicates the reflexes corresponding to the substrates. The gray areas refer to the Raman active modes of pure V<sub>2</sub>O<sub>3</sub> measured at room temperature according to ref. [247–249,251]..... 148
- Fig. 100 Dependence of Raman shift of the two  $A_{1g}$  modes on the sample position. The black curve indicates the Raman shift of the first  $A_{1g}$  mode dependent on the sample position. The red curve indicates the Raman shift of the first  $A_{1g}$  mode dependent on the sample position..... 149
- Fig. 101 The IRRAS spectra of the  $\alpha$ -(V<sub>1-x</sub>Al<sub>x</sub>)<sub>2</sub>O<sub>3</sub> thin films with different composition deposited on  $\alpha$ -Al<sub>2</sub>O<sub>3</sub> substrates. The red dashed lines give the IR bands cited from ref. [139]. The curves with different colors indicate the films deposited in different positions (black, red, green, blue, and magenta represent the samples deposited in Pos. 1 to Pos. 5 respectively)..... 149
- Fig. 102 Plots of  $(ah\nu)^2$  vs.  $h\nu$  for the  $\alpha$ -(V<sub>1-x</sub>Al<sub>x</sub>)<sub>2</sub>O<sub>3</sub> thin films with different composition, deposited on  $\alpha$ -Al<sub>2</sub>O<sub>3</sub> substrates. The curves with different colors indicate the films deposited in different positions (black, red, green, blue, and magenta for the Pos. 1 to Pos. 5 respectively)..... 151
- Fig. 103 Dependence of the band gap of the films on the sample positions..... 151
- Fig. 104  $\theta - 2\theta$  XRD patterns of the  $\alpha$ -(V<sub>1-x</sub>Cr<sub>x</sub>)<sub>2</sub>O<sub>3</sub> films with different composition ( $x = 0.115, 0.094, 0.088, 0.087$  and  $0.078$ ) deposited on the  $\alpha$ -Al<sub>2</sub>O<sub>3</sub> substrates in the sample Pos. 1 to 5, respectively. The (0006) reflections of the films are observed at lower diffraction angle compared to the substrates. The dashed lines indicate the theoretical (0006) reflection positions of Cr<sub>2</sub>O<sub>3</sub> and V<sub>2</sub>O<sub>3</sub> according to the PDF card No. 38-1479 and No. 34-187 from the ICDD-database. (a)  $\theta - 2\theta$  XRD patterns in large range of the diffraction angle. (b) the (0006) reflections of

the films and the substrates in more detail for a narrow range of the diffraction angle.....	154
Fig. 105 Dependence of the lattice plane distance $d_{0006}$ on the Cr concentration of the films (the abscissa is the coefficient $x$ in $\alpha-(V_{1-x}Cr_x)_2O_3$ ). The dashed horizontal line represents the theoretical $d_{0006}$ value of $V_2O_3$ , $Cr_2O_3$ and $Al_2O_3$ according to the PDF card No. 34-187, No. 38-1479, and No. 42-1468 from the ICDD-database, respectively. ( $d_{0006}(V_2O_3) = 0.2336$ nm, $d_{0006}(Cr_2O_3) = 0.2266$ nm, and $d_{0006}(Al_2O_3) = 0.2165$ nm) .	155
Fig. 106 XRD rocking curves ( $\omega$ -scans) of the (0006) reflections of the $\alpha-(V_{1-x}Cr_x)_2O_3$ films with $x = 0.12, 0.09$ , and $0.07$ deposited in Pos. 1 (black), Pos. 3 (green) and Pos. 5 (magenta). The FWHM values of these mosaic spreading reflections are $0.358^\circ, 0.366^\circ$ and $0.365^\circ$ , respectively.....	155
Fig. 107 RSM results of the V-Cr-O films deposited on $\alpha-Al_2O_3$ substrates in different positions related to the target: (a) and (b) are in Pos. 1; (c) and (d) are in Pos. 3; (e) and (f) are in Pos. 5. (a), (c) and (e) are the symmetric (0006) reflections, and (b), (d) and (f) are the asymmetric $(10\bar{1}10)$ reflections.....	156
Fig. 108 The lattice constants (a) $c$ and (b) $a$ versus Cr concentration $x$ . ● (red solid circles) show the real lattice constants calculated from RSM data; ■ (black solid squares) show the theoretical lattice constants calculated using data from PDF card No. 34-187 and No. 38-1479 (the ICDD-database) according to Vegard's law.....	158
Fig. 109 X-ray pole figures taken from (a) the (0006) reflection and (b) the $(10\bar{1}10)$ reflection of the $\alpha-(V_{1-x}Cr_x)_2O_3$ film deposited on the substrate without plasma plasma-etching process. ....	159
Fig. 110 TEM images of the $\alpha-(V_{1-x}Cr_x)_2O_3$ film deposited in Pos. 3. (a) BF image showing a cross sectional view of the film grown on the $\alpha-Al_2O_3$ substrate. (b) SAED patterns revealing an epitaxial orientation relationship between the film and the substrate. (c) IFFT image of the HRTEM image shown in the inset, pointing to the interface between the substrate and the film. (d) IFFT image of the HRTEM image shown in the inset, describing the film.....	160
Fig. 111. Raman spectra of the V-Cr-O films of different composition deposited on $\alpha-Al_2O_3$ substrates. The films vary from the Cr-rich side to Cr-poor side from	

Pos. 1 to Pos. 5. The cyan areas refer to the Raman active modes of pure Cr <sub>2</sub> O <sub>3</sub> cited from ref. [230,242–244]. The gray areas refer to the Raman active modes of pure V <sub>2</sub> O <sub>3</sub> cited from ref. [247–249,251].	161
Fig. 112 The IRRAS spectra of the V-Cr-O thin films with different composition deposited on $\alpha$ -Al <sub>2</sub> O <sub>3</sub> substrates. The curves with different colors indicate the films deposited in different positions (black, red, green, blue, and magenta represent the samples deposited in Pos. 1, Pos. 2, Pos. 3, Pos. 4 and Pos. 5 respectively).	162
Fig. 113 Plots of $(ah\nu)^2$ vs. $h\nu$ for the V-Cr-O thin films of different composition deposited on $\alpha$ -Al <sub>2</sub> O <sub>3</sub> substrates. The sample positions are marked in the graph correspondingly.	163
Fig. 114 Dependence of the band gap of the films on the relative Cr concentration $x$ .	163
Fig. 115 The lattice constant $a$ of the different corundum-type systems including Al <sub>2</sub> O <sub>3</sub> , Cr <sub>2</sub> O <sub>3</sub> , V <sub>2</sub> O <sub>3</sub> , V-rich (V,Al) <sub>2</sub> O <sub>3</sub> , Cr-rich (Cr,Al) <sub>2</sub> O <sub>3</sub> , and V-rich (V,Cr) <sub>2</sub> O <sub>3</sub> .	173
Fig. 116 The in-plane strain of the different corundum-type systems including Al <sub>2</sub> O <sub>3</sub> , Cr <sub>2</sub> O <sub>3</sub> , V <sub>2</sub> O <sub>3</sub> , V-rich (V,Al) <sub>2</sub> O <sub>3</sub> , Cr-rich (Cr,Al) <sub>2</sub> O <sub>3</sub> , and V-rich (V,Cr) <sub>2</sub> O <sub>3</sub> .	174
Fig. 117 The band gap of the different corundum-type systems including Al <sub>2</sub> O <sub>3</sub> , Cr <sub>2</sub> O <sub>3</sub> , V <sub>2</sub> O <sub>3</sub> , V-rich (V,Al) <sub>2</sub> O <sub>3</sub> , Cr-rich (Cr,Al) <sub>2</sub> O <sub>3</sub> , and V-rich (V,Cr) <sub>2</sub> O <sub>3</sub> . ■ indicates the experimental data, and ▲ indicates the cited data from ref. [79,105,184,237,246,271].	174
Fig. 118 Film growth, structure and optical property of Al <sub>2</sub> O <sub>3</sub> -Cr <sub>2</sub> O <sub>3</sub> -V <sub>2</sub> O <sub>3</sub> system deposited at 400 °C. SZM indicates the structure-zone-model which is described in Fig. 12 (Z1, Z2 and Z3 are zone 1, zone 2 and zone 3, respectively). The red regions are the composition of the ternary films studied in this work. $D$ , $f_a$ , $E_g$ , and $T_{min}$ indicate the crystal grain size, in-plane lattice misfit, band gap and minimum temperature to crystallize, respectively.	175

# List of tables

Table 1 Lattice parameters and atomic distances of  $\alpha$ -Al<sub>2</sub>O<sub>3</sub>, Cr<sub>2</sub>O<sub>3</sub>, and V<sub>2</sub>O<sub>3</sub> at room temperature and pressure of  $1.01 \times 10^5$  Pa. Lattice parameters of  $\alpha$ -Al<sub>2</sub>O<sub>3</sub>, Cr<sub>2</sub>O<sub>3</sub>, and V<sub>2</sub>O<sub>3</sub> are according to the PDF card No. 42-1468, No. 38-1479, and No. 34-187 from the International Center for Diffraction Data (ICDD) database, respectively. Unit cell volumes are calculated by the formula  $V = \frac{\sqrt{3}a^2c}{2}$ . The atom distances of  $\alpha$ -Al<sub>2</sub>O<sub>3</sub> are cited from ref. [62], and the atom distances of Cr<sub>2</sub>O<sub>3</sub> and V<sub>2</sub>O<sub>3</sub> are from ref. [54]. Me denotes metal (Al, Cr, or V). Me, O<sub>1</sub>, O<sub>2</sub>, O<sub>3</sub>, O<sub>4</sub>, and O<sub>5</sub> are shown in Fig. 3..... 13

Table 2 Properties of  $\alpha$ -Al<sub>2</sub>O<sub>3</sub>..... 15

Table 3 Properties of Cr<sub>2</sub>O<sub>3</sub>. ..... 19

Table 4 The equilibrium solid phases of the V-O system (Condensed System, 0.1 MPa; “bcc” indicates body centered cubic structure; “bct” indicates body centered tetragonal structure; “fcc” indicates face centered cubic structure). ..... 23

Table 5 Properties of V<sub>2</sub>O<sub>3</sub>. ..... 24

Table 6 The mean free path of target atoms in an Ar plasma in this thesis..... 41

Table 7 Materials for sputtering targets used for thin film deposition. (A and B denote the target materials of the half plates in Fig. 15.) ..... 43

Table 8 Parameters of the X-ray diffractometer used for the texture / pole figure measurements..... 54

Table 9 The chemical composition of the Cr<sub>2</sub>O<sub>3</sub> films deposited on the  $c$ -Al<sub>2</sub>O<sub>3</sub> substrates (standards used for calibrating see section 3.2.1)..... 72

Table 10 Optical properties of the Cr<sub>2</sub>O<sub>3</sub> films ( $E_g$ : the band gap;  $B$ : a constant in Eq.(18)). ..... 85

Table 11 The chemical composition of the V<sub>2</sub>O<sub>3</sub> films deposited on the  $c$ -Al<sub>2</sub>O<sub>3</sub> substrates (standards used for calibrating see section 3.2.1) at 400 °C. .... 93

Table 12 The wavenumber positions of the Raman active modes of the V<sub>2</sub>O<sub>3</sub> films deposited at different temperatures and the reference value of bulk V<sub>2</sub>O<sub>3</sub> cited from ref. [247,249]..... 103

Table 13 The Raman shift and FWHM of the bands attributed to the $V_2O_3$ films grown on $\alpha$ - $Al_2O_3$ substrates without and after plasma-etching (The data are after fitting by Gaussian; $E_g^1$ indicates the first $E_g$ mode and $A_{1g}^1$ indicates the first $A_{1g}$ mode in the range of $200\text{ cm}^{-1}$ - $250\text{ cm}^{-1}$ in Fig. 70).....	111
Table 14 The chemical composition of the Al-Cr-O films deposited on the substrates at $400\text{ }^\circ\text{C}$ in different positions related to the target: $x$ and $\delta$ describe the Al concentration and the deviation from a perfect theoretical stoichiometry in $(Cr_{1-x}Al_x)_{2+\delta}O_3$ respectively (standards used for calibrating see section 3.2.1). ....	114
Table 15 The intensity ratio of the (0006) reflection of the $\alpha$ - $(Cr_{1-x}Al_x)_2O_3$ film and the corresponding reflection of the substrate ( $I_{film(0006)} / I_{substrate(0006)}$ ). ....	117
Table 16 Texture evolution of the $\alpha$ - $(Cr_{1-x}Al_x)_2O_3$ films with different Al concentration ( $x=0.16, 0.13$ and $0.08$ ) grown on the $\alpha$ - $Al_2O_3$ substrates after plasma-etching at different substrate temperatures. ....	126
Table 17 Infrared band assignments of the $Cr_2O_3$ and $\alpha$ - $(Cr_{1-x}Al_x)_2O_3$ ( $x = 0.08, 0.10, 0.13, 0.15,$ and $0.16$ ) films deposited on $\alpha$ - $Al_2O_3$ substrates at $400\text{ }^\circ\text{C}$ in this study, and the reference of the bulk $Cr_2O_3$ cited from ref. [207]. ....	132
Table 18 Optical parameters of the $\alpha$ - $(Cr_{1-x}Al_x)_2O_3$ films ( $x$ is the Al concentration; $E_g$ is the band gap; $B$ is a constant in Eq. (18)). ....	136
Table 19 The chemical composition of the V-Al-O films deposited on the substrates in different positions related to the target: $x$ and $\delta$ describe the relative Al concentration and the deviation from a perfect theoretical stoichiometry in Eq. (23) and (24) respectively (standards used for calibrating see section 3.2.1). .	137
Table 20 Optical parameters of the $\alpha$ - $(V_{1-x}Al_x)_2O_3$ thin films ( $E_g$ is the band gap; $B$ is a constant in Eq.(18)).....	150
Table 21 The chemical composition of the V-Cr-O films deposited on the substrates in different positions related to the target: $x$ and $\delta$ describe the relative Cr concentration and the deviation from a perfect theoretical stoichiometry in Eq. (27) and (28) respectively (standards used for calibrating see section 3.2.1). .	153
Table 22 Optical parameters of the V-Cr-O thin films ( $E_g$ is the band gap; $B$ is a constant in Eq. (18)). ....	164

# Symbols and abbreviations

Symbol	Unit	Meaning
$a$	nm	Lattice parameter in hexagonal lattices
$a_{film}$	nm	Actually measured lattice constant of a thin film
$a_{film}^{relax}$	nm	Totally relaxed lattice constant, i.e. the theoretical value from PDF card from ICDD
$a_{substrate}$	nm	Lattice constant of the substrate
$A$		The absorbance of the sample
$b$		The line broadening due to the instrument (= $0.07^\circ$ )
$B$		Measured full width at half maximum
$c$	nm	Lattice parameter in hexagonal lattices
$d$	m	Film thickness
$d(M)$	nm	Molecular diameter (M is chemical element)
$d_{hkl}$	nm	Lattice plane distance
$D$	nm	Grain size
$D(M)$		Diffusion coefficient (M is chemical element)
$E_g$	eV	Energy band gap
$f_a$		Misfit
$h$	J·s	Planck's constant (= $6.626 \times 10^{-34}$ J·s)
$hkl$		Miller indices
$hkil$		Miller-Bravais indices
$k$	J/K	Boltzmann constant
$K$		Scherrer constant
$N_A$	kg	Mass
$p$	Pa	Gas pressure
$q_{//}$	1/nm	The in-plane scattering vector component along one of the $\langle 11\bar{2}0 \rangle$ directions in reciprocal lattice units
$q_{\perp}$	1/nm	The out-of-plane scattering vector component perpendicular to the epilayer surface i.e. $\langle 0001 \rangle$ directions in reciprocal lattice units

$r$		Degree of in-plane relaxation
$R_a$	nm	Average roughness
$t_e$	nm	Plasma-etching depth
$t_m$	nm	Measured film thickness value by profiler
$T$	K or °C	Temperature in Kelvin and Celsius
$V$	nm <sup>3</sup>	Unit cell volume
$\alpha_1$	°	Angles between axial vectors in crystals
$\alpha_2$	1/nm	Optical absorption coefficient
$\beta_1$	°	Angles between axial vectors in crystals
$\beta_2$		Correction coefficient by Gaussian profile
$\gamma$	°	Angles between axial vectors in crystals
$\gamma_{substrate}$	J/m <sup>2</sup>	The surface energy of the substrate
$\gamma_{film}$	J/m <sup>2</sup>	The surface energy of the film
$\gamma_{interface}$	J/m <sup>2</sup>	The interface energy between the film and the substrate.
$2\theta$	°	Angle between the incident and diffracted (reflected) X-ray beams
$\epsilon_a$		The in-plane strain
$\lambda_1$	nm	Mean free path
$\lambda_2$	nm	X-ray wavelength
$\lambda_i$	m	Excitation wavelength, i.e. the incident laser wavelength
$\lambda_s$	m	Raman spectrum wavelength
$\varphi$	°	Angle between two lattice planes
$\phi$	°	Azimuth angle in-plane
$\psi$	°	Tilting angle between the scattering vector and the normal to the sample surface
$\omega$	°	Angle between the X-ray source and the sample
$\nu$	Hz	Frequency
$\Delta\nu$	cm <sup>-1</sup>	Raman shift

<b>Abbreviation</b>	<b>Meaning</b>
3D	Three Dimensional
AC	Alternating Current
AES	Auger Electron Spectroscopy
AFI	Antiferromagnetic Insulating
BF	Bright-Field
bcc	body centered cubic
bct	body centered tetragonal
CVD	Chemical Vapor Deposition
DC	Direct Current
DF	Dark-Field
EPMA	Electron Probe Micro-Analysis
FFT	Fast Fourier Transformation
FIB	Focused Ion Beam
Fig.	Figure
FM	Frank-van der Merwe
FWHM	Full Width at Half Maximum
fcc	face centered cubic
hcp	hexagonal close-packed
HRTEM	High-Resolution Transmission Electron Microscopy
ICDD	International Center for Diffraction Data
IFFT	Inverse Fast Fourier Transformation
IR	Infrared
IRRAS	Infrared Reflection Absorption Spectroscopy
MBE	Molecular Beam Epitaxy
MIT	Metal-Insulator Transition
MOCVD	Metal-organic Chemical Vapor Deposition
OPA-MBE	Oxygen-Plasma-Assisted Molecular Beam Epitaxy
PDF	Powder Diffraction File
PI	Paramagnetic Insulator
PLD	Pulsed Laser Deposition

PM	Paramagnetic Metallic
P-MBE	Plasma-assisted Molecular Beam Epitaxy
PVD	Physical Vapor Deposition
RF	Radio-Frequency
RSM	Reciprocal Space Mapping
SAED	Selected Area Electron Diffraction
SK	Stranski-Krastanov
TEM	Transmission Electron Microscopy
UHV	Ultra High Vacuum
UV-VIS	Ultraviolet-Visible
VW	Volmer-Weber
XRD	X-ray Diffraction

# 1 Introduction, Motivation and Objectives

In this chapter, a brief overview of the background, motivation and objectives of this study are given.

## 1.1 Introduction

Thin film technology is a key technology that includes both surface modification and surface coatings. This technology can be beneficially applied to many technical applications, such as surface functionalization, protection and decoration, and optical and micro-electronic devices. Thin film deposition processes can be realized by the deposition of atoms, ions, and molecules. They can be tailored to functionalize a substrate material in a desired way. The chemical composition, microstructure and properties of a growing thin film are also controlled by the deposition conditions [1,2]. Epitaxial is a film grown on the crystalline substrate in ordered fashion that atomic arrangement of the film accepts crystallographic structure of the substrate. The novel properties of the films are strongly dependent on stoichiometry, composition, crystalline state, thickness, etc. High crystal quality is needed especially for electronics and optics applications. Epitaxial growth is one of the most important film techniques to fabricate various electronic and optical devices [3].

Typical deposition methods encompass for example techniques of physical vapor deposition (PVD), chemical vapor deposition (CVD) and the chemical solvent deposition including sol-gel deposition [1,4–8]. Each deposition process has its own advantages, disadvantages and applications. CVD is the deposition of atoms and molecules by the reduction and decomposition of a chemical vapor precursor species which contains the materials to be deposited at high temperatures many hundreds of degrees than the melting point which is close to thermodynamic equilibrium [9]. CVD is extremely useful in the process of atomic layer deposition at depositing extremely thin layers of material for epitaxial films. CVD offers a lot of advantages such as good film uniformity, compatibility,

conformal growth with good step coverage, high deposition rates and scalability from laboratory to industrial production. However, there are many disadvantages of CVD such as serious toxic or flammable gases are used, adequate precursors should be found and high deposition temperature is needed. The main use of CVD in industry is Si technology and growing for III-IV compounds. PVD is the most promising technique which allows for the synthesis of thin films in metastable solid solution with regard of their kinetic non-equilibrium conditions at low deposition temperature. The PVD process is divided into thermal evaporation (i.e. molecular beam epitaxy (MBE), electron-beam evaporation, pulsed laser deposition (PLD), etc.), sputtering (i.e. direct current (DC), alternating current (AC), radio-frequency (RF), ion-beam, reactive and magnetron sputtering), and arc discharge [10]. Among these PVD processes for growing epitaxial films, MBE is used for which are required for lower substrate temperature, but ultrahigh-vacuum (typical around  $10^{-8}$  Pa) and very low deposition rate (around 1 nm/min) [5,9]. Therefore, MBE is mainly applied for laboratory experiments because it is inefficient for mass production. Sputtering is another main vaporization film technique, in which the condensation and film growth processes frequently occur far from the thermodynamic equilibrium, due to kinetic restrictions. Thus, a good control of both the thermodynamic and the kinetic conditions has implications on the growth dynamics and enables the tailoring of the structural, optical, electrical, and mechanical properties of the films [6]. The deposition temperature can affect the energy transferred to the film forming species (adatoms), which enables control over the film morphology and structural characteristics [7]. One way to control the growth dynamics is by heating the substrate during the deposition [9]. Another way to achieve epitaxial layer is by low energy ion implantation [8]. Among these sputtering methods, magnetron sputtering is one of the most promising techniques by which a wide variety of thin films can be made with little film contamination and at a high deposition rate, low temperature and low pressure. It has led to the development of lots of commercial applications such as hard coatings, wear-resistant coatings, low friction coatings, corrosion-resistant coatings, decorative coatings and coatings with specific optical, or electrical properties [11]. Magnetron sputtering technology can deposit metals, alloys, compounds, organic matters, oxides, nitrides etc. on the substrate surface through selecting the appropriate sputtering process, different target materials and ambient gases [12].

Oxides display a remarkable range of materials properties: some are hardening, insulating and ferroelectric while others demonstrate specific optical, electrical and magnetic properties.  $\text{Al}_2\text{O}_3$  is a widely used material in industry in both the bulk and thin film forms. Particularly, the corundum phase ( $\alpha\text{-Al}_2\text{O}_3$ ) coatings are associated with high melting point (2327 K), excellent mechanical properties as well as superior chemical stability. Therefore,  $\alpha\text{-Al}_2\text{O}_3$  thin films have been used in tool industries as wear resistant and protective coatings [13–16], thermal and diffusion barriers [15,17–19], microelectronics applications [20,21] and optical industries [22–24].  $\text{Cr}_2\text{O}_3$  is one of the hardest among the common oxides with the microhardness of 29 GPa [25]. It also shows good mechanical, chemical inertness, magnetic and optical properties. Therefore, it has been used for protective coatings [26], optics [27], electronics [28], and various catalytic systems [29,30].  $\text{V}_2\text{O}_3$  displays a metal-insulator transition (MIT) as a function of temperature, pressure, and doping concentration [31].  $\alpha\text{-Al}_2\text{O}_3$ ,  $\text{Cr}_2\text{O}_3$  and  $\text{V}_2\text{O}_3$  are iso-structural with the space group of  $R\bar{3}c$ , which is advantageous for the hetero-epitaxial growth. In this work,  $\alpha\text{-Al}_2\text{O}_3$  substrates with the same crystal structure as the films ( $\text{Cr}_2\text{O}_3$ ,  $\text{V}_2\text{O}_3$ , etc.) are used in order to get epitaxial films at lower temperature by PVD. However, the film and the substrate have similar lattice parameters with lattice mismatches of less than 5 % in  $a$ -axis, which results in challenges to grow the epitaxial films. Various research groups [32–34] have explored several ways to improve epitaxial quality of the films by sputtering methods, such as increasing the deposition temperature, pre or post treatments, decreasing the film thickness and so on. More details are given in section 2.

The so-called “Holleck triangle” which classifies the most common protective coating materials according to their chemical bonds has often been used for a first approach to the design of novel hard and functional coatings [35,36]. Its philosophy can also be applied to develop novel ceramic layer materials including metal nitrides, carbides, borides etc., i.e. new oxide thin films in form of metastable solid solution structures. Such materials exhibit strong ionic bonds (with energies up to several thousand kilojoules per mole, while the Al-O bonding energy is  $507.5 \text{ kJ/mol} \pm 2.9 \text{ kJ/mol}$ , the Cr-O bonding energy is  $461 \text{ kJ/mol} \pm 8 \text{ kJ/mol}$ , and the V-O bonding energy is  $626 \text{ kJ/mol} \pm 9 \text{ kJ/mol}$ ) and covalent bonds (with energies about several hundred kilojoules per mole) [37,38]. This mixed bonding state can influence the materials properties significantly, for example it could

result in enhanced hardness and thermal stability of the material. Combination of two binary materials into ternary materials can be beneficial due to the simultaneous presence of the metals in the structures. For example,  $\text{Al}_2\text{O}_3\text{-Cr}_2\text{O}_3$  system offers complete solid solubility over the compositional range above a certain higher temperature. More detailed are introduced in section 2.5, 2.6 and 2.7. PVD which is a non-equilibrium deposition process would be a tool to get such new solid solutions at lower substrate temperature. Alloying impact on material properties can be well explained. In this work, new ternary solid solution oxides Al-Cr-O, V-Al-O, and V-Cr-O films with composition variation was carried out. A combinatorial approach based on the use of a segmented target consisting of  $\text{A}_2\text{O}_3$  and  $\text{B}_2\text{O}_3$  (A and B indicate different metal elements, e.g. Al, Cr, V) half plates was used for the thin film synthesis.

In order to obtain stoichiometric oxide films by magnetron sputtering, there are two options for the deposition process: a) one can do a reactive magnetron sputtering process using a metal target, and such processes require precise oxygen gas flow control during deposition; b) the alternative synthesis route is a non-reactive magnetron sputtering process using ceramic (oxide) targets for sputtering. In this thesis, the synthesis route of non-reactive magnetron sputtering is used, and single oxide ceramic targets  $\text{Cr}_2\text{O}_3$  and  $\text{V}_2\text{O}_3$  are applied for the growth of  $\text{Cr}_2\text{O}_3$  and  $\text{V}_2\text{O}_3$  films, respectively; segmented targets for a combinatorial approach are used for the ternary Al-Cr-O, V-Cr-O and V-Al-O systems in solid solution state which is an innovative way to get ternary solid solutions with composition variation in one step. To sputter conductive targets in magnetron sputtering process, a DC power supply is generally used. For insulating or semiconducting targets, an RF power supply is required. Therefore, RF magnetron sputtering is used in this thesis.

## **1.2 Motivation and objectives**

$\text{Me}_2\text{O}_3$  ( $\text{M}_e$  indicates Al, Cr, V and so on) is an important class of materials which is widely used for protective layers in cutting tools, optical, electronic, magnetic device technology, etc.. For most applications, it is important to control precisely the microstructure (including lattice parameters), stain, and stoichiometry of the films, because the properties of thin films are influenced by many factors, including microstructure, composition, defect concentrations and so on [39]. Due to the films with different orientation exhibit

different properties, for most technological applications, it is desired that the deposited materials form crystalline overlayers that have one well-defined orientation with respect to the substrate crystal structure [40,41].

Oxide films with corundum microstructure, e.g.  $\text{Cr}_2\text{O}_3$  and  $\text{V}_2\text{O}_3$  grown on iso-structural oxide substrates e.g.  $\alpha\text{-Al}_2\text{O}_3$  can be considered a model system for studying oxide - oxide heterojunctions. This is motivated by (1) the films and the substrates have same crystal structure; (2) the materials do not react or interdiffuse under the growth conditions in the present study; (3) these individual corundum-type structure oxides have been studied and can be widely used in many applications. The  $\alpha\text{-Al}_2\text{O}_3$  substrates with the same corundum-type structure as the films were used to assist the low temperature epitaxial growth of the iso-structural binary systems or to form a homogenous solid solution of ternary systems.

The objectives are to understand the principle of the crystals growth on the iso-structural substrates at low deposition temperature ( $\leq 400$  °C) and how and why the composition affects the microstructure and properties in the ternary solid solution.

In this thesis, first, the epitaxial grown binary stoichiometric  $\text{Cr}_2\text{O}_3$  and  $\text{V}_2\text{O}_3$  thin films on the  $\alpha\text{-Al}_2\text{O}_3$  substrates were obtained by non-reactive RF magnetron sputtering using a ceramic target. Then new ternary solid solutions were studied which was based on the results of the binary systems. In order to obtain the stoichiometric films with systematic composition gradients in the ternary systems of Al-Cr-O, V-Al-O and V-Cr-O, a combinatorial approach using segmented ceramic targets was applied. The segmented ceramic targets also result in the growth of the films with varying microstructure and properties. The films properties are influenced by the microstructure which depends on the elemental composition, the substrate, the film thickness and the deposition temperature.

In this thesis, the microstructure including the epitaxial quality of the thin films relative to the substrates were characterized by different techniques X-ray diffraction (XRD), transmission electron microscopy (TEM), Raman spectroscopy and Infrared reflection-absorption spectroscopy (IRRAS) and the band gap was obtained by ultraviolet-visible-near infrared (UV-VIS-NIR) spectroscopy. The variation of the microstructure and properties dependent on the deposition conditions and the film composition was discussed.

The influence of the film thickness, the deposition temperature and the perfection of the substrate surface on the epitaxial films was studied. Based on these results, deposition process parameters for the epitaxial film growth can be developed.

The solid solutions of ternary oxides in various systems with the same corundum-type structures were successfully obtained. The crystal growth is developed from the binary systems to the ternary systems. The deposited films were polycrystalline with (0001) orientation and epitaxial grown on the  $\alpha$ -Al<sub>2</sub>O<sub>3</sub> substrates. We investigated the influence of a substitution of the metal cation in a ternary system (in single-phase solid solution crystallized thin films) on the epitaxial growth, the microstructure and the properties of the films. In ternary systems, the films with higher Al content possesses poorer crystal quality than the films with higher V content. The higher the Al content, the higher the tendency to build extremely nanocrystalline or even amorphous structures.

In other words, the aim of this work is to explain the conditions under which epitaxial layer growth of binary and ternary oxides with corundum microstructure on iso-structural substrates by non-reactive magnetron sputtering is possible at low deposition temperatures.

## 2 Material systems and state of the art

In this chapter, material systems in which phases with corundum-type structures can be found studied in this thesis are presented. Firstly, the basic knowledge of crystals and the structure of the corundum crystallography are introduced. Secondly, various corundum materials such as binary  $\alpha$ -Al<sub>2</sub>O<sub>3</sub>, Cr<sub>2</sub>O<sub>3</sub>, V<sub>2</sub>O<sub>3</sub>, and ternary Al-Cr-O, V-Al-O, and V-Cr-O systems are presented, including their properties, recent and potential applications, as well as the possibilities to produce these materials by means of thin film technology.

### 2.1 Crystal structure

In this part, the definition of a crystal is introduced in general. The materials studied in this thesis have the same corundum-type structure which is also presented in detail in this part.

#### 2.1.1 Definition of a crystal

A crystal consists of atoms arranged in a pattern that repeats periodically in three dimensions to a grid [42]. In crystals, atoms are arranged in a highly ordered fashion with specific periodic positions and symmetry.

In 1611, Johannes Kepler made the first attempt to relate the external shape of a crystal (snowflakes) with its structure [43]. Robert Hooke extended Kepler's ideas to other crystals and suggested that the different shapes of crystals which occur in form of rhombs, trapezia, hexagons and other geometries could arise from the packing together of spheres or globules, which was first published in 1665 [44]. In 1669, Nicolaus Steno [45] stated a law that the crystal faces are 60° or 120° angles which arise from the close-packing of the spheres from simple observation of quartz crystals, which was developed as a general law by Rome de L' Isle in 1783 [46]. In 1784, René Just Haüy [47] pointed out the connection between the internal order and the external symmetry of a crystal, however the existence of an internal order could not be certified at that time and until X-ray and electron diffraction techniques have been developed recently. Since then we have extended these ideas to three dimensions [48]. In 1926, Goldschmidt [49] found the relationship

between the crystal structure and the chemical composition which is called the laws of crystal chemistry, and he also considered physical properties dependent on the crystal structure.

Crystals can be regarded as being built up by a continuing three dimensional (3D) translational repetition of the basic structural pattern, and this simplest component of the 3D pattern is called the “unit cell” [50]. The unit cell can be defined by three noncoplanar vectors  $\vec{a}$ ,  $\vec{b}$ , and  $\vec{c}$ , and the angles between these axial vectors  $\alpha$ ,  $\beta$ , and  $\gamma$ . A crystal face or crystal plane is indexed with a set of integers,  $(hkl)$ , which is called Miller index. A crystal face or plane  $(hkl)$  makes intercepts  $a/h$ ,  $b/k$ ,  $c/l$  with the edges of the unit cell of lengths  $a$ ,  $b$  and  $c$ . If crystal planes in hexagonal systems are indexed using Miller indices, then crystallographically equivalent planes have indices which appear dissimilar. The planes parallel to the  $z$  axis, such as  $(1\bar{1}0)$  and  $(100)$ , are crystallographically equivalent, but it is not too easy to deduce this from their Miller indices. To overcome this, the Miller-Bravais indexing system is used. In Miller-Bravais index, a fourth axis,  $u$ , which is oriented at an angle of  $120^\circ$  to  $x$  and  $y$  axes and in the same plane, is introduced. A plane is then specified using four indices  $(hkil)$  that obey the constraint  $i = -(h+k)$ , where  $h$ ,  $k$ , and  $l$  are identical to the corresponding Miller indices.

### 2.1.2 Hexagonal close-packed crystal structure

First, we consider the atoms in one layer in a crystal are packed together in the same way. Then we extend one dimension to three dimensions by considering many layers of atoms stacked one on top of the other, i.e., atoms in the crystals arrange in certain patterns or lattice arrangements, which are known as close-packed structures [51].

The simplest way of stacking the layers is to place the atom centers directly above one another. However, in reality the atoms in the second layer tend to slip into the ‘hollows’ or interstices between the atoms in the layer below, in accordance with energetical considerations suggesting that layers of atoms stacked in this “close-packed” way generally have the lowest energy and most stable state [48]. There are two possibilities how a third layer is placed upon the second one when the atoms in the third layer slip into the interstices of the second layer: one case is that the atoms in the third layer are positioned directly above the atom centers in the first layer as shown in Fig. 1; the other case is when

the atoms in the third layer are positioned directly above the unoccupied interstices between the atoms in the first layer. In Fig. 1, atoms marked as “a” with a solid circles outline the first layer, atoms marked as “b” with dashed circles outline the second layer, and the atom-positions of the third layer are the same as those of the first layer. The stacking sequence is ababab..., which is called the hexagonal close-packed (hcp) structure.

The atoms in a crystal can be mathematically represented as points in a 3D real space lattice. If these lattice points are arranged in a periodic arrangement, then the lattice can be defined by space unit vectors  $\vec{a}$ ,  $\vec{b}$ , and  $\vec{c}$ , and the angles  $\alpha$ ,  $\beta$ , and  $\gamma$ . For the hexagonal system, the unit vector lengths are  $a = b \neq c$ , and the angle between the unit vectors are  $\alpha = \beta = 90^\circ$ ,  $\gamma = 120^\circ$ , which is shown in Fig. 2.

For the hexagonal structure, the distance  $d_{hkl}$  between a family of planes ( $hkl$ ) is:

$$d_{hkl} = \frac{a}{\sqrt{\frac{4}{3}(h^2 + k^2 + hk) + \left(\frac{a}{c}\right)^2 l^2}} \quad (1)$$

The angle  $\phi$  between planes ( $h_1k_1l_1$ ) and ( $h_2k_2l_2$ ) is [52]:

$$\cos \phi = \frac{\frac{h_1h_2}{a^2} + \frac{k_1k_2}{b^2} + \frac{l_1l_2}{c^2}}{\sqrt{\left[\frac{h_1^2}{a^2} + \frac{k_1^2}{b^2} + \frac{l_1^2}{c^2}\right] \left[\frac{h_2^2}{a^2} + \frac{k_2^2}{b^2} + \frac{l_2^2}{c^2}\right]}} \quad (2)$$

$$\text{or } \cos \phi = \frac{h_1h_2 + k_1k_2 + \frac{1}{2}(h_1k_2 + h_2k_1) + \frac{3}{4}\left(\frac{a}{c}\right)^2 l_1l_2}{\sqrt{\left[h_1^2 + k_1^2 + h_1k_1 + \frac{3}{4}\left(\frac{a}{c}\right)^2 l_1^2\right] \left[h_2^2 + k_2^2 + h_2k_2 + \frac{3}{4}\left(\frac{a}{c}\right)^2 l_2^2\right]}} \quad (3)$$

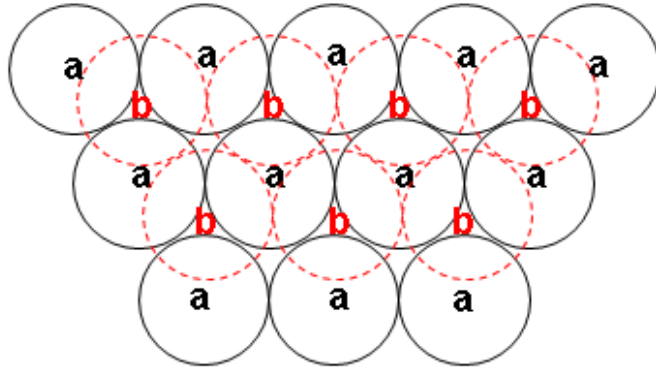


Fig. 1 Stacking sequences of the hcp layers of atoms. “a” are the atoms in the first layer, and “b” are the atoms in the second layer.

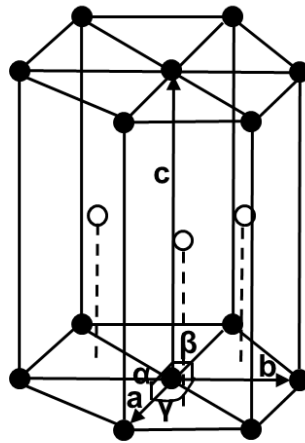


Fig. 2 A hcp structure where  $a = b \neq c$ , and  $\alpha = \beta = 90^\circ$ ,  $\gamma = 120^\circ$  [53].

### 2.1.3 Corundum-type crystal structure

Corundum-type crystals have been extensively investigated because of their importance applications in mineralogical, thin film commercial production and so on. Corundum ( $\alpha\text{-Al}_2\text{O}_3$ ), eskolaite ( $\text{Cr}_2\text{O}_3$ ), karelianite ( $\text{V}_2\text{O}_3$ ), hematite ( $\alpha\text{-Fe}_2\text{O}_3$ ), as well as  $\text{Ti}_2\text{O}_3$ ,  $\alpha\text{-Ga}_2\text{O}_3$ ,  $\alpha\text{-Rh}_2\text{O}_3$ ,  $\alpha\text{-B}_2\text{O}_3$ ,  $\alpha\text{-In}_2\text{O}_3$  and  $\alpha\text{-Ir}_2\text{O}_3$  exhibit the same crystal structure which is called the corundum-type structure [54–59].

Although corundum-type crystals have a rhombohedral primitive unit cell, the equivalent hexagonal lattice, which contains three primitive cells and belongs one of six lattice families, is used [52]. Fig. 3 illustrates the corundum structure with the space group of  $D_{3d}^6 (R\bar{3}c)$  in ideal hexagonal description. In the hexagonal view along the  $[0001]$  direction, the oxygen atoms (shown as red circles in Fig. 3) form parallel and nearly ideal

(slightly distorted) hcp array, while the metal atoms (shown as blue filled circles in Fig. 3) occupy two thirds of the octahedral interstitial sites between two oxygen layers, forming graphite-like layers parallel to the oxygen layers with *ABCABC...* stacking sequence in the *c*-axis. Metal atoms show a coordination with six oxygen atoms, and oxygen atoms show a coordination with four metal atoms. Each MeO<sub>6</sub> (Me denotes metal) octahedron is linked with three other octahedrals through common edges and with one octahedron through a common face along *c*-direction [52,60–63]. From the stacking sequence shown in Fig. 3 (b), (c) and (d), one can observe that the oxygen has 6-fold symmetry, and the metal only has 3-fold symmetry. For Me<sub>2</sub>O<sub>3</sub> corundum-type, the trivalent metal occupies the octahedral site at (0, 0, *z*) and the oxygen is placed at (*x*, 0,  $\frac{1}{4}$ ) in the Me-centered setting. In an ideal hcp corundum both *z* and *x* are  $\frac{1}{3}$ , and  $\frac{c}{a} = 2.833$  [54]. The lattice parameter *c* in a hexagonal structure is determined by six layers of oxygens with six intervening sheets of cations and holes [60]. However, lattice distortion with deviations of the corundum-type structure from ideality is observed caused by electrostatic cation-cation repulsion due to the fact that one third of octahedral interstitial sites are unoccupied by cations, which is dependent on the temperature and pressure [54,55].

The lattice parameters and the interatomic distances at room temperature and pressure in  $\alpha$ -Al<sub>2</sub>O<sub>3</sub>, Cr<sub>2</sub>O<sub>3</sub> and V<sub>2</sub>O<sub>3</sub> are listed in Table 1. These isomorphous corundum structures possess similar lattice parameters with a lattice misfit of less than 5 % in *a*-axis. Compared to  $\alpha$ -Al<sub>2</sub>O<sub>3</sub> (*a* = 0.47588 nm and *c* = 1.2992 nm, according to Powder Diffraction File (PDF) card No. 42-1468), Cr<sub>2</sub>O<sub>3</sub> (*a* = 0.495876 nm and *c* = 1.35942 nm, according to PDF card No. 38-479) has lattice mismatches of 4.2 % and 4.6 % for the *a* and *c* axes, respectively. While the V<sub>2</sub>O<sub>3</sub> (*a* = 0.49540 nm, and *c* = 1.40083 nm, according to PDF card No. 34-187) has lattice mismatches to  $\alpha$ -Al<sub>2</sub>O<sub>3</sub> of 4.1 % and 7.8 % for the *a* and *c* axes, respectively. As expected for an essentially ionic structure, the metal atoms are displaced from the octahedral centers towards the unshared faces, and shared edges are shorter than unshared edges. Concerning the values of the interatomic distances shown in Table 1, one should note there are two non-equivalent Me-O distances: the larger one with Me towards the shared face and the smaller towards the unshared face. There are also two different Me-Me distances in Me<sub>2</sub>O<sub>3</sub>, in which the relatively short distance along

the  $c$ -axis may be due to the particular geometrical features of the structure and not to a bonding interaction. For O-O distances in one material, there are four non-equivalent values in shared faces, unshared faces, shared edges and unshared edges, respectively [63].

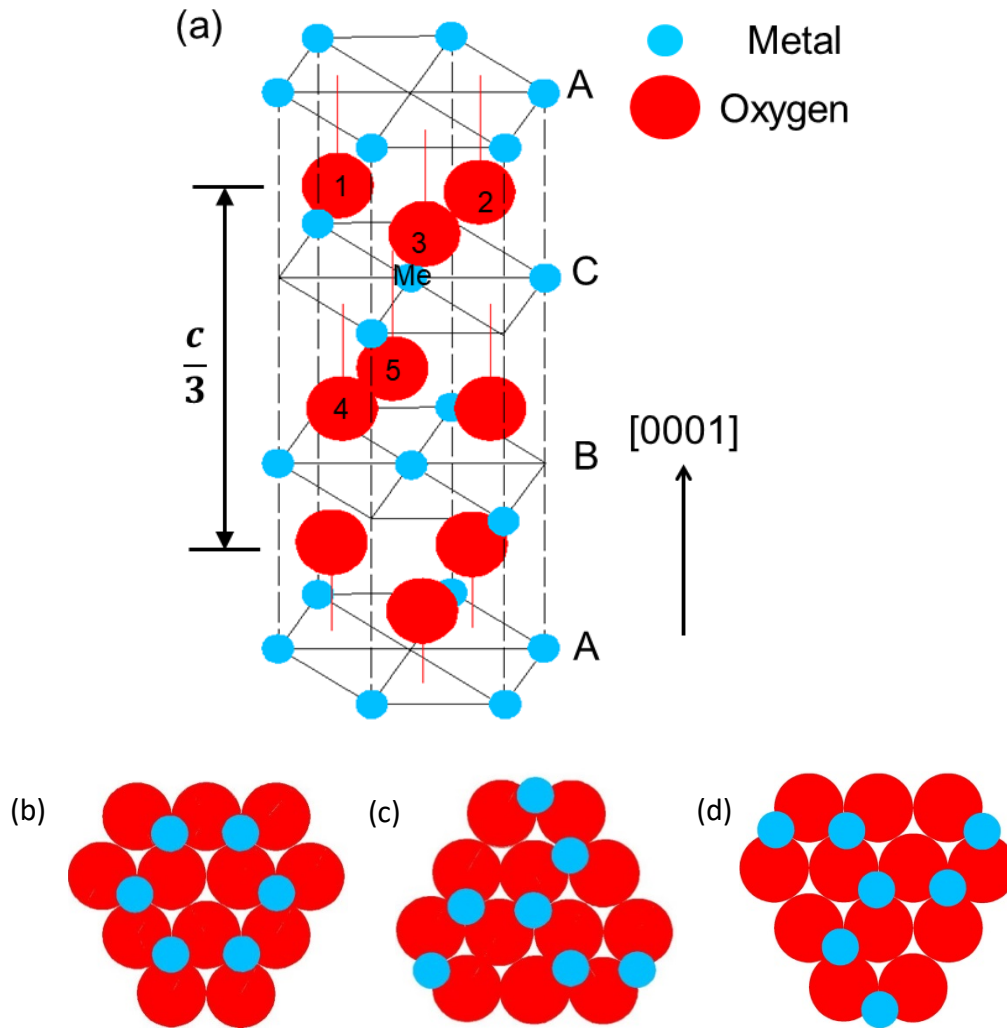


Fig. 3 (a) The corundum structure in ideal hexagonal description. The oxygen atoms (red-filled circles) form an hcp array. The metal atoms (blue-filled circles) occupy two-thirds of the octahedral interstices between two oxygen layers.  $c$  is the lattice parameter. The metal layers stack as  $\dots ABCABC\dots$  (b) (c) and (d) show the stacking model. The top views of the (b) A layer, (c) B layer and (d) C layer show that the oxygen-sublattice exhibits 6-fold symmetry while the metal sublattice exhibits only 3-fold symmetry.

Table 1 Lattice parameters and atomic distances of  $\alpha$ -Al<sub>2</sub>O<sub>3</sub>, Cr<sub>2</sub>O<sub>3</sub>, and V<sub>2</sub>O<sub>3</sub> at room temperature and pressure of  $1.01 \times 10^5$  Pa. Lattice parameters of  $\alpha$ -Al<sub>2</sub>O<sub>3</sub>, Cr<sub>2</sub>O<sub>3</sub>, and V<sub>2</sub>O<sub>3</sub> are according to the PDF card No. 42-1468, No. 38-1479, and No. 34-187 from the International Center for Diffraction Data (ICDD) database, respectively. Unit cell volumes are calculated by the formula  $V = \frac{\sqrt{3}a^2c}{2}$ . The atom distances of  $\alpha$ -Al<sub>2</sub>O<sub>3</sub> are cited from ref. [62], and the atom distances of Cr<sub>2</sub>O<sub>3</sub> and V<sub>2</sub>O<sub>3</sub> are from ref. [54]. Me denotes metal (Al, Cr, or V). Me, O<sub>1</sub>, O<sub>2</sub>, O<sub>3</sub>, O<sub>4</sub>, and O<sub>5</sub> are shown in Fig. 3.

Parameters	$\alpha$ -Al <sub>2</sub> O <sub>3</sub>	Cr <sub>2</sub> O <sub>3</sub>	V <sub>2</sub> O <sub>3</sub>
$a$ / nm	0.47588	0.495876	0.49540
$c$ / nm	1.2992	1.35942	1.40083
$c/a$	2.73	2.74	2.83
Unit cell volume / nm <sup>3</sup>	0.2549	0.2895	0.2977
Me-O distances			
Me-O <sub>1</sub>	0.1969	0.2009	0.2037
Me-O <sub>5</sub>	0.1857	0.1962	0.1978
Me-Me distances			
Me-Me (shared face)	0.2649	0.2649	0.2735
Me-Me (shared edge)	0.2792	0.2885	0.2887
O-O distances			
O <sub>1</sub> -O <sub>2</sub> (shared face)	0.2524	0.2617	0.2615
O <sub>1</sub> -O <sub>4</sub> (shared edge)	0.2619	0.2730	0.2790
O <sub>1</sub> -O <sub>5</sub> (unshared edge)	0.2725	0.2844	0.2902
O <sub>1</sub> -O <sub>3</sub> (unshared face)	0.2869	0.2987	0.2988

## 2.2 Aluminium oxide, Al<sub>2</sub>O<sub>3</sub>

In this part, the phases, properties and applications of Al<sub>2</sub>O<sub>3</sub> are presented. Various techniques to prepare the Al<sub>2</sub>O<sub>3</sub> from literatures are introduced.

### 2.2.1 Structure, properties and applications

$\text{Al}_2\text{O}_3$  exists in many metastable polymorphs, such as  $\gamma$ -,  $\eta$ -,  $\theta$ -, and  $\delta$ -phases which structures are based on fcc packing of oxygen;  $\alpha$ -,  $\kappa$ -, and  $\chi$ -phases which are based on hcp packing, and additional monoclinic phases including  $\theta'$ ,  $\theta''$  and  $\lambda$ -phases [61]. Among these phases,  $\alpha$ - $\text{Al}_2\text{O}_3$  is the only thermodynamically stable phase with corundum-type structure over a wide range of temperatures up to 1100 °C which is characterized by a mixed ion-covalent bonding with 61 % of ionic character and 39 % of covalent character [64]. The other phases are called metastable phases, which can transform irreversibly to  $\alpha$ - $\text{Al}_2\text{O}_3$  at a sufficiently high temperature [65–67]. Fig. 4 shows the Al-O phase diagram, which indicates no solid solubility of O in solid Al or deviation from stoichiometry in  $\text{Al}_2\text{O}_3$  and the high melting point of  $\alpha$ - $\text{Al}_2\text{O}_3$ .

$\alpha$ - $\text{Al}_2\text{O}_3$  possesses the corundum-type crystal structure with the space group of  $D_{3d}^6 (R\bar{3}c)$  which has detailed described in section 2.1.3.

$\alpha$ - $\text{Al}_2\text{O}_3$  possesses good thermal stability, mechanical, chemical, electrical and optical properties which are specified in Table 2, and has been widely used in various technologies from metallurgy (e.g. as a refractory material) to microelectronics (e.g. as a substrate for the growth of Si and GaN) [68,69].  $\alpha$ - $\text{Al}_2\text{O}_3$  is one of the most common phases among all  $\text{Al}_2\text{O}_3$  phases with a high melting point of 2327 K as shown in Fig. 4 [70,71], which has no phase transition between room temperature and its melting point [17,72,73]. Due to its high melting point,  $\alpha$ - $\text{Al}_2\text{O}_3$  has been used as a refractory (fire resistant) material [74,75].  $\alpha$ - $\text{Al}_2\text{O}_3$  is one of the hardest oxides in the world [76] and microhardness of 22 GPa - 23 GPa [77]. Due to this high hardness and its superior chemical stability, good mechanical strength at high temperatures and favourable thermal properties, it is used as wear resistant and protective coatings [13–16].  $\alpha$ - $\text{Al}_2\text{O}_3$  films are effective thermal or diffusion barriers against hot gas especially under the loading conditions in fusion reactors due to its high density (3.93 g/cm<sup>3</sup> - 4.01 g/cm<sup>3</sup>), thermomechanical stability and hcp crystal structure with a very small number of defects [15,17–19,78]. Considering its electrical properties like the large band gap (8.8 eV) [79], a high dielectric constant (around 10), and high electrical insulating,  $\text{Al}_2\text{O}_3$  films can be used in metal-oxide-semiconductor gate dielectric applications [20,21], or as passivation layers in

metal-oxide-semiconductor devices [22]. Besides,  $\text{Al}_2\text{O}_3$  is also used in magneto-resistive and magneto-optic read and write devices [80–82]. Further,  $\text{Al}_2\text{O}_3$  films have been used in optical applications, e.g. as protective films for metal reflectors and dark mirrors, due to its low optical absorptance (i.e. high transparency with an index of refraction of 1.64 - 1.77) [22–24].

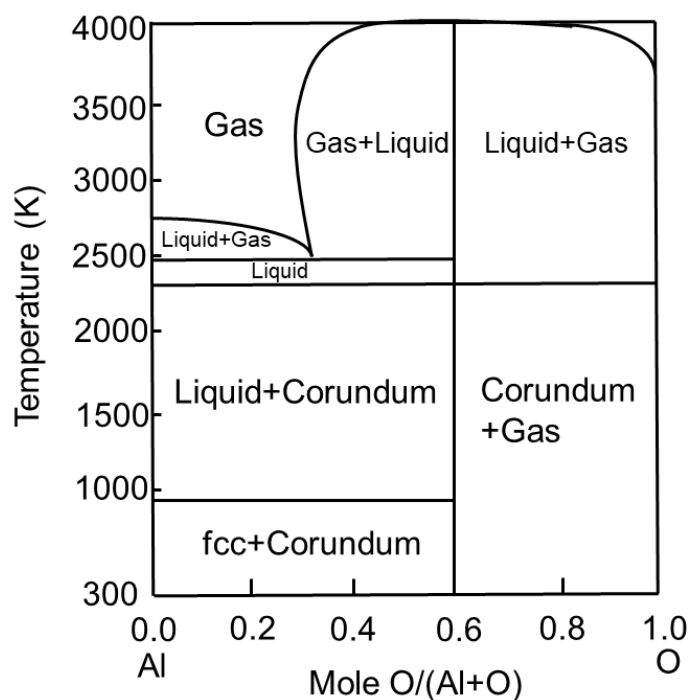


Fig. 4 Al-O Phase diagram [83,84].

Table 2 Properties of  $\alpha\text{-Al}_2\text{O}_3$ .

Property	Value
Molecular weight	101.96 g/mol
Melting point [83,84]	2327 K
Boiling point [85]	3000 °C
Density [38]	3.93 g/cm <sup>3</sup> - 4.01 g/cm <sup>3</sup>
Dielectric Constant [20]	~ 10
Microhardness [77]	22 GPa - 23 GPa
Index of Refraction [25]	1.64 - 1.77
Band Gap [79]	8.8 eV

### 2.2.2 Methods for Al<sub>2</sub>O<sub>3</sub> thin film deposition

For achieving crystalline  $\alpha$ -Al<sub>2</sub>O<sub>3</sub> films, high temperature deposition processes such as CVD are the domain methods. However, the substrate temperatures above 1000 °C are required for CVD [16,65,66]. Only amorphous Al<sub>2</sub>O<sub>3</sub> films were grown at 600 °C - 700 °C and polycrystalline  $\gamma$ -Al<sub>2</sub>O<sub>3</sub> could be grown at 900 °C - 1050 °C by metal-organic chemical vapor deposition (MOCVD) [86]. Textured polycrystalline  $\alpha$ -Al<sub>2</sub>O<sub>3</sub> layers with different orientation were deposited at 1000 °C by CVD [14]. Crystalline (0001)-oriented  $\alpha$ -Al<sub>2</sub>O<sub>3</sub> layers were obtained on (0001)-oriented Ti<sub>2</sub>O<sub>3</sub> at 1000 °C by CVD [65]. With development of the CVD technology, the required substrate temperature towards lower. Kyrylov et al. [87] studied the effect of ion irradiation during the deposition of alumina films by plasma assisted CVD and prepared  $\alpha$ -Al<sub>2</sub>O<sub>3</sub> films at 580 °C in a bipolar pulsed plasma with a cathode power density of 6.6 W/cm<sup>2</sup>.

Only amorphous or very poorly crystallized  $\alpha$ -Al<sub>2</sub>O<sub>3</sub> films could be obtained by conventional PVD processes which operate usually at lower temperature under kinetic non-equilibrium conditions. Hiesinger and Koenig reported earlier the preparation of amorphous Al<sub>2</sub>O<sub>3</sub> films by reactive DC sputtering in 1951 [88]. Dragoo and Diamond [73] reported amorphous alumina films were prepared by condensing vapor from evaporating molten alumina on glass substrates. To obtain crystalline Al<sub>2</sub>O<sub>3</sub> films, annealing of the amorphous films was done. Initial crystallization began at 570 °C for an annealing time of more than 8 h, then poorly crystalline alumina was converted from  $\gamma$ -Al<sub>2</sub>O<sub>3</sub> to  $\delta$ -Al<sub>2</sub>O<sub>3</sub> and finally to  $\alpha$ -Al<sub>2</sub>O<sub>3</sub>, or films converted from  $\theta$ -Al<sub>2</sub>O<sub>3</sub> to  $\alpha$ -Al<sub>2</sub>O<sub>3</sub> (i.e. from the cubic phases to the corundum phase) with increasing the annealing temperature to 1200 °C. Amorphous Al<sub>2</sub>O<sub>3</sub> films were prepared in Ar-O<sub>2</sub> mixtures by DC and RF reactive magnetron sputtering by Deshpandey and Holland in 1982 [22].

In order to get crystalline  $\alpha$ -Al<sub>2</sub>O<sub>3</sub> films at lower deposition temperature, the developments of the PVD technology (e.g. pulsed deposition) are underway. Polycrystalline  $\alpha$ -Al<sub>2</sub>O<sub>3</sub> films were synthesized by PLD at 850 °C from a high density Al<sub>2</sub>O<sub>3</sub> target by Hirschauer et al. [23]. The substrate temperature required for the formation of the  $\alpha$ -Al<sub>2</sub>O<sub>3</sub> phase could be reduced to 760 °C by pulsed magnetron sputtering in recent developments in sputtering technology [89].

In the present work, a different approach with application of an iso-structure template layer for growing crystalline  $\alpha$ -Al<sub>2</sub>O<sub>3</sub> at low temperature was taken. Andersson et al. [90] reported that stoichiometric and crystalline Al<sub>2</sub>O<sub>3</sub> thin films with  $\alpha$ - and  $\gamma$ -phases mixture were grown on Cr<sub>2</sub>O<sub>3</sub> nucleation layers at 500 °C by reactive Ar/O<sub>2</sub> magnetron sputtering of a Al target. Jin et al. put forwards an approach of using a Cr<sub>2</sub>O<sub>3</sub> thin layer as a structural template to deposit  $\alpha$ -Al<sub>2</sub>O<sub>3</sub> films with an orientation relationship of [011] Al<sub>2</sub>O<sub>3</sub>/[011] Cr<sub>2</sub>O<sub>3</sub> at 400 °C - 600 °C by RF magnetron sputtering [13,72]. Eklund [91] grew  $\alpha$ -Al<sub>2</sub>O<sub>3</sub> films on [0001]-textured Cr<sub>2</sub>O<sub>3</sub> templates at 450 °C by reactive inductively coupled plasma magnetron sputtering from an Al target in Ar and O<sub>2</sub> atmosphere. Crystalline  $\alpha$ -Al<sub>2</sub>O<sub>3</sub> films with a thickness of only 1 nm were grown epitaxially on Cr<sub>2</sub>O<sub>3</sub> (0001) by evaporation of Al in O<sub>2</sub> at a substrate temperature of 550 °C  $\pm$  100 °C by Dumbuya et al. [32]. Ashenford et al. [92] reported  $\alpha$ -Al<sub>2</sub>O<sub>3</sub> films which were grown on Cr<sub>2</sub>O<sub>3</sub> which acted as a template in the temperature range of 300 °C - 500 °C by MBE. Further, the innovations of the (Al,Cr)<sub>2</sub>O<sub>3</sub> solid solution thin films have been crystallized in a corundum-type structure at lower temperature by PVD process [93] and this will be described in detail in section 2.5.

## 2.3 Chromium oxide, Cr<sub>2</sub>O<sub>3</sub>

In this part, the structure, properties and applications of Cr<sub>2</sub>O<sub>3</sub> are presented. Various techniques to prepare Cr<sub>2</sub>O<sub>3</sub> thin films described in literatures are introduced.

### 2.3.1 Structure, properties and applications

Chromium oxides are widely used in a variety of applications, such as refractory materials, protective coatings, electronics, optics, catalysts, etc. [26–29,94]. However, one needs to mention that there are many different oxide phases of chromium, including CrO, Cr<sub>2</sub>O, CrO<sub>2</sub>, CrO<sub>3</sub>, CrO<sub>5</sub>, Cr<sub>2</sub>O<sub>5</sub>, Cr<sub>2</sub>O<sub>3</sub>, Cr<sub>3</sub>O<sub>4</sub>, Cr<sub>8</sub>O<sub>11</sub>, Cr<sub>8</sub>O<sub>21</sub>, and others. The assessed Cr-O phase diagram is shown in Fig. 5. Only two solid intermediate phases, Cr<sub>2</sub>O<sub>3</sub> and Cr<sub>3</sub>O<sub>4</sub>, are stable at high temperatures. The Cr<sub>2</sub>O<sub>3</sub> is the dominating stable oxide phase over a wide temperature range, while the Cr<sub>3</sub>O<sub>4</sub> is formed in a narrow temperature range from 1910 K to 2000 K at high temperature [95,96]. Among all the chromium oxides, Cr<sub>2</sub>O<sub>3</sub> is the most thermodynamic stable phase and the hardest material of all chromium oxides [25]. Table 3 shows the physical properties of Cr<sub>2</sub>O<sub>3</sub>. Cr<sub>2</sub>O<sub>3</sub> exhibits a high melting

point of 2675 K (see Fig. 5) [97,98] and high temperature oxidation resistance, which makes it as an important refractory material [94]. Cr<sub>2</sub>O<sub>3</sub> possesses an insulating antiferromagnetic behavior with a Néel temperature at 307 K, which has been considered for use of Cr<sub>2</sub>O<sub>3</sub> in tunnel junction barriers [4,99–103]. Cr<sub>2</sub>O<sub>3</sub> is one of the most important p-type semiconductor transition metal-oxide materials with wide band gap of 3 eV - 3.2 eV [103–105], making it a suitable material for many potential applications in optical and electronic devices, like in gate-dielectrics [28], UV-light emitters using nanolasers, and optical memory systems [27]. Cr<sub>2</sub>O<sub>3</sub> coatings exhibit excellent properties of high hardness, chemical inertness, outstanding wear resistance, oxidation and corrosion resistance [106,107]. For Cr<sub>2</sub>O<sub>3</sub> thin films, microhardness values of 29 GPa have been reported [25,108,109], and Hones et al. achieved single crystalline Cr<sub>2</sub>O<sub>3</sub> thin films with nanohardness values up to 32 GPa [25]. Therefore, Cr<sub>2</sub>O<sub>3</sub> coatings have been used as protective coatings of mechanical components or in tribological applications [26], as corrosion resistant coatings for stainless steels [25] and have been developed for protection against corrosion and wear in magnetic heads and media such as magnetic rigid disks and magnetic disk heads [110] and in gas bearing applications [109]. Besides, Cr<sub>2</sub>O<sub>3</sub> coatings have also been used in electronic, magnetic, optic and chemical fields. Furthermore, Cr<sub>2</sub>O<sub>3</sub> coatings are also used in solar absorber surfaces. So-called Cr<sub>2</sub>O<sub>3</sub>-Cr black chromium coatings have been used as selective solar absorber coatings, due to their attractive solar absorption characteristics with high absorptance over the visible spectrum but low emittance over a large temperature range [111–116]. Chromium-based catalysts have been studied for various petrochemical and environmental applications. Cr<sub>2</sub>O<sub>3</sub> is an important catalyst widely examined for polymerization, hydrogenation-dehydrogenation, isomerization, aromatization, and partial oxidation reactions, due to the peculiar characteristics of Cr<sub>2</sub>O<sub>3</sub> species on the surface of the support, e.g. oxidation state, coordination environment, and degree of polymerization [29,30]. Cr<sub>2</sub>O<sub>3</sub> is used as commercial catalyst for dehydrogenation of alkanes [117]. In addition, crystalline Cr<sub>2</sub>O<sub>3</sub> thin films have been used as a buffer layer for the growth of various films. For example, high quality epitaxial ZnO films were grown on *c*-Al<sub>2</sub>O<sub>3</sub> substrates with Cr<sub>2</sub>O<sub>3</sub> buffer layer by plasma-assisted molecular beam epitaxy (P-MBE) [118]. Cr<sub>2</sub>O<sub>3</sub> films could also be used as a potential buffer layer for the growth of GaN layers for the fabrication of GaN-based light-emitting

diodes (LEDs), because the lattice mismatch between the  $\text{Cr}_2\text{O}_3$  and GaN is smaller than that between the most commonly used  $\text{Al}_2\text{O}_3$  substrate and GaN [33].

In summary,  $\text{Cr}_2\text{O}_3$  as an important high temperature, mechanical, optical, electric, magnetic and chemical industrial material has attracted the attention of many researchers.  $\text{Cr}_2\text{O}_3$  is regarded as one of the best candidates to replace  $\text{Al}_2\text{O}_3$  in some special applications [119].

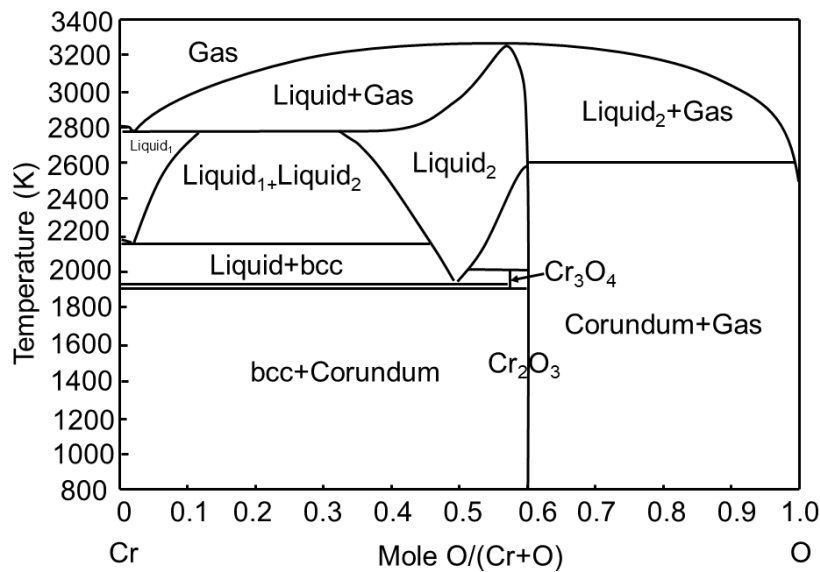


Fig. 5 Cr-O phase diagram [95,96].

Table 3 Properties of  $\text{Cr}_2\text{O}_3$ .

Property	Value
Molecular weight [120]	151.989 g/mol
Melting point [95,96]	2675 K
Boiling point [121]	~ 4000 °C
Density [122]	5.18 g/cm <sup>3</sup>
Dielectric Constant [123]	~ 11.9
Microhardness [25,108,109]	29 GPa
Index of Refraction [25]	2.5
Band Gap [103–105]	3 eV - 3.4 eV for film, 3 eV - 3.2 eV for bulk

### 2.3.2 Methods for Cr<sub>2</sub>O<sub>3</sub> thin film deposition

Cr<sub>2</sub>O<sub>3</sub> thin films can be synthesized by various techniques, including CVD and PVD methods, at much lower temperature compared with the deposition of  $\alpha$ -Al<sub>2</sub>O<sub>3</sub> thin films. The chemical methods include chemical spray pyrolysis which uses a liquid source for thin film coating and CVD where process gases are used for the generation of film forming chromium and oxygen particles on hot substrate surfaces. Misho reported that polycrystalline Cr<sub>2</sub>O<sub>3</sub> thin films were prepared on glass substrates that were preheated at around 500 °C by chemical spray pyrolysis [104]. Polycrystalline Cr<sub>2</sub>O<sub>3</sub> thin films with corundum-type structure on Ni were obtained at 450 °C by MOCVD [124]. Polycrystalline Cr<sub>2</sub>O<sub>3</sub> coatings on SiC and TiB<sub>2</sub> were deposited by electrochemical deposition [125]. Multi-oxide-phases of chromium including Cr<sub>2</sub>O<sub>3</sub> were grown by low temperature CVD using Cr(CO)<sub>6</sub> and O<sub>2</sub> gases [126]. Furthermore, PVD is the most promising technique to deposit crystalline Cr<sub>2</sub>O<sub>3</sub> thin films because the required substrate temperature is lower than in the case of CVD. Amorphous thin films of chromium oxide were deposited at 300 °C by electron-beam evaporation reported by Al-Kuhaili and Durrani [127]. Both amorphous and crystalline Cr<sub>2</sub>O<sub>3</sub> films were obtained using DC magnetron reactive sputtering with a Cr target by varying the substrate temperature from room temperature to 300 °C [128]. Cr<sub>2</sub>O<sub>3</sub> films with mixed crystalline and amorphous phases were deposited on silicon and steel substrates at low substrate temperature (around 60 °C) by pulsed DC reactive unbalanced magnetron sputtering using Cr targets [106]. Polycrystalline Cr<sub>2</sub>O<sub>3</sub> phase was presented on low carbon steel substrates by reactive magnetron sputtering in mixed Ar and O<sub>2</sub> and post-annealing above 470 °C [129]. Polycrystalline Cr<sub>2</sub>O<sub>3</sub> films were obtained from metallic chromium target by RF reactive magnetron sputtering in the range of 15 % - 25 % gas flow ratio of oxygen to the sum of oxygen and argon and the substrate temperature exceeding 227 °C which was reported by Hones et al. [119]. Cr<sub>2</sub>O<sub>3</sub> films with fiber texture were grown on Si (100) substrates using inductively coupled plasma assisted reactive DC magnetron sputtering with a Cr target at substrate temperatures of 300 °C - 450 °C by Pedersen [130].

Epitaxial Cr<sub>2</sub>O<sub>3</sub> (0001) films with thickness of only 4.4 nm were produced by oxidation of Cr (110) films in high oxygen with pressure of  $5 \times 10^{-5}$  Torr at 330 °C and the (0001) Cr<sub>2</sub>O<sub>3</sub> plane being parallel to the (110) Cr plane [131]. Cr<sub>2</sub>O<sub>3</sub> films were grown on Pt

(111) with thicknesses ranging from one to eight monolayers by Cr evaporation in oxygen with pressure of  $2 \times 10^{-6}$  mbar at a substrate temperature of 327 °C [99,132,133]. Cr<sub>2</sub>O<sub>3</sub> (0001) epitaxial films have been grown on  $\alpha$ -Al<sub>2</sub>O<sub>3</sub> (0001) by oxygen-plasma-assisted molecular beam epitaxy (OPA-MBE) with a film grow rate of only around 0.6 nm/min at a substrate temperature of 500 °C as reported by Chambers et al. [134]. Epitaxial Cr<sub>2</sub>O<sub>3</sub> (0001) sublayers with a thickness of less than 5 nm were grown on  $\alpha$ -Al<sub>2</sub>O<sub>3</sub> (0001) substrates by the evaporation of Cr at 350 °C [135]. An appropriate flow of oxygen is needed for the deposition of stoichiometric oxide films in the case of sputtering from a metallic target. Stoichiometric oxides films could be obtained using a ceramic target without oxygen reactive gas during sputtering, but RF power needs to be applied on the target due to the ceramic targets possess poor electrical conductivities (e.g. Al<sub>2</sub>O<sub>3</sub> and Cr<sub>2</sub>O<sub>3</sub> target exhibit the volume resistivity of larger than  $10^{12}$   $\Omega \cdot \text{cm}$  and  $3 \times 10^6$   $\Omega \cdot \text{cm}$  at room temperature, respectively). Furthermore, due to the iso-structure between  $\alpha$ -Al<sub>2</sub>O<sub>3</sub> and Cr<sub>2</sub>O<sub>3</sub>, epitaxial crystalline Cr<sub>2</sub>O<sub>3</sub> films with higher thickness and better crystal quality could be grown on  $\alpha$ -Al<sub>2</sub>O<sub>3</sub> at low temperature. Jeong et al. [33] obtained the epitaxial Cr<sub>2</sub>O<sub>3</sub> (0001) phase on  $\alpha$ -Al<sub>2</sub>O<sub>3</sub> (0001) substrates by RF magnetron sputtering at room temperature (from a stoichiometric Cr<sub>2</sub>O<sub>3</sub> target in an Ar/O<sub>2</sub> mixture with a gas flow ratio of 9:1) and a post rapid thermal annealing process at 900 °C in vacuum for 2 min. In this work, epitaxial Cr<sub>2</sub>O<sub>3</sub> (0001) films with strong texture were grown on  $\alpha$ -Al<sub>2</sub>O<sub>3</sub> (0001) substrates at 320 °C by RF magnetron sputtering using Cr<sub>2</sub>O<sub>3</sub> targets which will be described in detail in section 4.1.

## 2.4 Vanadium sesqui-oxide, V<sub>2</sub>O<sub>3</sub>

The structure, properties and applications of V<sub>2</sub>O<sub>3</sub> are presented in this section. Meanwhile, various techniques to prepare V<sub>2</sub>O<sub>3</sub> thin films described in literatures are introduced.

### 2.4.1 Structure, properties and applications

The V-O phase diagram according to Wriedt [136] is shown in Fig. 6. The equilibrium solid phases, structure and composition are listed in Table 4. Among these phases, V<sub>2</sub>O<sub>3</sub> possesses the highest melting point of 1940 °C [137]. Besides, V<sub>2</sub>O<sub>3</sub> is a dimorphic materials and undergoes a metal-insulator transition (MIT) at  $T_c$  ( $T_c \approx -112$  °C) from a low

temperature antiferromagnetic insulating (AFI) phase with monoclinic crystal structure to a high temperature paramagnetic metallic (PM) phase with a corundum-type structure [138–142]. From AFI phase to PM phase transition, the electrical resistivity decreases by seven orders of magnitude [143]. The MIT property in  $V_2O_3$  is accompanied by changes in the lattice structure and the optical properties. The low temperature insulating phase is transparent to the radiation from infrared to near ultraviolet regions. For  $T > T_c$ , the high temperature electrically conducting phase is still transparent to the near infrared, visible light and near ultraviolet regions, while the reflectivity in the infrared region increases with decreasing the light frequency and it decreases over the whole infrared wavelength range as the temperature increases, which is attributed to the high temperature metallic behavior [144].

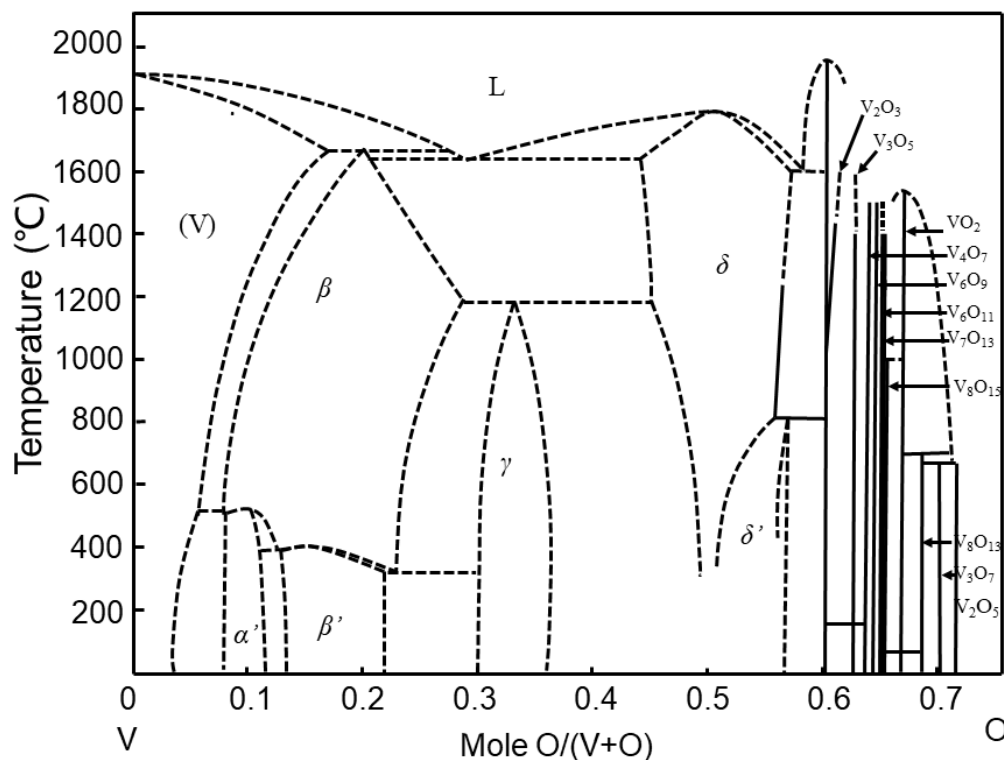


Fig. 6 V-O Phase diagram (Condensed System, 0.1 MPa) according to H.A. Wriedt (ref. [136]). (V),  $\alpha'$ ,  $\beta$ ,  $\beta'$ ,  $\delta$ ,  $\delta'$ ,  $\gamma$  indicate the various solid phases of V-O system, and the structure and composition of the phases are shown in Table 4. “L” indicates “liquid”.

Table 4 The equilibrium solid phases of the V-O system (Condensed System, 0.1 MPa; “bcc” indicates body centered cubic structure; “bct” indicates body centered tetragonal structure; “fcc” indicates face centered cubic structure).

Phase	Structure	Composition (at. % O)	Hazards
(V)	bcc	0 - 17	
$\alpha'$	bct	8.1 - 11.7	
$\beta$	bct	7.9 - 28.5	
$\beta'$	bct	13 - 22	
$\delta$ , VO	fcc	42 - 57	
$\delta'$ , V <sub>52</sub> O <sub>64</sub>	bct	54 - 56	
$\gamma$	monoclinic	30 - 35	
V <sub>2</sub> O <sub>3</sub>	rhombohedral (T > -112 °C)	60	
	monoclinic ( T < -112 °C)		
V <sub>3</sub> O <sub>5</sub>	monoclinic	62.5	
V <sub>4</sub> O <sub>7</sub>		63.6	
V <sub>5</sub> O <sub>9</sub>		64.3	
V <sub>6</sub> O <sub>11</sub>	triclinic	64.7	
V <sub>7</sub> O <sub>13</sub>		65.0	
V <sub>8</sub> O <sub>15</sub>		65.2	
VO <sub>2</sub>	$\alpha$ -VO <sub>2</sub> : monoclinic (T < 68 °C)	66.7	
	$\beta$ -VO <sub>2</sub> : tetragonal (T > 68 °C)	66.6 - 66.9	
V <sub>6</sub> O <sub>13</sub>	monoclinic	68.4	
V <sub>3</sub> O <sub>7</sub>	monoclinic	70	
V <sub>2</sub> O <sub>5</sub>	orthorhombic	71.4	<p style="text-align: center;">Toxic</p> <p>Lethal dose : 10 mg/kg (rat, oral), 23 mg/kg (mouse, oral)</p> <p>Lethal concentration: 500 mg/m<sup>3</sup> (cat, 23 min), 70 mg/m<sup>3</sup> (rat, 2 h)</p>

The significant changes in the electronic and optical properties associated with the phase transition are of interest for applications [145].  $V_2O_3$  has been found to show thermochromism in the infrared region, which is transparent at low temperature and opaque at high temperature [142,146]. Since the transition temperature  $T_c$  of  $V_2O_3$  is far below room temperature, and the resistance and the level of noise are relatively low,  $V_2O_3$  is a good candidate for the fabrication of efficient micro-bolometers which are thermal infrared detectors and can be used in infrared imaging applications such as thermal cameras, night vision cameras, surveillance, mine detection, early fire detection, medical imaging, and detection of gas leakage [142]. Further selected physical properties of  $V_2O_3$  are listed in Table 5.

Table 5 Properties of  $V_2O_3$ .

Property	Value
Molecular weight [147]	149.88 g/mol
Melting point [148]	1940 °C (2213 K)
Boiling point [149]	~ 3000 °C
Density [150]	4.87 g/cm <sup>3</sup>
Microhardness [151]	17.5 GPa
Index of Refraction [76]	2.36
Band Gap [142]	0.66 eV at 343 °C (70 K)

#### 2.4.2 Methods for $V_2O_3$ thin film deposition

$V_2O_3$  thin films can be obtained by both physical and chemical methods. Crystalline or epitaxial  $V_2O_3$  films can be synthesized at lower temperature compared to the deposition of  $\alpha$ - $Al_2O_3$  and  $Cr_2O_3$  thin films.

Chemical solution processes is a common method for obtaining crystalline  $V_2O_3$  films. Piao et al. [152] synthesized polycrystalline  $V_2O_3$  single phase thin films by the reduction of sol-gel-synthesized  $V_2O_5$  films above 500 °C for 2 h in hydrogen atmosphere. Partlow et al. [153] also deposited thin polycrystalline  $V_2O_3$  films on a variety of substrates using a sol-gel process.

Electron-beam evaporation, PLD and magnetron sputtering are used to realize crystalline epitaxial  $V_2O_3$  thin films. Thin epitaxial films of (0001) oriented  $V_2O_3$  were grown on (0001) oriented sapphire substrates by reactive electron-beam evaporation from sintered  $V_2O_3$  powder targets at substrate temperatures between 500 °C and 800 °C with a low deposition rate only 0.1 nm/min - 3 nm/min which was reported by Schuler et al. [154]. Epitaxial polycrystalline  $V_2O_3$  films with columnar structure on (10 $\bar{1}$ 2) sapphire substrates were achieved by DC reactive sputtering in an Ar- $O_2$  atmosphere in an ultra high vacuum (UHV) system at a substrate temperature of 350 °C, using a high purity vanadium target [155]. (0001) and (11 $\bar{2}$ 0) oriented  $V_2O_3$  films of thickness from 4 nm to 300 nm were deposited on (0001) and (11 $\bar{2}$ 0) oriented sapphire substrates using reactive DC magnetron sputtering from a vanadium target in an Ar/ $O_2$  gas atmosphere at 600 °C as reported by Sass et al. [143]. Deposition of  $V_2O_3$  thin films using a vanadium target represents significant challenges because the range of the deposition parameters for stoichiometric  $V_2O_3$  is relatively small due to the existence of many different vanadium oxides as described in Fig. 6 [31]. To obtain the stoichiometric  $V_2O_3$  films easily, a  $V_2O_3$  target could be used. To increase the epitaxial crystal quality and decrease the deposition temperature, iso-structure substrates could be used. Allimi et al. [31,156] reported that epitaxial 215-nm-thick  $V_2O_3$  films could be grown on *a*- and *c*-plane sapphire substrates with the epitaxial relationship of (0001)  $V_2O_3$  // (0001)  $Al_2O_3$  and (11 $\bar{2}$ 0)  $V_2O_3$  // (11 $\bar{2}$ 0)  $Al_2O_3$  by PLD from powder pressed  $V_2O_3$  target in an evacuated deposition chamber devoid of  $O_2$  at the substrate temperature of 750 °C. In this thesis, epitaxial  $V_2O_3$  (0001) films with strong texture were grown on  $\alpha$ - $Al_2O_3$  (0001) substrates at the temperature less than 400 °C by RF magnetron sputtering using  $V_2O_3$  target and this will be described in detail in section 4.2.

## 2.5 Materials in the ternary system of Al-Cr-O

Materials in the system Al-Cr-O attracted strong interests of material scientists and engineers in recent years, as new ceramics in this system are promising candidates for advanced property profiles. Especially materials forming a solid solution structure show excellent properties similar to  $\alpha$ - $Al_2O_3$  or  $Cr_2O_3$  in terms of high hardness, good wear resistance, high thermal stability, chemical inertness and corrosion resistance with regard to their mixed ionic and covalent bonds [5,16,157].

Detailed thermodynamical information on the  $\text{Al}_2\text{O}_3\text{-Cr}_2\text{O}_3$  quasi-binary section of the Cr-Al-O phase diagram has been provided in various studies [74,158]. Fig. 7 shows the binary section  $\text{Al}_2\text{O}_3\text{-Cr}_2\text{O}_3$  according to [74]. Two important regions in the  $\text{Al}_2\text{O}_3\text{-Cr}_2\text{O}_3$  phase diagram are described: one is the solid solution region at higher temperature and over the complete compositional range, and the other one is the immiscibility gap at lower temperature, where the single-phase solid solution should decompose into two co-existing corundum-type phases. In consequence, the homogeneous single phase solid solution  $(\text{Al,Cr})_2\text{O}_3$  is metastable at standard conditions. For the ternary system of Al-Cr-O, in which the two binary materials  $\text{Al}_2\text{O}_3$  and  $\text{Cr}_2\text{O}_3$  have a huge solubility in each other and are iso-structural, the properties (e.g. conductivity, ferromagnetism) can be easily designed and modified in a continuous range simply by changing the ratio of the two starting materials [159].

The Al-Cr-O solid solutions exist for the whole composition range down to the temperatures of 1300 °C as shown in Fig. 7, alumina-chromium refractories have been found to resist corrosion in oxide and other melts and in gasifiers and steel production [160,161].

The studies on the Al-Cr-O solid solution are mainly related to thin films. Ternary Al-Cr-O films are forming dense layers under optimal coating conditions; in these the film density can be up to 4.86 g/cm<sup>3</sup> for Cr-rich films, as shown for  $(\text{Al}_{0.25}\text{Cr}_{0.75})_2\text{O}_3$  coatings in [162] or down to 4.00 g/cm<sup>3</sup> for Al-rich films, as shown for the  $(\text{Al}_{0.71}\text{Cr}_{0.29})_2\text{O}_3$  coatings in [162]. Thus, Al-Cr-O films have been investigated as a new hydrogen permeation barrier candidate [157]. The Al-Cr-O films exhibit high hardness of about 26 GPa [163] and chemical inertness. These films could be used in cutting tools as wear resistant coating [164].

The dominated synthesis methods of thin films in the system Al-Cr-O are PVD methods, allowing the synthesis of thin films in such metastable solid solution with regard of their kinetic non-equilibrium conditions. In recent years, a substantial number of reports on polycrystalline single-phase  $(\text{Cr, Al})_2\text{O}_3$  thin films, and even more complex coatings (i.e. by additional alloying with other elements (see section 2.8), such as Fe have been published [165,166], covering magnetron sputtering, cathodic arc evaporation [166] and other methods. Witthaut et al. [167] have prepared ternary Al-Cr-O layers mixed with

$\text{Cr}_2\text{O}_3$  and  $\gamma\text{-Al}_2\text{O}_3$  on cemented carbide insert tips at a substrate temperature of 500 °C by reactive magnetron sputtering. A comprehensive investigation on the synthesis of polycrystalline  $(\text{Al}_x\text{Cr}_{1-x})_2\text{O}_3$  solid solution thin films have been carried out at 500 °C - 600 °C using reactive cathodic arc evaporation by Pohler et al. [168,169] and Ramm et al. [170], who studied the phase formation, growth morphology, the effects of the target surface and substrate surface and the effects of an iso-structural seed or template layer in detail. Diechle et al. [162,171] reported that corundum-type solid solution  $\alpha\text{-(Al}_{1-x}\text{Cr}_x)_2\text{O}_3$  thin films were deposited at 500 °C by reactive RF magnetron sputtering in Ar and  $\text{O}_2$  with a segmented target consisting of two half plates of Al and Cr. The template or prelayer approach was also investigated. Pedersen et al. [130] have synthesized corundum-type  $(\text{Al,Cr})_2\text{O}_3$  films with Cr/Al ratios of between 2 and 10 on  $\langle 1\ 0\ \bar{1}\ 4 \rangle$ -textured  $\text{Cr}_2\text{O}_3$  prelayers by reactive inductively coupled plasma magnetron sputtering. They used Cr and Al targets at substrate temperatures of 300 °C - 450 °C, and found that the films with lowest Cr/Al ratio of 2 were single phase crystalline but well within the miscibility gap, i.e., the  $\alpha\text{-(Al,Cr)}_2\text{O}_3$  was a metastable solid solution. In this thesis, epitaxial  $\alpha\text{-(Al}_{1-x}\text{Cr}_x)_2\text{O}_3$  thin films were obtained on the iso-structure  $\alpha\text{-Al}_2\text{O}_3$  substrates at 320 °C and 400 °C by RF magnetron sputtering with a segmented ceramic target.

Furthermore, other structures in Al-Cr-O solid solution and the phase transform to the corundum-type have been investigated. A fcc- $(\text{Al,Cr})_2\text{O}_3$  solid solutions were obtained on cubic (CrN) and hexagonal  $((\text{Al}_{0.97}\text{Si}_{0.03})\text{N})$  buffer layers at an early stage from powder metallurgical Al-Cr targets with oxygen by reactive cathodic arc deposition at  $550\text{ °C} \pm 10\text{ °C}$ , and the fcc phase transforms to more thermodynamically stable corundum-type structure at higher film thickness beyond 2  $\mu\text{m}$ , which was reported by Najafi et al. [172]. Khatibi et al. [163,173] deposited fcc- $(\text{Al}_{1-x}\text{Cr}_x)_2\text{O}_3$  solid solution thin films with  $0.6 < x < 0.7$  on Si (001) substrates at temperatures of 400 °C - 500 °C by reactive RF magnetron sputtering from metallic targets of Al and Cr in a flow controlled Ar/ $\text{O}_2$  gas mixture and they found phase transformation from cubic to corundum-type  $(\text{Al}_{0.32}\text{Cr}_{0.68})_2\text{O}_3$  starts at the annealing temperature of 925 °C.

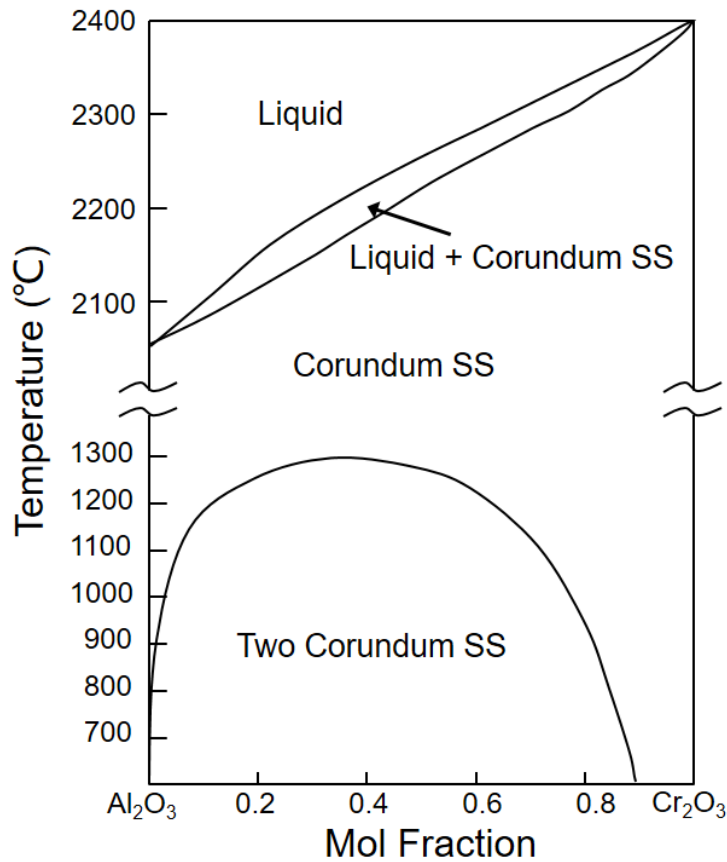


Fig. 7 Binary section  $\text{Al}_2\text{O}_3$ - $\text{Cr}_2\text{O}_3$  of the Al-Cr-O phase diagram according to [74]. “SS” is short for “solid solution”.

## 2.6 Materials in the ternary system of V-Al-O

Few works on Al-doped  $\text{V}_2\text{O}_3$ , V-doped  $\text{Al}_2\text{O}_3$  or V-Al-O system have been reported except for by Callaghan et al. [174] and Pryce and Runciman [175]. Some studies addressed the electronic properties of  $\text{V}^{3+}$  incorporated in  $\alpha$ - $\text{Al}_2\text{O}_3$  as a diamagnetic host lattice, notably the optical spectra [175], paramagnetic resonance and magnetic susceptibility [174]. The phase diagram in the  $\text{Al}_2\text{O}_3$ - $\text{V}_2\text{O}_3$  system has not been reported in the present works except for by Li as shown in Fig. 8 [176]. There is no intermediate compound phases in the binary section  $\text{Al}_2\text{O}_3$ - $\text{V}_2\text{O}_3$  which could be got from Fig. 8 as well as the results from Muan et al. [177,178]. The cation size difference in the  $\text{Al}_2\text{O}_3$ - $\text{V}_2\text{O}_3$  system is 19.6 %, which shows a large deviation from ideality and results in the eutectic or peritectic phase diagrams [158]. A eutectic reaction  $\text{Liquid} \rightarrow \text{Al}_2\text{O}_3 + \text{V}_2\text{O}_3$  occurs at the temperature of 1720 °C.

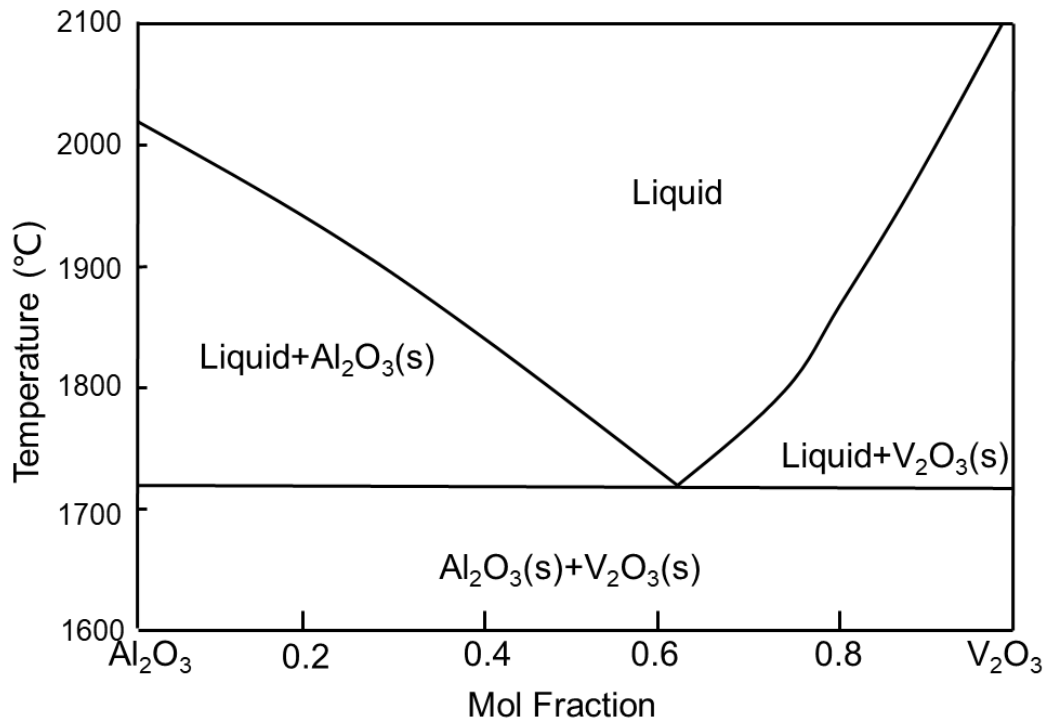


Fig. 8 Phase diagram in the  $\text{Al}_2\text{O}_3$ - $\text{V}_2\text{O}_3$  system [176].

Researchers have obtained V-Al-O solid solution bulk materials by chemical methods. Foëx and Martinez [179] stated that it was possible to prepare  $\text{Al}_2\text{O}_3$ - $\text{V}_2\text{O}_3$  solid solutions by direct heating mixtures of two components at a temperature of 1800 °C. In the publications of Callaghan et al. [174], a series of the  $\text{Al}_2\text{O}_3$ - $\text{V}_2\text{O}_3$  solid solutions with V concentrations between 0.99 % and 8.92 % have been prepared in the form of crystal powders. At first,  $\text{V}_2\text{O}_5$  and aluminium wire were dissolved in HCl and then all the vanadium ions were strongly adsorbed on the alumina by using ammonia solution. The conversion of the other vanadium to the corundum phase solid solutions was accomplished by heating in hydrogen at 1400°C for 10 min - 15 min. Within this concentration range they showed a linear change of lattice parameters according to Vegard's law. The  $(\text{V}_x\text{Al}_{1-x})_2\text{O}_3$  ( $x < 0.2$ ) solid solutions were produced from chemically fine  $\text{Al}_2\text{O}_3$  and  $\text{V}_2\text{O}_3$  oxide tablets by heating in vacuum 1497 °C during 5 h by Viktobov [180]. However, few works on the V-Al-O system thin films have been published. In this thesis, epitaxial corundum-type V-Al-O solid solution thin films were grown on  $\alpha$ - $\text{Al}_2\text{O}_3$  (0001) substrates at the temperature of 400 °C by RF magnetron sputtering using a segmented ceramic target and this will be described in detail in section 4.4.

## 2.7 Materials in the ternary system of V-Cr-O

The structure and properties of pure binary  $\text{Cr}_2\text{O}_3$  and  $\text{V}_2\text{O}_3$  have been presented in the previous sections of this chapter. Both materials possess outstanding properties and are regarded as promising materials in many areas (both in bulk and thin film forms), which has led to intense research since many years. However, relatively less work has been reported on the synthesis of new materials in the ternary system V-Cr-O (in comparison to published work on materials in the system Al-Cr-O). The exception of this statement is work that has focused on Cr-doped  $\text{V}_2\text{O}_3$  materials with low Cr concentration of less than 5 at. % [181].

Considering the iso-structure of  $\text{V}_2\text{O}_3$ ,  $\text{Cr}_2\text{O}_3$  and  $\text{Al}_2\text{O}_3$ , the binary section  $\text{V}_2\text{O}_3$ - $\text{Cr}_2\text{O}_3$  of the V-Cr-O phase diagram is expected to be similar to the binary section  $\text{Al}_2\text{O}_3$ - $\text{Cr}_2\text{O}_3$  of the Al-Cr-O phase diagram. Fig. 9 shows this binary section  $\text{V}_2\text{O}_3$ - $\text{Cr}_2\text{O}_3$  according to ref. [158]. There are also two important regions: one is the solid solution in corundum-type structure region at higher temperature and over the complete compositional range, and the other one is a decomposition into two co-existing corundum-type phases which is also called miscibility gap. Its critical point of decomposition was located at 50 mol %  $\text{Cr}_2\text{O}_3$  and 895 °C (1168 K). The ionic radii of  $\text{Al}^{3+}$ ,  $\text{Cr}^{3+}$  and  $\text{V}^{3+}$  are 0.0535 nm, 0.0615 nm and 0.0640 nm, respectively [182]. The cation size difference is no more than 15 % for  $\text{Al}_2\text{O}_3$ - $\text{Cr}_2\text{O}_3$  (15.0 %) and  $\text{V}_2\text{O}_3$ - $\text{Cr}_2\text{O}_3$  systems (4.1 %). It can be expected that the behavior of solutions in these two systems is expected to be close to the ideal solution. However, the cation size difference for  $\text{V}_2\text{O}_3$ - $\text{Cr}_2\text{O}_3$  system is smaller than of that for  $\text{Al}_2\text{O}_3$ - $\text{Cr}_2\text{O}_3$  system. The miscibility gap is wider and the critical temperature of the miscibility gap is lower than that described for the  $\text{Al}_2\text{O}_3$ - $\text{Cr}_2\text{O}_3$  system, which indicates less deviation from ideal solution behavior due to the smaller ionic radii [158].

Fig. 9 shows the small region of the phase diagram for the MIT in  $(\text{Cr}_x\text{V}_{1-x})_2\text{O}_3$ , which displays the presence of three main phases: antiferromagnetic insulator (AFI), paramagnetic insulator (PI) and paramagnetic metal (PM). The PM to AFI transition temperature increases slightly with increasing chromium concentration for  $x < 0.018$  in  $(\text{Cr}_x\text{V}_{1-x})_2\text{O}_3$ . In addition,  $(\text{Cr}_x\text{V}_{1-x})_2\text{O}_3$  with  $0.005 < x < 0.018$  (both in bulk and thin film forms) exhibits a PM to PI transition at higher temperature [156,181,183,184]. Homm et al. [185] have

found that the resistance increases with decreasing temperature for the highly Cr-doped samples ( $x > 0.03$ ), and a collapse of the insulating state is observed with a reduction of the low temperature resistivity by up to 5 orders of magnitude for the low Cr-doped samples ( $x < 0.03$ ). V-Cr-O system holds a great potential for different electronic devices.

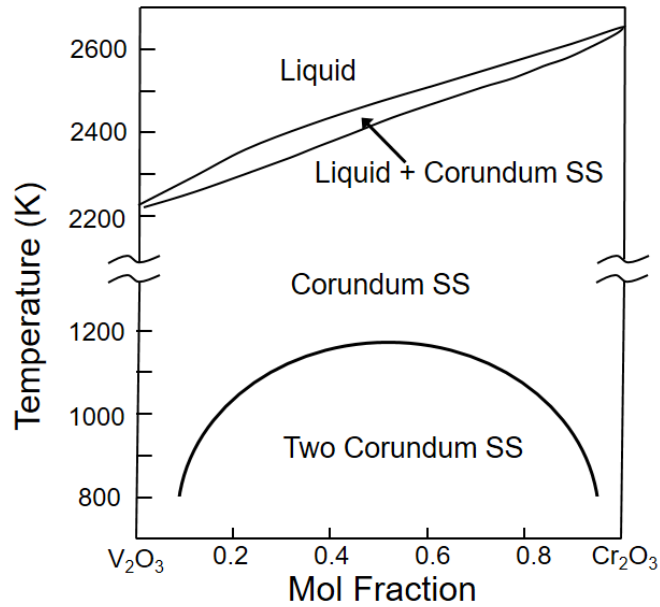


Fig. 9 Phase diagram in the  $V_2O_3$ - $Cr_2O_3$  system according to ref. [158].

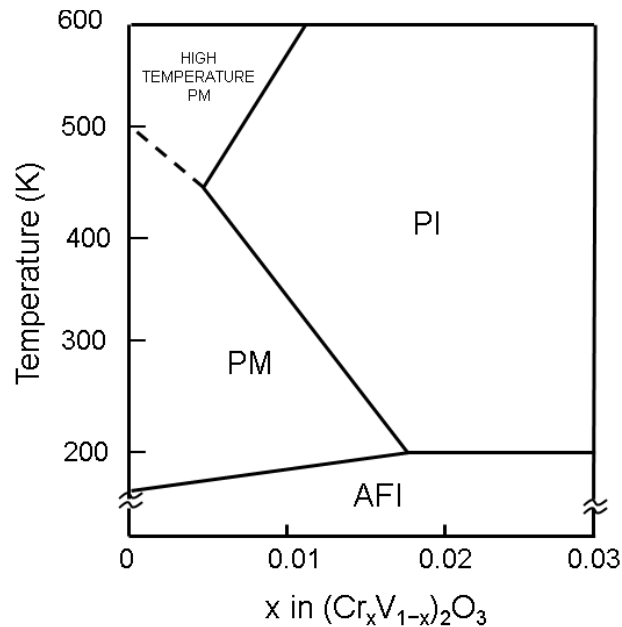


Fig. 10 Phase diagram for the metal-insulator transition in  $(Cr_xV_{1-x})_2O_3$  as a function of temperature (extracted from ref. [186]) AFI is short for antiferromagnetic insulator; PM is short for paramagnetic metal; PI is short for paramagnetic insulator.

V-Cr-O solid solution thin films can be synthesized by chemical and physical methods. Metcalf et al. [183] have prepared Cr-doped  $V_2O_3$  films on (0001) and  $(11\bar{2}0)$  oriented sapphire substrates by the reduction of sol-gel derived vanadium oxide films and found by optical transmission and resistivity measurements that the films undergo PM to AFI transition similar to  $V_2O_3$ . Single phase crystalline fine particles of  $(Cr_xV_{1-x})_2O_3$  ( $0 \leq x \leq 1$ ) thin films have been synthesized by a vapor-phase explosive reaction of a gas mixture of  $CrO_2Cl_2+VOCl_3+H_2+O_2$  induced by a single laser pulse. The lattice constants were investigated with varying Cr concentration by Oyama et al. [187]. The binary  $Cr_2O_3-V_2O_3$  shows a wide miscibility gap below 895 °C (1168 K) as shown in Fig. 7. Thus, it should be possible to obtain such solid solution by PVD at low or medium deposition temperatures. Homm et al. [185] have grown epitaxial  $(Cr_xV_{1-x})_2O_3$  thin films with Cr concentration between 0 % and 20 % on (0001)  $Al_2O_3$  substrates by oxygen-assisted molecular beam epitaxy, and the structural and electrical properties of these films are reported. Spitz et al. [188] reported that corundum-type V-Cr-O thin films were deposited by reactive RF magnetron sputtering of a segmented Cr-V target in an Ar/ $O_2$  atmosphere at 0.4 Pa at the temperature of 350 °C. In this thesis, epitaxial corundum-type V-Cr-O solid solution thin films were grown on  $\alpha-Al_2O_3$  (0001) substrates at the temperature of 400 °C by RF magnetron sputtering using a segmented ceramic target and this will be described in detail in section 4.5.

## 2.8 Additional corundum-type crystalizing systems

$Me_2O_3$  represent a very important class of materials. The extremely wide range of physical and chemical properties of  $Me_2O_3$  suggests considerable potential for diverse applications in cutting tools, optical, electronic, and magnetic device technology. With development of the film technology, control over surface morphology, structure, selective doping, controllable strain, lattice parameters and composition are all in principle possible. The structure, lattice parameters, and composition of the films strongly influence their surface physical and chemical properties. The epitaxial growth of crystalline oxide films has generated a wealth of scientific insight in several key areas of relevance to a wide variety of scientific and technological areas [80,189]. Future scientific growth in this field

thus depends critically on our ability to monitor and control both oxide epitaxial film growth processes and the film and interface structure and composition.

Other binary and ternary oxide films with the same corundum-type structure, for example  $\alpha$ -Fe<sub>2</sub>O<sub>3</sub>, (Cr,Zr)<sub>2</sub>O<sub>3</sub>, (Fe,Cr)<sub>2</sub>O<sub>3</sub>, (Fe,V)<sub>2</sub>O<sub>3</sub>, were also studied by many researchers [39,190–192].

A number of groups have worked on the growth of epitaxial crystalline  $\alpha$ -Fe<sub>2</sub>O<sub>3</sub> thin films by both the chemical and physical methods. Tietz et al. [193] have grown the epitaxial crystalline  $\alpha$ -Fe<sub>2</sub>O<sub>3</sub> films on  $\alpha$ -Al<sub>2</sub>O<sub>3</sub> substrates with different orientations of {0001}, {1 $\bar{1}$ 02}, {11 $\bar{2}$ 0}, and {10 $\bar{1}$ 0} by CVD at the temperature of 1150 °C and they found nucleation and growth of the island occurred preferentially at surface step on the (0001) surface which grew parallel to the substrate surface and the crystal growth was influenced by the interface energies and substrate surface structure. Wang et al. [194] have obtained  $\alpha$ -Fe<sub>2</sub>O<sub>3</sub> (0001) films with the thickness of 7 nm and 70 nm epitaxially grown on  $\alpha$ -Al<sub>2</sub>O<sub>3</sub> (0001) by OPA-MBE, and the interface misfit dislocations were characterized. Chambers and Droubay [195] reported that ultrathin epitaxial  $\alpha$ -Fe<sub>2</sub>O<sub>3</sub> films were grown on Pt (111) by OPA-MBE at a growth rate of about 1.38 nm/min and a substrate of about 550 °C.  $\alpha$ -Fe<sub>2</sub>O<sub>3</sub> was grown epitaxially on  $\alpha$ -Al<sub>2</sub>O<sub>3</sub> (0001) with a film thickness of only 16 nm by reactive magnetron sputtering from iron targets in an Ar-O<sub>2</sub> gas mixture at a substrate temperature of 300 °C (Lee et al.) [39]. Fujii et al. [196] reported that 100 nm thick  $\alpha$ -Fe<sub>2</sub>O<sub>3</sub> films epitaxially formed on (0001), (11 $\bar{2}$ 0), and (10 $\bar{1}$ 2) oriented  $\alpha$ -Al<sub>2</sub>O<sub>3</sub> single crystal substrates at a substrate temperature of 723 K (450 °C) by a reactive PVD method with deposition rate of 6 nm/min.  $\alpha$ -Fe<sub>2</sub>O<sub>3</sub> (0001) epitaxial ultra thin films (3 nm - 24 nm) were grown on Al<sub>2</sub>O<sub>3</sub> (0001) substrates with and without a Cr<sub>2</sub>O<sub>3</sub> buffer layer (15 nm) by MBE [197].

Because the non-equilibrium PVD technologies offer many options to synthesize metastable phases at low temperatures, PVD becomes the most common method for growing the ternary oxide films [198]. Spitz et al. [190] reported that a corundum-type structure (Cr,Zr)<sub>2</sub>O<sub>3</sub> solid solution thin films were synthesized by reactive RF magnetron sputtering of a segmented chromium-zirconium target, and the phase is dependent on the chemical composition. Mashiko et al. [191,199] have obtained (0001) oriented

$\alpha$ -(Cr<sub>x</sub>Fe<sub>1-x</sub>)<sub>2</sub>O<sub>3</sub> ( $0 < x < 1$ ) solid solution films on *c*-sapphire substrates by PLD at growth temperature above 740 °C; these films were subsequently annealed at 1000 °C for 1h in air to transform the spinel-type phase into the corundum-type phase and to improve the crystallinity. Chamberlin et al. [192,200] and Kaspar et al. [4] succeeded in growing epitaxial (Fe<sub>1-x</sub>Cr<sub>x</sub>)<sub>2</sub>O<sub>3</sub> and (Fe<sub>1-x</sub>V<sub>x</sub>)<sub>2</sub>O<sub>3</sub> thin films on  $\alpha$ -Al<sub>2</sub>O<sub>3</sub> (0001) substrates with a growth rate of only 1.44 nm/min at 700 °C - 750 °C by OPA-MBE.

## 3 Experimental details

In this chapter, the experimental details including the deposition process, materials and characterization of the thin films are presented. In section 3.1, the equipment used for thin film deposition, the deposition process and its parameters, and the target and substrate materials are introduced. In section 3.2, the film characterization with respect to composition, structure, and optical properties are described.

### 3.1 Thin film deposition

In this part, the thin film deposition process, the process parameters, the target and substrate materials and the various important aspects of sample preparation are presented in detail.

#### 3.1.1 Radio-frequency (RF) magnetron sputtering process

##### 3.1.1.1 RF magnetron sputtering

In short, sputtering deposition is the deposition of particles vaporized from a surface (i.e. target) by physical sputtering process [201]. Physical sputtering is a non-thermal vaporization process where a target material is bombarded with gaseous ions accelerated from a plasma. The vaporized atoms are deposited on a substrate where the atoms condense and form a thin film. The bombarding energetic particles are usually gaseous ions (e.g.  $\text{Ar}^+$ ) accelerated in an electric field which are used for creating the plasma. Free electrons are immediately accelerated by the electric field in proximity to the target and ionize Ar atoms to form  $\text{Ar}^+$  ions, resulting in plasma ignition.  $\text{Ar}^+$  ions are accelerated towards the cathode, from which material is ejected in the form of mainly individual atoms, but to a lesser extent molecules and clusters. Then the ejected particles cross the plasma and condense on a substrate [1]. Meanwhile, secondary electrons and sputtered atoms from the target surface are accelerated away from the cathode and these electrons play an important role in maintaining the plasma because these high energy electrons lead to further gas ionization and atoms are sputtered away from the surface [11,202].

The plasma may be generated by DC or RF power. In DC sputtering, the cathode electrode is the sputtering target and the substrate is placed on the anode which is at ground potential [201]. However, the target used in DC sputtering must be an electrical conductor since an insulating surface will develop a surface charge that will prevent ion bombardment of the surface. In case of ceramic targets, RF power must be applied instead of DC power. In RF sputtering, ions are accelerated to the surface with enough energy to cause sputtering, then electrons reach the surface to prevent any charge buildup. A commercial RF frequency which is often used for sputtering is 13.56 MHz RF sputtering can be performed at low gas pressures between 0.08 Pa and 10 Pa.

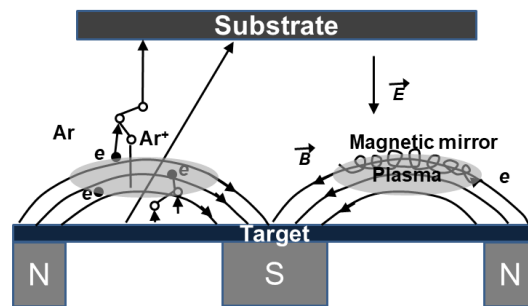


Fig. 11 Plasma formation in a magnetron sputtering system with a cylindrical magnetron.

In order to increase the density of plasma from which ions can be extracted to sputter the target material, a magnetron sputtering configuration is used. In magnetron sputtering with a cylindrical magnetron system as shown in Fig. 11, permanent magnets are located on the back side of the target to provide an “ionization region” with a magnetic field near the target surface. The electrons perform an  $E \times B$  drift and are magnetically confined in a ring above the magnet gap. These electrons are trapped in the magnetic field by the magnetic mirror and provide ionization of Ar [203]. The negative plasma glow is trapped in the magnetic mirror formed by magnets so that the plasma density increases in this magnetically confined region [204]. Therefore, ions can be accelerated from the plasma to the cathode without loss of energy due to physical and charge-exchange collisions. Electrons in a magnetic field are subject to a force  $F = qv \times B$  will cause the electrons move in a circular path with radius called Larmor radius [205]. This increases the effective path length of the electrons and the probability of the collision between ionizing electrons and atoms increases. This allows a high sputtering rate with a lower potential on the target. In

brief, the higher the current density, the higher the deposition rate of the films, and the higher the energy utilization efficiency [206]. In a word, RF magnetron sputtering has advantages of depositing thin films at low temperature with high film growth rate and insulating ceramic targets can be used.

### 3.1.1.2 Film growth

The film growth can be envisioned in three steps: 1) the transport of film species to the substrate including the adsorption of these species on the surface of the substrate; 2) the film species diffusion over the substrate surface including the movement of film atoms to their final positions; 3) nucleation, coalescence and continued film growth; 4) inter-diffusion [207]. Fig. 12 shows Thornton's well known structure zone model which qualitatively describes the structure of sputter deposited thin films changes according to the deposition conditions. The structure behaves in a certain temperature and working gas pressure range. The surface and volume diffusion as well as the temperature are considered when the various structure zones are interpreted. Four structure zones of thin film morphology can be identified: zone 1 describes an amorphous structure or a porous structure consisting of tapered crystallites separated by voids; zone  $T$  is a transition zone consisting of densely packed fibrous grains; zone 2 refers to a structure consisting of columnar grains, which width increases with increasing ratio  $T/T_m$  in accordance with the activation energies typical of surface diffusion; and zone 3 refers to a recrystallized grain structure, where an increase in grain size is in accordance with the activation energies typical of bulk diffusion.

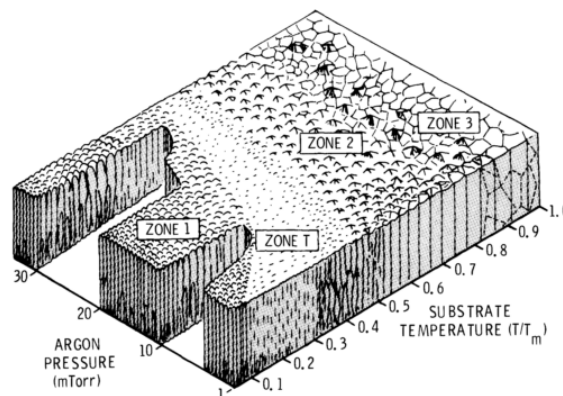


Fig. 12 Structure-zone-model of Thornton for the films deposited by magnetron sputtering [208] ( $T$  is the substrate temperature during deposition;  $T_m$  is the melting point of material.).

There are three different growth modes of thin films which are shown in Fig. 13 [207].

1) Vollmer-Weber (VW) mode is an island growth. In this case,  $\gamma_{substrate} < \gamma_{film} + \gamma_{interface}$ , where  $\gamma_{substrate}$  is the surface energy of substrate,  $\gamma_{film}$  is the surface energy of film,  $\gamma_{interface}$  is the interface energy between film and substrate. Growing layer increases the interface energy and its own surface energy, leading to the layer “balls up” on the substrate.

2) Frank-van der Merwe (FM) mode is a 2D growth mode, i.e. layer-by-layer growth. In this case,  $\gamma_{substrate} \geq \gamma_{film} + \gamma_{interface}$ , which indicates growing layer reduces surface energy, leading to complete wetting of the surface, thus smooth and layer-by-layer growth.

3) Stranski-Krastanov (SK) mode is first covering the surface layer by layer and then growing by hemispheres, i.e. layer-plus-island growth. Initially,  $\gamma_{substrate} \geq \gamma_{film} + \gamma_{interface}$ , and then due to the strain in the growing layer which is caused by a mismatch in lattice parameters between the substrates and the films  $\gamma_{substrate} < \gamma_{film} + \gamma_{interface}$ .

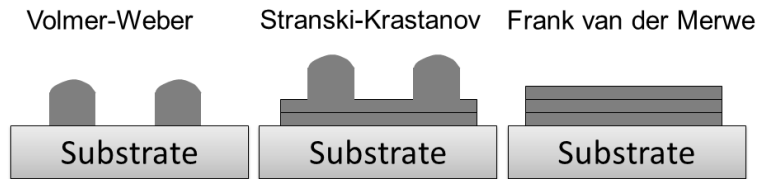


Fig. 13 A schematic representation of the different growth modes [209].

### 3.1.1.3 PVD equipment, deposition process and parameters

All thin films presented in this thesis were deposited by non-reactive RF (13.56 MHz) magnetron sputtering in a Leybold Z 550 PVD coater as shown in Fig. 14. The system is equipped with a CESAR series RF power generator (Advanced Energy Industries, Inc., USA) to supply RF power on the sputtering target, another RF power generator (type TIS 1,2/13560, Hüttinger Elektronik GmbH, Germany) to supply RF power on the substrate (which is used when the substrate surface is cleaned by a plasma plasma-etching process), a DC power supply (type GP060R-10, Takasago International Corporation, Japan; operated in DC current control mode) for the heater which is integrated in the substrate table, multi-gas controllers (type 647C, MKS Instruments Deutschland GmbH, Germany) and mass flow controllers (MKS Instruments Deutschland GmbH, Germany), and a Baratron pressure gauge (MKS Instruments Deutschland GmbH, Germany). A pumping unit combining a mechanical prevacuum pump (rotary vane pump D40B Trivac, Oerlikon Leybold GmbH, Germany) and a turbomolecular pump (Leybold Vacuum GmbH, Germany) is

used to make sure that a base pressure of the PVD system of can be reached to around  $2.0 \times 10^{-6}$  mbar.

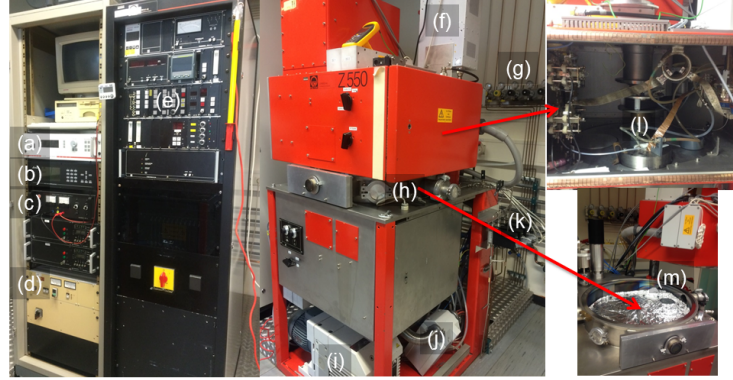


Fig. 14 The setup of the Leybold Z 550 PVD coater used in this thesis. The system is equipped with (a) a RF power supply connected with the sputtering target, (b) a multi-gas controller, (c) a DC power supply, (d) a RF power supply used for the plasma plasma-etching of the substrate, (e) the control panel of the system, (f) a RF matching unit, (g) supply of process gases and pressure gauge, (h) the vacuum chamber, (i) a mechanical prevacuum pump, (j) an oil condenser of the prevacuum pump, (k) the gas mass flow controllers, (l) a target holder with water cooling and connection to the RF power supply, and (m) the substrate table with an integrated heater, water cooling and with RF-bias / RF-plasma-etching line below the vacuum chamber.

Fig. 15 shows schematically the experimental setup for the RF magnetron sputtering processes used in this thesis. The distance between target and substrate table is 40 mm, which is in the order of the mean free path of the target atoms (Al, Cr or V) when the films are deposited at a higher temperature of 320 °C or 400 °C and is slightly higher than the films are deposited without heating. So the mainly sputtered neutral target atoms can fly with few collisions directly to the substrate surface without collisions when deposited at 320 °C or 400 °C. The collision probability will increase in case of deposition without additional heating, which broadens the angular distribution of atoms arriving at the substrate [10,210]. The mean free path of a target atom in this thesis is shown in Table 6, which is calculated according to the following formula [205]:

$$\lambda = \frac{kT}{\sqrt{2}\pi d^2 N_A p} \quad (4)$$

where  $\lambda$  is mean free path,  $d$  is the diameter of gas molecules ( $d(\text{Al}) = 0.118 \text{ nm}$ ,  $d(\text{Cr}) = 0.166 \text{ nm}$ ,  $d(\text{V}) = 0.171 \text{ nm}$ , according to [211]),  $N_A$  is molecular mass ( $N_A(\text{Al}) = 26.98 \text{ g/mol}$ ,  $N_A(\text{Cr}) = 52.00 \text{ g/mol}$ ,  $N_A(\text{V}) = 50.94 \text{ g/mol}$ , according to [212]),  $p$  is the gas pressure (here  $p = 0.6 \text{ Pa}$ ),  $T$  is the temperature (in K), and  $k$  is the Boltzmann constant ( $k = 1.38064852(79) \times 10^{-23} \text{ J/K}$ ).

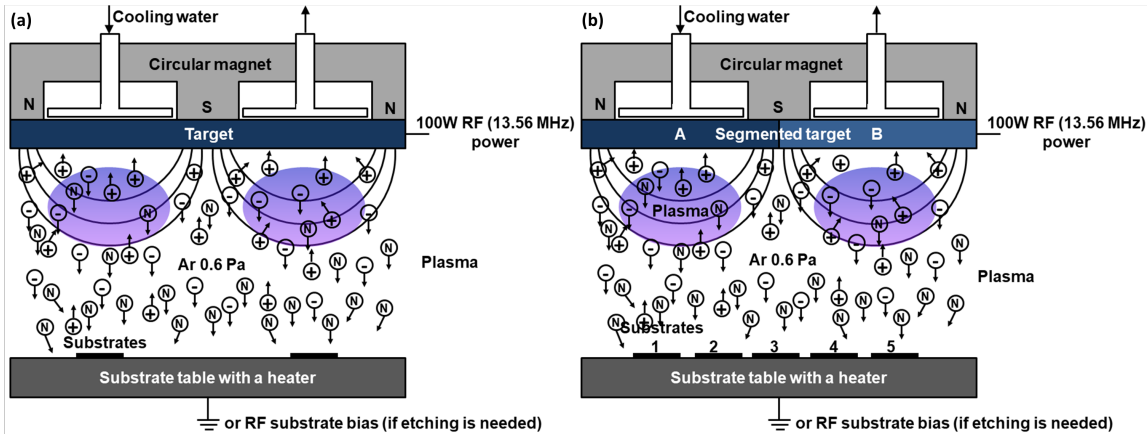


Fig. 15 Schematic experimental setup for the non-reactive RF magnetron sputtering processes used in this thesis: (a) with a circular ceramic target, and, (b) with a segmented ceramic target (one half plate is the material A, and the other half plate is the material B).  $\oplus$  indicates  $\text{Ar}^+$ ,  $\ominus$  indicates electron,  $\textcircled{\text{N}}$  indicates neutral atom.

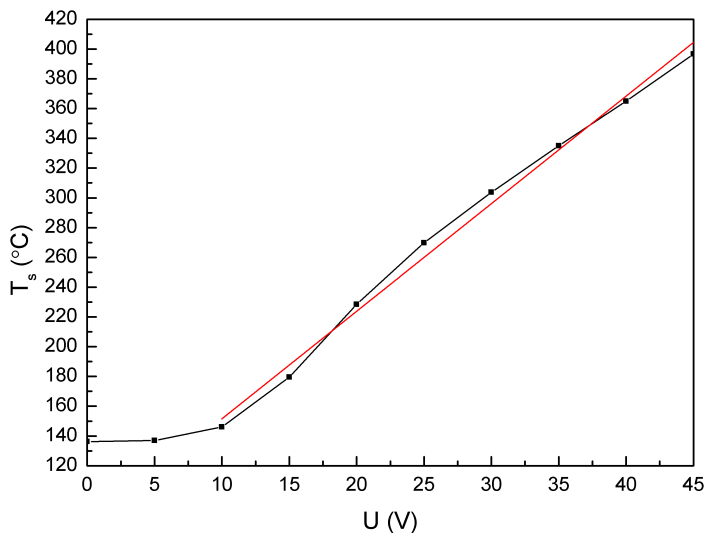


Fig. 16 The relationship between the substrate temperature and the DC voltage applied on the substrate heater when 100 W of RF power is applied to the sputtering target in Ar. The red line is a fitting line.

Table 6 The mean free path of target atoms in an Ar plasma in this thesis.

Substrate Temperature	Al	Cr	V
Without heating (135 °C)	34.2 mm	35.9 mm	29.4 mm
320 °C	49.2 mm	51.6 mm	42.1 mm
400 °C	54.9 mm	58.6 mm	47.8 mm

The different sputtering targets which are used for deposition of different thin films are introduced in detail in the following section. In general, there are two kinds of targets which are shown schematically in Fig. 15 (a) and (b), respectively. One type is a full circular target for deposition of binary thin films which has only one uniform composition as shown in Fig. 15 (a). The substrates were placed below the “race track” erosion circle of the target where the plasma has highest density and the films exhibit the same growth rate. The other type is a segmented target consisting of two half plates (one half is material A and the other half is material B) for deposition of ternary thin films as shown in Fig. 15 (b). Five substrates were placed in a row below the target to obtain thin films with a gradient of the elemental composition that varies from one extreme composition to the other from Pos. 1 to Pos. 5. The sample positions 1 and 5 are exactly below the “race track” erosion zone of the target. The substrate positions are shown schematically in Fig. 17 in the following section. Substrates were cleaned in an ultrasonic acetone bath for 15 min before placing them into the vacuum chamber, and after evacuation some of them were plasma-etched by an RF substrate bias voltage of -200 V in Ar at 0.6 Pa to remove contaminants and adsorbates on the substrate surfaces. For conditioning the substrate surface, a relaxation time of 10 min at the heating temperature before coating was used. The sputtering targets are operated at an RF power of 100 W in Ar 99.9999 % at a pressure of 0.6 Pa. A low power density of 2.26 W/cm<sup>2</sup> was used to deposit films with low deposition rate, but the deposition rate is also dependent on the target material (i.e. sputtering yield) and the position of the samples related to the target (which is shown in more detail in Table 7 in the following section). A heater was integrated in the substrate holder, and the substrates can be heated up to 400 °C during the deposition. The minimum substrate temperature is 135 °C without additional heating due to the 100 W of RF power applied to

the sputtering target. The relationship between the substrate temperature and the DC voltage applied by the heater via the DC power supply is shown in Fig. 16.

### **3.1.2 Experimental materials**

#### **3.1.2.1 Materials for substrates**

*c*-plane oriented (0001)  $\alpha$ -Al<sub>2</sub>O<sub>3</sub> single crystal substrates were used for the study of the growth of iso-structural rhombohedral metal-oxides thin films. These substrates were used for microstructure characterization and were supplied by Alineason Materials Technology GmbH, Germany, with a geometry of 10 mm × 10 mm × 1 mm, high purity of more than 99.99 %, polished on one side to an average roughness  $R_a < 1$  nm. The thin films were deposited on the polished surface. Two side polished  $\alpha$ -Al<sub>2</sub>O<sub>3</sub> substrates with *c*-plane orientation were used for optical measurements; these were supplied by the Roditi International Corporation Ltd., England, with a geometry of  $\varnothing$  100 mm × 0.5 mm, high purity of more than 99.996 %, and an the average roughness  $R_a < 0.2$  nm for both sides. Substrate pieces with a geometry of 10 mm × 10 mm × 0.5 mm were cutted from these sapphire wafers by hand with a diamond pen.

Si (100) single crystal substrate wafers with a geometry of  $\varnothing$  100 mm × 0.35 mm, two sides polished and p-type doped with boron were supplied by CrysTec GmbH Kristalltechnologie, Germany. These Si wafers were cutted into Si substrates with a geometry of 12 mm × 12 mm × 0.35 mm (and were used for the measurements of the thickness and elemental composition of the deposited thin films), and into smaller composition and Si stripes with a geometry of 12 mm × 2 mm × 0.35 mm (which were also used for the thickness measurements, by profilometry, as described in section 3.2.8).

#### **3.1.2.2 Materials for sputtering targets**

In order to obtain thin films with different composition, various targets were used as shown in Table 7. All targets were supplied by FHR Anlagenbau GmbH, Germany, with a diameter of  $\varnothing$  75 mm, thickness of 6 mm and purity of 99.9 %. The Cr<sub>2</sub>O<sub>3</sub> and V<sub>2</sub>O<sub>3</sub> thin films were deposited by using pure Cr<sub>2</sub>O<sub>3</sub> and V<sub>2</sub>O<sub>3</sub> ceramic targets with uniform chemical composition. Thin film deposition in the ternary systems (Cr-Al-O, V-Al-O, and V-Cr-O) with the intention to vary systematically the composition in the metal sublattice population of corundum-type Me<sub>2</sub>O<sub>3</sub> thin films (i.e. Me refers here in a simplified way to

all metals mentioned above) was done by using a segmented ceramic target consisting of two half plates of different materials and bonded on a copper holder. Due to it is difficult to deposit the Cr-Al-O and V-Al-O thin films with higher Al concentration at low temperature in this thesis, the Al<sub>2</sub>O<sub>3</sub> content should be small. In this thesis, only 20 % in the atomic weight of Al<sub>2</sub>O<sub>3</sub> is contained in the half plate of the segmented targets. For Cr-Al-O films, one half plate is made of a compound, i.e. a mixture of Cr<sub>2</sub>O<sub>3</sub> (80 at. %) and Al<sub>2</sub>O<sub>3</sub> (20 at. %), and the other half plate is made of pure Cr<sub>2</sub>O<sub>3</sub>. For V-Al-O films, one half plate is made of a compound, i.e. a mixture of V<sub>2</sub>O<sub>3</sub> (80 at. %) and Al<sub>2</sub>O<sub>3</sub> (20 at. %), and the other half plate is made of pure V<sub>2</sub>O<sub>3</sub>. In order to get V-Cr-O films with large range of V/Cr concentration, one half plate is pure Cr<sub>2</sub>O<sub>3</sub> and the other half plate is pure V<sub>2</sub>O<sub>3</sub>. The sputtering targets used in this thesis and the corresponding substrate positions during thin film deposition are shown in Fig. 17. The “race track” erosion zone on the target surface is more or less visible, where the circular magnet on the target backside is forcing the electrons into an toroidal plasma ring [213].

Table 7 Materials for sputtering targets used for thin film deposition. (A and B denote the target materials of the half plates in Fig. 15.)

Thin Film	Sputtering target		
	Constitution	Geometry	Purity
Cr <sub>2</sub> O <sub>3</sub>	Cr <sub>2</sub> O <sub>3</sub> (100 at. %)		
V <sub>2</sub> O <sub>3</sub>	V <sub>2</sub> O <sub>3</sub> (100 at. %)		
	Segmented target		
$\alpha$ -(Cr <sub>1-x</sub> Al <sub>x</sub> ) <sub>2</sub> O <sub>3</sub>	A: Al <sub>2</sub> O <sub>3</sub> (20 at. %) - Cr <sub>2</sub> O <sub>3</sub> (80 at. %) mixture B: Cr <sub>2</sub> O <sub>3</sub> (100 at. %)	ø 75 mm × 6 mm	99.9 %
	Segmented target		
$\alpha$ -(V <sub>1-x</sub> Al <sub>x</sub> ) <sub>2</sub> O <sub>3</sub>	A: Al <sub>2</sub> O <sub>3</sub> (20 at. %) - V <sub>2</sub> O <sub>3</sub> (80 at. %) mixture B: V <sub>2</sub> O <sub>3</sub> (100 at. %)		
	Segmented target		
$\alpha$ -(V <sub>1-x</sub> Cr <sub>x</sub> ) <sub>2</sub> O <sub>3</sub>	A: Cr <sub>2</sub> O <sub>3</sub> (100 at. %) B: V <sub>2</sub> O <sub>3</sub> (100 at. %)		

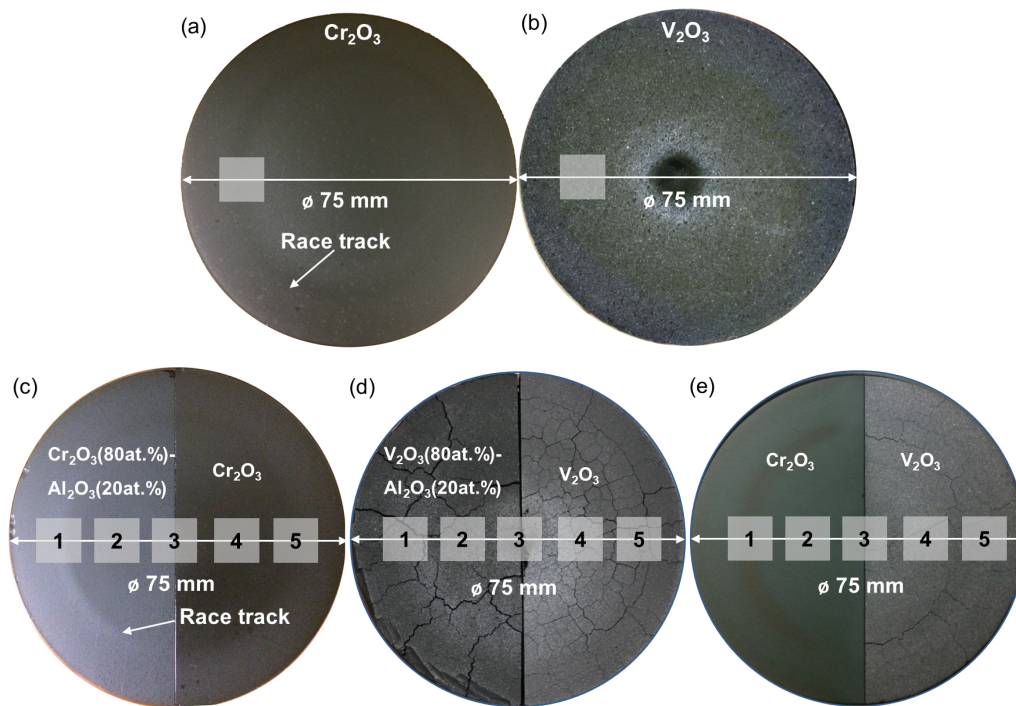


Fig. 17 Sputtering targets and the substrate positions during thin film deposition in relation to the targets in this thesis: (a) a pure  $\text{Cr}_2\text{O}_3$  target was used for depositing the pure  $\text{Cr}_2\text{O}_3$  film; (b) a pure  $\text{V}_2\text{O}_3$  target was used for depositing the pure  $\text{V}_2\text{O}_3$  thin film; (c) for the deposition of Cr-Al-O thin films, a segmented target was used; it consists of two half plates; one half plate is a compound of a mixture of  $\text{Cr}_2\text{O}_3$  (80 at. %) and  $\text{Al}_2\text{O}_3$  (20 at. %), and the other half plate is pure  $\text{Cr}_2\text{O}_3$ ; (d) for the deposition of V-Al-O thin films, a similar segmented target was used; one half plate is a compound of a mixture of  $\text{V}_2\text{O}_3$  (80 at. %) and  $\text{Al}_2\text{O}_3$  (20 at. %), and the other half plate is pure  $\text{V}_2\text{O}_3$ ; (e) for the deposition of V-Cr-O thin films, a different segmented target was used, consisting of one half plate of pure  $\text{Cr}_2\text{O}_3$ , and another half plate of pure  $\text{V}_2\text{O}_3$ . In case of the deposition of pure  $\text{Cr}_2\text{O}_3$  and  $\text{V}_2\text{O}_3$  thin films, substrates were located below the “race track” erosion zone of the targets; in case of deposition of the ternary thin films, the substrate positions were projected in the target plane and marked as Pos. 1 - Pos. 5 in the above images.

### 3.2 Thin film characterization

A variety of analytical methods were used to investigate the chemical composition, microstructure, phase composition, morphology, crystallinity and crystalline perfection, strain, defects, and selected optical properties. The chemical composition of the thin films

was determined by electron probe micro-analysis (EPMA) and Auger electron spectroscopy (AES). To determine the crystalline structure and phase composition of the thin films, detailed XRD analyses i.e. XRD in Bragg-Brentano geometry, rocking curve measurements, pole figures analysis, and reciprocal space mapping (RSM) were carried out. TEM was used to study the microstructure and describes the orientation and epitaxial relationship between the thin films and the substrates. Raman spectroscopy, IRRAS and UV-VIS-NIR spectroscopy were measured for spectroscopic and optical properties. Further, the film thickness and deposition rate was determined by a surface profiler. The individual methods and the experimental setups used are described in detail in the following sections.

### **3.2.1 Electron probe micro-analysis**

Electron probe micro-analysis (EPMA) is a method for non-destructive chemical analysis of the samples. With this method, all chemical elements except H, He and Li can be detected.

In EPMA (see Fig. 18, a schematic presentation of the principle functionality of EPMA), an electron beam emitted from a hot filament (e.g. made of W or LaB<sub>6</sub>) is accelerated by an electric field and focused on the sample in a small area with volume (depth) about 1  $\mu\text{m}$  - 2  $\mu\text{m}$ . Therefore, EPMA needs the film thickness in the range of micrometers in order to avoid get the chemical information from the substrate. Several signals including X-rays, Auger electrons, backscattered and secondary electrons are generated by the interaction of the primary incident electron beam on the sample as shown in Fig. 19. EPMA is a technique which is based on the detection of the emitted characteristic X-rays to determine the chemical composition of the sample, because each atom emits specific and identifiable wavelengths of X-rays. The characteristic X-rays emerging from the sample are analyzed in a Wavelength-Dispersive Spectrometer (WDS). When X-rays encounter the single-crystal monochromator, only those X-rays that satisfy Bragg's Law are reflected and a single wavelength is passed on to the detector by which X-rays are counted. Detectors used in WDSs are the most commonly gas proportional counter types, in which incoming X-rays enter the detector through a collimator and thin window, are absorbed by atoms of the counter gas, and then a photoelectron is ejected by each atom absorbing

an X-ray. The photoelectrons are accelerated to a central wire such that additional ionization produces an electrical pulse which has an amplitude proportional to the energy of the original X-ray photon. The chemical composition is exactly known by comparison of the wavelengths of spectral lines with the theoretical line positions. To determine the chemical composition quantitatively, standards of known composition are required. The concentration of each atomic element in the sample can be calculated by comparing the intensities of the characteristic X-rays with the corresponding intensities of the standards [214].

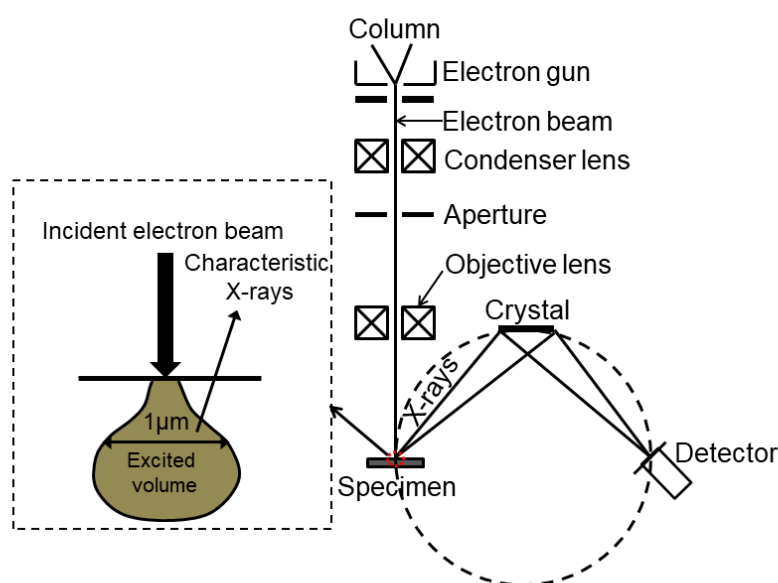


Fig. 18 Schematic drawing of the basic components of the electron probe micro-analyzer. The dashed square shows that the electron beam focuses on the sample surface and characteristic X-rays are generated from beneath the surface and collected by the spectrometer. The shaded area represents the excited volume, from which the chemical information can be obtained [214–216].

EPMA was carried out by a CAMECA Camebax Microbeam SX Five. A tungsten filament was operated at an accelerating voltage of 10 kV. During measurements, a pumping system ensures a vacuum of about  $1.3 \times 10^{-3}$  Pa in the gun chamber. Various standards were used to calibrate the system for quantitative compositional analyses: pure Cr for Cr, pure Al for Al, VC for V, YIG ( $Y_3Fe_5O_{12}$ ) for O, TiN for N, TiC for C, and ArSi (sputtered Si with 9.9 wt %  $\pm$  0.3 wt % Ar) for Ar. Ten times measurements for each sample were taken to obtain an average value for the elemental composition. Directing an electron

beam at the non-conductive samples can lead to electrical charging of the samples surface. In case of thin films being less or even non-conductive, a thin layer of amorphous carbon with the thickness of 5 nm - 30 nm was deposited on the sample surface by means of evaporation to avoid the charging effects.

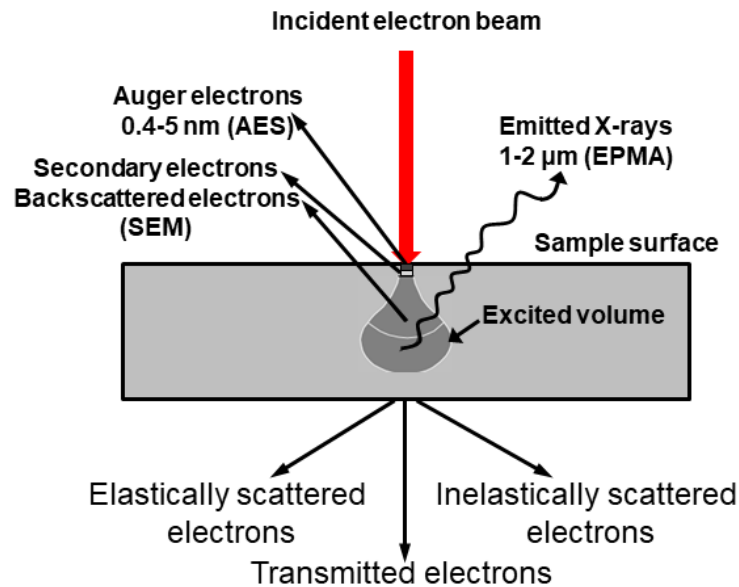


Fig. 19 Signals generated when high-energy incident electrons interact with a thin sample [217]. The typical analysis depth of AES and EPMA is 0.4 nm - 5 nm and 1 μm – 2 μm respectively.

### 3.2.2 Auger electron spectroscopy

Auger electron spectroscopy (AES) can provide quantitative chemical information and get concentration of an element in depth from the film surface to the substrate combining with sputter plasma-etching process. Similar to the EPMA, all elements except of H and He can be detected and quantified. In contrast to EPMA, AES has an analysis depth of less than 5 nm (normally about 3 monolayers, 1 nm - 2 nm) as shown in Fig. 19. Therefore, AES is suited for the compositional analysis of ultra-thin films. When a depth resolved information of the elemental composition from the film surface to the substrate wants to be obtained, Ar ion plasma-etching process should be used to remove the previous layer which has been measured by AES and then AES measurement is done on the new layer, and this well-defined procedure is repeated.

Similar to EPMA, AES is accomplished by exciting the sample's surface with a focused electron beam which generates Auger electrons, emerging from the sample surface as shown in Fig. 19. The difference of the principle between the Auger electron emission in AES and the characteristic X-rays emission in EPMA is shown in Fig. 20. The inner shell of an atom is ionized when high energy electrons bombard the atom creating a vacancy in the inner orbit. An electron from an outer shell moves to fill this vacancy. The released energy caused by the moved electron changes from a higher to a lower orbit can be emitted as characteristic X-ray. Alternatively, a third electron from another orbit might be ejected, which is called Auger electron. The kinetic energy of the emitted Auger electrons from the sample surface excited by electron beam is measured by an electron energy analyzer, where the atom is identified by its energy. In general, since the initial ionization is non-selective and the initial vacancy may therefore be in various shells, there will be many possible Auger transitions for a given element some weak and some strong in intensity. Therefore, each element in a sample being studied will give rise to a characteristic spectrum of peaks at various kinetic energies.

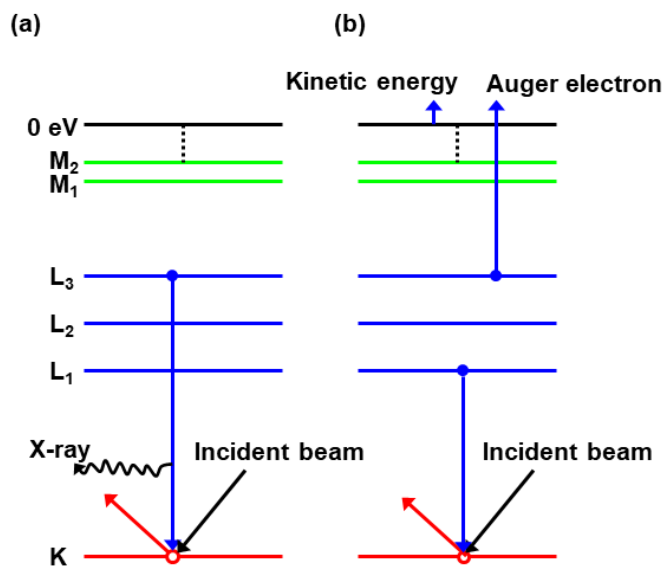


Fig. 20 Schematic representation of (a) the characteristic X-rays emission in EPMA and (b) Auger electron emission in AES [218]. K, L<sub>1</sub>, L<sub>2</sub>, L<sub>3</sub>, M<sub>1</sub>, M<sub>2</sub>...indicate the various electron energy levels.

AES depth profiling was carried out to evaluate the composition of the films over their cross-sections, using a PHI 680 Xi Auger Nanoprobe with an electron beam of only 24 nm

in diameter at an accelerating voltage of 10 keV and a beam current of 20 nA. During the measurements, the chamber was pumped to ultra high vacuum of  $1 \times 10^{-7}$  Pa. Samples were tilted with  $60^\circ$  from the surface normal to the electron gun. An Ar ion beam was used for plasma-etching the sample surface to obtain a depth information of the elemental composition with an accelerating voltage of 2 keV and a current of 500 nA in an etched area of  $1 \times 1$  mm<sup>2</sup> with an plasma-etching rate of 8.84 nm/min. Samples were tilted with  $45^\circ$  from the surface normal to the ion gun during the plasma-etching process. If the samples are non-conductive, silver was painted on the sample surface around the measured spot to retrieve the electric charge.

### **3.2.3 X-ray diffraction**

The mechanical, electrical, magnetic or optical properties are strongly influenced by the microstructural characteristics of the films such as crystalline or amorphous state, crystallographic orientation, crystallite size, strain and stress [219]. Therefore, it is very important to characterize the structure or crystallinity of the films. X-rays are electromagnetic radiations with wavelength of the order of 0.01 nm - 1 nm. Since the wavelengths of the X-rays are similar to the size of atoms in the materials, they can easily penetrate matter and determine crystal structures. X-ray diffraction (XRD) is a powerful non-destructive technique for characterizing crystalline materials.

#### **3.2.3.1 XRD in Bragg-Brentano geometry**

XRD in Bragg-Brentano geometry is used to distinguish between amorphous networks and crystalline films, and is used to identify phases with defined crystal structure, lattice parameter  $c$ , grain size and strain. In a diffraction mode, a primary X-ray beam is inclined into a material and the diffracted beam is outgoing from the film surface whose directions and intensities will be recorded by a detector. XRD is normally performed in Bragg reflection: the theoretical background was put forward by W. H. Bragg and W. L. Bragg [220] who managed to express the conditions for diffraction of X-rays in crystalline materials in a mathematical form. This is called Bragg's law and gives the condition for constructive interference for X-rays incident on a set of lattice planes. Fig. 21 shows schematically three sets of parallel crystallographic lattice planes with interplanar spacing  $d$  with incident and diffracted (reflected) X-ray beams under the angles  $2\theta$ . As shown in this figure, the path difference between two X-rays reflected at the first and the second

lattice plane is  $2d\sin\theta$ . If the path difference of waves reflected by adjacent lattice planes is equal to the integral multiple of the X-ray wavelength  $\lambda$ , there is constructive interference and the reflected beam is very intense. Therefore:

$$2d\sin\theta = n\lambda \quad n = 1, 2, 3, \dots \quad (5)$$

This equation is called Bragg's law. Cu  $K_\alpha$  radiation is used as the X-ray source, so here  $\lambda = 0.154184$  nm [221].

For the XRD in Bragg-Brentano geometry i.e. symmetric  $\theta/2\theta$  scans as shown in Fig. 22, the incident beam and reflected beam have the same angles with respect to the film surface i.e.  $\omega = \theta$ . The scattering vector is normal to the sample surface, therefore, only the lattice planes parallel to the sample surface can be probed. To determine the crystalline phases of the sample, the intensity and the location of the peaks are recorded with the line detector by probing the sample for an adequate range of  $2\theta$  angles, then compared to the theoretical data listed in the XRD diffraction databases, i.e. PDF cards from ICDD-database. For the hexagonal crystal structure, the crystallographic planes with  $hkil$  ( $i=-(h+k)$ ) Miller-Bravais indices where  $l$  is odd and  $h+2k=3n$  ( $n$  is an integer) will not give any diffraction i.e. these peaks are not present in the  $\theta/2\theta$  diffractogram, and are called forbidden peaks (rule of extinction) [222].

The grain size of the crystals can be estimated from the  $\theta/2\theta$  reflexes by the Scherrer formula with Gaussian profile modification.

$$D = K\lambda / (\beta \cos\theta) \quad (6)$$

where  $K = 0.89$  is the Scherrer constant,  $\lambda = 0.154184$  nm is the wavelength of the X-ray radiation,  $\theta$  is the Bragg diffraction angle, and  $\beta$  is the full width at half maximum (FWHM) of the peak in radians. Here considering the instrumental broadening of the peaks,  $\beta$  was corrected by Gaussian profile:  $\beta = \sqrt{B^2 - b^2}$ , where  $B$  is the measured FWHM, and  $b$  is the broadening of the used instrument ( $b = 0.07^\circ$ , which is measured by a standard in the used instrument in this thesis) [223].

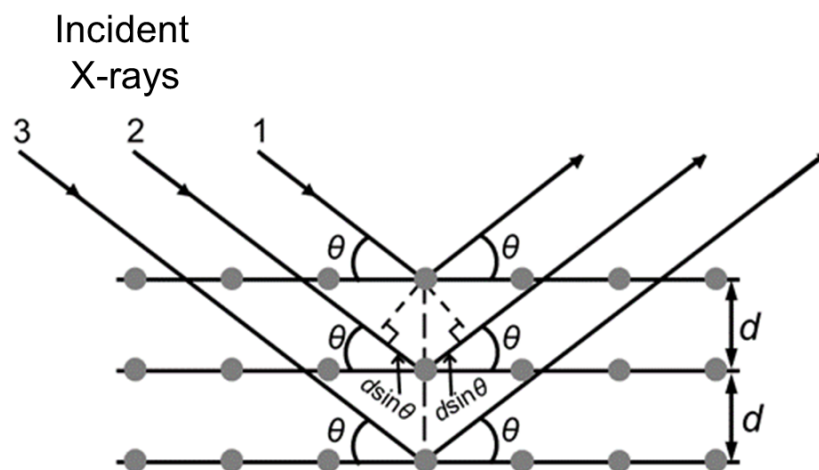


Fig. 21 Schematic drawing of X-rays incident into and reflected from parallel lattice planes and the illustration of the Bragg's law.  $d$  is the interplanar spacing and  $\theta$  is the scattering angle of the X-rays.

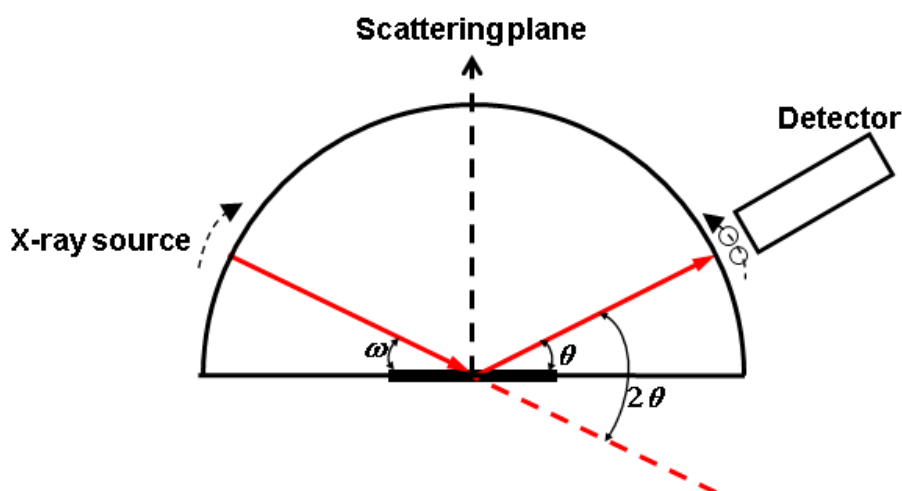


Fig. 22 Schematic representation of XRD in Bragg-Brentano geometry. The incident angle  $\omega$  is defined as the angle between the X-ray source and the sample, and the diffracted angle  $2\theta$  is the angle between the incident beam and the detector.

XRD in Bragg-Brentano geometry was performed with a Seifert C-3000 diffractometer with a line detector (Type Meteor 1D from company Dectris Ltd) using Cu  $K_{\alpha 1/2}$  (the wavelength of Cu  $K_{\alpha 1}$  is 0.154054 nm and Cu  $K_{\alpha 2}$  is 0.154432 nm [221]) radiation source with a Ni filter at a generator voltage of 40 kV and a current of 30 mA. The scattering angle  $2\theta$  was varied from  $20^\circ$  to  $100^\circ$  with a step size of  $0.01^\circ$  and accumulation time (collection time) of 360 seconds/step for 45 parallel measurements.

### 3.2.3.2 Rocking curves ( $\omega$ scans)

To determine the mosaic spread created by slight misorientations of different crystals as they grow on the substrates in this thesis, rocking curve analyses were carried out. In a rocking curve measurement, the detector is set at a specific Bragg angle (a reflecting position) and the sample is tilted (only in  $\omega$ ). A plot of X-ray intensity versus  $\omega$  is obtained in a rocking curve analysis ( $\omega$  is the angle between the X-ray source and the sample as shown in Fig. 22).

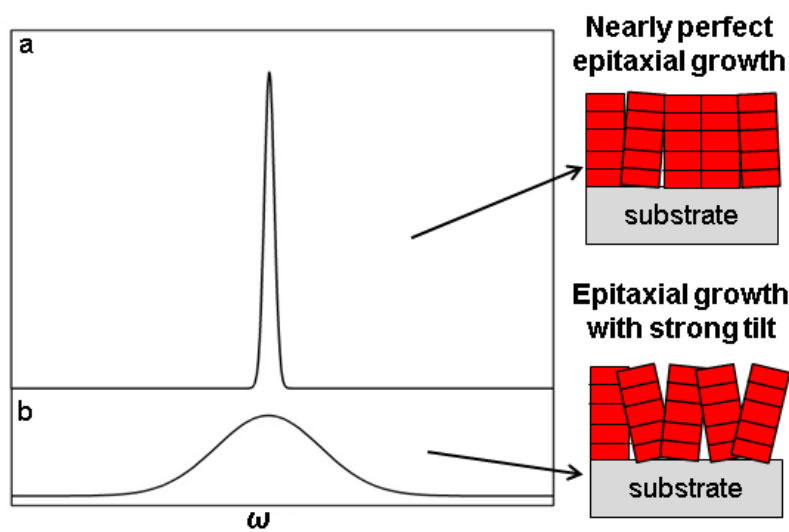


Fig. 23 A schematic drawing of rocking curves of the films grown on the substrates (a) with nearly perfect epitaxial growth and (b) with strong tilt.

If the films possess perfect crystals (perfect epitaxial growth on the substrates), the rocking curves show a very sharp peak and the width of the peak of the rocking curve is determined by the beam geometry and the spectral width of the source as shown in Fig. 23 (a). Defects in the crystals like mosaicism, dislocations, and curvature create disruptions in the perfect parallelism of atomic planes, which cause the broadening of the rocking curve signal as shown in Fig. 23 (b).

In this thesis, the rocking curve analyses were performed with a high resolution X-ray diffractometer (Model XRD 3003 PTSHR Seifert) with a slit focus X-ray tube at 40 kV and 40 mA, attached with a Ge (220) monochromator. The samples were tilted with a step

size of  $0.02^\circ$  and measurements were taken with an accumulation time (collection time) of 10 seconds/step.

### 3.2.3.3 Texture measurements / pole figure analyses

Texture is the distribution of crystallographic orientations of the sample. If the crystallographic orientations in the samples are random, a random texture will be obtained. If the crystallographic orientations have some preferred directions, the sample possesses a weak, strong, or moderate texture which is dependent on the percentage of crystals that have the preferred orientation. A texture can be described by a characteristic pole figure, which is a map of a selected crystal plane normal plotted with respect to the sample frame. In other words: a pole figure shows the intensity distribution of the scattering vector in reciprocal space. Texture measurement (or pole figure analysis) is an efficient way to reveal the orientation distribution of polycrystalline materials.

The pole figure technique uses a scattering vector to map such “points” in reciprocal lattice space. The difference between an incident and diffracted X-ray wave vector is defined as scattering vector. Fig. 24 (a) shows texture analysis configuration schematically.  $\varphi$  is the azimuth angle in-plane, and the sample undergoes a  $360^\circ$  azimuth rotation along the normal of the sample surface during the measurement.  $\psi$  is the tilting angle between the scattering vector and the normal to the sample surface. In pole figure analysis, first of all, the lengths of scattering vectors were selected i.e. fix  $\omega/2\theta$  ( $\omega = \theta$ ) according to the crystal planes which are investigated. Then a continuous repetition of  $360^\circ$  azimuth rotation for  $\psi$  tilts from  $0^\circ$  to  $60^\circ$  (in this thesis) is carried out. Therefore, stereographic projections (pole figures) of the distribution of the selected orientations are presented.

The pole figure technique can help to determine the crystal structure of the material. An example is shown in Fig. 24 (b) which belongs to the (0001) oriented  $\text{Cr}_2\text{O}_3$  film deposited on *c*-plane  $\alpha\text{-Al}_2\text{O}_3$  substrate deposited at  $320^\circ\text{C}$ . The pole figure is measured at  $\omega = 36.472^\circ$  and  $2\theta = 72.944^\circ$ , which corresponds to the  $(10\bar{1}10)$  plane of the theoretical  $\text{Cr}_2\text{O}_3$  according to the PDF card No. 38-1479 from ICDD. The texture shows a 6-fold symmetry at  $\psi = 17.6^\circ$ , which is the angle between crystal planes  $\{0006\}$  and  $\{10\bar{1}10\}$ .

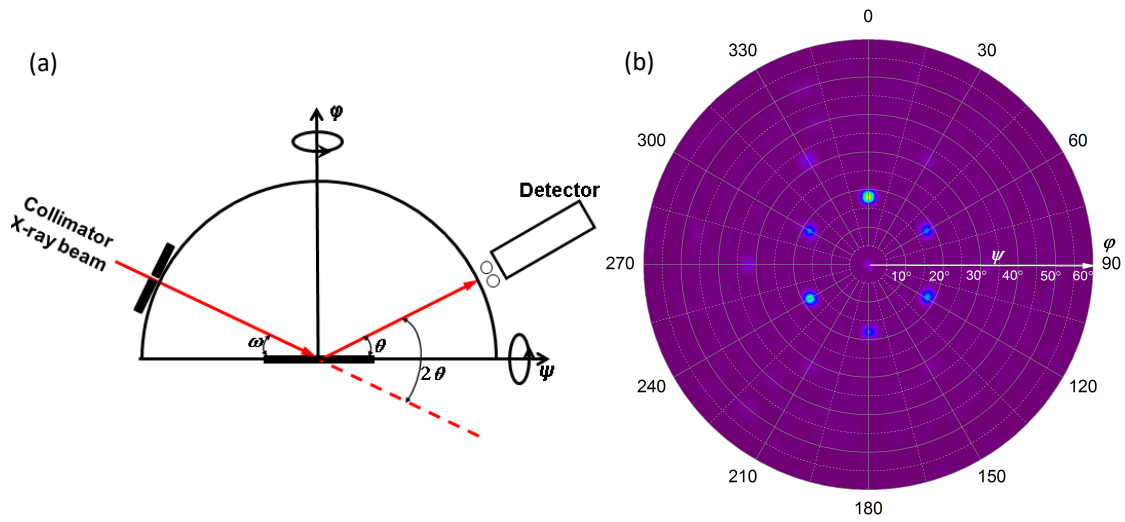


Fig. 24 (a) schematic representation of texture measurements configuration in pole figures analyses. (b) Pole figure measured at  $\omega = 36.472^\circ$  and  $2\theta = 72.944^\circ$  from a  $(10\bar{1}10)$  oriented  $\text{Cr}_2\text{O}_3$  film deposited on  $c$ -plane  $\alpha\text{-Al}_2\text{O}_3$  substrate deposited at  $320^\circ\text{C}$ .  $\varphi$  and  $\psi$  are azimuth and tilt angles, respectively.

The texture of all films was investigated via pole figure measurements by a high resolution X-ray diffractometer (Model XRD 3003 PTSHR Seifert). A point focus tube with collimator of  $\Phi$  2 mm was used. A 0.3 mm slit was placed in front of the detector when measuring the coated  $\alpha\text{-Al}_2\text{O}_3$  substrate, while a Cu slice with the thickness of 0.1 mm as absorber replaced the slit when measuring the  $\alpha\text{-Al}_2\text{O}_3$  single crystal to avoid destroying the detector from the high intensity of the X-rays. The parameters used for the X-ray diffractometer for pole figure analyses are shown in Table 8.

Table 8 Parameters of the X-ray diffractometer used for the texture / pole figure measurements.

U	I	$\lambda_{\text{CuK}\alpha 1}$	Angular range	Step Width		Time
				Coated sample	single crystal / substrate	
40 kV	40 mA	0.15406 nm	$\psi$ : $0 - 80^\circ$ $\varphi$ : $0 - 360^\circ$	$\psi$ : $2^\circ$ $\varphi$ : $5^\circ$	$\psi$ : $1^\circ$ $\varphi$ : $2.5^\circ$	5s

### 3.2.3.4 Reciprocal space mapping

Reciprocal space mapping (RSM) shows a two-dimensional region of the reciprocal space, which is used to investigate the lattice parameters, strain relaxation and epitaxy quality of the films grown on the substrates. More information regarding interplanar spacings and defect-related broadening of the reciprocal space lattice points also can be analyzed by RSM.

RSM can be carried out by performing a series of  $\omega$ - $2\theta$  scans at successive  $\omega$  values in the following way: first a  $\omega$ -scan is performed for a given length of the scattering angle; then the  $2\theta$  scan is employed with a slightly different tilt  $\delta q$  in  $\omega$  direction (i.e.  $2\theta = 2\omega + \delta q$ ); after that a  $\omega$ -scan is performed again and so on. RSM will present the results in the map form ( $I(\omega, 2\theta)$ ) and the intensity is normally a projection of the 3D intensity of the diffraction spots onto a 2D plane.

All maps in RSM are reported in reciprocal lattice units, with the horizontal axis  $q_{//}$  representing the in-plane scattering vector component along one of the  $\langle 11\bar{2}0 \rangle$  directions and the vertical axis  $q_{\perp}$  representing the out-of-plane scattering vector component perpendicular to the epilayer surface i.e.  $\langle 0001 \rangle$  directions. The relationship between the reciprocal lattice units ( $q_{//}$  and  $q_{\perp}$ ) and the incident and diffracted angles ( $\omega$  and  $2\theta$ ) in the real space is as follows:

$$q_{//} = 1/\lambda \{ \cos(2\theta - \omega) - \cos \omega \} \quad (7)$$

$$q_{\perp} = 1/\lambda \{ \sin(2\theta - \omega) + \sin \omega \} \quad (8)$$

where  $\omega$  is the angle between the incident beam and the sample surface and  $2\theta$  is the angle between the scattered beam and the incident beam in the real space as shown in Fig. 25;  $\lambda$  is the wavelength of Cu  $K_{\alpha 1}$  (0.15406 nm).

A section through the reciprocal space for an [0001]-oriented  $\text{Al}_2\text{O}_3$  substrate is shown in Fig. 26, in which the Ewald sphere construction is used to illustrate which diffraction can be obtained. Not all diffraction spots can be accessed. The larger circle in Fig. 26 shows the outer limit and the inner gray shaded areas show where the sample would block either

the incoming or the outgoing beam [224]. Therefore, the characterization of the symmetric (0006) and asymmetric (10 $\bar{1}$ 10) RSM measurements of the films deposited on *c*-plane  $\alpha$ -Al<sub>2</sub>O<sub>3</sub> substrates are carried out. The diffraction geometry is shown in Fig. 25, where  $\omega = \theta$  when symmetric (0006) RSM is measured and  $\omega = \theta \pm \chi$  ( $\chi$  is the angle between {0006} and {10 $\bar{1}$ 10} planes) when asymmetric (10 $\bar{1}$ 10) RSM is measured. The symmetric and asymmetric reciprocal lattice points can be used to determine the in-plane and out-of-plane lattice parameters and the strain of the films deposited on the substrate. The relationship between the length of reciprocal spacing and the associated interplanar spacing is  $q = 1 / d$ . In detail, a pair of lattice constants ( $a$ ,  $c$ ) of a hexagonal lattice can be calculated by determining the components ( $q_{\parallel}$ ,  $q_{\perp}$ ) of the peak center.

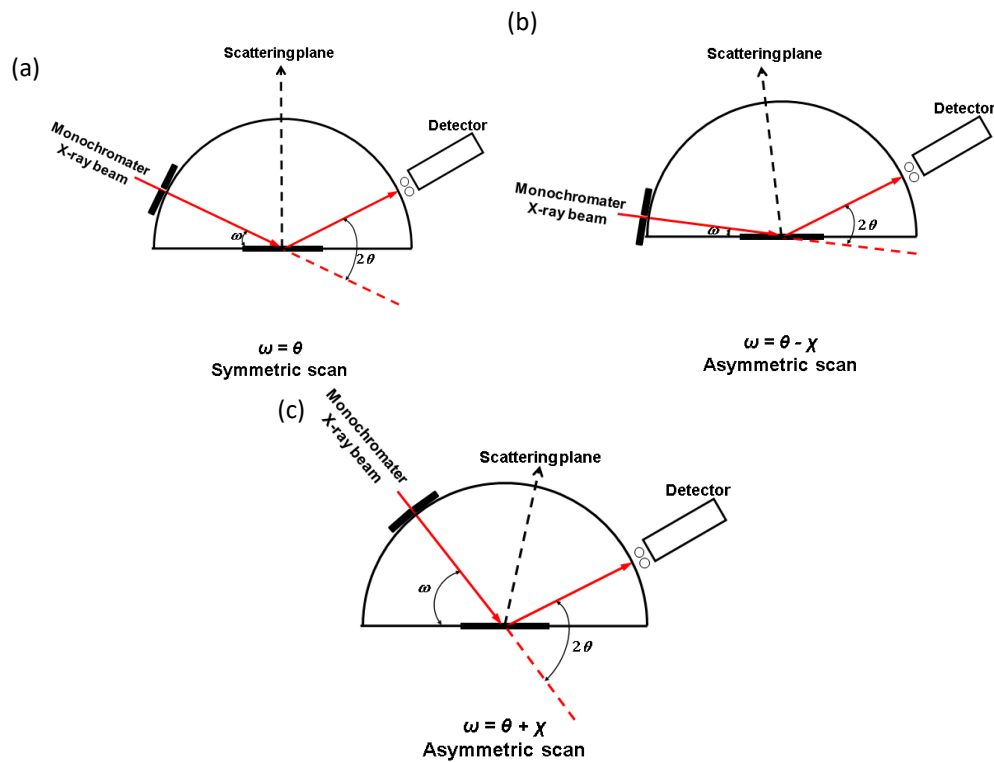


Fig. 25 schematic representation of RSM configuration (a) symmetrical diffraction geometry, (b) and (c) asymmetrical diffraction geometry.  $\omega$  is the angle between the incident beam and the sample surface;  $2\theta$  is the angle between the scattered beam and the incident beam; and  $\chi$  is the angle between the scattering plane tilted to the in-plane of the sample surface.

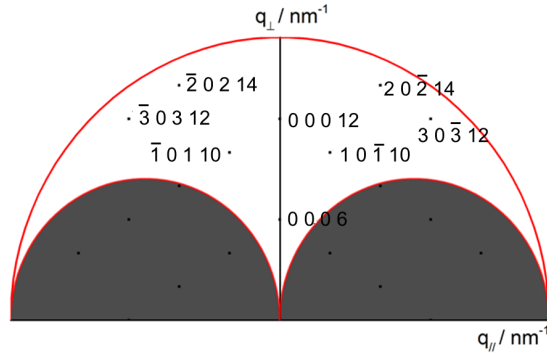


Fig. 26 A section through the reciprocal space for an [0001]-oriented  $\text{Al}_2\text{O}_3$  substrate. Regions of reciprocal space in gray could not be detected by RSM.

The value of lattice constant  $c$  can be calculated from both the symmetric  $(000l)$  RSM and the asymmetric  $(h0il)$  RSM by:

$$c = \frac{l}{q_{\perp}} \quad (9)$$

The lattice constant  $a$  is given from asymmetric  $(h0il)$  RSMs by:

$$a = \frac{2h}{\sqrt{3}q_{\parallel}} \quad (10)$$

In this thesis, all films are locally epitaxially grown on the  $\alpha\text{-Al}_2\text{O}_3$  substrates in the hexagonal structure similar to the substrate, and the broader and weaker lines from the films are found nearby the strong lines from the substrates in the reciprocal space. The in-plane lattice parameter of the films is larger than that of the substrates, so the films tend to be constrained by the substrate. However, the films can also be partially relaxed or completely relaxed depending on the layer thickness and the film content. The degree of in-plane relaxation  $r$  of a film with respect to the substrate is given by [224]:

$$r = \frac{a_{\text{film}} - a_{\text{substrate}}}{a_{\text{film}}^{\text{relax}} - a_{\text{substrate}}} \quad (11)$$

Where  $a_{\text{film}}$  denotes the actually measured lattice constant of a thin film;  $a_{\text{film}}^{\text{relax}}$  is the totally relaxed lattice constant, i.e. the theoretical value from the corresponding PDF card from ICDD;  $a_{\text{substrate}}$  is the lattice constant of the substrate.

If an asymmetric RSM resembles Fig. 27 (a) in which the film-substrate reflection center line is perpendicular to the  $q_{||}$  axis in reciprocal space, the film in-plane lattice constant  $a$  is coherent with the substrate and the degree of in-plane relaxation  $r = 0$ , indicating that the film is fully epitaxial (strained) grown on the substrate. If the RSM resembles Fig. 27 (b) in which the film-substrate reflection center line goes to the origin of the reciprocal space coordinate system, the film is fully relaxed and grown with the theoretical lattice constant  $a$  value and  $r = 1$ . If the RSM state is between the Fig. 27 (a) and (b), the film is partially relaxed.

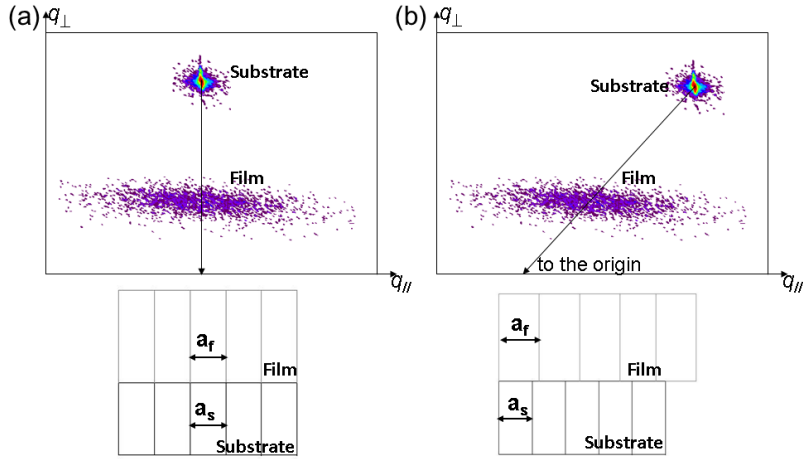


Fig. 27 Two examples of RSMs measured in asymmetric geometry of (a) fully strained film and (b) fully relaxed film grown on the substrate. The schematic representations below the RSM results indicate the relationship of the in-plane lattice constant  $a$  between the film and the substrate.

To define the strain in a film, the in-plane misfit and strain are estimated. The misfit i.e. the relative difference of the lattice constants between the substrate and the film is given by:

$$f_a = \frac{a_{\text{film}} - a_{\text{substrate}}}{a_{\text{substrate}}} \quad (12)$$

The in-plane strain of the film is defined as

$$\varepsilon_a = \frac{a_{\text{film}} - a_{\text{film}}^{\text{relax}}}{a_{\text{film}}^{\text{relax}}} \quad (13)$$

where  $a_{film}$  denotes the actually measured lattice constant  $a$  of a thin film;  $a_{substrate}$  denotes the lattice constant  $a$  of the substrate, here the measured value is equal to the theoretical value from the corresponding PDF card from ICDD;  $a_{film}^{relax}$  is the lattice constant  $a$  for the film in the fully relaxed state, i.e. the theoretical value from the corresponding PDF card from ICDD.

All RSM analyses were performed with a high resolution X-ray diffractometer (Model XRD 3003 PTSHR Seifert) with a line focus X-ray tube at 40 kV and 40 mA. The incident X-ray beam was monochromatized by a Ge (220) monochromator to get pure  $K_{\alpha 1}$ , and a scintillation detector for high resolution scanning in  $2\theta$ .

### 3.2.4 Raman Spectroscopy

Raman spectroscopy is a light scattering technique, in which laser light interacts with the phonons of a sample to produce scattered radiation of different wavelengths. It is used to identify organic substances or inorganic solids by characteristic vibration modes and get the chemical composition of the materials indirectly [225].

In Raman spectroscopy measurements, light from a monochromatic light source (usually a single mode laser) is incident on the sample surface and the scattered light is detected. For the total energy of the system to remain constant after the molecule moves to a new rovibronic state, the scattered photon shifts to a different energy, and therefore a different frequency. This energy difference is equal to that between the initial and final rovibronic states of the molecule. An energy-level diagram is shown in Fig. 28, which illustrates light scattering from a molecule. If the energy of the incident photon is equal to that of the scattered one, the process is called Rayleigh scattering, in which the scattered phonon has the same frequency as the incoming radiation. If the energy of the incident photon is different to that of the scattered one, the process is called Raman scattering, which is inelastic scattering because of the energy and momentum transfer between the photons and the molecules during the interaction. If the molecule gains vibrational energy, i.e. the final vibrational state has a higher energy than the initial state, then the scattered photon will be shifted to a lower frequency, the process is called Stokes Raman scattering. If the molecule loses vibrational energy, i.e. the final vibrational state is less energetic than the initial state, then the scattered photon will be shifted to a higher frequency, the process is

called anti-Stokes Raman scattering. In one word, the Raman scattering is a process of energy and momentum exchange among the incident photon, the scattered photon, and the scattering substance which is associated. The energy difference between the incident and scattered light is called Raman shift, which is determined by the rotational and vibrational states of the sample. The Raman shift is typically expressed in wavenumbers ( $\text{cm}^{-1}$ ) and the relationship between the Raman shift and the wavelength of the incident and scattered light is described by the following formula:

$$\Delta\nu = \frac{10^7}{\lambda_i} - \frac{10^7}{\lambda_s} \quad (14)$$

Where  $\Delta\nu$  is the Raman shift in unit of  $\text{cm}^{-1}$ ;  $\lambda_i$  is the excitation wavelength, i.e. the incident laser wavelength in unit of nm;  $\lambda_s$  is the scattered Raman wavelength in unit of nm.

The Raman spectra are usually plotted in intensity versus Raman shift in wavenumber.

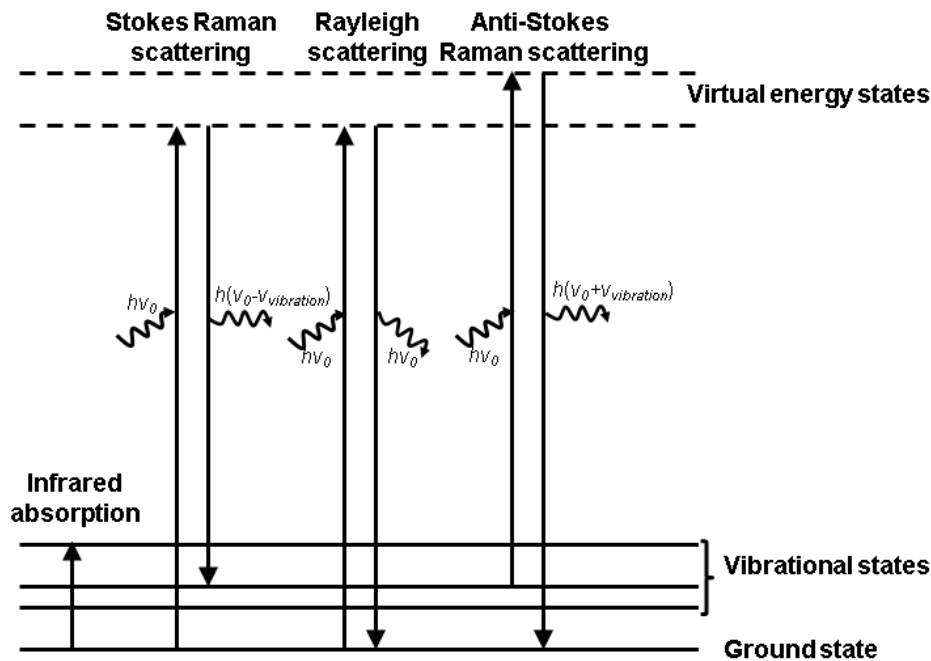


Fig. 28 Energy-level diagram for light scattering (Stokes Raman scattering, Rayleigh scattering, and anti-Stokes Raman scattering) and the infrared absorption according to [226] and [227]. The incident laser radiation energy is  $h\nu_0$ , and the vibrational energy is  $h\nu_{\text{vibration}}$ .

All Raman spectra were performed with a Micro-Raman-Spectroscope, Renishaw System 1000 at room temperature. The excitation source was a 514.5 nm argon ion laser, and the 50× objective was utilized to observe the samples through a Leica microscope. The diameter of the analyzed area on the sample was about 1  $\mu\text{m}$  - 2  $\mu\text{m}$ . In order to avoid the thermal damage of the sample surface, the laser power at the sample spot was attenuated to 2 mW - 4 mW from the incident power of 20 mW. The Raman spectra were measured in the range from 160  $\text{cm}^{-1}$  to 1200  $\text{cm}^{-1}$  with exposure time of 120 s.

In crystalline solids, the Raman effect deals with phonons. Only small wavevector (close to the Brillouin zone center) phonons can be seen in the single phonon Raman spectra of crystals. In amorphous materials, all the phonons contribute to the Raman spectrum, leading to very broad bands of poor intensity that reflect the vibrational density of states. In nano crystalline materials, the Raman spectra display the crystalline Raman features broadened and shifted by the phonon confinement. Therefore, the size of the nanocrystals could be estimated by an adequate model. It is possible to analyze the disorder and the strains present in the crystalline lattice from the Raman band shift and the presence of the forbidden bands.

Raman spectroscopy is based on group theory. The group theory classifies vibrational modes in corundum structured crystals from the Bhagavantam and Venkataryudu method [228] into the following irreducible representation:

$$\Gamma_{vib} = 2A_{1g} + 3A_{2g} + 5E_g + 2A_{1u} + 3A_{2u} + 5E_u \quad (15)$$

The vibrational modes are shown in Fig. 29, Among these vibrational modes,  $A_{2u}$  and  $E_u$  are acoustical modes, in which two adjacent different atoms move together; and others are optical modes, in which two adjacent different atoms move against each other. Therefore, the representation corresponding to the optical modes is [229,230]:

$$\Gamma_{opt} = 2A_{1g} + 3A_{2g} + 5E_g + 2A_{1u} + 2A_{2u} + 4E_u \quad (16)$$

Among these optical modes, the  $2A_{1g}$  and  $5E_g$  modes are Raman active; the  $2A_{2u}$  and  $4E_u$  are infrared (IR) active; and the  $2A_{1u}$  and  $3A_{2g}$  are spectroscopically inactive (silent

modes). But not all modes expected from factor analysis can be observed owing to the limit in the available spectral range of our apparatus [9].

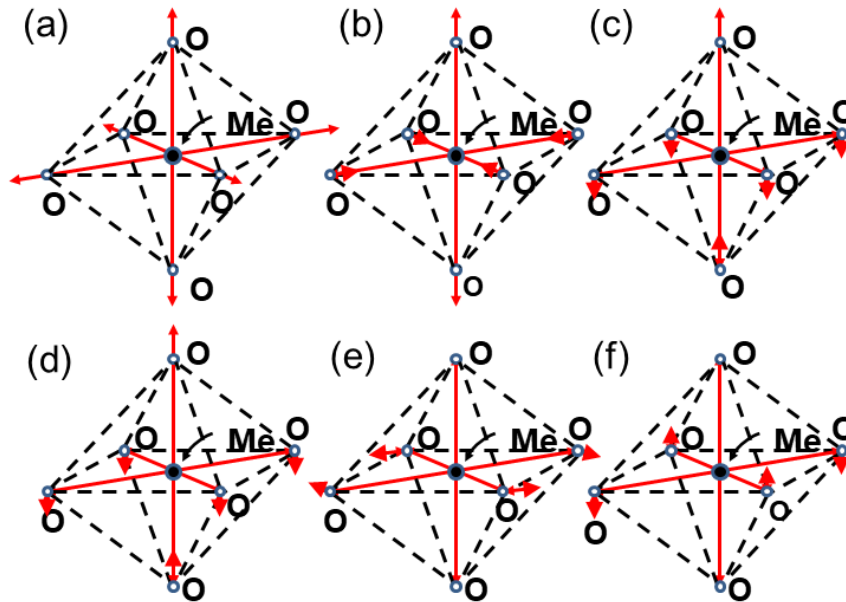


Fig. 29 Vibrational modes in corundum structured crystals. Me is metal and O is oxygen. (a), (b), (c), (d), (e) and (f) indicate the vibrational modes of  $A_{1g}$ ,  $E_g$ ,  $A_{1u}$ ,  $E_u$ ,  $A_{2g}$ ,  $A_{2u}$ , respectively.

### 3.2.5 Infrared reflection-absorption spectroscopy

Like Raman spectroscopy, IR spectroscopy is also used to obtain information about the chemical composition of the materials indirectly and properties of molecules from their vibrational modes of the chemical bonds in the materials [231].

Absorption of IR radiation is typical of molecular species that have a small energy difference between the rotational and vibrational states.

Different from Raman scattering, IR absorption is a one-photon event [227]. IR absorption arises from a direct resonance between the frequency of the IR radiation and the vibrational frequency of a particular normal mode of vibration, i.e. IR absorptions occur at the frequency of the absorbed radiation matches the vibrational frequency. The photon encounters the molecule in the materials and disappears, then the molecule is excited from the ground energy state to vibrational energy state by the energy of the photon at the

frequency of vibrational resonance as shown in Fig. 28. From Fig. 28, it is clear that IR absorption achieves this energy change in one step, but Raman requires two steps.

IRRAS was used because the material systems we studied are absorbing in reflection mode in the infrared region. IRRAS mainly measures a complete spectrum in the mid-infrared region of  $4000\text{ cm}^{-1}$  -  $400\text{ cm}^{-1}$  wavenumber ( $2.5\text{ }\mu\text{m}$  -  $25\text{ }\mu\text{m}$  wavelength) to study the fundamental vibrations and associated rotational-vibrational structure. In IRRAS experiments, the samples are investigated in reflection geometry under grazing incidence as shown in Fig. 30, which means the radiation from the spectrometer source must be directed at the film at a selected (optimum) angle of incidence, and the reflected radiation must be analyzed at the same angle [232]. In general, both incident and reflected infrared light can be decomposed into two vectors: one is the p-polarized component with the electric vector parallel to the plane of incidence; the other is the s-polarized component with the electric vector perpendicular to the p-polarized component. Only the p-polarized component can excite the vibrational modes of the probed molecule in the samples [233].

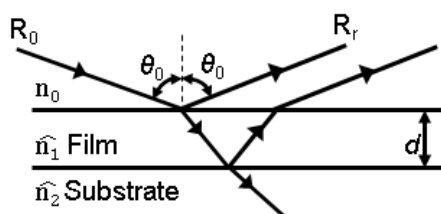


Fig. 30 IRRAS optical configuration:  $\theta_0$  is the incident angle ( $\theta_0 = 80^\circ$  in this thesis);  $R_0$  and  $R_r$  are incident and reflected infrared in p-polarization, respectively;  $n_0$  is the refractive index of the incident medium (air);  $\hat{n}_1$  and  $\hat{n}_2$  are the complex refractive index of the film and the substrate, respectively;  $d$  is the film thickness.

In solids, IR bands are sharper for a crystalline material than for those of amorphous materials. The IR spectra of crystalline and amorphous solids of the same chemical composition can be significantly different primarily because of the presence or absence of spatial order and long range translational symmetry.

All IRRAS spectra were measured with a Fourier transform infrared (FTIR) spectrometer (Bruker VERTEX 80, Bruker Optics, Ettlingen, Germany) in the range of

400  $\text{cm}^{-1}$  - 4000  $\text{cm}^{-1}$ . A pure  $\alpha\text{-Al}_2\text{O}_3$  single crystal substrate was used as reference for the characterization of coated samples. An incident angle of  $80^\circ$  with respect to the sample surface normal and a resolution of  $2 \text{ cm}^{-1}$  were applied during the measurements. Liquid  $\text{N}_2$  was used to cool the mercury cadmium tellurite (MCT) detector in order to reduce the noise-to-signal ratio (i.e. have high sensitivity). Dry air was purged continuously through the spectrometer and the sample compartment to eliminate or decrease the disturbance from atmospheric absorptions (i.e. water vapor and  $\text{CO}_2$ ). At least 500 scans for each sample were integrated and the measurements were stopped when absorption bands of the ambient humidity appeared.

### 3.2.6 Ultraviolet-visible-near infrared spectroscopy

Ultraviolet-visible-near infrared (UV-VIS-NIR) spectroscopy is a useful technique of “electronic spectroscopy”, in which the outer electrons of atoms or molecules absorb energy and undergo transitions to high energy levels [234,235]. With this technique one can measure a complete absorption spectrum in the UV-VIS-NIR region of 190 nm - 900 nm, in which 200 nm - 400 nm is the UV range, 400 nm - 700 nm is the visible light range, and 700 nm - 900 nm is the near infrared range. For UV, VIS and NIR, the electrons are promoted from their ground state to an excited state after absorbing the energy which corresponds to the electronic states of atoms or molecules.

When light comes into a solid, the light maybe absorbed, reflected, transmitted or scattered, which is shown as Fig. 31. According to the Beer-Lambert Law:

$$A = \lg(1/T) \quad (17)$$

Where  $A$  is the absorbance of the sample;  $T$  is the transmittance which represents the percentage of the incident light transmitted by the sample ( $T=I/I_0$ ,  $I_0$  is the incident light intensity,  $I$  is the intensity of transmitted light).

If no absorption has occurred,  $T = 1$  and  $A = 0$ . Most spectrometers display absorbance on the vertical axis, and the commonly observed range is from 0 (100 % transmittance) to 2 (1 % transmittance).

The UV-VIS-NIR spectrophotometer use light to qualitatively and quantitatively analyze samples based on how much light travels through the sample and how much is reflected off of it. The spectra in the visible region can be used to determine the color of the sample; the spectra in ultraviolet and near infrared region are often needed for evaluating the performance of solar radiation control films.

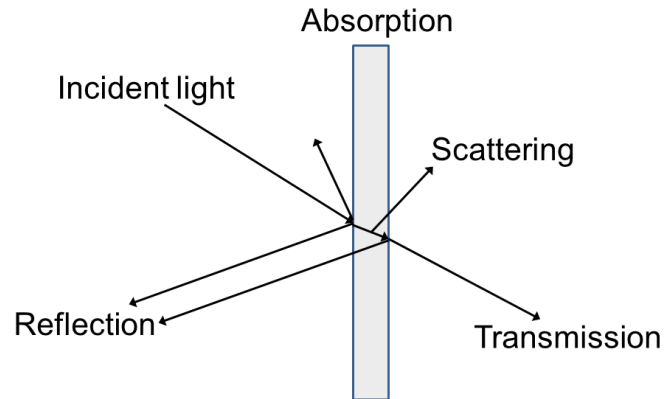


Fig. 31 Interactions of light with a solid.

The optical absorption can be analyzed to get information on the energy band gap of the materials [236]. The direct optical band gap energy,  $E_g$ , can be determined using optical spectra by Tauc's equation as follows [104,105,237]:

$$\alpha = \frac{B(h\nu - E_g)^n}{h\nu} \quad (18)$$

Where  $\alpha$  is the optical absorption coefficient, and it can be calculated according to the following relation:  $\alpha = \ln(10)A/d$  (where  $A$  is the absorbance of the film;  $d$  is the film thickness);  $h\nu$  is the photon energy, and  $h\nu = hc/\lambda = 1240.7/\lambda$ ;  $n$  is a constant for a given transition which is equal to  $\frac{1}{2}$  for direct band gap.  $E_g$  is in eV and  $\lambda$  in nm;  $B$  is a constant.

To verify the direct band gap  $E_g$ , the plot of  $(\alpha h\nu)^2$  as a function of the photon energy can be drawn, and the  $E_g$  value is given by the extrapolation of the linear portion of the plot to the energy axis at  $\alpha=0$ .

The UV-VIS-NIR spectra were recorded in the wavelength range of  $350 \text{ nm} < \lambda < 800 \text{ nm}$  using a CARY 5000 Scan UV-VIS-NIR Spector-Photometer with a Cary Universal Measurement Accessory (UMA) unit from Agilent. The UV-VIS-NIR spectra of the samples were measured in a transmission mode.

### **3.2.7 Transmission electron microscopy**

Transmission electron microscopy (TEM) is a premier analytical technique to characterize the microstructure of the materials, especially the crystal structure, crystallite size, lattice plane distance, orientation, grain boundaries or the epitaxial relationship between the films and the substrates for the film study. In TEM, a highly energetic electron beam passes through a very thin sample with thickness of 40 nm - 100 nm in high vacuum, and the electrons which are transmitted through the sample are collected onto a phosphorescent screen or through a camera. The sample preparation is extremely important because the TEM samples should be thinned for example by ion milling or focused ion beam (FIB) to thickness lower than 50 nm.

Several TEM techniques are used to investigate the films microstructure in this thesis. Cross-sections of the films and their interfaces with the substrates were analyzed in different imaging modes, selected area electron diffraction (SAED) and high resolution TEM imaging (HRTEM). Fig. 32 schematically illustrates the transmitted and diffracted path in the imaging and diffraction modes in TEM [238]. The objective lens forms a diffraction pattern in the back focal plane with electrons scattered by the sample and combines them to generate an image in the first intermediate image plane. Thus, the image and diffraction patterns are simultaneously present in the TEM. In the imaging mode, an objective aperture is inserted and a selected area aperture is removed in the back focal plane to select one or more of the diffracted beams. Diffraction contrast is the variation in intensity of electron diffraction across the specimen, which can be controlled by the objective aperture, and contribute to the final image in bright-field (BF) mode or dark-field (DF) mode. If the objective aperture passes only one diffracted beam, a dark-field (DF) image can be obtained. If both the direct and diffracted beams are passed, a bright-field (BF) image can be obtained. SAED is a method in which the reciprocal lattice is imaged with high resolution.

In SAED patterns, the recorded electron diffraction patterns can help to determine if the materials are amorphous, polycrystalline, or single crystals. In SAED, the intermediate lens is now focused on the back focal plane of the objective lens as shown in Fig. 32. The transmitted and diffracted beams are now imaged. The objective aperture is removed and a selected area aperture in the back focal plane of the objective lens (diffraction plane) is used to define the diffraction pattern to a selected area of the specimen. In the SAED patterns, the diffraction spots in reciprocal space can be identified based on the Miller or Miller-Bravais indices of the lattice planes correspondingly and interplanar spacings in crystals can be determined by the separation of the diffraction spots on the viewing screen.

HRTEM is an imaging mode of TEM which provides qualitative information about the atomic structure of the specimen. HRTEM images are formed by phase contrast, which results from the interaction between the high energy electrons and the sample when the electron wave passes through a TEM sample. The electrons can continue their path or diffract as a result of scattering from the crystallographically ordered atoms in the samples, thus the electron waves divide into the transmitted waves and the diffracted waves. The phase shift of the electron waves which produces intensity variations is used to map the samples' atomic structure. When two or more electron beams scattered from the sample interfere and are transferred at high magnification to the detector plane, an interference pattern which is regarded as HRTEM image is formed.

Fast Fourier transformation (FFT) and inverse fast Fourier transformation (IFFT) were carried out using a Digital Micrograph software package by GATAN in this work. The FFT of a HRTEM image is an image processing to switch the real space image to the diffraction pattern, and IFFT transforms the diffraction pattern back to a real space image as a HRTEM image. We analyzed the defects of the films by images processing as the following steps: 1. FFT of the HRTEM image is used; 2. "Mask" is used to allow only some spots or other parts of the information present in reciprocal space to contribute to the image formed by IFFT. In TEM, similar effects are achieved by the use of apertures. 3. IFFT is used to get a filtered image.

All the cross-sections of the films and their interfaces with the substrates were analyzed in BF imaging mode, SAED and HRTEM with a FEI Tecnai F20 electron microscope operated at an acceleration voltage of 200 kV.

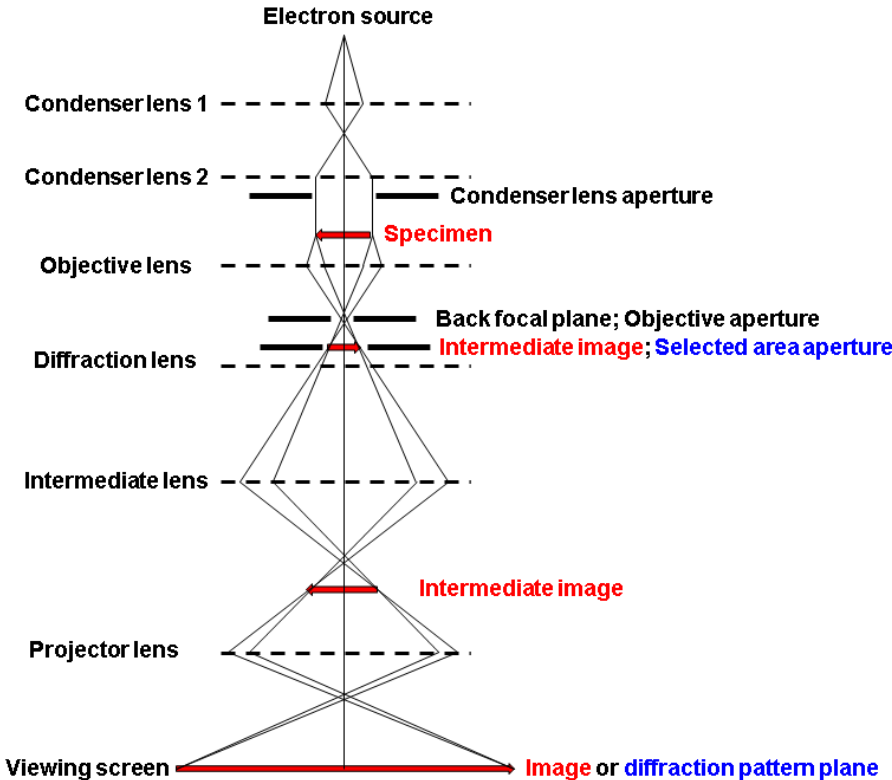


Fig. 32 Schematic representation of imaging and diffraction modes in the TEM [238]. In the imaging mode, an objective aperture is inserted in the back focal plane to select one or more beams that contribute to the final image (BF mode, DF mode, or HRTEM). In the SAED mode, a selected area aperture in the plane of the first intermediate image is inserted to define the diffraction region to be obtained.

### 3.2.8 Film thickness and deposition rate

The film thickness were determined by a KLA Tencor P-10 surface profiler. Then deposition rate can be calculated from the film thickness and the deposition time. A diamond stylus with a radius of  $5 \mu\text{m}$  was moved with a normal force of  $9.8 \times 10^{-3} \text{ mN}$  on the sample

surface during the measurement. The surface profiler has high sensitivity with a resolution of 0.008 nm. Each profile was measured at a scan speed of 200  $\mu\text{m/s}$ , scan length of 4 mm and a frequency of 200 Hz.

The film thickness were measured on a coated Si substrate with a size of 12 mm  $\times$  12 mm  $\times$  0.35 mm which are partly covered with a Si stripe with a size of 12 mm  $\times$  2 mm  $\times$  0.35 mm prior to deposition as shown in Fig. 33 (a). The Si stripe is removed after deposition when the film thickness is measured by the surface profiler. If there is no plasma-etching process before deposition, the film thickness is the value measured by the profiler. If the substrate is plasma-cleaned by a plasma-etching process before deposition, as shown in Fig. 33 (b) (c) and (d), the thickness of the substrate except the part covered by the Si stripe is reduced by the ion bombardment during the plasma-etching which is called plasma-etching depth ( $t_e$ ). The measured value by the profiler ( $t_m$ ) is the height difference between the Si substrate surface without being etched and the film surface as shown in Fig. 33 (d). Therefore, the real film thickness ( $d$ ) is the sum of the plasma-etching depth ( $t_e$ ) and the measured value by the profiler ( $t_m$ ), i.e.  $d=t_m+t_e$ . Then, the deposition rate can be calculated by the film thickness divided by the deposition time.

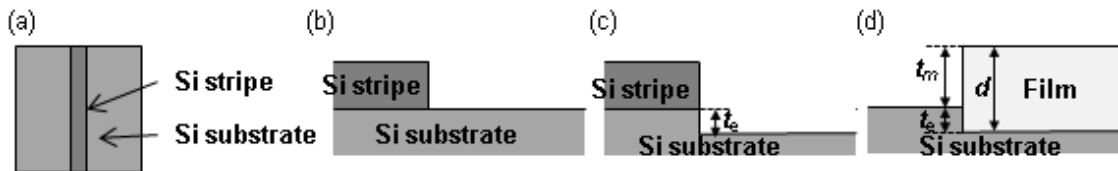


Fig. 33 Schematic representation of film thickness determination by surface profiler. (a) the top view and (b) cross-section of Si substrate covered by a Si stripe; (c) after the plasma-etching process,  $t_e$  denotes the plasma-etching depth of the Si substrate; (d) after etching, deposition and removing the covered Si stripe,  $t_m$  denotes the measured thickness by the surface profiler,  $d$  is the film thickness.  $d = t_m + t_e$ .



## 4 Results

This chapter describes the characterization of the binary  $\text{Cr}_2\text{O}_3$  (section 4.1) and  $\text{V}_2\text{O}_3$  (section 4.2) films, as well as films in the ternary systems Cr-Al-O (section 4.3), V-Al-O (section 4.4), and V-Cr-O (section 4.5) with locally epitaxial grown on *c*-plane  $\alpha\text{-Al}_2\text{O}_3$  substrates. The chemical composition, microstructure, and optical properties of the films are characterized.

### 4.1 $\text{Cr}_2\text{O}_3$ films deposited on *c*-plane $\alpha\text{-Al}_2\text{O}_3$ substrates

In this section, the  $\text{Cr}_2\text{O}_3$  thin films synthesized on *c*-plane  $\alpha\text{-Al}_2\text{O}_3$  substrates at 400 °C are analyzed. The samples were placed in relation to the sputtering target as shown in Fig. 17 (a). Films with a thickness of 2.1  $\mu\text{m}$  were prepared for the EPMA analysis, and films with a thickness variation (30 nm, 75 nm, 105 nm, 188 nm and 407 nm) were prepared for the structural, spectroscopic and optical analyses, and the microstructure and properties of the films dependent on the film thickness was discussed (section 4.1.1 - 4.1.3). All the films were deposited on the substrates following a plasma-etching of 50 nm for removing the contaminations before deposition. In section 4.1.4, films with a thickness of 320 nm deposited on substrates with and without plasma-etching before deposition are compared to investigate the influence of this plasma-etching process on the microstructure of the films.

#### 4.1.1 Compositional and structural analysis

The chemical composition of the films synthesized by sputtering of the  $\text{Cr}_2\text{O}_3$  target with thickness of 2.1  $\mu\text{m}$  at 400 °C was determined by EPMA. The results are displayed in Table 9. The chemical composition of the films deposited at different temperatures (without heating and at  $T = 400$  °C) were also measured and the deviation of the atomic percentage of the elements in the films is less than 1 %. The atomic percentages of Cr and O in the films are 38.8 % and 60.1 %, respectively, which suggests the Cr/O stoichiometry of these films is very close to the ideal value of 2/3. The argon concentration in the films from the sputtering gas during deposition is not detectable. Other contaminations such as carbon and nitrogen are also very low, in the sum around 1 at. %. The carbon content is

relatively larger than the nitrogen and argon content, and we correlate this with the fact that all electrically insulating oxide films were overcoated with a very thin amorphous carbon layer for EPMA measurements to avoid electrical charging. With respect to these very low concentrations of impurities (i.e. C, N, and Ar), it can be concluded that stoichiometric films of  $\text{Cr}_2\text{O}_3$  within the measuring accuracy were grown on the  $c\text{-Al}_2\text{O}_3$  substrates.

Table 9 The chemical composition of the  $\text{Cr}_2\text{O}_3$  films deposited on the  $c\text{-Al}_2\text{O}_3$  substrates (standards used for calibrating see section 3.2.1).

Cr (at. %)	O (at. %)	C (at. %)	N (at. %)	Ar (at. %)
$38.8 \pm 0.18$	$60.1 \pm 0.19$	$0.8 \pm 0.13$	$0.3 \pm 0.03$	0.0

Fig. 34 (a) shows the XRD patterns obtained in Bragg-Brentano mode of the  $\text{Cr}_2\text{O}_3$  films grown on  $\alpha\text{-Al}_2\text{O}_3$  (0001) substrates at the substrate temperature of 400 °C with different thickness of 30 nm, 75 nm, 105 nm, 188 nm and 407 nm. The reflections at  $2\theta$  values of 41.69° and 90.71° are assigned to the (0006) and (00012) reflections from  $\alpha\text{-Al}_2\text{O}_3$  substrates, respectively, which are in complete agreement with the theoretical data listed in PDF card No. 42-1468 from the ICDD-database. For all films, only the (0006) and (00012) reflections can be observed. The figure shows the (0006) and (00012) reflections of the films at  $2\theta$  values at lower diffraction angles (i.e. larger lattice constant  $c$ ) in comparison to the corresponding reflections of the  $\alpha\text{-Al}_2\text{O}_3$  substrate. The films grown on (0001)-orientated  $\alpha\text{-Al}_2\text{O}_3$  in Fig. 34 show a  $c$ -axis orientation, because no other reflections of  $\text{Cr}_2\text{O}_3$  are present, suggesting a growth preference aligned with the underlying substrate lattice. The theoretical reflections corresponding to (0006) and (00012) of rhombohedral  $\text{Cr}_2\text{O}_3$  are at 39.79° and 85.66°, respectively, and the theoretical X-ray powder diffraction intensity of the  $\text{Cr}_2\text{O}_3$  (0006) reflection relative to the (00012) reflection is 3.5 (PDF card No. 38-1479 from the ICDD-database), which corresponds well with our results. We observed a shift of the reflections of the  $\text{Cr}_2\text{O}_3$  films with thickness variation. Fig. 34 (b) shows the (0006) reflections of the films with different thickness in more detail for a narrow range of the diffraction angle. With increasing film thickness, the (0006) reflection become much more pronounced (i.e. show much larger intensity) and shift to the

diffraction angles towards to the position of the theoretical  $\text{Cr}_2\text{O}_3$  value at  $39.79^\circ$ . This suggests that the thicker films exhibit smaller (0006) lattice plane distances  $d_{0006}$  according to Bragg's law as shown in Eq. (5). Fig. 35 shows the (0006) lattice plane distance in dependence of the film thickness. It indicates that the film has larger  $d_{0006}$  (i.e. larger lattice constant  $c$ ) with decreasing the film thickness, approaching but not reaching the theoretical value of  $\text{Cr}_2\text{O}_3$ . If we assume that the crystal volume is a constant, then the thinner films should have smaller lattice constant  $a$  and should be more strained in theory, which is in agreement with the RSM results discussed in the following. The FWHM values of the (0006) reflections of the films are between  $0.4^\circ$  and  $0.8^\circ$ , showing a relatively broad XRD reflex compared to the single crystal  $\alpha\text{-Al}_2\text{O}_3$  substrate (i.e. the FWHM of the (0006)  $\alpha\text{-Al}_2\text{O}_3$  peak is only  $0.06^\circ$ ). This indicates that the crystals of the  $\text{Cr}_2\text{O}_3$  films should be more imperfect compared to the single crystal of the substrates. Fig. 36 shows the dependence of the FWHM of (0006) reflections of the films on the film thickness, indicating that thicker films have smaller FWHM values (i.e. larger grain size). Fig. 37 shows the mosaic spreading in the rocking curve measurements of the (0006) reflections of the films with different thickness, allowing to evaluate the epitaxial growth quality of the films with respect to the substrates. The FWHM values of these reflections were  $1.07^\circ - 1.32^\circ$ , indicating that there are many individual crystals with a  $1.07^\circ - 1.32^\circ$  tilt of (0006) planes in the film, while the FWHM of the single crystal  $\alpha\text{-Al}_2\text{O}_3$  substrate is only  $0.2^\circ$ . Compared to the perfect single crystal, the mosaic spreading of the films is larger, indicating the imperfect epitaxial crystal growth of the films. With increasing the film thickness, the FWHM value of the  $\omega$  scans is slightly decreasing, i.e. the mosaic spreading of the (0006) planes is smaller, which indicates the crystal quality becomes better during the film growth (i.e. with increasing film thickness). At the beginning of the film growth, there is a strong impact of the lattice mismatch between substrate and films (4.2 % in  $a$ -axis) on the film crystal quality, which will cause the strain in the films. With increasing deposition time, the films grow more relaxed and the mismatch does not have that strong impact anymore. Therefore, we observe the films with larger film thickness exhibit better crystal quality.

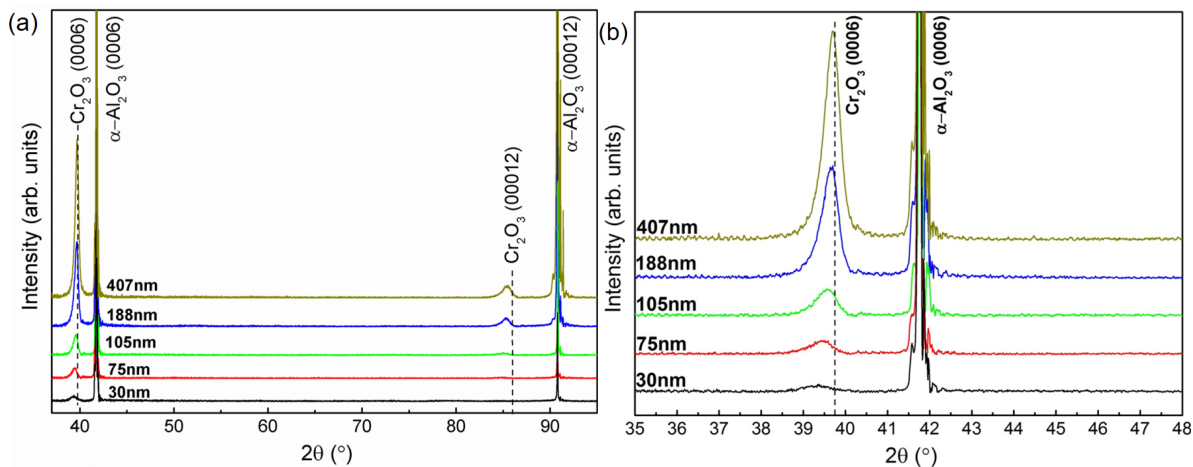


Fig. 34 (a)  $\theta - 2\theta$  XRD patterns of the  $\text{Cr}_2\text{O}_3$  films with different thickness (30 nm, 75 nm, 105 nm, 188 nm, and 407 nm) deposited on the  $\alpha\text{-Al}_2\text{O}_3$  substrates at the substrate temperature of 400 °C. The film thickness is marked on the corresponding line. The (0006) and (00012) reflections of the films are observed at lower diffraction angles of the corresponding reflections from substrates. The dashed vertical lines show the theoretical positions of the (0006) and (00012) reflections of  $\text{Cr}_2\text{O}_3$  according to PDF card No. 38-1479 from the ICDD-database. (b) shows the (0006) reflections of the films in more detail for a narrow range of the diffraction angle.

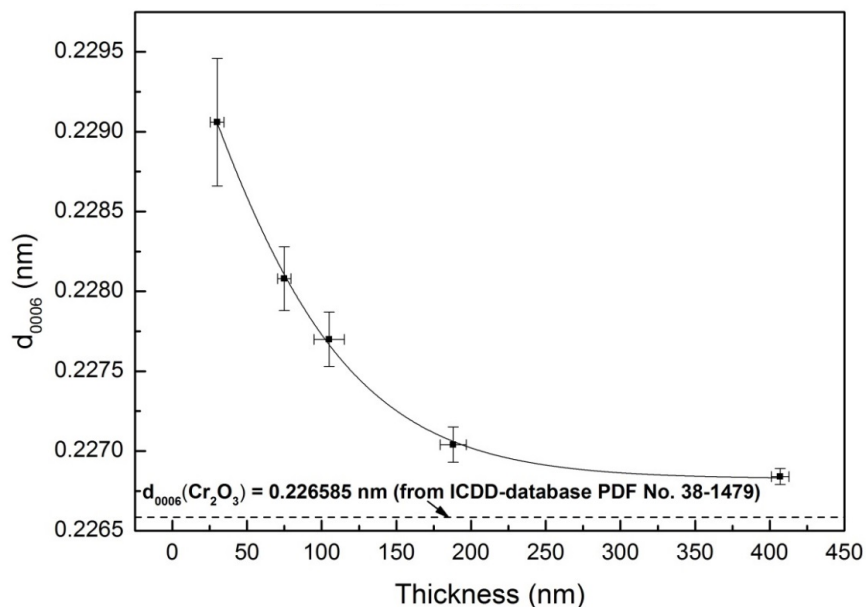


Fig. 35 Dependence of the lattice plane distance  $d_{0006}$  on the film thickness for  $\text{Cr}_2\text{O}_3$  films deposited at 400 °C. The dashed line indicates the theoretical value of  $d_{0006}$  of  $\text{Cr}_2\text{O}_3$  according to PDF card No. 38-1479 from the ICDD-database.

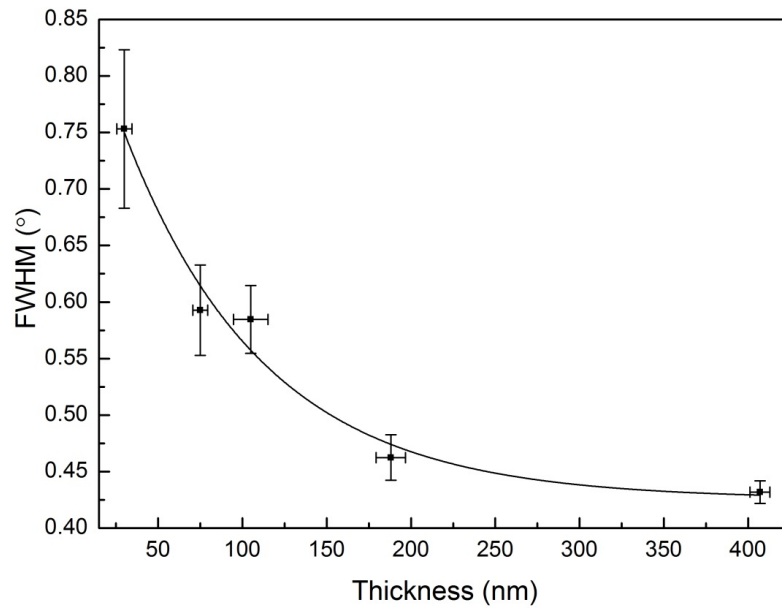


Fig. 36 Dependence of the FWHM values of (0006) reflections on film thickness for the films deposited at 400 °C.

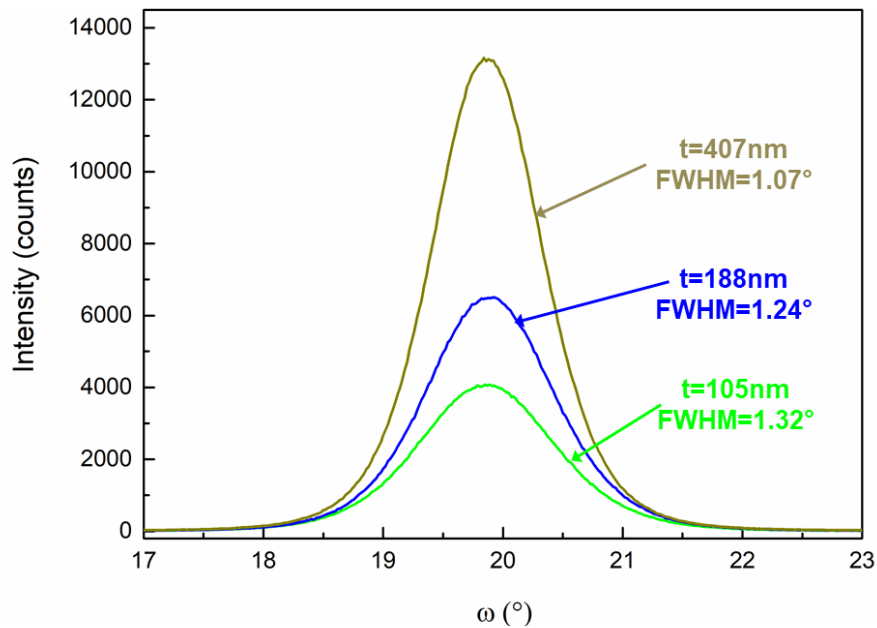


Fig. 37 XRD rocking curves ( $\omega$ -scans) of the (0006) reflection of the  $\text{Cr}_2\text{O}_3$  films with the thickness of 105 nm, 188 nm, and 407 nm. The FWHM is 1.32°, 1.24°, and 1.07°, respectively.

Further, the crystallite size of the films is evaluated according to Eq.(6) from the  $\theta - 2\theta$  XRD data of (0006) reflexes. The  $\text{Cr}_2\text{O}_3$  grain sizes are between 13.5 nm (for films with

30 nm thickness) and 24.0 nm (for films with 407 nm thickness), respectively. This indicates that the grain size is larger for thicker film, which can be explained by the VW growth mode of the films (i.e. island growth).

This is verified by TEM results presented in the following. In the early stages of the film growth, the Cr<sub>2</sub>O<sub>3</sub> films grow in strained state on the  $\alpha$ -Al<sub>2</sub>O<sub>3</sub> substrate and exhibit smaller values of lattice parameter  $a$ . Structural defects such as stacking faults and misfit dislocations should appear in such films according to literatures [239,240]. With increasing thickness, the films usually become less defective. Meanwhile, the distance between the islands is large at the beginning of the film growth and then becomes smaller and smaller as increasing the thickness because the grain size increases with increasing film thickness and it will grow up to the coalescence when a critical thickness is reached [239]. This is supported by our results. When the films thickness is between 30 nm and 75 nm (i.e. the thickness increases by 150 %), the grain size increases from 13.5 nm to 17.3 nm (which is an increase of 28.1 %). If the film thickness increases from 188 nm to 407 nm (which means an increase of 116 %), the grain size only increases by 7.6 % (from 14.0 nm to 22.3 nm). When the film thickness is around or above 188 nm, the coalescence of grains seems to be widely done, and the grain size does not increase as strong as in the thinner films.

Fig. 38 shows the symmetric (0006) and asymmetric (10 $\bar{1}$ 10) RSM of the Cr<sub>2</sub>O<sub>3</sub> thin films with the thickness of 188 nm and 407 nm grown on the  $\alpha$ -Al<sub>2</sub>O<sub>3</sub> substrates. From the (0006) and (10 $\bar{1}$ 10) reciprocal lattice points, the lattice constants of the Cr<sub>2</sub>O<sub>3</sub> films were calculated. The lattice parameters of the film with thickness of 188 nm are  $a = 0.493$  nm and  $c = 1.367$  nm, while the thicker film with 407 nm has a slightly larger  $a$  value of 0.496 nm and a smaller  $c$  value of 1.366 nm, which is in agreement with the  $\theta - 2\theta$  XRD results. The degree of relaxation (according to Eq.(11)) of the film with 188 nm thickness is 0.85, indicating the film is in strained state, while that of the film with 407 nm thickness is near 1, indicating this film is in nearly fully relaxed state. The misfit of the in-plane interface between the film and the substrate are 3.6 % (in case of the 188 nm thick film) and 4.2 % (in case of the 407 nm thick film), respectively. The in-plane strain (estimated from the lattice parameter  $a$ ) of the film with the thickness of 188 nm is 0.5 % while only

0.03 % for the film with the thickness of 407 nm. The film changes from strained state to relaxed state gradually during the film growth.

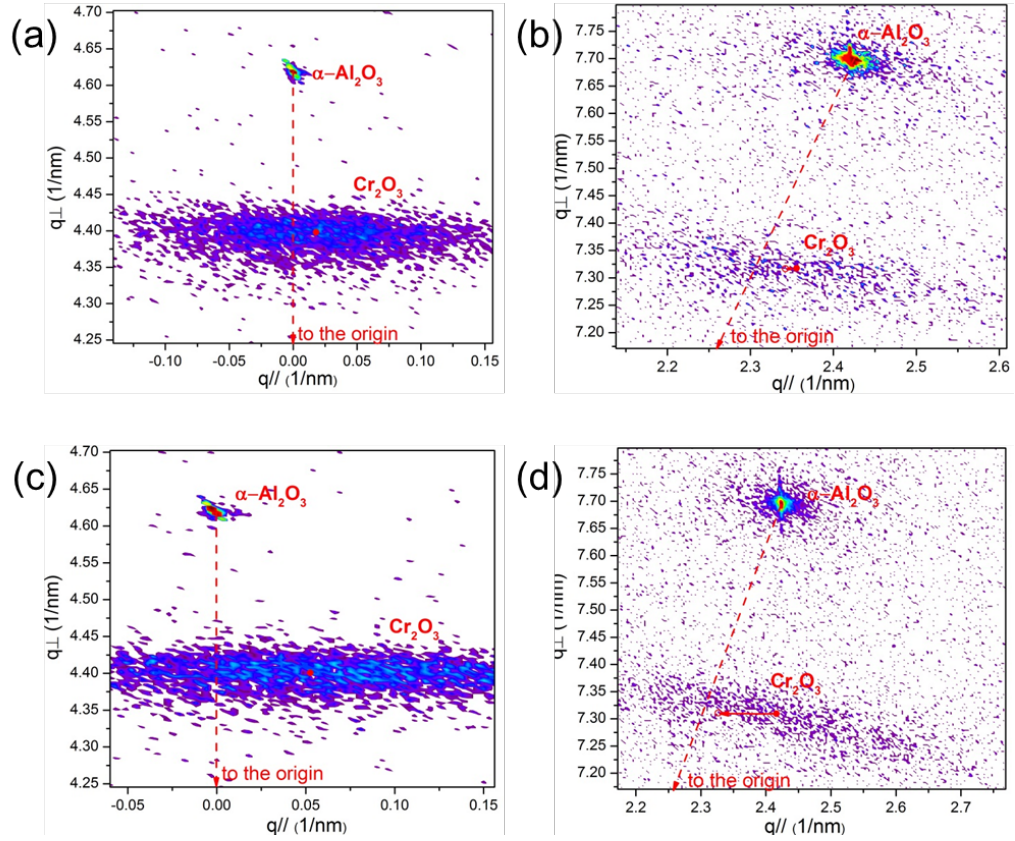


Fig. 38 Reciprocal space mapping (RSM) results of the samples with the film thickness of 188 nm and 407 nm. (a) and (b) are the symmetric (0006) reflection and the asymmetric (10 $\bar{1}$ 10) reflection of the  $\alpha$ -Al $_2$ O $_3$  substrate upon which the Cr $_2$ O $_3$  thin film thickness is 188 nm respectively. (c) and (d) are the symmetric (0006) reflection and the asymmetric (10 $\bar{1}$ 10) reflection of the  $\alpha$ -Al $_2$ O $_3$  substrate upon which the Cr $_2$ O $_3$  thin film thickness is 407 nm respectively.

The texture of the films with different thickness and the substrate was examined by X-ray pole figures taken from both symmetric (0006) reflections and asymmetric (10 $\bar{1}$ 10) reflections. The texture of the films is independent of the film thickness. Therefore, here only the texture of the film with the thickness of 188 nm is presented. Fig. 39 (a) shows the X-ray pole figure taken from the (0006) reflection, which suggests that the film grew in a fiber texture in direction of the  $c$ -axis. The X-ray pole figure taken from the (10 $\bar{1}$ 10) peak of this Cr $_2$ O $_3$  film is shown in Fig. 39 (b). There are two 6-fold symmetry reflections

in the circle of  $\psi=18^\circ$  and  $\psi=32^\circ$ , respectively. The outer 6-fold symmetry of the  $(10\bar{1}10)$   $\text{Cr}_2\text{O}_3$  reflections can be attributed to double diffraction patterns produced by the primary beam [241]. The  $\varphi$ -scan in Fig. 40 presents six peaks separated equally at an interval of  $60^\circ$  which indicates a six-fold symmetry, while a 3-fold symmetry for the  $c$ -cut  $\alpha\text{-Al}_2\text{O}_3$  can be observed when a  $\varphi$ -scan at  $\psi=18^\circ$  is taken. The 6-fold symmetry observed in the pole figure of  $\text{Cr}_2\text{O}_3$  ( $10\bar{1}10$ ) on  $\alpha\text{-Al}_2\text{O}_3$  substrates illustrates that the  $\text{Cr}_2\text{O}_3$  has a strong texture on  $\alpha\text{-Al}_2\text{O}_3$  with rhombohedral structure. The presence of a 6-fold symmetry of the  $\text{Cr}_2\text{O}_3$  ( $10\bar{1}10$ ) reflection, instead of a 3-fold symmetry as observed for the  $\alpha\text{-Al}_2\text{O}_3$  substrate, indicates that there are two different in-plane ( $10\bar{1}10$ ) orientations rotated by  $60^\circ$  domain variants because of stacking faults (suggested to be caused by dislocations).

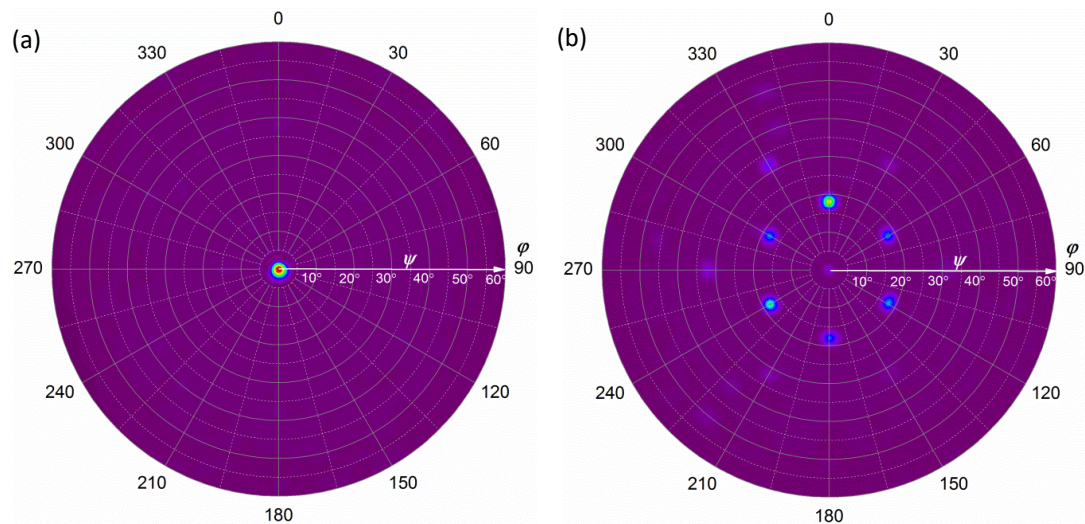


Fig. 39 X-ray pole figures taken from (a) the  $(0006)$  peak and (b) the  $(10\bar{1}10)$  peak of the  $\text{Cr}_2\text{O}_3$  film with the thickness of 188 nm deposited on  $\alpha\text{-Al}_2\text{O}_3$   $(0001)$  substrates at  $400^\circ\text{C}$ .

The stacking faults are illustrated in Fig. 41. Fig. 41 (b) shows the  $(10\bar{1}10)$  Bragg-Brentano peaks of the  $\text{Cr}_2\text{O}_3$  film (yellow and green dots) grown on  $\alpha\text{-Al}_2\text{O}_3$  (red dots) with two domains of different orientation. The first domain ( $\text{Cr}^{3+}$  in yellow color in Fig. 41 (b)) grows epitaxially with  $\alpha\text{-Al}_2\text{O}_3$   $[10\bar{1}0] \parallel \text{Cr}_2\text{O}_3$   $[10\bar{1}0]$ , while the second domain ( $\text{Cr}^{3+}$  in green color in Fig. 41 (b)) is rotated by  $60^\circ$  with  $\alpha\text{-Al}_2\text{O}_3$   $[10\bar{1}0] \parallel \text{Cr}_2\text{O}_3$   $[11\bar{2}0]$ . The rotation by  $60^\circ$  is caused by cation ( $\text{Al}^{3+} / \text{Cr}^{3+}$ ) stacking faults in the interface between  $\alpha\text{-Al}_2\text{O}_3$  and  $\text{Cr}_2\text{O}_3$  or in the  $\text{Cr}_2\text{O}_3$  layer. The  $\text{Al}^{3+}/\text{Cr}^{3+}$  cation positions can be described by an  $\dots ABCABC\dots$  sequence as described in section 2.1.2. If there were no stacking

faults, the occupation should be ... *ABCABC/ABCABC* ... in the interface and in the film layer. In fact, the  $\text{Cr}^{3+}$  cation sequence becomes */ACBACB...*, */BCABCA...* or */BAC-BAC.....* in the film when stacking faults occur in the interface. A second possibility is the development of the stacking faults in the  $\alpha\text{-Cr}_2\text{O}_3$  film rather than in the interface. In this case, the  $\text{Cr}^{3+}$  cation occupies as *ABC...ABCBCABCA...*, but the exact position cannot be deduced. The 6-fold symmetry could also be found in very thin films, so we suggest the stacking fault is in or near to the interface to the substrate.

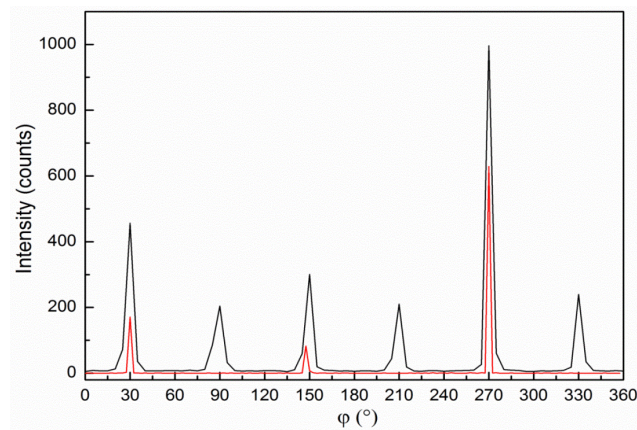


Fig. 40  $\varphi$ -scan of the  $(10\bar{1}10)$  reflex of the  $\text{Cr}_2\text{O}_3$  film (black line) and  $\alpha\text{-Al}_2\text{O}_3$  substrate (red line).

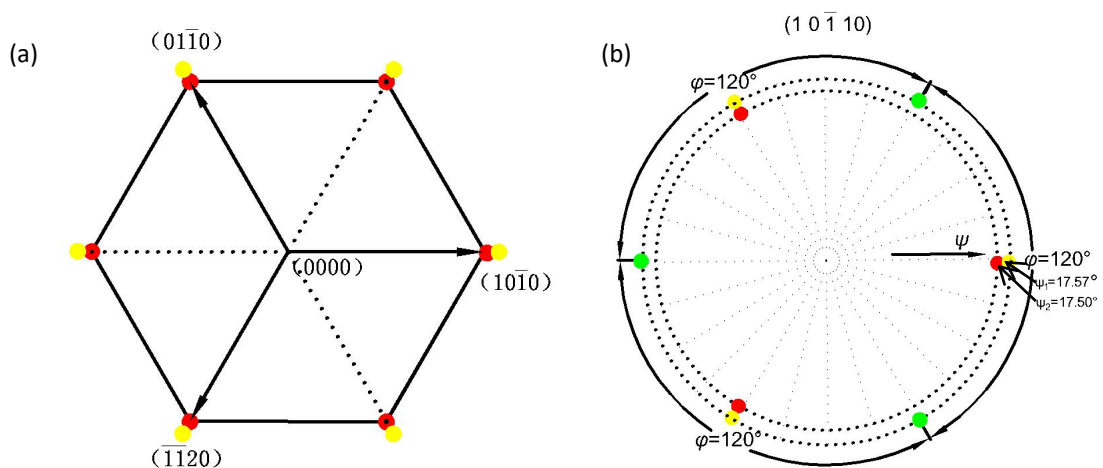


Fig. 41 Schematic drawing illustrating the pole figure of the  $(10\bar{1}10)$  reflection of the  $\text{Cr}_2\text{O}_3$  film with the thickness of 188 nm on the  $\alpha\text{-Al}_2\text{O}_3$  substrate: (a) the top view of the structure in real space from the direction  $\langle 0001 \rangle$  (b) pole figure from the  $(10\bar{1}10)$  peak of the  $\alpha\text{-Al}_2\text{O}_3$  substrate and the  $\text{Cr}_2\text{O}_3$  film with two different domains of orientation. ●  $\text{Al}^{3+}$ ; ●  $\text{Cr}^{3+}$  of the first domain; ●  $\text{Cr}^{3+}$  of the second domain rotated by  $60^\circ$ .

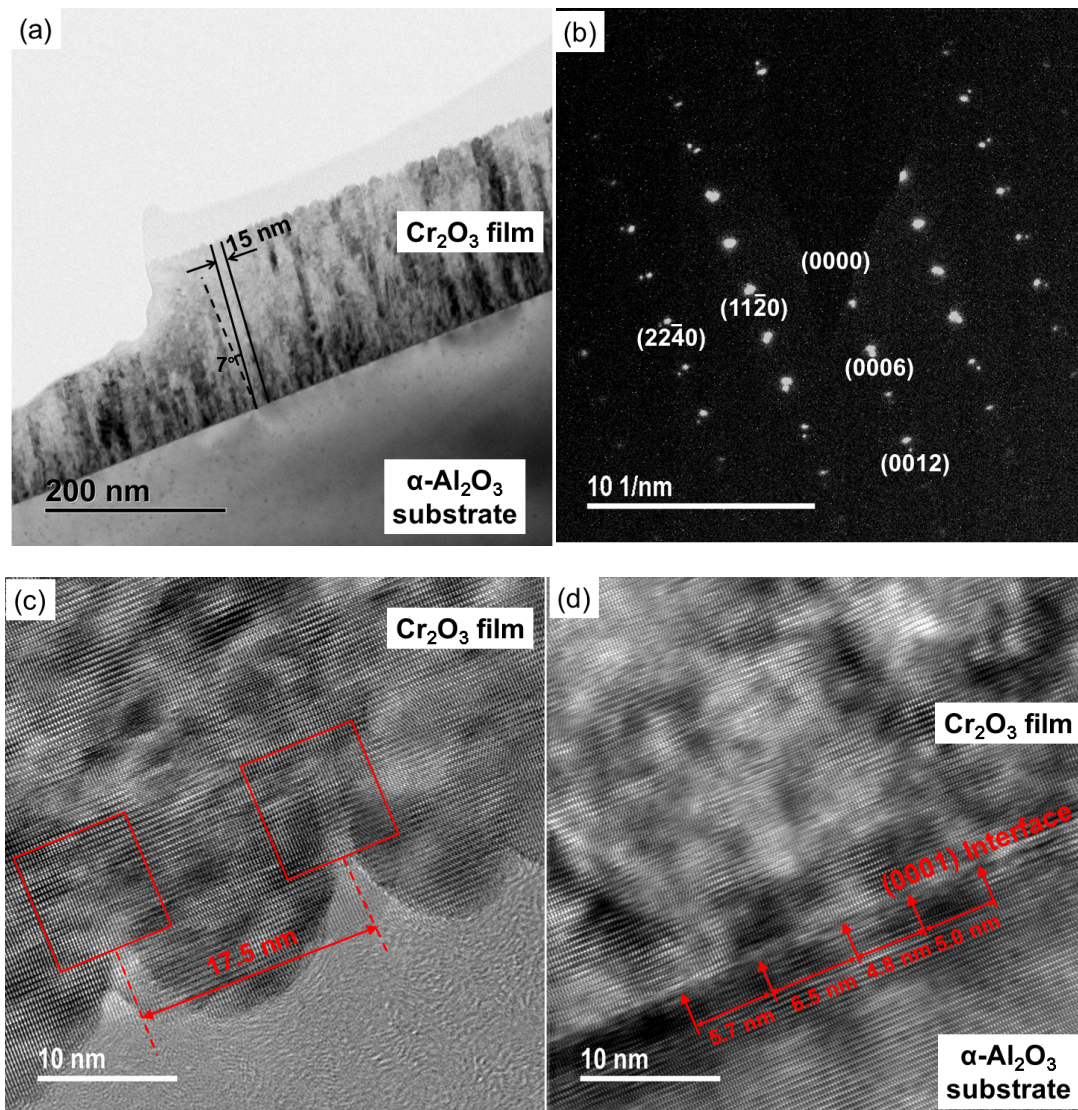


Fig. 42 TEM results of the  $\text{Cr}_2\text{O}_3$  film with the thickness of 188 nm grown on  $\alpha\text{-Al}_2\text{O}_3$  substrate at 400 °C: (a) BF image showing a cross sectional view, (b) the SAED pattern revealing a partially epitaxial orientation relationship between the film and the substrate, (c) a HRTEM image of the film and (d) a high resolution TEM image of the interface between the film and the substrate.

More detailed information on the microstructure of the films and the relationship between the films and the substrate was obtained by TEM on the sample with the film thickness of 188 nm. Fig. 42 (a) shows a TEM BF image of the film cross section. In this image, we observed the lateral grain size of around 15 nm. The individual columnar grains with

a slight tilt of around  $7^\circ$  of the crystals but not of the orientation with respect to the substrate can be observed. The tilting could be caused by the asymmetric position of the substrates under the target during deposition. The substrates were placed below the erosion zone (section 3.1.2.1) of the target, not in the center during the deposition. The surface of the film shows long period corrugation because of the tops of the individual grains which are determined in high resolution TEM images, shown in Fig. 42 (c). The crystals seem to develop a faceted growth, which approves that the film was grown in the VW growth mode. The selected area electron diffraction (SAED) patterns dominated by both the film and the substrate are shown in Fig. 42 (b). This reveals the expected epitaxial relationship, which can be written as  $(11\bar{2}0) \text{ Al}_2\text{O}_3 // (11\bar{2}0) \text{ Cr}_2\text{O}_3$  and  $(0001) \text{ Al}_2\text{O}_3 // (0001) \text{ Cr}_2\text{O}_3$ . The reflections of the  $(0003)$  lattice plane are forbidden but shown in SAED, which is due to the double diffraction [52]. This is in agreement with the result of the outer 6-fold symmetry shown in pole figure analysis. The good orientation relationship between the film and the substrate is also due to the fact that the film and the substrate possess the same crystallographic structure. The red squares in Fig. 42 (c) show grain boundaries indicating that the lattice planes continue between the neighboring crystals. The high resolution TEM image in Fig. 42 (d), showing the interface between the  $\text{Cr}_2\text{O}_3$  film and the  $\alpha\text{-Al}_2\text{O}_3$  substrate, indicates the occurrence of misfit dislocations along the interface induced by lattice mismatch. The average spacing between dislocations is about  $5.5 \text{ nm} \pm 0.77 \text{ nm}$ , and the misfit dislocation occur in every 24 lattice planes, which is in agreement to the result of the relaxed state in the film from RSM.

#### 4.1.2 Raman spectroscopy analysis

Raman spectroscopy was used further to approve the chemical composition and crystal quality of the films indirectly. These analyses support the claim that single phase  $\text{Cr}_2\text{O}_3$  films were grown on  $\alpha\text{-Al}_2\text{O}_3$  substrates. The Raman spectra of the  $\text{Cr}_2\text{O}_3$  films with thickness of 30 nm, 75 nm, 105 nm, 188 nm and 407 nm are shown in Fig. 43. A  $\text{Cr}_2\text{O}_3$  bulk single crystal supplied by EVOCHEM Advanced Materials GmbH was also measured as reference, and the corresponding Raman spectrum can also be seen in Fig. 43 (curve in magenta color). This  $\text{Cr}_2\text{O}_3$  bulk single crystal Raman spectrum shows one sharp peak with highest intensity corresponding to  $A_{1g}$  mode and three relatively broader peaks corresponding to  $E_g$  mode. The Raman spectra of the  $\text{Cr}_2\text{O}_3$  films show two different

features: on one hand, various signals (marked with “s”) can be attributed to characteristic signals of the underlying  $\alpha$ -Al<sub>2</sub>O<sub>3</sub> substrate (these are observed here due to the thin Cr<sub>2</sub>O<sub>3</sub> film thickness). On the other hand, some signals around 295 cm<sup>-1</sup> and 550 cm<sup>-1</sup> can be clearly attributed to vibrational states of the Cr<sub>2</sub>O<sub>3</sub> crystal. The signal in the range of 530 cm<sup>-1</sup> - 570 cm<sup>-1</sup> is obviously not symmetric, and this peak can be considered to be a superposition of both  $E_g$  and  $A_{1g}$  modes of Cr<sub>2</sub>O<sub>3</sub>. The strongest and sharpest feature of the vibrational phonon  $A_{1g}$  mode which corresponds to the metal-oxygen vibration occurs at 546.3 cm<sup>-1</sup> - 549.1 cm<sup>-1</sup> for the films and 552 cm<sup>-1</sup> for the Cr<sub>2</sub>O<sub>3</sub> single crystal, which fits very well with the values of 547 cm<sup>-1</sup> - 556 cm<sup>-1</sup> reported for such vibration in pure Cr<sub>2</sub>O<sub>3</sub> [230,242–244]. Another wide band with low intensity around 295 cm<sup>-1</sup> appear for the films with larger thickness, which can also be attributed to vibrational states of Cr<sub>2</sub>O<sub>3</sub>.

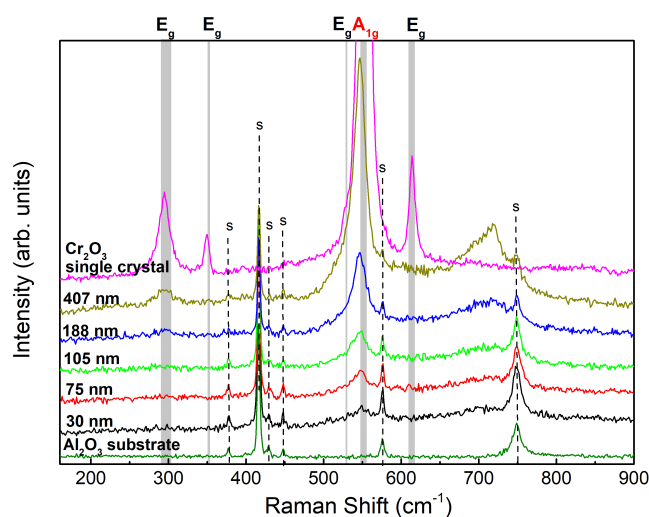


Fig. 43 Raman spectra of the Cr<sub>2</sub>O<sub>3</sub> films with different thickness (30 nm, 75 nm, 105 nm, 188 nm, and 407 nm) deposited on  $\alpha$ -Al<sub>2</sub>O<sub>3</sub> substrates and of a Cr<sub>2</sub>O<sub>3</sub> single crystal (supplied by EVOCHEM Advanced Materials GmbH) from bottom to top. The film thickness is marked on the corresponding line. “s” indicates reflexes corresponding to the  $\alpha$ -Al<sub>2</sub>O<sub>3</sub> substrates. The gray areas refer to the areas of the Raman shift of the Raman active modes of pure Cr<sub>2</sub>O<sub>3</sub> according to ref. [230,242–244].

Some general observations are made on the Raman spectra of the Cr<sub>2</sub>O<sub>3</sub> films: The intensities of the signals attributed to the Cr<sub>2</sub>O<sub>3</sub> vibrational states increase with film thickness, and the intensities of the signals attributed to the  $\alpha$ -Al<sub>2</sub>O<sub>3</sub> substrates decrease with increasing film thickness. The Raman spectra of the Cr<sub>2</sub>O<sub>3</sub> films show a significant shift of

phonon frequency with the film thickness. This behavior is suggested to be caused by the lattice constants variation with the film thickness which has been derived from XRD measurements. The bands around  $550\text{ cm}^{-1}$  are separated into two modes by fitting (the fitting is not shown) and the  $A_{1g}$  mode is discussed. The Raman  $A_{1g}$  mode shifts to the smaller wavenumber value side with decreasing the film thickness (i.e. increasing the  $(000l)$  lattice plane distance) and this trend is drawn in Fig. 44. With decreasing film thickness, the films have larger lattice parameter  $c$  values and are more strained (as has been discussed on basis of the RSM results). At the meantime, the  $A_{1g}$  mode Raman shifts to the smaller Raman wavenumber side with the film changing from relaxed to strained state. The  $A_{1g}$  mode corresponds to the vibration of “total symmetric stretching” or “breathing” as shown in the insert of Fig. 44 [227]. The strain will cause a change of the vibrational states because the distances between atoms will be influenced. It is also noticed that the Raman spectra of the  $\text{Cr}_2\text{O}_3$  films show additional asymmetric, weak and broad features in the range of  $650\text{ cm}^{-1} - 750\text{ cm}^{-1}$  in Fig. 43. These features arise definitely from the  $\text{Cr}_2\text{O}_3$  films but not from the  $\text{Cr}_2\text{O}_3$  single crystal, and they may due to surface induced defects [242]. A potential interpretation is that the appearance of these additional features is caused by film stress occurring during the partly epitaxial growth of  $\text{Cr}_2\text{O}_3$  films on  $\alpha\text{-Al}_2\text{O}_3$  substrates because of the larger lattice constants of  $\text{Cr}_2\text{O}_3$  compared to  $\alpha\text{-Al}_2\text{O}_3$  [245].

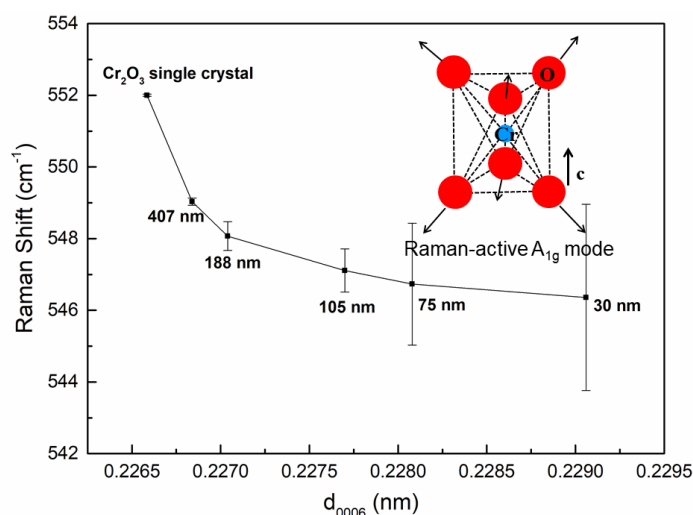


Fig. 44 Correlation of the Raman shift of the  $A_{1g}$  mode on the film thickness with a corresponding lattice plane distance  $d_{0006}$  obtained from  $\theta - 2\theta$  XRD measurements. The inset is the  $A_{1g}$  vibrational mode [227].

### 4.1.3 Optical properties characterization

UV-VIS-NIR spectra were obtained due to optical absorption to get optical properties of the film. Fig. 45 shows the optical absorption spectra of the  $\text{Cr}_2\text{O}_3$  films with the different thicknesses deposited on  $\alpha\text{-Al}_2\text{O}_3$  substrates. The absorbance of the films displays a steep decrease in UV range (from 300 nm to 400 nm) and a steady decrease in the visible range (from 400 nm to 800 nm). These spectra show a general trend of absorption, i.e. the absorbance of the films decreases with decreasing the frequency of the incident radiation, which is independent of the film thickness. The absorbance increases with increasing the film thickness at the same wavelength. The  $\text{Cr}_2\text{O}_3$  films absorb light totally in the UV range below 360 nm, 325 nm and 300 nm for the films with thickness of 407 nm, 188 nm and 105 nm respectively, which reveals the total absorbance wavelength decreases with decreasing the film thickness. The minimum transmittance in the visible range for the films with the film thickness of 105 nm, 188 nm and 407 nm is 52.6 %, 43.5 % and 35.7 % respectively, which is calculated according to Eq.(17). The films are transparent or semi-transparent and the transparency is worse with increasing the film thickness. The film with a thickness thinner than 105 nm displays an absorbance band around 470 nm, so the film shows the yellow color. While the films with the thicker thickness of 188 nm and 407 nm display absorbance bands both around 470 nm and 600 nm, so these films show the blue or green color.

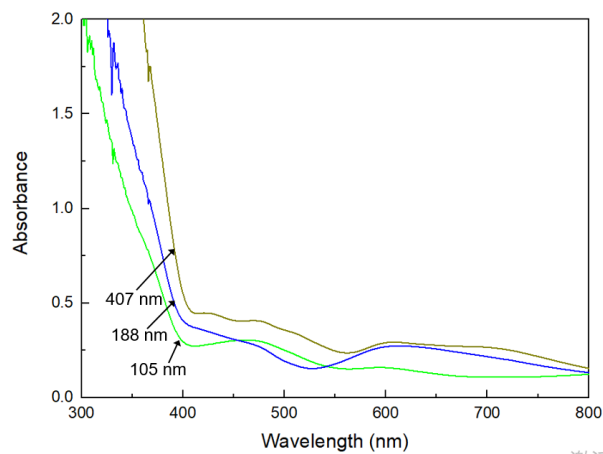


Fig. 45 UV-VIS-NIR spectra of  $\text{Cr}_2\text{O}_3$  films with different thickness.

The optical band gap is calculated by Tauc's relation shown as Eq.(18).  $E_g$  and  $B$  values in Tauc's equation (Eq.(18)) are shown in Table 10. In order to determine the value of the

optical band gap, the plot of  $(\alpha h\nu)^2$  as a function of the photon energy ( $h\nu$ ) is shown in Fig. 46, where  $\alpha$  indicates the optical absorption co-efficient, and  $h\nu$  is the photon energy. The values of the optical band gap ( $E_g$ ) are given by the extrapolation of the linear portion of the plot to the energy axis at  $\alpha = 0$ . The  $E_g$  values for the  $\text{Cr}_2\text{O}_3$  films deposited on  $\alpha\text{-Al}_2\text{O}_3$  substrate with the different thickness of 105 nm, 188 nm, and 407 nm are 3.01 eV, 3.01 eV, and 3.07 eV, respectively, which agrees with values reported by other authors [27,105,128,237,246]. The thicker films possess the larger  $E_g$  value.

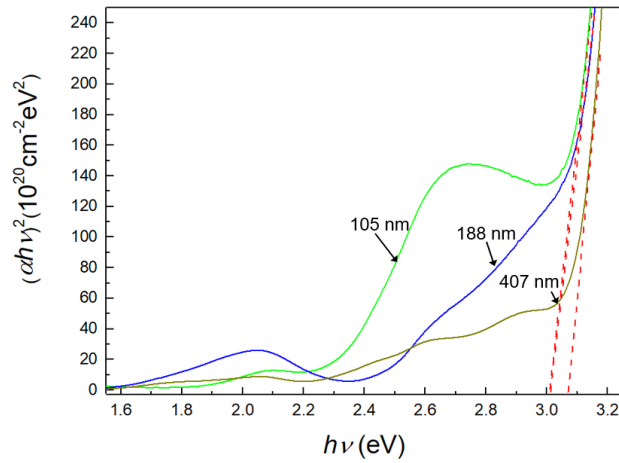


Fig. 46 Plots of  $(\alpha h\nu)^2$  vs.  $h\nu$  for the  $\text{Cr}_2\text{O}_3$  films with different thickness.

Table 10 Optical properties of the  $\text{Cr}_2\text{O}_3$  films ( $E_g$ : the band gap;  $B$ : a constant in Eq.(18)).

Film thickness (nm)	$E_g$ (eV)	$B$ ( $10^{24} \text{ cm}^{-1} \text{ eV}^{-1}$ )
105	3.01	2.0
188	3.01	1.9
407	3.07	7.2

#### 4.1.4 Influence of the plasma-etching process on the crystal growth

Two types of  $\text{Cr}_2\text{O}_3$  films with the same thickness of 320 nm were deposited on the  $c$ -plane  $\alpha\text{-Al}_2\text{O}_3$  substrates and are compared in this part of the study: one is deposited on the substrate after plasma plasma-etching with a depth of 50 nm to clean the substrate surface before coating to remove the contaminations on the substrate; the other is deposited on the substrate without the plasma-etching process. Fig. 47 shows results of the XRD analysis in Bragg-Brentano geometry. The red curve shows the reflections of the

Cr<sub>2</sub>O<sub>3</sub> film deposited on the  $\alpha$ -Al<sub>2</sub>O<sub>3</sub> substrate which was plasma-etched before deposition, and the black curve shows the reflections of the Cr<sub>2</sub>O<sub>3</sub> film deposited on the  $\alpha$ -Al<sub>2</sub>O<sub>3</sub> substrate without plasma-etching process. Both of these two films are single-phase nanocrystalline. Only (0006) and (00012) reflections of the films and the  $\alpha$ -Al<sub>2</sub>O<sub>3</sub> substrates were observed in the XRD in Bragg-Brentano geometry; these are marked in Fig. 47. For both films, the (0006) reflections are observed at the similar position of  $2\theta \approx 39.83^\circ$ , which indicates the plasma-etching of the substrate before deposition has no or only little influence the lattice constant  $c$  (or  $d_{0006}$ ) as derived from XRD. The FWHM value of the (0006) reflections of the film deposited on the substrate without plasma-etching process is  $0.19^\circ$ , which is smaller than that of with plasma-etching ( $0.20^\circ$ ). This indicates that the grain size of Cr<sub>2</sub>O<sub>3</sub> on the substrate without plasma-etching could be minimal larger.

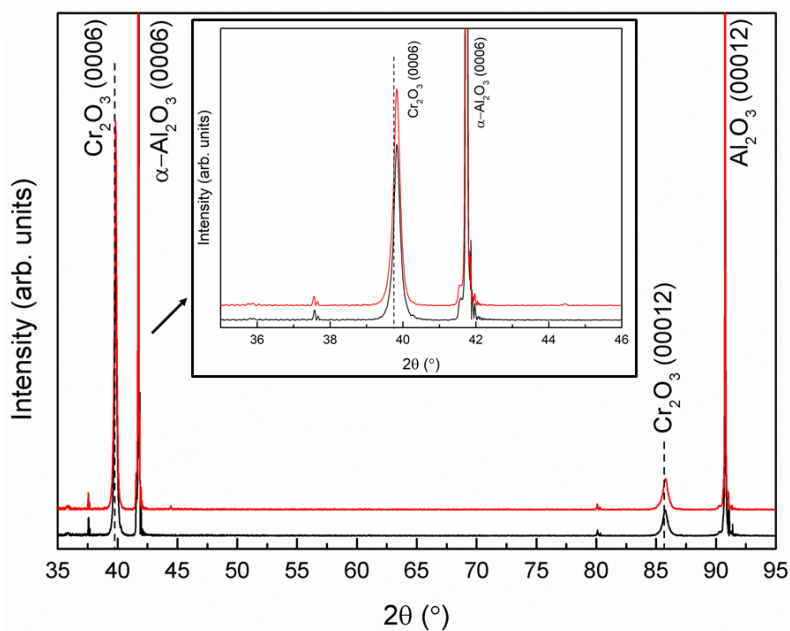


Fig. 47  $\theta - 2\theta$  XRD patterns of the Cr<sub>2</sub>O<sub>3</sub> films with thickness of 320 nm deposited on the  $c$ -plane  $\alpha$ -Al<sub>2</sub>O<sub>3</sub> substrates. The black curve corresponds to the film grown without plasma-etching process before deposition. The red curve corresponds to the film grown after plasma-etching before deposition. The dashed lines indicate the theoretical (0006) and (00012) reflection positions of Cr<sub>2</sub>O<sub>3</sub> according to the PDF card No. 38-1479 from the ICDD-database. The inset shows the magnification of the (0006) reflections of the film and the substrate.

The mosaic spreading of the (0006) reflections of these two films are shown in Fig. 48.

The FWHM values of these reflections of the films deposited without and with plasma-etching process before deposition are  $0.93^\circ$  and  $1.08^\circ$ , respectively, indicating the tilt of the (0006) planes with respect to the (0006) planes of the substrate in the individual crystals of the film deposited on the substrates without plasma-etching process before deposition is smaller, i.e. the film presents better epitaxial quality.

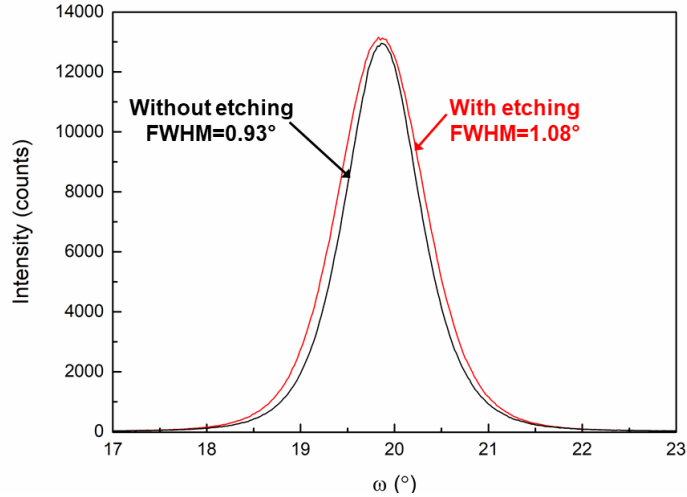


Fig. 48 XRD rocking curves ( $\omega$ -scans) of the (0006) reflections of the  $\text{Cr}_2\text{O}_3$  films with thickness of 320 nm deposited on the  $c$ -plane  $\alpha\text{-Al}_2\text{O}_3$  substrates. The black curve corresponds to the film grown without plasma-etching process before deposition. The red curve corresponds to the film grown after plasma-etching before deposition.

The Raman spectra of these two  $\text{Cr}_2\text{O}_3$  films are shown in Fig. 49. Both of these two Raman spectra show two different features: features marked with “s” can be attributed to characteristic signals of the substrates and other features can be clearly attributed to vibrational states of the  $\text{Cr}_2\text{O}_3$  crystal. We mainly discuss the strongest feature of  $A_{1g}$  band. The width of the  $A_{1g}$  band of the film deposited without plasma-etching process ( $\text{FWHM} = 13.25 \text{ cm}^{-1}$ ) is a tiny bit smaller than that of the film deposited with plasma-etching process ( $\text{FWHM} = 13.52 \text{ cm}^{-1}$ ), indicating again that the crystal quality of the film deposited without plasma-etching process is better. The  $A_{1g}$  mode position of the film deposited without plasma-etching process is at  $548.5 \text{ cm}^{-1}$ , while that of the film deposited with plasma-etching process is at  $547.7 \text{ cm}^{-1}$ . As presented in section 4.1.1, the Raman  $A_{1g}$  band position of the  $\text{Cr}_2\text{O}_3$  single crystal is at  $552 \text{ cm}^{-1}$ . According to the discussion in section 4.1.1 that the strain in the films can influence the atom vibration frequency,

the film deposited with plasma-etching process is more strained, which might be as a result of disturbed atom arrangement after plasma-etching.

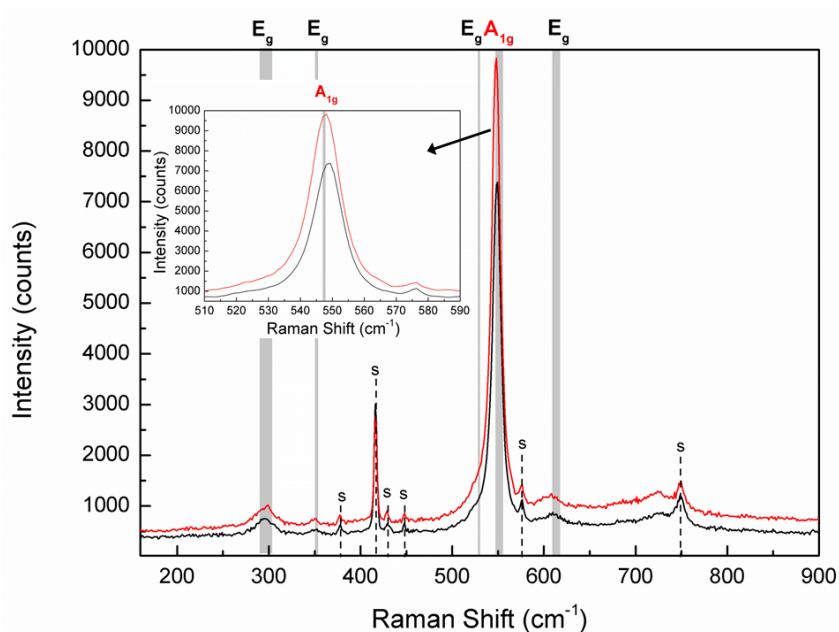


Fig. 49 RAMAN spectra of the  $\text{Cr}_2\text{O}_3$  films with thickness of 320 nm deposited on the  $c$ -plane  $\alpha\text{-Al}_2\text{O}_3$  substrates. The black curve corresponds to the film grown without plasma-etching process before deposition. The red curve corresponds to the film grown after plasma plasma-etching before deposition. “s” indicates reflexes corresponding to the  $\alpha\text{-Al}_2\text{O}_3$  substrate. The gray areas refer to the Raman active modes of pure  $\text{Cr}_2\text{O}_3$  cited from ref. [230,242–244]. The inset shows the magnification of the Raman signal in the wavenumber area characteristic of the  $A_{1g}$  mode of bulk  $\text{Cr}_2\text{O}_3$ .

Fig. 50 shows the IRRAS spectra of these two  $\text{Cr}_2\text{O}_3$  films. Absorbance bands near  $726\text{ cm}^{-1}$  which are assigned to the  $A_{2u}$  mode of  $\text{Cr}_2\text{O}_3$  are observed for both films [207]. Compared to the film grown without plasma-etching before deposition, the  $A_{2u}$  mode band position shifts towards larger wavenumbers (smaller wavelengths) from  $725.5\text{ cm}^{-1}$  to  $726.6\text{ cm}^{-1}$  and the FWHM value of the band becomes larger from  $34.6\text{ cm}^{-1}$  to  $37.5\text{ cm}^{-1}$  if there is plasma-etching process before deposition. The film deposited without plasma-etching process possesses smaller band width, indicating the crystal quality is better. This observation is in good agreement to the XRD and Raman spectroscopy results discussed above.

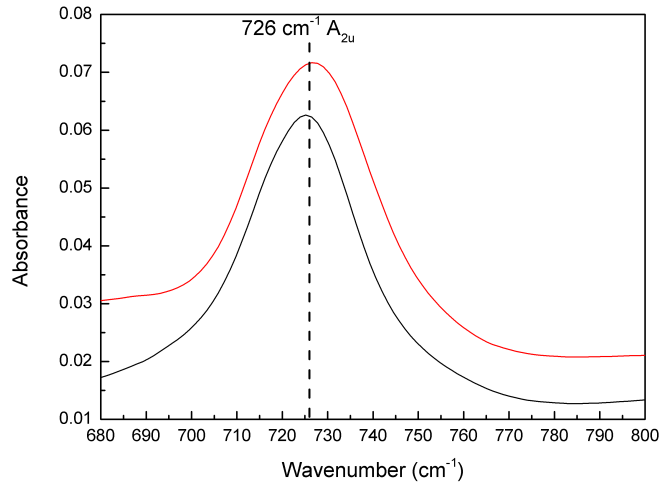


Fig. 50 The IRRAS spectra of the  $\text{Cr}_2\text{O}_3$  films with thickness of 320 nm deposited on the  $c$ -plane  $\alpha\text{-Al}_2\text{O}_3$  substrates. The black curve corresponds to the film grown without plasma-etching process before deposition. The red curve corresponds to the film grown after plasma-etching. The dashed line is the position of  $A_{2u}$  mode of single crystalline  $\text{Cr}_2\text{O}_3$  according to ref. [207].

The texture evolution of these two films were compared by X-ray pole figures taken from both symmetric (0006) reflection and asymmetric ( $10\bar{1}10$ ) reflection. The texture of the films grown with plasma-etching process before deposition was shown in Fig. 39. Fig. 51 shows the texture of the film deposited without plasma-etching process.

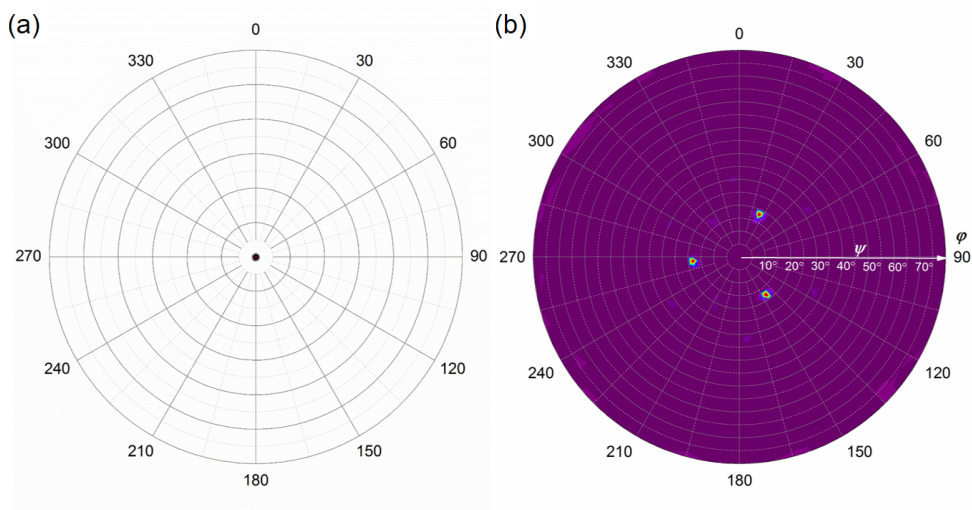


Fig. 51 X-ray pole figures taken from (a) the (0006) reflection and (b) the ( $10\bar{1}10$ ) reflection of the  $\text{Cr}_2\text{O}_3$  films with the thickness of 320 nm deposited on the  $c$ -plane  $\alpha\text{-Al}_2\text{O}_3$  substrates without plasma-etching process before coating.

Both X-ray pole figures taken from the (0006) reflection of the films show a film microstructure grown with a fiber texture along the  $c$ -axis, and this observation is independent of the substrate pre-treatment (i.e. if there is an plasma-etching process applied or not). The X-ray pole figures taken from the  $(10\bar{1}10)$  reflection of the film grown without plasma-etching process shows a 3-fold symmetry of the reflections in the circle of  $\psi = 18^\circ$  instead of a 6-fold symmetry which is the same as  $c$ -plane  $\alpha$ - $\text{Al}_2\text{O}_3$  substrate. This indicates there is no or only very few stacking faults in the interface between the substrates and the films. Here the “interface” indicates the early growth zone of the films, following nucleation and coalescence occur. If the substrates are plasma-etched before deposition, the perfect single crystal substrates can be destroyed (i.e. the early growth zone is disturbed), which causes the epitaxial growth more difficult. The plasma-etching on the substrate could lead to stacking faults.

In order to investigate the influence of the plasma-etching process before deposition on the film growth, the interface between the film and the substrate was characterized by TEM. Fig. 52 (a) and (b) reveal the SAED patterns of the  $\text{Cr}_2\text{O}_3$  films grown on the  $c$ -plane  $\alpha$ - $\text{Al}_2\text{O}_3$  substrates with and without plasma-etching process before deposition. There are two diffraction spots dominated by both the film and the substrate and indicating the same lattice planes: the inner larger diffraction spots are originating from the  $\text{Cr}_2\text{O}_3$  films, and the outer smaller diffraction spots are originating from the  $\alpha$ - $\text{Al}_2\text{O}_3$  substrate. The lattice planes (0001) and  $(11\bar{2}0)$  have been figured out on the SEAD images in Fig. 52 (a) and (b). Therefore, the relationship between the  $\text{Cr}_2\text{O}_3$  films and the  $\alpha$ - $\text{Al}_2\text{O}_3$  substrates in both cases can be described as  $(0001) \text{Al}_2\text{O}_3 // (0001) \text{Cr}_2\text{O}_3$  and  $(11\bar{2}0) \text{Al}_2\text{O}_3 // (11\bar{2}0) \text{Cr}_2\text{O}_3$ . In order to obtain a better contrast in high-resolution micrographs, FFT and IFFT of atomic planes was used on HRTEM as shown in Fig. 52 (c) - (f). Fig. 52 (c) shows a HRTEM image of the film grown on the substrate without plasma-etching process. It reveals a clear interface between the film and the substrate with a regular atomic arrangement where the (0006) lattice planes of the substrate are parallel between the film and the substrate. Compared to the substrate without plasma-etching process, the substrate after plasma-etching process was damaged and its perfect atomic arrangement disturbed as is clearly shown in Fig. 52 (d). The depth of the disordered area in the substrate near the interface is about 5 nm (i.e. six hexagonal unit cells

shown in Fig. 3). To a certain extent, the ordered arrangement of atoms in the substrate can be destroyed by the plasma-etching, and then the quality of the film crystals grown on the irregular atomic substrate is worse, which is in agreement with the XRD, Raman spectroscopy and IRRAS results. The images in the red squares in Fig. 52 (c) and (d) are magnified as shown in Fig. 52 (e) and (f). The interplanar distances were measured and have been marked in Fig. 52 (e) and (f). For the film grown on the substrate without plasma-etching process,  $(11\bar{2}0)$  planes were identified, which continue from the substrate to the film. The calculated interplanar distance of the  $(11\bar{2}0)$  planes in the film is 0.21 nm; this value is more close to the theoretical value of  $\alpha\text{-Al}_2\text{O}_3$  ( $d_{11\bar{2}0}=0.2085$  nm according to PDF card No. 42-1468 from the ICDD-database) than to that of  $\text{Cr}_2\text{O}_3$  ( $d_{11\bar{2}0}=0.21752$  nm according to PDF card No. 38-1479 from the ICDD-database). The angle between the  $(11\bar{2}0)$  and  $(0006)$  plane is around  $56^\circ$  as measured from the HRTEM image in Fig. 52 (e), which is similar to the theoretical angle of  $61^\circ$  according to Eq.(2) or Eq.(3). For the film grown on the substrate with plasma-etching process,  $(11\bar{2}0)$  planes which are perpendicular to the  $(0006)$  planes (or interface) were clearly observed, which also continue from the substrate to the film. The calculated interplanar distance of the  $(11\bar{2}0)$  planes in the film is 0.24 nm; this value is also more close to the theoretical value of  $\alpha\text{-Al}_2\text{O}_3$  ( $d_{11\bar{2}0}=0.2379$  nm according to PDF card No. 42-1468 from the ICDD-database) rather to that of  $\text{Cr}_2\text{O}_3$  ( $d_{11\bar{2}0}=0.247969$  nm according to PDF card No. 38-1479 from the ICDD-database). In summary, the plasma-etching process on the substrate before deposition does not influence the phase formation of the films and has a limited effect on the lattice parameters. However, it will destroy the original ordered atomic substrate surface and causes the worse epitaxial crystal quality of the films grown with plasma-etching.

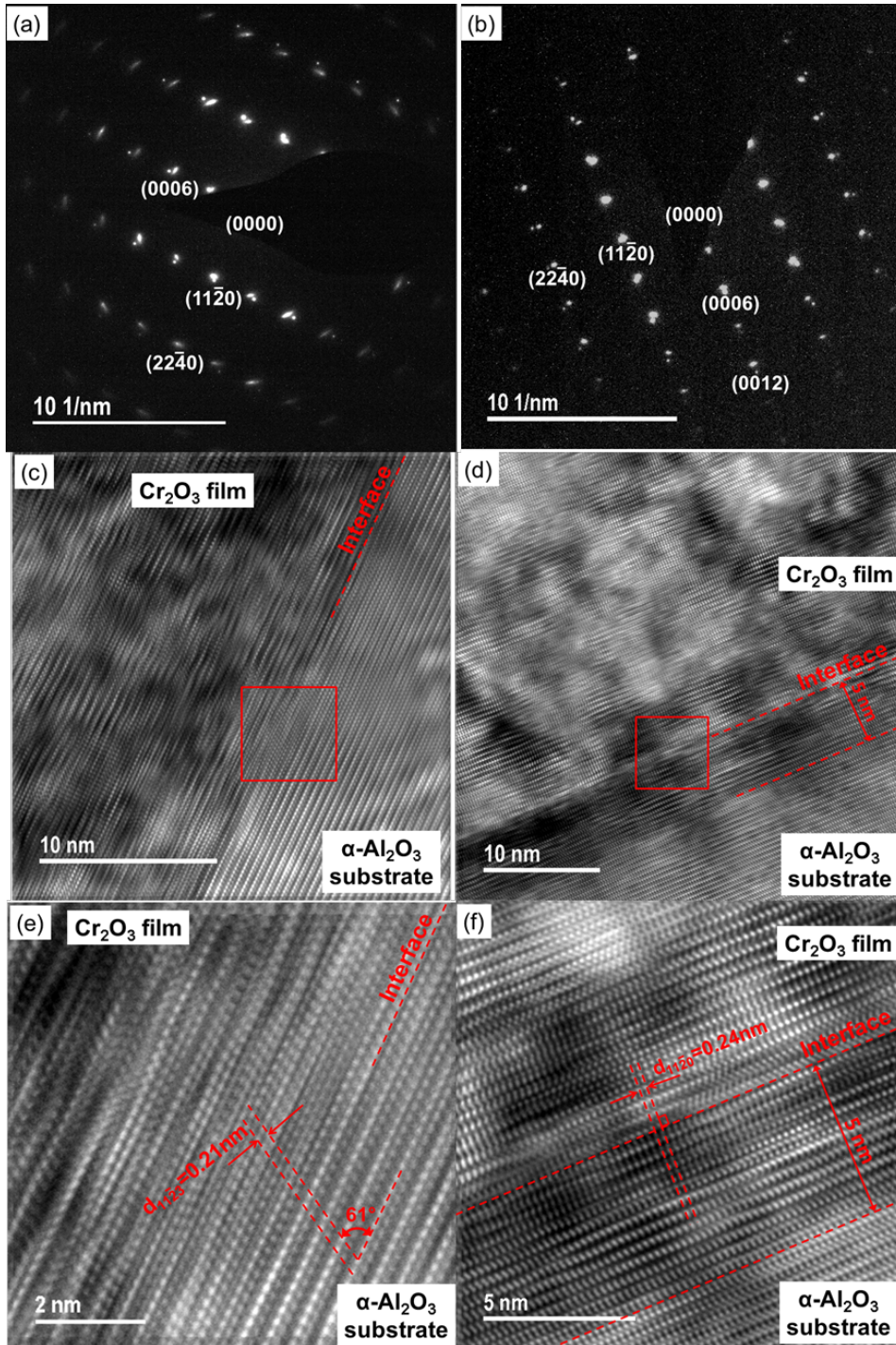


Fig. 52 TEM analysis of the  $\text{Cr}_2\text{O}_3$  films (320 nm) deposited on the  $c$ -plane  $\alpha\text{-Al}_2\text{O}_3$  substrates: (a), (c) and (e): the film grown on the  $\alpha\text{-Al}_2\text{O}_3$  substrate without plasma-etching process before deposition. (b), (d) and (f): the film grown on the  $\alpha\text{-Al}_2\text{O}_3$  substrate after plasma-etching. (a) and (b): SAED patterns showing the epitaxial relationship between the film and the substrate. (c) and (d): HRTEM images after FFT and IFFT process. (e) and (f): the partial enlargement for the red square in (c) and (d) respectively.

## 4.2 V<sub>2</sub>O<sub>3</sub> films deposited on *c*-plane $\alpha$ -Al<sub>2</sub>O<sub>3</sub> substrates

In this chapter, V<sub>2</sub>O<sub>3</sub> thin films synthesized on *c*-plane  $\alpha$ -Al<sub>2</sub>O<sub>3</sub> substrates are investigated. The samples were placed in the vacuum chamber and in relation to the sputtering target as shown in Fig. 17 (b). Films with a thickness of 2.4  $\mu$ m were deposited on the substrates after plasma-etching for removing the contaminations on the substrates at 400 °C and were used for the EPMA analysis in section 4.2.1. Films with a thickness of 300 nm, deposited on the substrates after plasma-etching at different deposition temperatures, were used for the structural analysis (except of TEM analysis; the film thickness for TEM characterization is 50 nm), spectroscopic and optical analysis (section 4.2.1 - 4.2.3). In section 4.2.4, films with thickness of 60 nm grown on the substrates with and without plasma-etching before deposition were compared to investigate the influence of the plasma-etching process on the locally epitaxial film growth.

### 4.2.1 Compositional and structural analysis

The chemical composition of the 2.4  $\mu$ m thick films synthesized on the *c*-Al<sub>2</sub>O<sub>3</sub> substrates at the deposition temperature of 400 °C was determined by EPMA, and the results are shown in Table 11. The atomic percentages of V and O in the films are 40.1 % and 58.6 %, respectively, which indicates the metal/oxygen stoichiometry of the films is close to the ideal value of 2/3. There is no V<sub>2</sub>O<sub>5</sub> in the films, which can be approved by XRD in the following. There are only minor impurities with very low concentrations, such as C, N, and Ar appearing in these films, similar to the Cr<sub>2</sub>O<sub>3</sub> films described in section 4.1. Therefore, without respect to the contaminations, it is suggested that stoichiometric V<sub>2</sub>O<sub>3</sub> films were grown on the *c*-Al<sub>2</sub>O<sub>3</sub> substrates.

Table 11 The chemical composition of the V<sub>2</sub>O<sub>3</sub> films deposited on the *c*-Al<sub>2</sub>O<sub>3</sub> substrates (standards used for calibrating see section 3.2.1) at 400 °C.

V (at. %)	O (at. %)	C (at. %)	N (at. %)	Ar (at. %)
40.1 $\pm$ 0.29	58.5 $\pm$ 0.31	0.6 $\pm$ 0.08	0.8 $\pm$ 0.04	0.0

Films with thickness of 300 nm were deposited on the  $\alpha$ -Al<sub>2</sub>O<sub>3</sub> substrates after plasma-etching at different substrate temperatures (without heating, 150 °C, 200 °C, 320 °C,

400 °C) and were used for the structural analysis. Fig. 53 (a) shows results of XRD in Bragg-Brentano geometry of the films deposited on the  $\alpha$ -Al<sub>2</sub>O<sub>3</sub> substrates at different substrate temperatures. The films grown on the substrates without heating are amorphous and crystalline films are grown at the substrate temperature above 150 °C. For the films grown at the substrate temperature above 150 °C, only (0006) and (00012) reflections of the films are observed at the lower diffraction angle side of the corresponding reflections of the substrates. No other reflections except of (0006) and (00012) are present, indicating the films possess a single V<sub>2</sub>O<sub>3</sub> phase with corundum-type structure and verifying that no other phase in the films is obtained (at these growth conditions). Compared to the growth of the Cr<sub>2</sub>O<sub>3</sub> films, V<sub>2</sub>O<sub>3</sub> films grow in crystalline structure at significantly lower temperatures. Crystalline V<sub>2</sub>O<sub>3</sub> films can be obtained at the substrate temperature of 150 °C, but Cr<sub>2</sub>O<sub>3</sub> films cannot be obtained at such low temperature. Because the (00012) reflections are much weaker and broader, Fig. 53 (b) shows only (0006) reflections of the films in more detail for a narrow range of the diffraction angle. The (0006) reflections of the films deposited at higher substrate temperature are shifted towards larger  $2\theta$  or the (0006) reflections of the substrates, due to the better epitaxial quality for the films deposited at higher substrate temperature. The relative (0006) intensity ratios (i.e. the ratio between the intensities of the (0006) reflections of the film and the corresponding (0006) reflection of the substrate) increase and the width of the (0006) reflections of the films decrease with increasing the substrate temperature as shown in Fig. 54 and Fig. 55, respectively. The increase in intensity and the narrowing of the (0006) reflections observed for films grown with higher substrate temperature suggests the films grown at higher substrate temperature have larger grain size and better crystalline quality. A gradual shift of the (0006) reflections of the films to larger diffraction angles with increasing substrate temperature indicates that the films deposited at higher temperature possess smaller lattice plane distance  $d_{0006}$  (or lattice constant  $c$ ). Fig. 56 shows the value of the lattice plane distance  $d_{0006}$  of the V<sub>2</sub>O<sub>3</sub> films dependent on the substrate temperature. There is a deviation between the values obtained for the films and the theoretical value of bulk V<sub>2</sub>O<sub>3</sub> because of the crystal defects in the films.

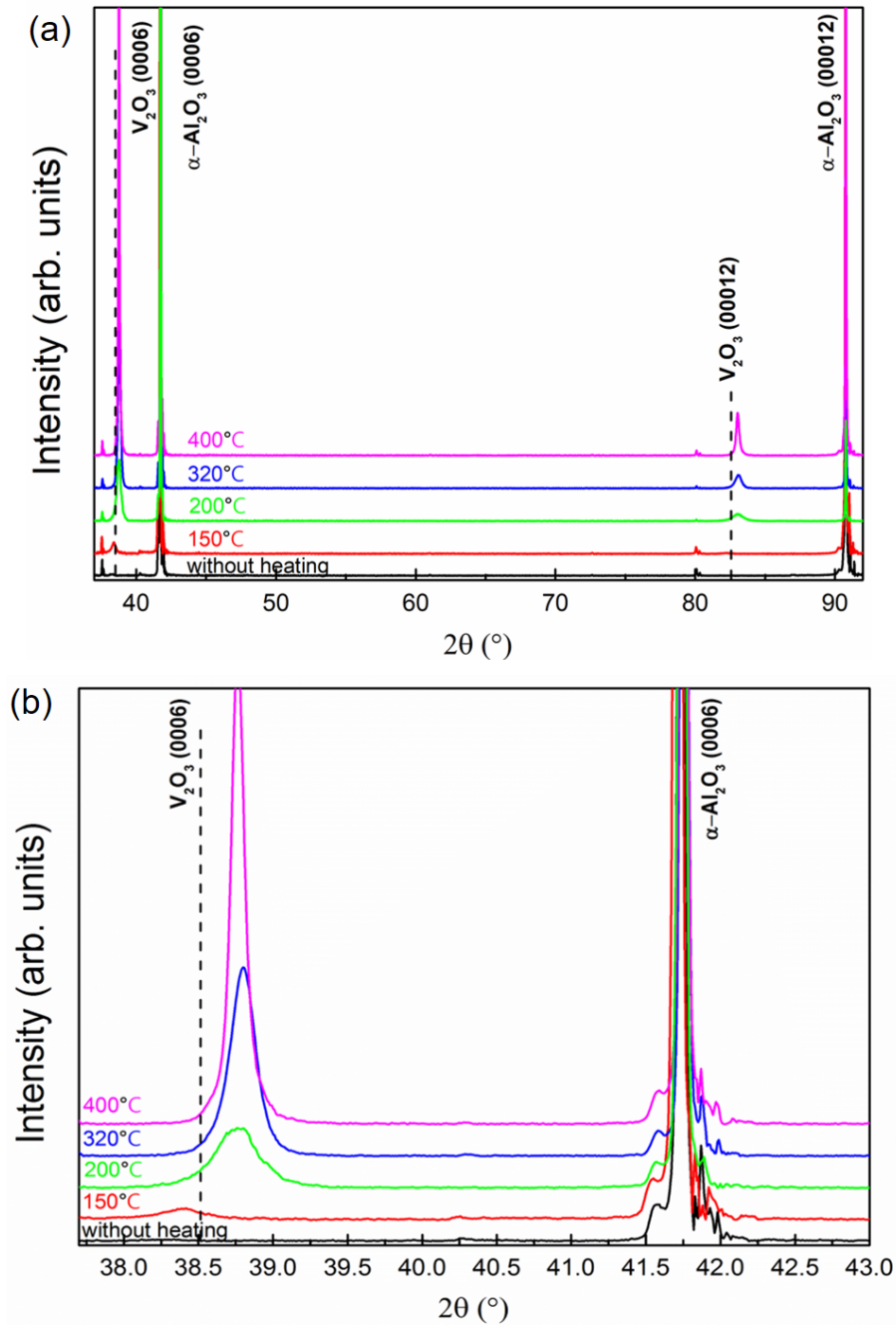


Fig. 53 (a)  $\theta$  -  $2\theta$  XRD results of the  $V_2O_5$  films deposited on the  $\alpha$ - $Al_2O_3$  substrates at different substrate temperatures. The substrate temperatures are marked on the corresponding lines. The (0006) and (00012) reflections of the films are at lower diffraction angles of the corresponding reflections from substrates. The dashed vertical line is the theoretical positions of the (0006) and (00012) reflections of  $V_2O_5$  according to PDF card No. 34-187 from the ICDD-database. (b) shows the (0006) reflections of the films in more detail for a narrow range of the diffraction angle.

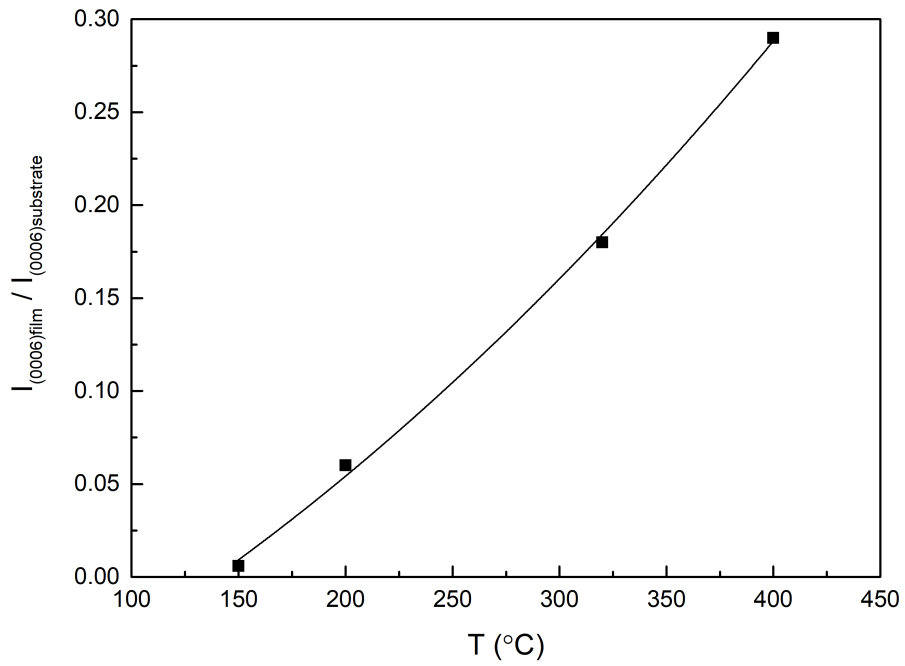


Fig. 54 Dependence of the relative (0006) intensity ratio of the intensity of the (0006) reflections of the  $V_2O_3$  films and the substrate on the substrate temperature.

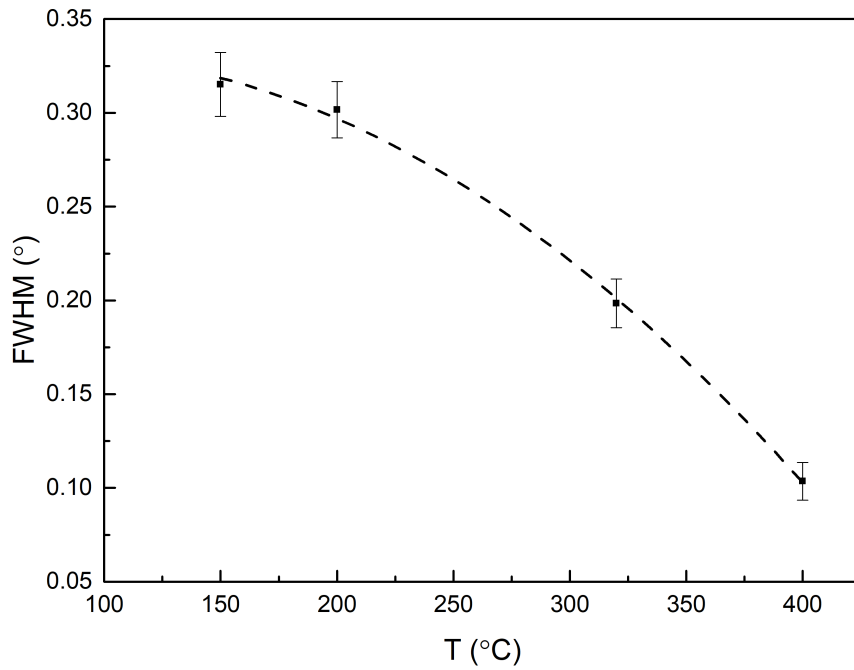


Fig. 55 Dependence of the FWHM of the (0006) reflections of the  $V_2O_3$  films on the substrate temperature.

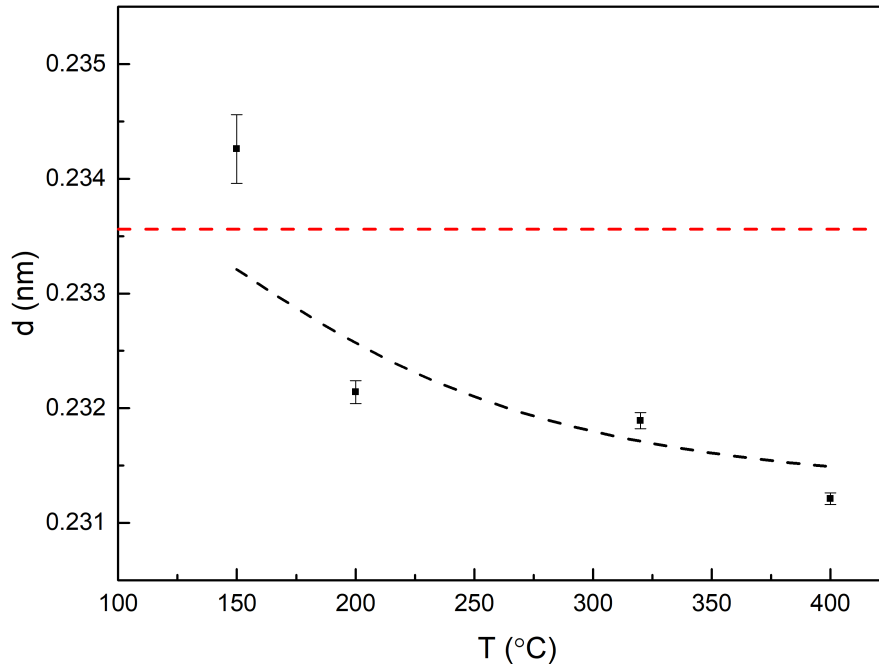


Fig. 56 Dependence of the lattice distance  $d_{0006}$  values of the  $V_2O_3$  films on the substrate temperature. The dashed line shows the theoretical  $d_{0006}$  value of  $V_2O_3$  according to PDF card No. 34-187 from the ICDD-database.

Fig. 57 shows the mosaic spreading of the (0006) reflections of the  $V_2O_3$  films deposited at 150 °C, 200 °C, 320 °C, 400 °C to evaluate the epitaxial quality of the films with respect to the substrates. With increasing substrate temperature, the mosaic spreading of the films gets narrower and shows higher intensity, indicating higher quality of the epitaxial growth of the films. Further, the dependence of the FWHM values of the rocking curves on the substrate temperature is shown in Fig. 58. The FWHM values of these mosaic spreading reflections decrease from 9.49° to 0.75° with increasing the substrate temperature from 150 °C to 400 °C. The  $V_2O_3$  films deposited at 150 °C and 200 °C possess poor epitaxial quality, in which many individual crystals have a strong tilt of the (0006) planes with respect to the (0006) planes of the substrate. While individual crystals with a slight tilt ( $< 1^\circ$ ) in the  $V_2O_3$  films deposited at a substrate temperature higher than 320 °C show better epitaxial quality.

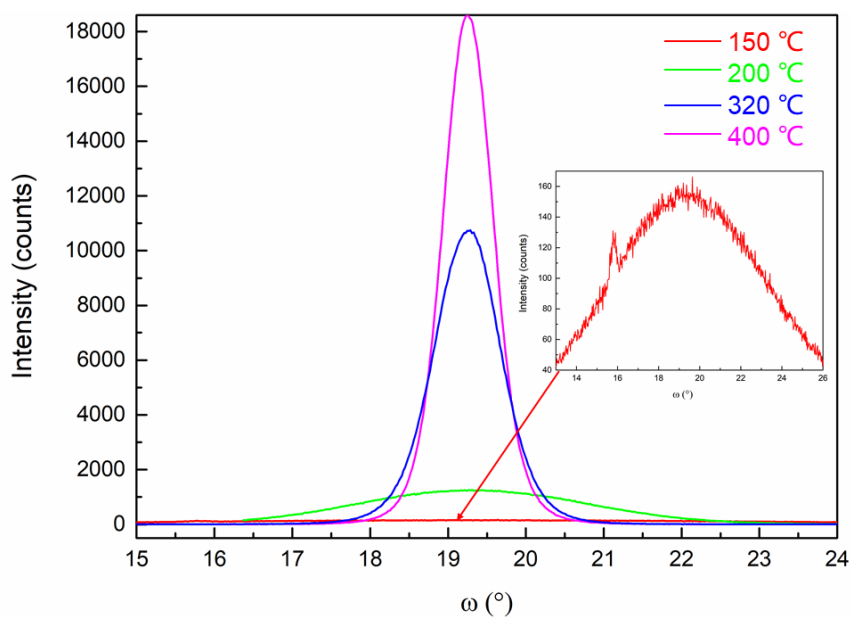


Fig. 57 XRD rocking curves ( $\omega$ -scans) of the (0006) reflections of the  $V_2O_3$  films deposited at 150 °C, 200 °C, 320 °C, 400 °C. The insert shows the enlargement of the mosaic spreading of the film deposited at 150 °C.

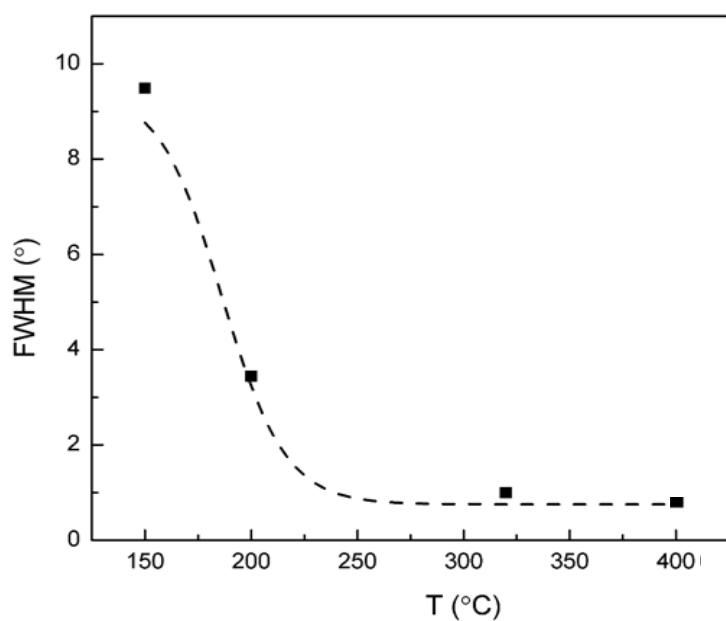


Fig. 58 The FWHM values of the mosaic spreading of (0006) reflections in Fig. 57 (9.49°, 3.44°, 0.99°, and 0.75° for films grown at 150 °C, 200 °C, 320 °C, and 400 °C, respectively).

XRD pole figures were recorded for the  $V_2O_3$  films deposited on the  $\alpha$ - $Al_2O_3$  substrates at different temperatures. Fig. 59 gives an example of the pole figures taken from the

(0006) reflection and the  $(10\bar{1}10)$  reflection of the  $V_2O_3$  film grown at 150 °C and 400 °C. Both films grow with a strong texture. A strong fiber texture appears in the films according to the (0006) reflections. 6-fold symmetry from the  $(10\bar{1}10)$  reflection at  $\psi = 18^\circ$  indicates the existence of stacking faults in the films. These are independent of the substrate temperature.

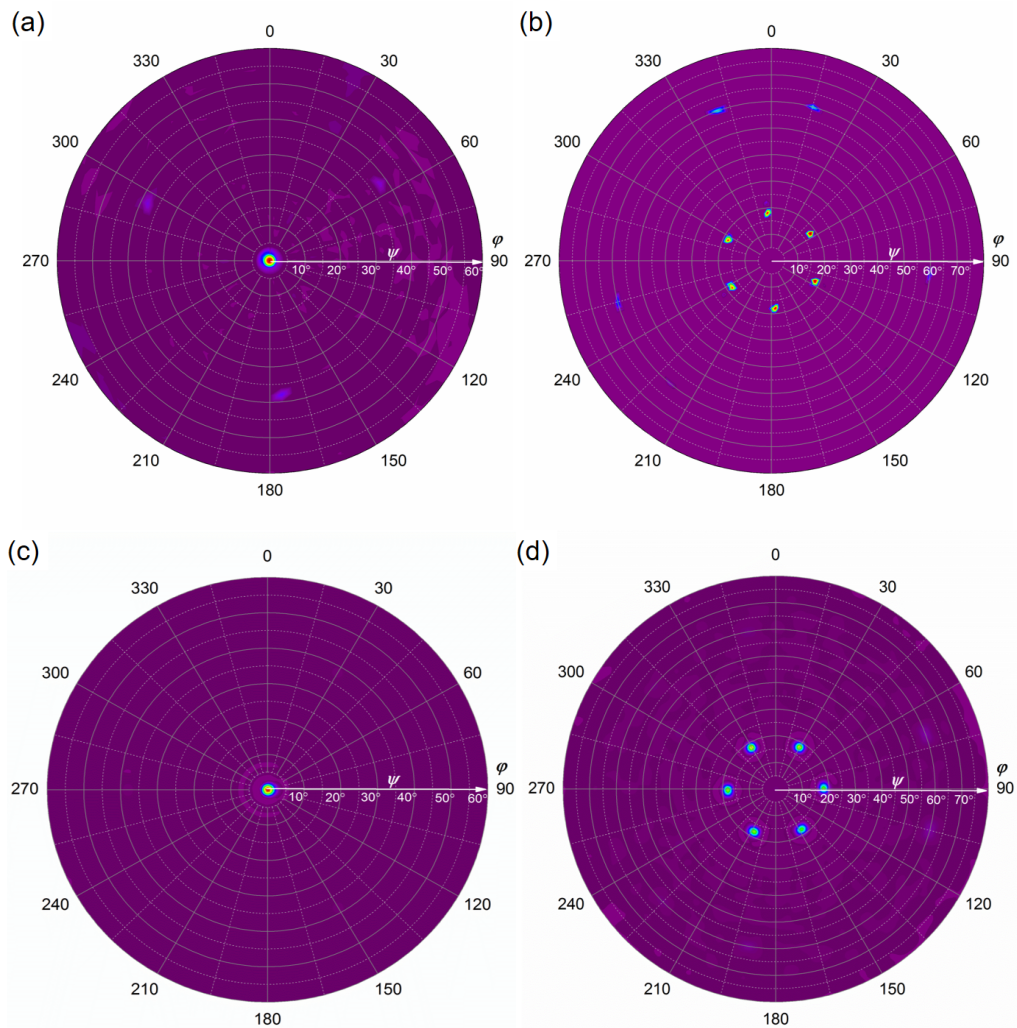


Fig. 59 X-ray pole figures taken from the reflections of the  $V_2O_3$  film grown at (a) (b) 150 °C and (c) (d) 400 °C on the  $\alpha$ - $Al_2O_3$  (0001) substrate which was plasma-etched before deposition. (a) and (c) are taken from the (0006) reflections, and (b) and (d) are taken from the  $(10\bar{1}10)$  reflections.

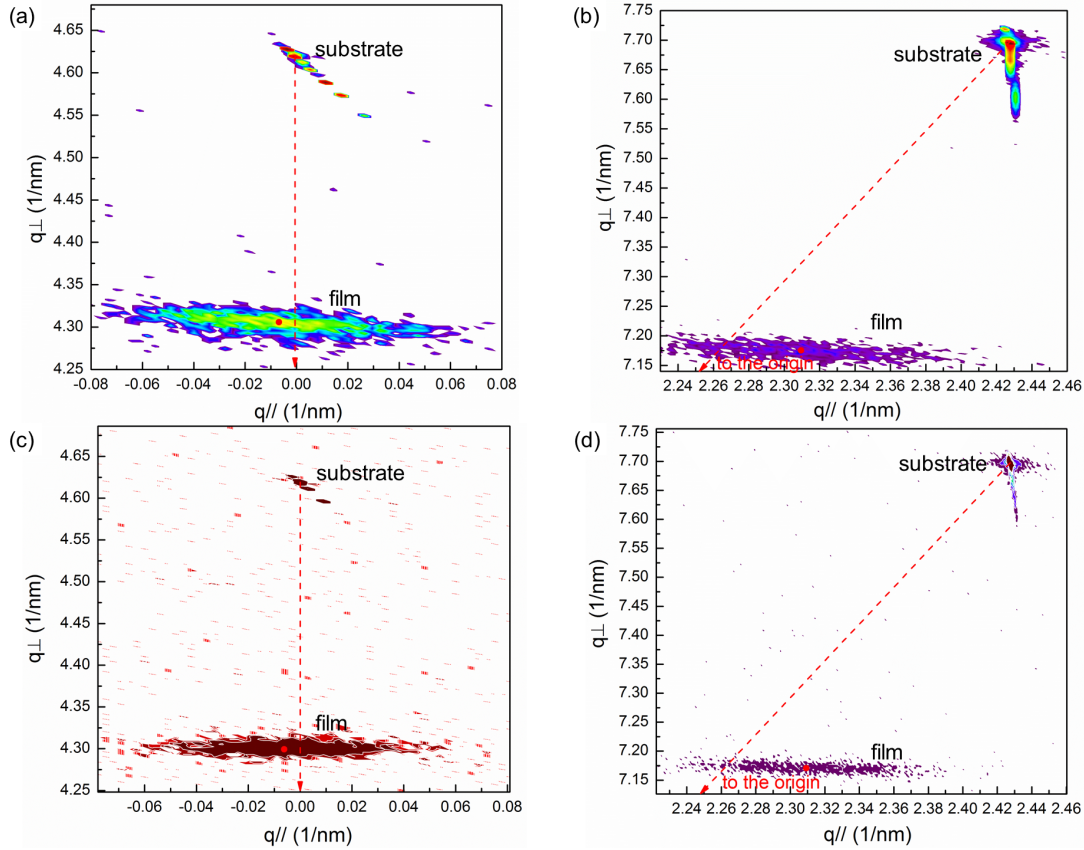


Fig. 60 RSM results of  $V_2O_5$  films grown at 320 °C and 400 °C. (a) is the symmetric (0006) reflection of the  $\alpha$ - $Al_2O_3$  substrate upon which the  $V_2O_5$  film is grown at 320 °C; (b) is the asymmetric (10 $\bar{1}$ 10) reflection of the  $\alpha$ - $Al_2O_3$  substrate upon which the  $V_2O_5$  film is grown at 320 °C; (c) is the symmetric (0006) reflection of the  $\alpha$ - $Al_2O_3$  substrate upon which the  $V_2O_5$  film is grown at 400 °C; (d) is the asymmetric (10 $\bar{1}$ 10) reflection of the  $\alpha$ - $Al_2O_3$  substrate upon which the  $V_2O_5$  film is grown at 400 °C.

In order to investigate the epitaxial quality of the films with respect to the substrates, RSM measurements were carried out. There is no information about the films from RSM when the films are grown at low temperature ( $\leq 200$  °C) due to the very low intensity of the films. Therefore, only results of RSM of the  $V_2O_5$  thin films deposited at 320 °C and 400 °C are shown in Fig. 60. The lines of the (0006) reflections of the films and the substrates are nearly perpendicular to the abscissa at  $q_{//} = 0$  in Fig. 60 (a) and (c), which indicates the crystals in these films have almost no tilt. The width of both the (0006) and (10 $\bar{1}$ 10) reflections of the films grown at 320 °C are larger than those of the films grown at 400 °C, suggesting the crystalline (epitaxial) quality of the films is higher with higher

substrate temperature. The values of the  $q_{//}$  of the center of the  $(10\bar{1}10)$  reflections of the films grown at 320 °C and 400 °C are 2.315 1/nm and 2.306 1/nm, respectively. The  $(10\bar{1}10)$  reflection of the film deposited at 400 °C shifts to the substrate compared to the film grown at 320 °C, which indicates again better epitaxial quality of the film deposited at higher temperature.

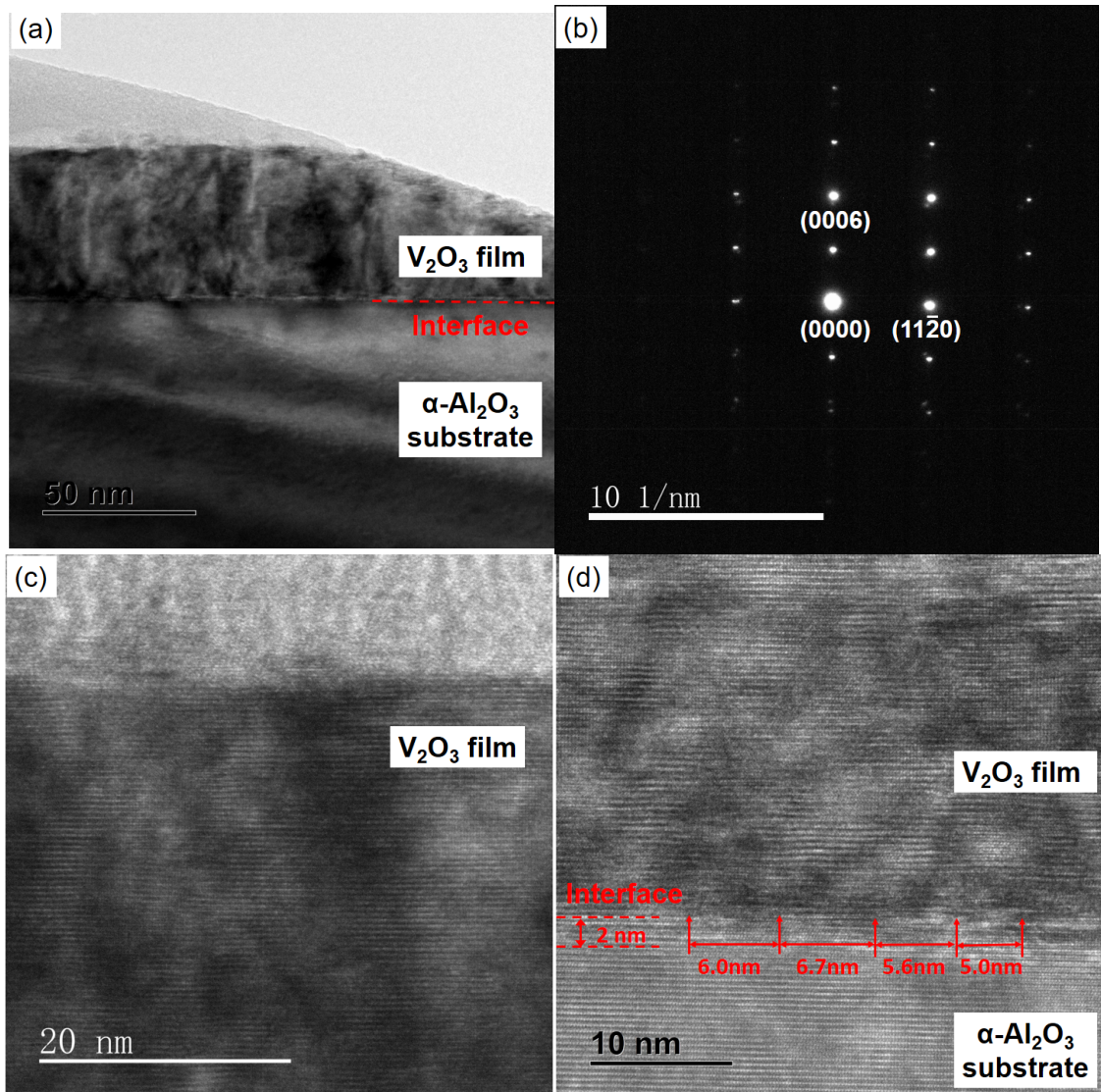


Fig. 61 TEM results of a  $V_2O_3$  film with thickness of 50 nm grown on  $\alpha\text{-Al}_2\text{O}_3$  substrate after plasma-etching before deposition at 400 °C. (a) BF image showing a cross sectional view, (b) the SAED pattern revealing a partially epitaxial orientation relationship between the film and the substrate, (c) a high resolution TEM (HRTEM) image of the film and, (d) a high resolution TEM image of the interface between the film and the substrate.

Further more, the microstructure of the films grown at 400 °C and their oriental relationship to the substrate was characterized by TEM analyses as shown in Fig. 61. The 50 nm thick  $V_2O_3$  film exhibits a relatively flat surface as is shown in the cross-sectional BF image (Fig. 61 (a)). Fig. 61 (b) shows SAED patterns that are dominated by both the film and the substrate, which indicates the epitaxial relationship between the film and the substrate as  $(11\bar{2}0) Al_2O_3 // (11\bar{2}0) V_2O_3$  and  $(0001) Al_2O_3 // (0001) V_2O_3$ . Reflections of the  $(0003)$  lattice planes are also observed; this is due to the double diffraction effect as discussed already in the case of the  $Cr_2O_3$  films in the previous section [52]. Fig. 61 (c) and (d) show the high resolution TEM images of the film and the interface between the film and the substrate. There are no obvious crystal boundaries, which reveals a layer by layer growth mode of the film. The misfit dislocations along the interface are shown in Fig. 61 (d), and the average spacing between dislocations is about  $5.8 \text{ nm} \pm 0.71 \text{ nm}$ , which indicates that the dislocation occur in every 24 lattice planes. A disordered area on the substrate with the depth of about 2 nm is created by the plasma-etching process before the coating.

#### 4.2.2 Raman spectroscopy analysis

In order to get more insight into the microstructure and characterize the chemical bonds in the films, Raman spectroscopy measurements were done. Fig. 62 shows the Raman spectra of the films (with 300 nm thickness) grown on  $\alpha$ - $Al_2O_3$  substrates at different temperatures. The referenced Raman active modes of the pure  $V_2O_3$  cited from ref. [247-250] are also shown in Fig. 62. There are no features attributable to the substrates in these Raman spectra. All signals observed can be attributed to the  $V_2O_3$  films. Two vibrational bands with high intensity are discussed: one is the band near  $210 \text{ cm}^{-1}$  which can be considered as superposition of  $E_g$  and  $A_{1g}$  modes of  $V_2O_3$  crystals, and the other is located close to the second  $A_{1g}$  mode near  $500 \text{ cm}^{-1}$ . These bands have higher intensity and smaller width for films grown at higher substrate temperature, supporting the conclusion that the films deposited at higher temperature have better crystalline quality. This is in agreement with the XRD results. The main band positions are defined by fitting the Raman spectra and the results are shown in Table 12. Fig. 63 shows the dependence of the  $E_g$  mode position on the substrate temperature as well as the films lattice

parameter. The  $E_g$  modes shift to the larger wavenumbers with increasing substrate temperature (i.e. decreasing (000 $l$ ) lattice plane distance). The  $E_g$  mode corresponds to the vibration of V and O atoms as shown in the insert of Fig. 63 [227]. The atom vibration frequency changes with the lattice parameters (the distance between the atoms).

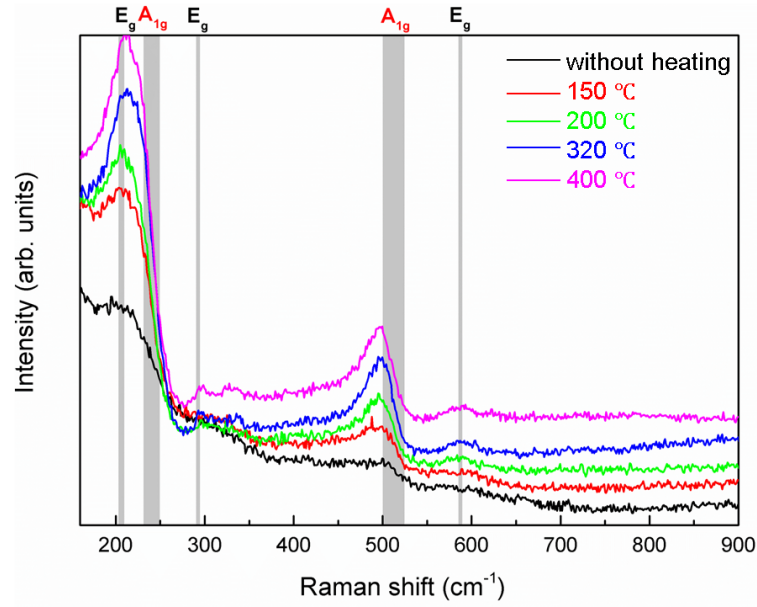


Fig. 62 Raman spectra of the  $V_2O_3$  films grown on  $\alpha$ - $Al_2O_3$  substrates at different temperatures. The gray areas refer to the Raman active modes of pure  $V_2O_3$  according to ref. [247–249,251].

Table 12 The wavenumber positions of the Raman active modes of the  $V_2O_3$  films deposited at different temperatures and the reference value of bulk  $V_2O_3$  cited from ref. [247,249].

	Substrate temperature	$E_g$ mode position (cm <sup>-1</sup> )
PRESENT WORK	150 °C	193
	200 °C	195
	320 °C	214
	400 °C	219
	REFERENCE [247,249]	203 - 210

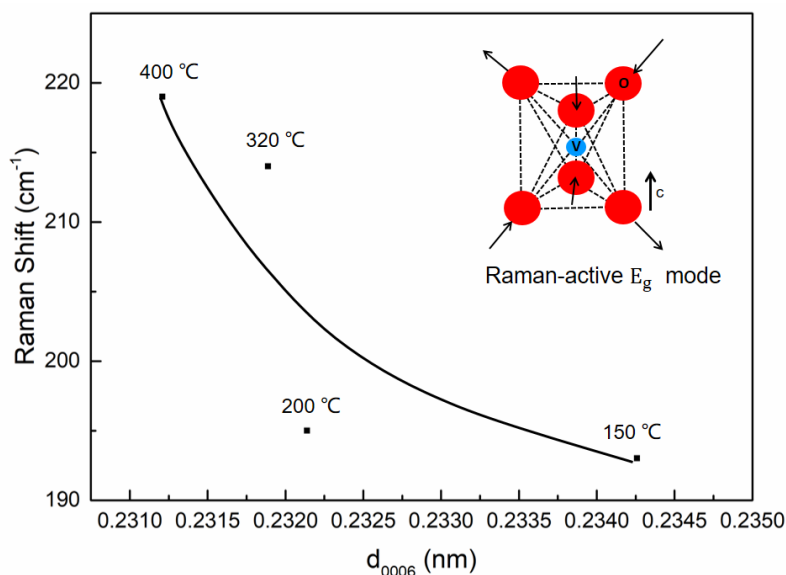


Fig. 63 Correlation of the Raman shift of the  $E_g$  mode of the  $V_2O_3$  films grown at different substrate temperatures with the corresponding lattice plane distance  $d_{0006}$  obtained from  $\theta - 2\theta$  XRD measurements. The curve is fitted by an exponential function. The inset schematically represents the  $E_g$  vibrational mode of  $V_2O_3$  [227].

### 4.2.3 Optical properties characterization

The outcome of the UV-VIS-NIR spectroscopy measurements of the  $V_2O_3$  films is simple: The optical absorbance is almost independent of the growth temperature of the films. Fig. 64 shows the UV-VIS-NIR spectroscopy data of a  $V_2O_3$  film with thickness of 300 nm, deposited at 150 °C and 400 °C, in the range from 200 nm to 1200 nm. The offset at 720 nm is caused by the filter change of the spectrograph. High absorbance in the visible light region can be explained by the dark color of the films (their appearance was nearly black). Absorption bands are present at 373 nm, 444 nm, 605 nm and 661 nm. These absorption bands are superimposed by a continuous absorption which increases from the UV region to the VIS region. The absorbance decreases in the range of 200 nm - 340 nm and 560 nm - 1200 nm and increases in the range of 340 nm - 560 nm with increasing the crystal quality of the films. Since  $V_2O_3$  exhibits a metal to insulator transition (MIT) at 160 K [142] and all the optical measurements are carried out at room temperature, the  $V_2O_3$  films show metallic properties. Fig. 65 shows plots of  $(ah\nu)^2$  vs.  $h\nu$  for the  $V_2O_3$  films. From these the band gaps of  $V_2O_3$  films grown at 400 °C and 150 °C

are derived: these are 1.92 eV and 1.84 eV, respectively. This is in very good agreement with data from ref. [184,250].

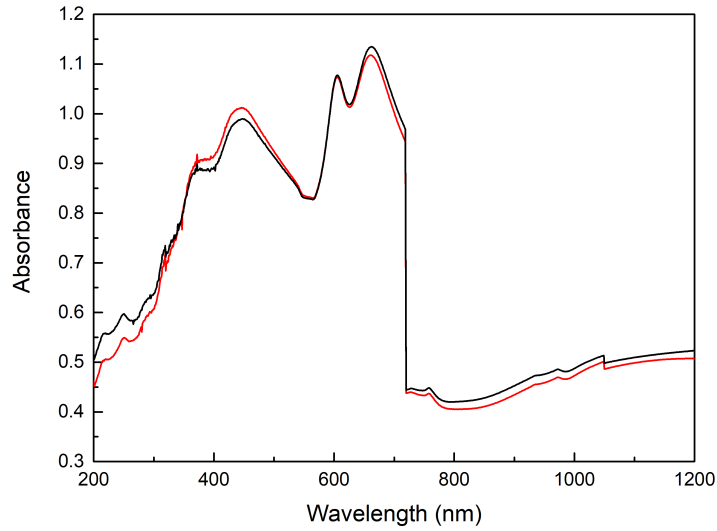


Fig. 64 UV-VIS-NIR spectroscopy data from 200 nm to 1200 nm of a  $V_2O_3$  film deposited at 150 °C (black curve) and 400 °C (red curve).

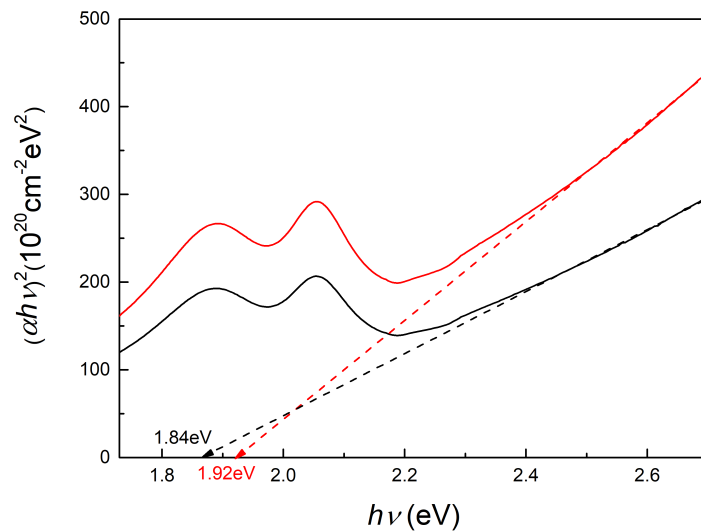


Fig. 65 Plots of  $(\alpha h\nu)^2$  vs.  $h\nu$  for the  $V_2O_3$  films grown at 150 °C (black curve) and 400 °C (red curve).

#### 4.2.4 Influence of the plasma-etching process on the crystal growth

The  $V_2O_3$  films with a thickness of 60 nm were deposited on the  $c$ -plane  $\alpha$ - $Al_2O_3$  substrates at 400 °C with and without plasma-etching process before deposition. Fig. 66 shows the  $\theta - 2\theta$  XRD results, in which the red curve shows the reflections from the  $V_2O_3$

film grown on the  $\alpha$ -Al<sub>2</sub>O<sub>3</sub> substrate which was plasma-etched for the depth of 50 nm before deposition, and the black curve shows the reflections from the V<sub>2</sub>O<sub>3</sub> film grown on the  $\alpha$ -Al<sub>2</sub>O<sub>3</sub> substrate without plasma-etching process. Only (0006) and (00012) reflections of the films and the substrates were observed in the XRD Bragg-Brentano geometry. Compared to the theoretical positions of V<sub>2</sub>O<sub>3</sub>, all of these reflections of the films shift towards to the larger diffraction angle side, because both of these two films are epitaxially grown on the Al<sub>2</sub>O<sub>3</sub> substrates. The  $2\theta$  value of the film with plasma-etching is very close to that of the film without plasma-etching, indicating that the lattice constant  $c$  (or  $d_{0006}$ ) has not been effected by the plasma-etching process on the substrate. The FWHM of the (0006) reflections of the film grown on the substrate without plasma-etching process is  $0.19^\circ$ , which is smaller than that of the film grown after plasma-etching ( $0.22^\circ$ ). This is similar to the results of the Cr<sub>2</sub>O<sub>3</sub> films presented in section 4.1.4. The film grown without plasma-etching before deposition possesses a larger grain size and better crystal quality in comparison with that grown after plasma-etching.

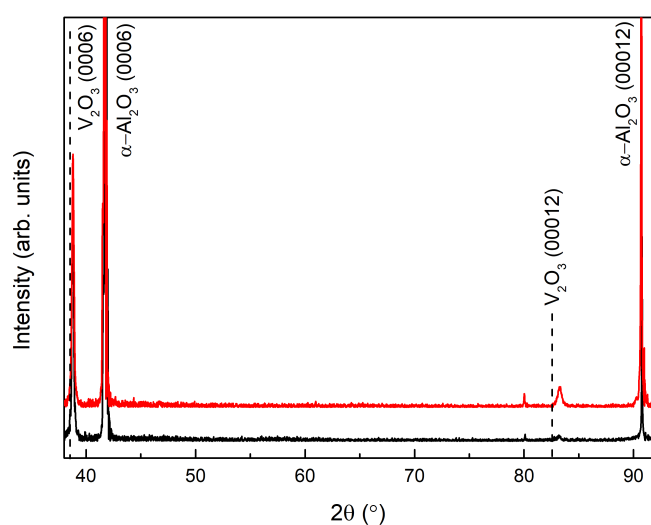


Fig. 66  $\theta - 2\theta$  XRD patterns of the V<sub>2</sub>O<sub>3</sub> films with 60 nm thickness grown on the  $c$ -plane  $\alpha$ -Al<sub>2</sub>O<sub>3</sub> substrates at 400 °C. The black curve corresponds to the film grown without plasma-etching process before deposition. The red curve corresponds to the film grown after plasma-etching for 50 nm before deposition. The dashed lines indicate the theoretical positions of the (0006) and (00012) reflections of V<sub>2</sub>O<sub>3</sub> according to the PDF card No. 34-187 from the ICDD-database.

Fig. 67 shows the mosaic spreading of the (0006) reflections of these two films. The FWHM of these reflections of the films grown on the substrates without and after plasma-etching process before deposition are  $0.36^\circ$  and  $1.01^\circ$ , respectively, indicating the film grown without plasma-etching process before deposition presents better epitaxial quality. The plasma-etching process may partially destroy the perfect surface of the single crystal substrate, which will influence the nucleation and coalescence and further will influence the film growth.

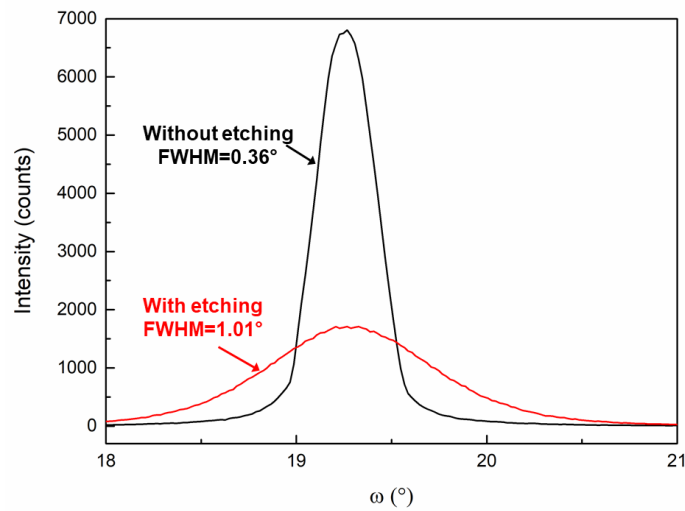


Fig. 67 XRD rocking curves ( $\omega$ -scans) of the (0006) reflections of the  $V_2O_3$  films with a thickness of 60 nm grown on the  $c$ -plane  $\alpha$ - $Al_2O_3$  substrates at  $400^\circ C$ . The black curve corresponds to the film grown without plasma-etching process before deposition. The red curve corresponds to the film grown after plasma-etching for 50 nm before deposition.

The texture of films grown on the substrates without plasma-etching process before deposition has been examined by X-ray pole figures taken from both symmetric (0006) reflections and asymmetric  $(10\bar{1}10)$  reflections. These pole figure analyses are shown in Fig. 68. In comparison to the texture of a film grown on the substrate after plasma-etching process (as shown in Fig. 59), both films show a fiber texture grown along the  $c$ -axis, which indicates the fiber texture is independent of the substrate surface. The X-ray pole figures taken from the  $(10\bar{1}10)$  peak of the film grown without plasma-etching process shows 3-fold symmetry reflections in the circle of  $\psi=18^\circ$  as  $c$ -plane  $\alpha$ - $Al_2O_3$  substrates in Fig. 68. There are two different in-plane  $(10\bar{1}10)$  orientations rotated by  $60^\circ$  domain

variants in the film grown on the substrate after plasma-etching which is caused by stacking faults (which was shown in Fig. 59). The plasma-etching of the substrates could lead to the disturbed substrate surface, which could lead to stacking faults in further.

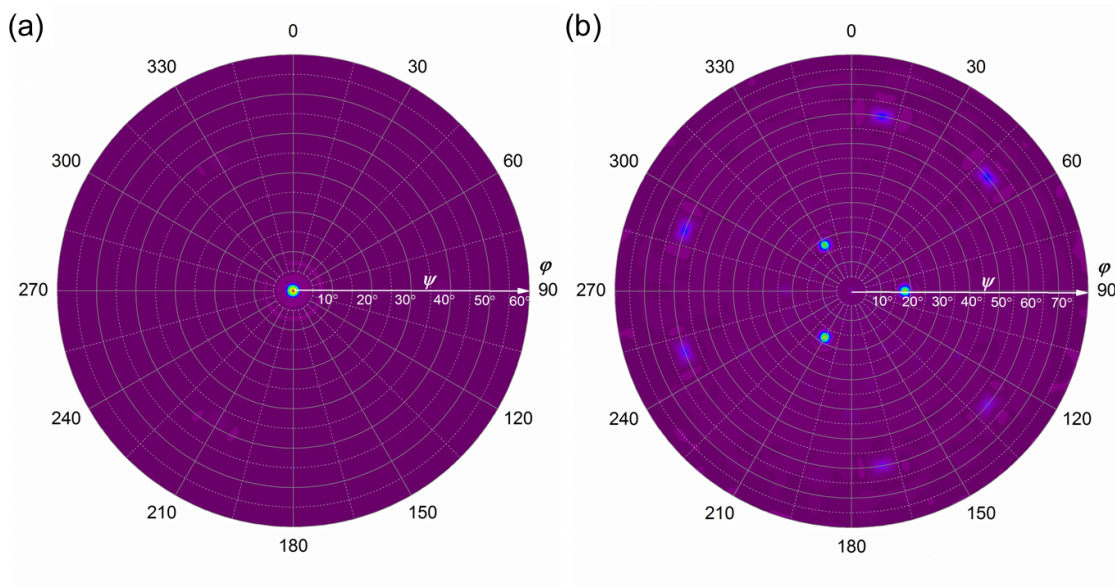


Fig. 68 X-ray pole figures taken from (a) the (0006) reflections and (b) the (10 $\bar{1}$ 10) reflections of a V<sub>2</sub>O<sub>5</sub> film with a thickness of 60 nm grown on an  $\alpha$ -Al<sub>2</sub>O<sub>3</sub> (0001) substrate without plasma-etching before deposition at 400 °C.

Fig. 69 shows the results of reciprocal space mapping of the symmetric (0006) reflections (see Fig. 63 (a), and (c)) and of the asymmetric (10 $\bar{1}$ 10) reflections (see Fig. 63 (b), and (d)) of the V<sub>2</sub>O<sub>5</sub> thin films with a thickness of 60 nm grown on the  $\alpha$ -Al<sub>2</sub>O<sub>3</sub> substrates at 400 °C. Fig. 69 (a) and (b) show the reflections of a film on a substrate without plasma-etching process before deposition, and Fig. 69 (c) and (d) show the reflections of a film on a substrate with plasma-etching process before deposition. The intensity of the RSM signals of the film grown without plasma-etching process is much higher than that of the film grown after plasma-etching. Besides, the horizontal width of both the (0006) and (10 $\bar{1}$ 10) reflections of the film grown without plasma-etching process is 0.019 1/nm and 0.057 1/nm, respectively. On the other side, the reflections of the film grown after plasma-etching process are too broad to define the center of the reflections of the film. Comparing the (0006) reflections of the films grown without and after plasma-etching, the crystals of the film grown after the plasma-etching process have larger tilt with respect to the

substrate. The lattice parameters of the film grown after the plasma-etching process are  $a = 0.5007$  nm and  $c = 1.3947$  nm, while the lattice parameters of the film grown without plasma-etching process are  $a = 0.4962$  nm and  $c = 1.3968$  nm. The misfit of the in-plane interface between the film and the substrate with and without plasma-etching process before deposition are 5.2 % and 4.3 %, respectively. These results indicate that the epitaxial quality of the film grown on the substrate without plasma-etching is better than that of a film grown after plasma-etching.

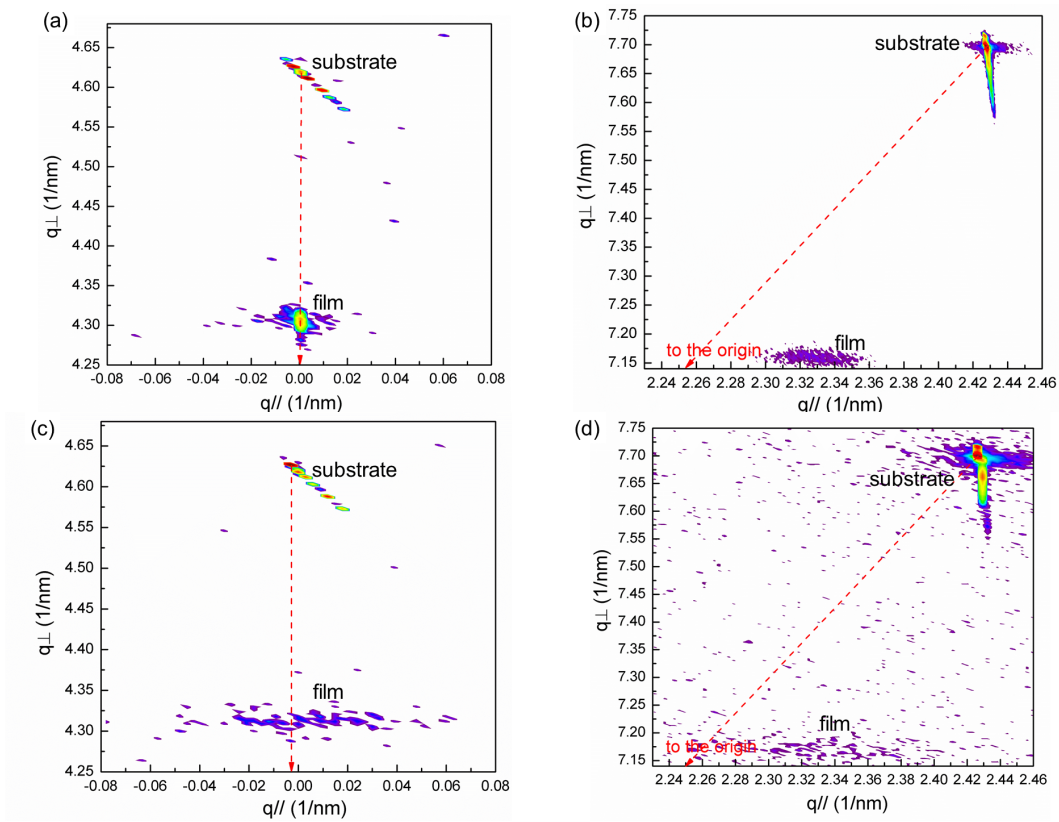


Fig. 69 RSM results of the  $V_2O_3$  films (60 nm thickness) grown on the  $\alpha-Al_2O_3$  substrates at 400 °C. (a) is the symmetric (0006) reflection of the substrates without plasma-etching before deposition; (b) is the asymmetric (10 $\bar{1}$ 10) reflection of the substrates without plasma-etching before deposition; (c) is the symmetric (0006) reflection of the substrates after plasma-etching of 50 nm depth before deposition; (d) is the asymmetric (10 $\bar{1}$ 10) reflection of the substrates after plasma-etching of 50 nm depth before deposition.

The Raman spectra of these two types of  $V_2O_3$  films (with 60 nm thickness) are shown in Fig. 70. Compared to the Raman spectra of the  $V_2O_3$  films (with 300 nm thickness) discussed in section 4.2.2, additional features from the substrates appear because of the very thin films. But again, Raman signals attributable to the  $V_2O_3$  films can be clearly observed. There are two vibrational bands with high intensity from these two films: one is the band near  $210\text{ cm}^{-1}$  which can be considered as superposition of  $E_g$  and  $A_{1g}$  modes of  $V_2O_3$  crystals, and the other is located close to the second  $A_{1g}$  mode near  $500\text{ cm}^{-1}$ . These Raman active bands originating from these two films are listed in Table 13. Compared to the film grown without etching, both the first  $E_g$  and  $A_{1g}$  bands of the film grown after plasma-etching shift slightly to the smaller frequency side, which can be related with the variation of the lattice parameters of both films. The FWHM of these two bands of the film grown without plasma-etching process before deposition is smaller than that of the film grown after plasma-etching process, indicating that the crystal quality of the film grown without plasma-etching process is better. These conclusions are in good agreement with other results for the  $V_2O_3$  films and is similar to the results of  $Cr_2O_3$  films in section 4.1.4.

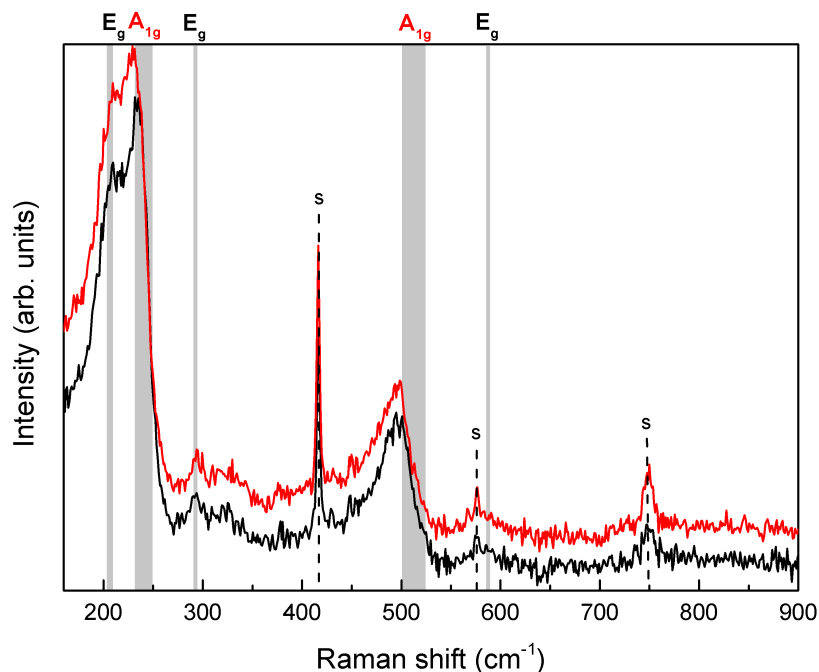


Fig. 70 Raman spectra of the  $V_2O_3$  films (60 nm thick) grown on  $\alpha\text{-Al}_2\text{O}_3$  substrates without (black curve) and after (red curve) plasma-etching. The areas marked in gray refer to the Raman active modes of pure  $V_2O_3$  according to refs. [247–249,251]. “s” indicates the Raman signals attributed to the substrates.

Table 13 The Raman shift and FWHM of the bands attributed to the  $V_2O_3$  films grown on  $\alpha$ - $Al_2O_3$  substrates without and after plasma-etching (The data are after fitting by Gaussian;  $E_g^1$  indicates the first  $E_g$  mode and  $A_{1g}^1$  indicates the first  $A_{1g}$  mode in the range of  $200\text{ cm}^{-1}$  -  $250\text{ cm}^{-1}$  in Fig. 70).

	$E_g^1$		$A_{1g}^1$	
	Raman shift ( $\text{cm}^{-1}$ )	FWHM ( $^\circ$ )	Raman shift ( $\text{cm}^{-1}$ )	FWHM ( $^\circ$ )
Without etching	208.7	58.9	236.1	18.8
After etching	198.2	61.2	229.3	31.2

The microstructure and the epitaxial relationship between these two types of films and the substrates were characterized by TEM analyses. Fig. 71 (a) and (b) show the SAED patterns of the  $V_2O_3$  films grown on the  $c$ -plane  $\alpha$ - $Al_2O_3$  substrates without and after plasma-etching process before deposition. These reveal the relationship between the films and the substrates, which in both cases can be described as  $(0001) Al_2O_3 // (0001) V_2O_3$  and  $(11\bar{2}0) Al_2O_3 // (11\bar{2}0) V_2O_3$ . Fig. 71 (c) shows a HRTEM image of the fracture cross section of a  $V_2O_3$  film grown on the substrate without plasma-etching process before deposition. The  $(0006)$  and  $(11\bar{2}0)$  lattice plane distances of this film near the film-substrate interface are  $d_{0006} = 0.232\text{ nm}$  and  $d_{11\bar{2}0} = 0.240\text{ nm}$ , which is in agreement with the values given in the PDF card No. 34-187 from the ICDD-database ( $0.234\text{ nm}$  and  $0.248\text{ nm}$ , respectively). Fig. 71 (d) shows a HRTEM image of the fracture cross section of a  $V_2O_3$  film grown on the substrate after plasma-etching before deposition. A disordered area with a depth of about  $2\text{ nm}$  in the substrate surface near the interface to the film can be observed. This distorted area is the result of the ion bombardment of the substrate during the plasma-etching. The lattice plane distances of the film near the interface to the substrate are  $d_{0006} = 0.228\text{ nm}$  and  $d_{11\bar{2}0} = 0.242\text{ nm}$ . The lattice parameter  $d_{0006}$  (or  $c$ ) of the film grown directly on the substrate (without etching) before deposition is clearly larger than that of the film grown indirectly on the substrate (after plasma-etching), which is in agreement with the results derived from XRD analyses. The degree of in-plane relaxation  $r$  of the film grown without and after plasma-etching with respect to the substrate is  $20.8\%$  and  $40.6\%$ , respectively, which is calculated by Eq. (11). The epitaxial quality of

the film grown after plasma-etching process is worse, which is again in agreement with the results of XRD. This is related with the plasma-etching process on the substrate which destroys the perfect crystalline ordering which will have negative impact on the epitaxial growth of the films.

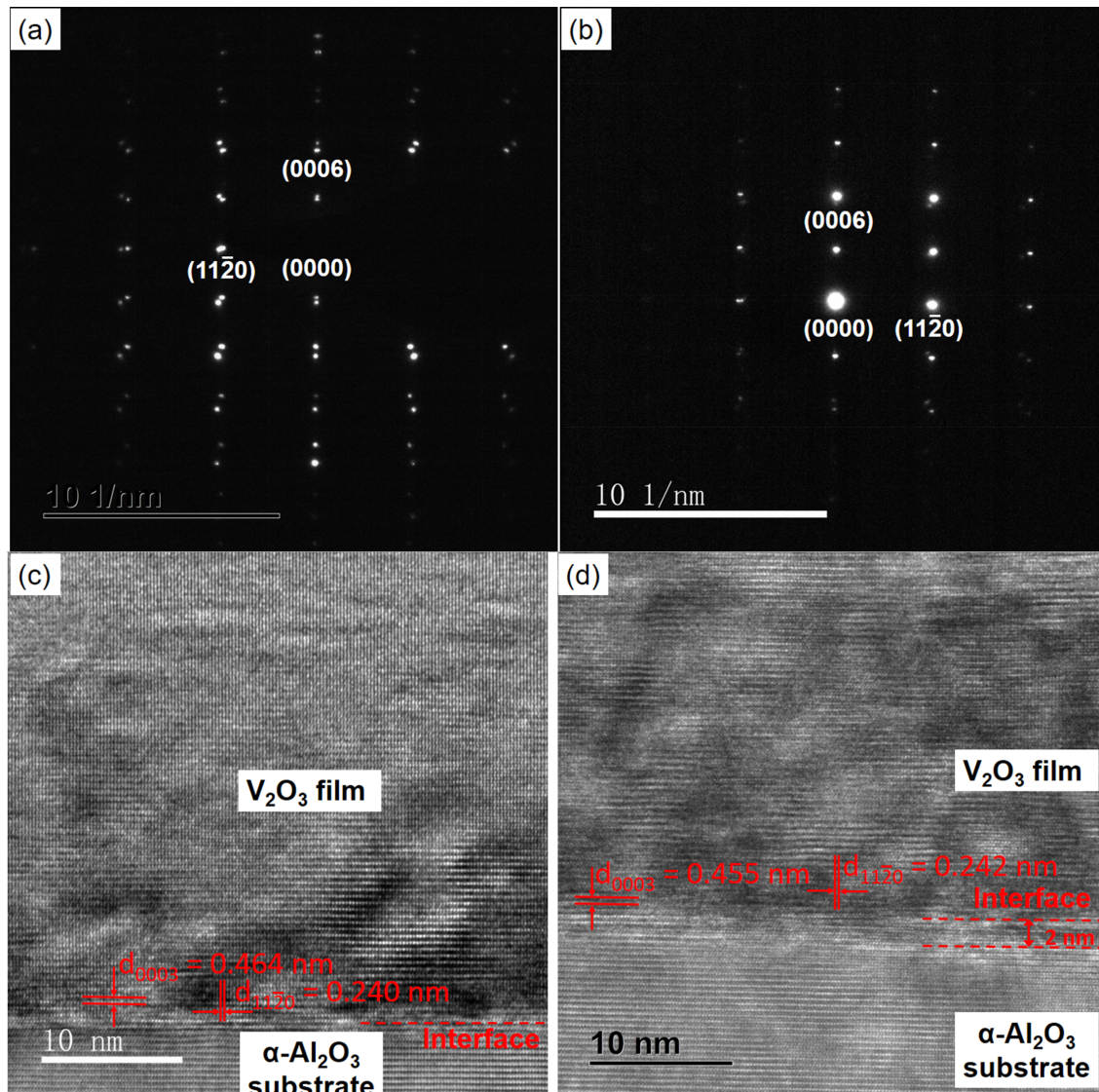


Fig. 71 TEM analysis of the  $V_2O_3$  films with thickness of 60 nm grown on the  $c$ -plane  $\alpha$ - $Al_2O_3$  substrates. (a) and (c): the film grown on the  $\alpha$ - $Al_2O_3$  substrate without plasma-etching process before deposition. (b) and (d): the film grown on the  $\alpha$ - $Al_2O_3$  substrate which was plasma-etched for 50 nm before deposition. (a) and (b): the SAED patterns showing the epitaxial relationship between the films and the substrates. (c) and (d): HRTEM images of cross sections of these samples.

### 4.3 $\alpha$ -(Cr<sub>1-x</sub>Al<sub>x</sub>)<sub>2</sub>O<sub>3</sub> solid solution thin films grown on *c*-plane $\alpha$ -Al<sub>2</sub>O<sub>3</sub> substrates

In this chapter, the microstructure and optical properties of the Cr-Al-O films (Cr-rich) with various Al concentration deposited on the substrates with plasma-etching process are described and discussed. The Cr-Al-O ternary system has been introduced in section 2.5. It is difficult to grow Al<sub>2</sub>O<sub>3</sub> or Al-rich Cr-Al-O films at low temperature. This is why Cr-rich Cr-Al-O system are discussed in this chapter. These films were grown on *c*-plane (0001)  $\alpha$ -Al<sub>2</sub>O<sub>3</sub> substrates by using a segmented ceramic target (one half plate is a mixture of Cr<sub>2</sub>O<sub>3</sub> (80 at. %) and Al<sub>2</sub>O<sub>3</sub> (20 at. %), and the other half plate is made of pure Cr<sub>2</sub>O<sub>3</sub>, see in section 3.1.2.2) at different temperatures (without heating, 320 °C and 400 °C). During film deposition the substrates were placed as shown in Fig. 17 (c). Films with a thickness of 1.5  $\mu$ m were deposited on the substrates without heating and at 400 °C. They were used for the EPMA analysis in section 4.3.1. Among these films prepared for EPMA, films deposited at 400 °C in the Pos. 2 are also characterized by AES. The  $\alpha$ -(Cr<sub>1-x</sub>Al<sub>x</sub>)<sub>2</sub>O<sub>3</sub> films with a thickness of 300 nm deposited at different temperatures on the substrates for various XRD analysis methods (section 4.3.2), Raman spectroscopy analyses (section 4.3.3), IRRAS (section 4.3.3) and UV-VIS-NIR analyses (section 4.3.4). Among these films, the ones deposited at 400 °C were analyzed by TEM (section 4.3.2).

#### 4.3.1 Chemical composition

The chemical composition of the Cr-Al-O films deposited without heating and at 400 °C were measured by EPMA and the deviation of the atomic percentage of the elements in the films is less than 1 %. Therefore, only the results for the Cr-Al-O films deposited at 400 °C are displayed in Table 14. The oxygen concentration is constant for all films and it is very close to the theoretically expected value of 60 at. %, and the metal concentration in all films is very close to 40 at. %. So all the films exhibit the stoichiometry of 2:3 for the ratio of metal to oxygen, which is the characteristic of Me<sub>2</sub>O<sub>3</sub>. Very poor contaminations of N and C are observed and these are negligible for the further discussion. A gradient composition of the Al and Cr concentration in the films from Pos. 1 (Al-rich side of the target) to Pos. 5 (Cr-rich side of the target) in Fig. 15 (b) was observed and the composition dependent on the position where the substrates are placed during the deposition is shown in Fig. 72.

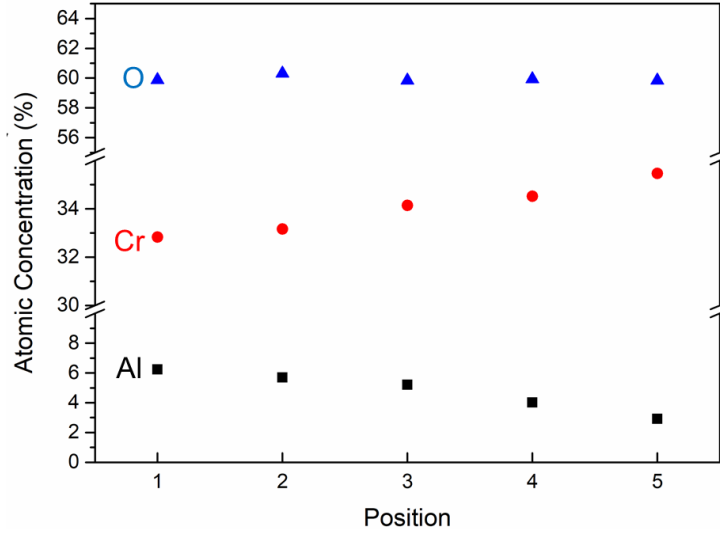


Fig. 72 The chemical composition of the Al-Cr-O films deposited on the substrates in different positions related to the target.

Table 14 The chemical composition of the Al-Cr-O films deposited on the substrates at 400 °C in different positions related to the target:  $x$  and  $\delta$  describe the Al concentration and the deviation from a perfect theoretical stoichiometry in  $(\text{Cr}_{1-x}\text{Al}_x)_{2+\delta}\text{O}_3$  respectively (standards used for calibrating see section 3.2.1).

Pos.	Al (at. %)	Cr (at. %)	O (at. %)	C (at. %)	N (at. %)	Ar (at. %)	$x$	$\delta$
1	6.2 ± 0.08	32.8 ± 0.28	59.9 ± 0.35	0.7 ± 0.12	0.4 ± 0.01	0.0	0.16	-0.05
2	5.7 ± 0.04	33.2 ± 0.34	60.3 ± 0.28	0.6 ± 0.22	0.2 ± 0.03	0.0	0.15	-0.08
3	5.2 ± 0.07	34.1 ± 0.38	59.9 ± 0.48	0.5 ± 0.13	0.3 ± 0.01	0.0	0.13	-0.02
4	4.0 ± 0.04	34.5 ± 0.12	59.9 ± 0.32	1.1 ± 0.18	0.5 ± 0.02	0.0	0.10	-0.08
5	2.9 ± 0.06	35.5 ± 0.58	59.9 ± 0.42	1.3 ± 0.39	0.4 ± 0.02	0.0	0.08	-0.08

We define the relative concentration of Al as  $x$ :

$$x = \frac{\omega(\text{Al})}{\omega(\text{Al}) + \omega(\text{Cr})} \quad (19)$$

And the deviation from the ideal metal to oxygen stoichiometry  $\delta$  is given by:

$$\delta = 3 \cdot \frac{\omega(\text{Al}) + \omega(\text{Cr})}{\omega(\text{O})} - 2 \quad (20)$$

where  $\omega(\text{Al})$  and  $\omega(\text{Cr})$  are the absolute concentrations atomic percentage of Al and Cr in the films measured by EPMA, respectively.

The Al-Cr-O film deposited in Pos. 1 exhibits the highest Al concentration of 6.2 at. % ( $x = 0.16$ ), while the film deposited in Pos. 5 exhibits the lowest Al concentration of 2.9 at. % ( $x = 0.08$ ). The contaminations of these ternary films are in the same order of magnitude as those reported for the  $\text{Cr}_2\text{O}_3$  films as described in section 4.1.1. The values of  $\delta$  vary from -0.08 to -0.02, which suggests the metal/oxygen stoichiometry of these films is very close to the ideal value of  $2/3$ . Therefore, the Al-Cr-O films in this study can be generally described by the structure formula  $(\text{Cr}_{1-x}\text{Al}_x)_2\text{O}_3$ , where the coefficient  $x$  is defined according to Eq. (19).

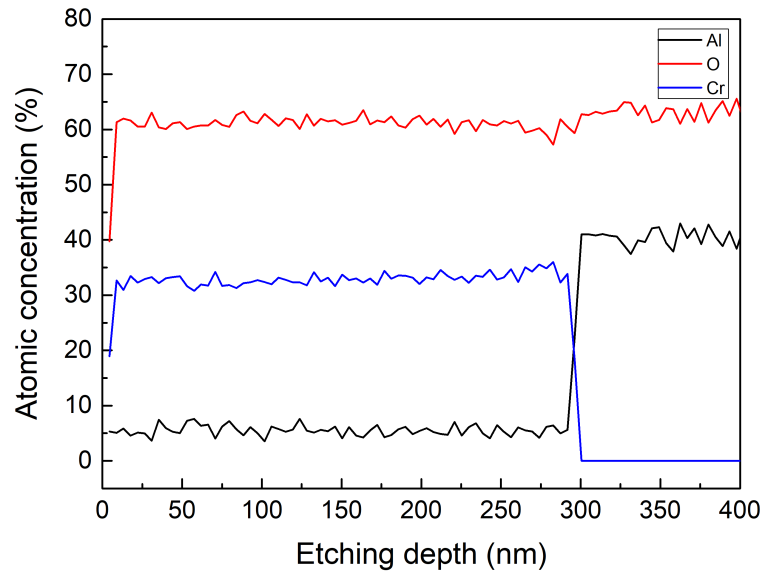


Fig. 73 AES depth profile of the Cr-Al-O film deposited on the  $\alpha\text{-Al}_2\text{O}_3$  substrate in Pos. 2 according to Fig. 15 (b).

The films exhibit a nearly ideal stoichiometric composition of a corundum phase, which is also confirmed by AES measurements. Fig. 73 shows representatively the AES depth profile of the Al-Cr-O film deposited on the  $\alpha\text{-Al}_2\text{O}_3$  substrate in Pos. 2. The AES depth profile of Al, Cr and O elements implies that the content of each element keeps constant over the cross-section of the film. The atomic concentrations of Al, Cr, and O in the film

are  $5.5 \% \pm 0.97 \%$ ,  $32.9 \% \pm 0.95 \%$ , and  $61.3 \% \pm 0.90 \%$ , respectively, which are similar to the values measured by EPMA. The (Al+Cr)/O stoichiometry is also near 2/3.

### 4.3.2 Structural analysis

XRD analysis in Bragg-Brentano mode was used to determine the phase composition and the crystallographic lattice constant  $c$  of the Cr-Al-O films deposited with different Al concentration at different temperatures. Fig. 74 shows  $\theta - 2\theta$  XRD patterns of the films with different composition deposited on the  $\alpha$ -Al<sub>2</sub>O<sub>3</sub> substrates at different temperatures. The films deposited without heating show no reflections, independent of the film composition, indicating that these films are amorphous. The films are however crystalline at a deposition temperature of 320 °C and 400 °C. The (0006) and (00012) reflections of the films are observed at the lower diffraction angle side of the corresponding reflections of the substrates. Very strong (0006) and (00012) reflections from the substrates and reflections with less intensity from the films for both temperatures are observed. No reflections other than (0006) and (00012) are present, suggesting that the films possess a single phase structure of corundum-type and a single out-of-plane orientation. Therefore, the films deposited at 320 °C and 400 °C are expressed by  $\alpha$ -(Cr<sub>1-x</sub>Al<sub>x</sub>)<sub>2</sub>O<sub>3</sub>. Intensities of the (00012) reflections are much weaker and broader compared to the (0006) reflections, so the (0006) reflections in more detail for a narrow range of the diffraction angle are discussed and shown in Fig. 74 (b). The diffraction patterns with the most intense and sharp peaks at the position of  $2\theta = 41.69^\circ$  correspond to the (0006) plane of the  $\alpha$ -Al<sub>2</sub>O<sub>3</sub> substrates, which fits well with the theoretical position ( $2\theta = 41.685^\circ$ ) of the (0006) reflection of  $\alpha$ -Al<sub>2</sub>O<sub>3</sub> according to the PDF card No. 42-1468 from the ICDD database. The (0006) reflections attributed to the films are observed next to the  $\alpha$ -Al<sub>2</sub>O<sub>3</sub> reflections of the substrates. The width of the (0006) reflections of the films is broader and the intensity is lower in comparison to the (0006) reflections of the substrate, because the substrates are single crystals while the films are nanocrystalline. We observed different intensity of the reflections, but the intensity is determined not only by the crystal quality but also by the perfection of the mounting of the sample during the XRD measurement. So we will discuss the relative intensity values (the ratio between the intensity of (0006) of the film and the corresponding (0006) of the substrate) instead of the absolute intensity values shown in Table 15.

Table 15 The intensity ratio of the (0006) reflection of the  $\alpha$ -(Cr<sub>1-x</sub>Al<sub>x</sub>)<sub>2</sub>O<sub>3</sub> film and the corresponding reflection of the substrate ( $I_{film(0006)} / I_{substrate(0006)}$ ).

Deposition temperature	$I_{film(0006)} / I_{substrate(0006)}$		
	x = 0.08	x = 0.13	x = 0.16
400 °C	0.075	0.160	0.040
320 °C	0.018	0.086	0.015

The films deposited at 400 °C have higher intensity compared to the films deposited at the lower temperature of 320 °C, which is independent of the film composition. This is due to the crystal quality of the films deposited at higher temperature is better. Furthermore, the relative intensity of the films with  $x = 0.13$  are the highest no matter if the film was deposited at 320 °C or 400 °C, which is induced by the different crystal tilting during the growth caused by the different deposition position of the samples below the target (the films with  $x = 0.13$  were positioned below the center of the two half targets, and the crystals almost have no tilt as observed in the TEM, which will be discussed later).

Following the model of a single phase solid solution of the Cr-Al-O films one can also derive the lattice constant  $c$  from the  $\theta - 2\theta$  XRD patterns. The theoretical position of the (0006) reflection of Cr<sub>2</sub>O<sub>3</sub> at  $2\theta = 39.749^\circ$  according to the PDF card No. 38-1479 from the ICDD-database is marked as vertical dashed line in Fig. 74. All the (0006) reflections of the films are observed at the larger Bragg angle side related to the theoretical Cr<sub>2</sub>O<sub>3</sub> position, which suggests a smaller value of the lattice plane distance  $d_{0006}$  of the films, i.e. a decreasing lattice constant  $c$  of the films in comparison to pure Cr<sub>2</sub>O<sub>3</sub>. The (0006) reflections of the films deposited at 400 °C shift stronger to the larger Bragg angles side than those of the films deposited at 320 °C, independent of the film composition. This indicates that the lattice plane distance  $d_{0006}$  (i.e. the lattice constant  $c$ ) is smaller when the films are deposited at higher temperature of 400 °C, independent of the Al concentration. There is a hint that the ordering in the structure increases with increasing deposition temperature.

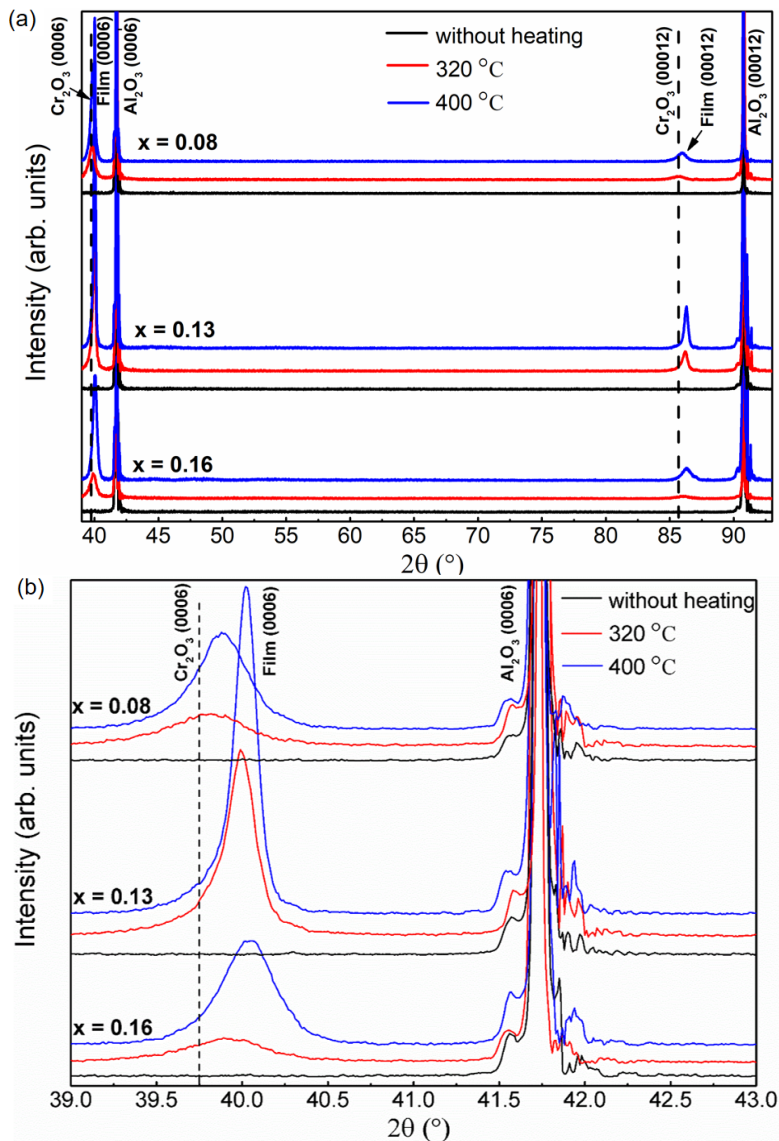


Fig. 74  $\theta - 2\theta$  XRD patterns of the  $\alpha\text{-(Cr}_{1-x}\text{Al}_x)_2\text{O}_3$  films with different Al concentration of  $x = 0.08$  (curves on top of the diagrams),  $0.13$  (curves in the mid of the diagrams), and  $0.16$  (curves at the bottom of the diagrams) deposited on the  $\alpha\text{-Al}_2\text{O}_3$  substrates without heating (black curves), at  $320^\circ\text{C}$  (red curves), and  $400^\circ\text{C}$  (blue curves). The dashed lines indicate the theoretical position of the (0006) reflection of  $\text{Cr}_2\text{O}_3$  according to the PDF card No. 38-1479 from the ICDD-database. (a)  $\theta - 2\theta$  XRD patterns in large range of the diffraction angle. (b) the (0006) reflections of the films and the substrates in more detail for a narrow range of the diffraction angle. The (0006) reflections of the films are shifted significantly to lower diffraction angles compared to reflections of the substrates (indicated by the (0006) reflections of  $\text{Al}_2\text{O}_3$ ) and are shifted to higher diffraction angles in comparison to those of the pure  $\text{Cr}_2\text{O}_3$ .

Fig. 75 shows the FWHM of the (0006) reflections of the films deposited at 320 °C and 400 °C dependent on the Al concentration. The films with the same composition deposited at higher temperature of 400 °C show lower FWHM values than those deposited at 320 °C. This indicates that the films deposited at higher temperature possess larger grain size and / or lower microstrain independent of the film composition. The values of the FWHM of the (0006) reflections of the films deposited at 400 °C and 320 °C are in the range between 0.1° and 0.6° as shown in Fig. 75, indicating a good quality of the crystalline growth of the films. The film with the Al content  $x = 0.13$  exhibits the smallest FWHM (i.e. the largest crystal grain size), which results from the symmetric position placed under the segmented target.

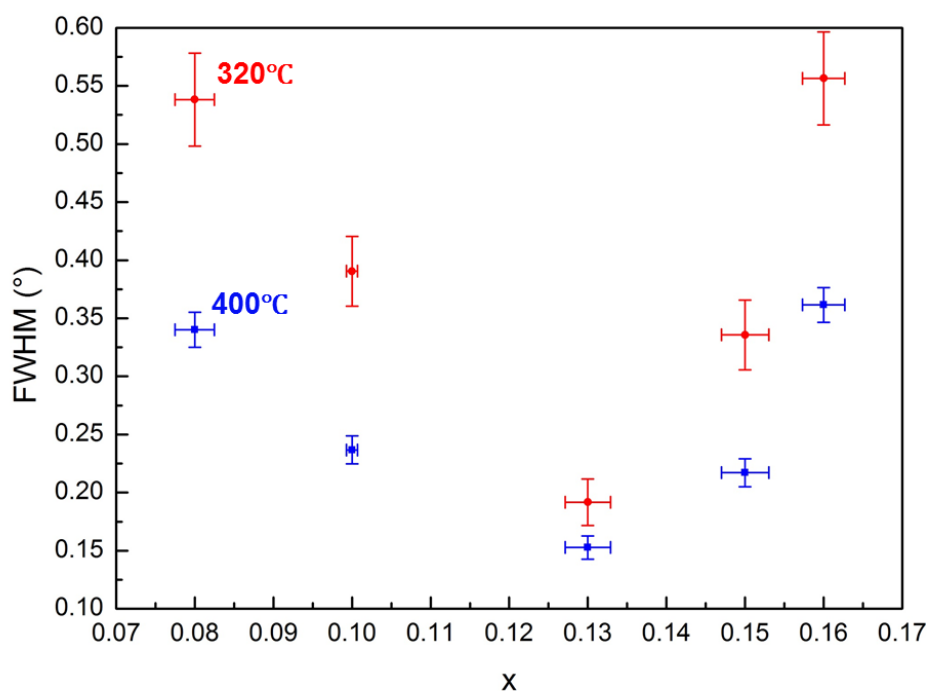


Fig. 75 Dependence of the FWHM of the (0006) reflections of the Cr-Al-O films on the Al concentration. The red and blue points correspond to the films deposited at 320 °C and 400 °C, respectively.

In the following the structure of the  $\alpha$ -(Cr<sub>1-x</sub>Al<sub>x</sub>)<sub>2</sub>O<sub>3</sub> films with different composition ( $x = 0.08, 0.10, 0.13, 0.15,$  and  $0.16$ ) deposited at 400 °C is discussed in more detail. Fig. 76 shows the XRD  $\theta - 2\theta$  patterns for the  $\alpha$ -(Cr<sub>1-x</sub>Al<sub>x</sub>)<sub>2</sub>O<sub>3</sub> thin films with  $x = 0.08, 0.10, 0.13, 0.15,$  and  $0.16$  deposited on the  $\alpha$ -Al<sub>2</sub>O<sub>3</sub> substrates at 400 °C. A gradual shift of the (0006) reflections of the films to the larger Bragg angles side with increasing the

Al concentration, which indicates that the films with less Al possess larger lattice plane distance  $d_{0006}$  (i.e. lattice constant  $c$ ).

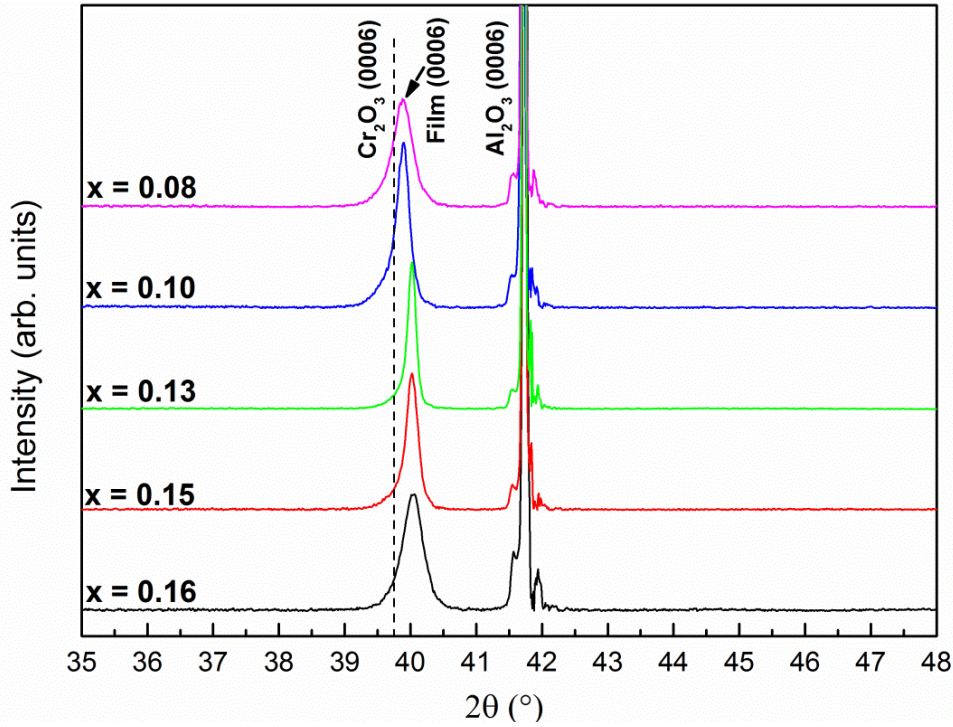


Fig. 76  $\theta - 2\theta$  XRD patterns of  $\alpha$ -( $\text{Cr}_{1-x}\text{Al}_x$ ) $_2\text{O}_3$  films with different composition ( $x = 0.08, 0.10, 0.13, 0.15, \text{ and } 0.16$ ) deposited on the  $\alpha$ - $\text{Al}_2\text{O}_3$  substrates at  $400\text{ }^\circ\text{C}$ . The dashed line indicates the theoretical position of the (0006) reflection of  $\text{Cr}_2\text{O}_3$  according to the PDF card No. 38-1479 from the ICDD-database.

An even more detailed observation is made: Fig. 77 shows the values of the lattice plane distance  $d_{0006}$  of the  $\alpha$ -( $\text{Cr}_{1-x}\text{Al}_x$ ) $_2\text{O}_3$  thin films as a function of the Al concentration  $x$ . Obviously, there is a nearly linear relationship of the value of the lattice plane distance  $d_{0006}$  and the Al concentration of the films: the higher the Al concentration in the films, the smaller the lattice plane distance  $d_{0006}$ , i.e. the smaller the lattice constant  $c$ . This result is in excellent agreement with the investigations in ref. [252–254], suggesting that the lattice parameters obey the Vegard's law.

The theoretical lattice parameters  $a$  and  $c$  of the  $\alpha$ -( $\text{Cr}_{1-x}\text{Al}_x$ ) $_2\text{O}_3$  films are estimated according to the Vegard's law as follows:

$$a_{\text{relaxed}} = x \cdot a_{\text{Al}_2\text{O}_3} + (1-x) \cdot a_{\text{Cr}_2\text{O}_3} \quad (21)$$

$$c_{relaxed} = x \cdot c_{Al_2O_3} + (1-x) \cdot c_{Cr_2O_3} \quad (22)$$

where  $a_{Al_2O_3}=0.47588$  nm,  $c_{Al_2O_3}=1.2992$  nm according to the PDF card No. 42-1468 from the ICDD-database,  $a_{Cr_2O_3}=0.495876$  nm,  $c_{Cr_2O_3}=1.35942$  nm according to the PDF card No. 38-1479 from the ICDD-database,  $x$  is “ $x$ ” in  $\alpha-(Cr_{1-x}Al_x)_2O_3$ ,  $a_{relaxed}$  and  $c_{relaxed}$  are the lattice parameters  $a$  and  $c$  in the films in the relaxed state.

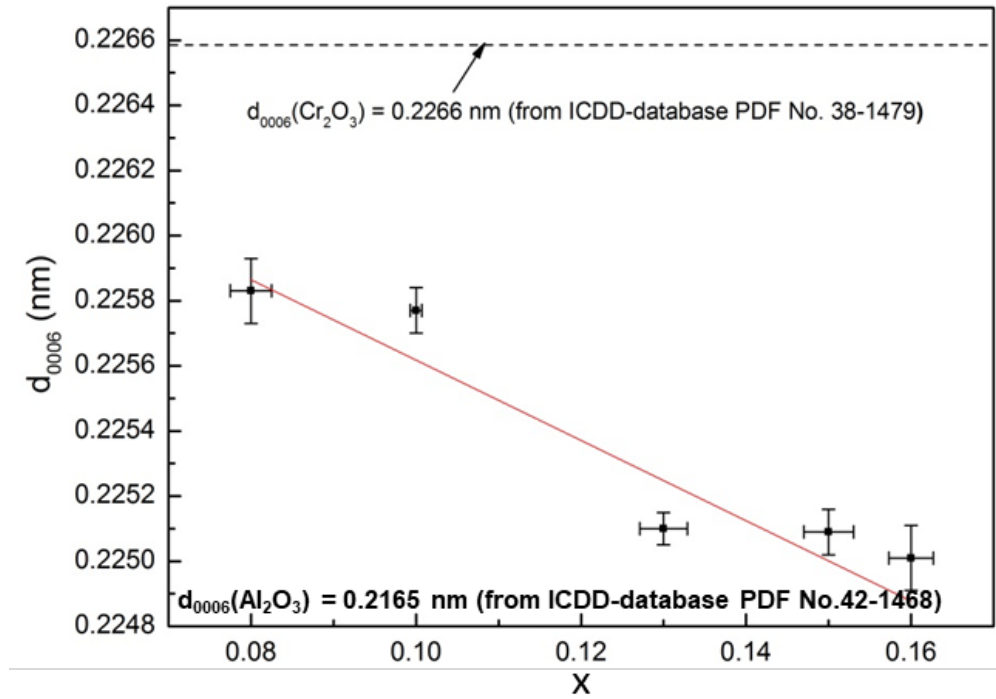


Fig. 77 Dependence of the lattice plane distance  $d_{0006}$  on the Al concentration of the films (the abscissa is the coefficient  $x$  in  $\alpha-(Cr_{1-x}Al_x)_2O_3$ ). The dashed horizontal line represents the theoretical  $d_{0006}$  value of  $Cr_2O_3$  according to the PDF card No. 38-1479 from the ICDD-database ( $d_{0006}(Cr_2O_3) = 0.2266$  nm).

The estimated theoretical lattice parameters  $a$  and  $c$  decrease in proportion to the increase of the Al concentration as shown in Fig. 78 (black lines). The ionic radius of  $Al^{3+}$  (0.0535 nm) is smaller than that of  $Cr^{3+}$  (0.0615 nm), which contributes to the decrease of the lattice parameters of the  $\alpha-(Cr_{1-x}Al_x)_2O_3$  solid solution structure with substitution of Al for Cr [170]. In order to obtain the in-plane and out-of-plane lattice parameters, symmetric (0006) and asymmetric ( $10\bar{1}10$ ) RSM analyses were performed. The measured lattice parameters of the  $\alpha-(Cr_{1-x}Al_x)_2O_3$  thin films from reciprocal lattice points are shown as the red circles in Fig. 78.

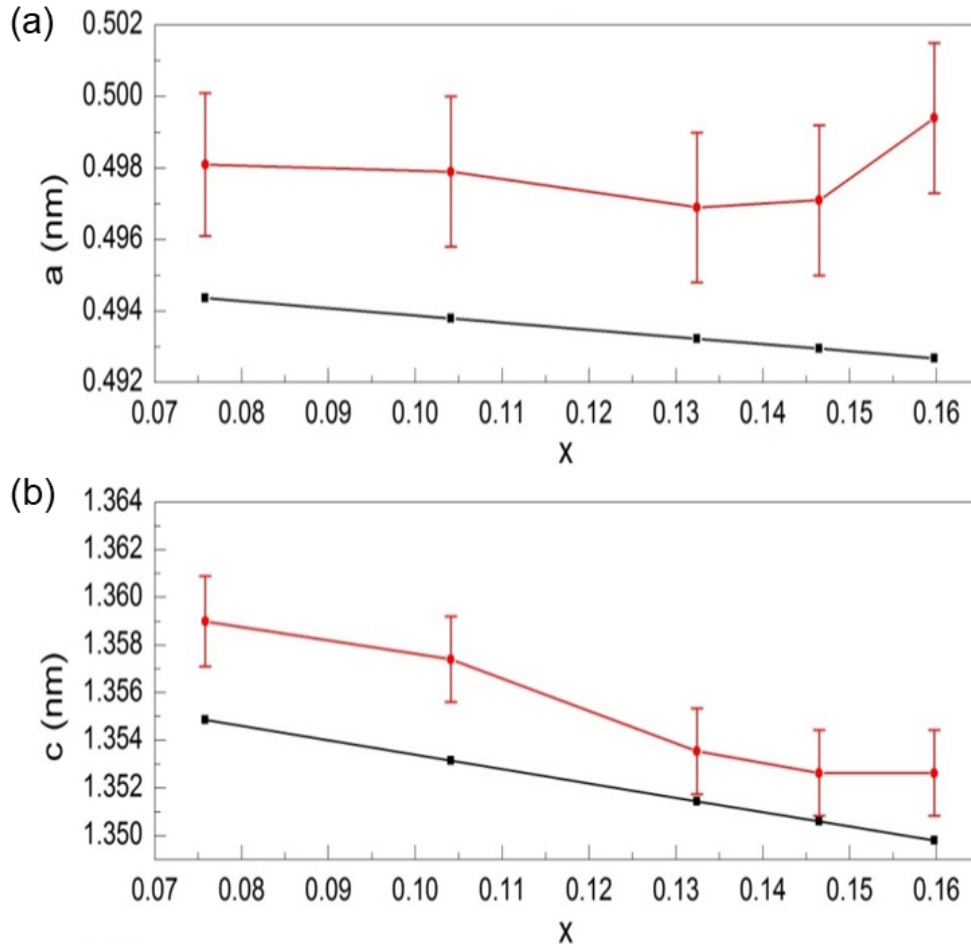


Fig. 78 (a) The lattice constants  $a$  and (b)  $c$  of the films versus the Al concentration (the abscissa is the coefficient  $x$  in  $\alpha$ -(Cr<sub>1-x</sub>Al<sub>x</sub>)<sub>2</sub>O<sub>3</sub>). ● (red solid circles) show the measured lattice constants calculated from asymmetric RSM. ■ (black solid squares) show the theoretical lattice constants calculated using data from PDF cards No. 38-1479 and No. 42-1468 (the ICDD-database) according to Vegard's law.

The films show a nearly linear variation of the lattice constants with  $x$  when the Al concentration  $x \leq 0.13$ . However, the lattice parameters of  $\alpha$ -(Cr<sub>1-x</sub>Al<sub>x</sub>)<sub>2</sub>O<sub>3</sub> films do not exactly follow the Vegard's law. Both curves of the lattice parameters over Al concentration show a deviation from the linear Vegard relation, probably due to the strains in the films, and change their features at  $x = 0.13$ , where an inflection in both curves can be seen in the red lines in Fig. 78. Especially, the lattice parameter  $a$  increases when  $x > 0.13$  with further increasing the Al concentration. More defects should occur in these films with more substitution of Al for Cr, which should induce an elongation of the lattice parameter

a. This suggestion is in agreement with the results reported for the  $\text{Cr}_{2-x}\text{Ti}_x\text{O}_3$  films, suggesting that Cr vacancies and O interstitials dominate with more Ti-doped  $\text{Cr}_2\text{O}_3$  [255]. The misfit of the in-plane interface between the film and the substrate in the films deposited from Pos. 1 to Pos. 5 are 4.5 %, 4.3 %, 4.0 %, 3.2 % and 1.3 %, respectively, which indicates the epitaxial quality is better with less Al content in the films.

Fig. 79 shows the mosaic spreading of the (0006) reflections of the films with different Al concentration deposited at 400 °C to evaluate the epitaxial quality of the films with respect to the substrates. The FWHM values of these reflections are between 1.07° and 1.43°, indicating that there are many individual crystals with a slight tilt (1.07° - 1.43°) of the (0006) planes with respect to the (0006) planes of the substrates. Compared to the FWHM of the single crystal  $\alpha\text{-Al}_2\text{O}_3$  substrate (only 0.2°), the mosaic spreading of the films is larger. This is due to the films are nanocrystalline and fine-scaled while the substrates are perfect single crystal. Further, the FWHM of the rocking curves is dependent not only on the Al concentration but also on the sample position below the target (i.e. the films forming from the species coming with different angle to the substrate surface). The FWHM of the Al-rich side film is larger than that of a film on the Cr-rich side, indicating a better epitaxial quality with lower Al content. The FWHM of the film in Pos. 3 (the center of the target) is the smallest among all these films. It reveals that the films create the smallest misorientation as they grow on the (0001)  $\alpha\text{-Al}_2\text{O}_3$  substrates when the substrate below the center of the segmented target where has most probably normal incidence of sputtered species on the substrate surface. This can be explained by TEM results showing that the crystals grow perpendicular to the substrate when the substrate is located below the center of the target (Pos. 3) while the crystals exhibit a tilt when the substrates are in other positions.

The texture of the films with different composition deposited at different temperatures was examined by X-ray pole figures taken from both symmetric (0006) reflections and asymmetric (10 $\bar{1}$ 10) reflections which are shown in Table 16. Naturally, films in amorphous state deposited without substrate heating show no texture. The texture of the films grown in crystalline structure is independent of the Al concentration and the substrate temperature (320 °C or 400 °C). A strong fiber texture in the *c*-axis is observed from

(0006) reflections, and a 6-fold symmetry is derived from the  $(10\bar{1}10)$  reflections observations, which illustrates clearly that stacking faults in the films are caused by the ion bombardment during the plasma-etching process before deposition. These results are similar to those reported for  $\text{Cr}_2\text{O}_3$  films described in the previous section and in the earlier work [245]. From the width of the reflection spots in the pole figures it can be concluded, that the crystal tilting in the films deposited at 320 °C is larger than in those deposited at 400 °C. This indicates that the higher the substrate temperature, the better the crystalline quality of the films.

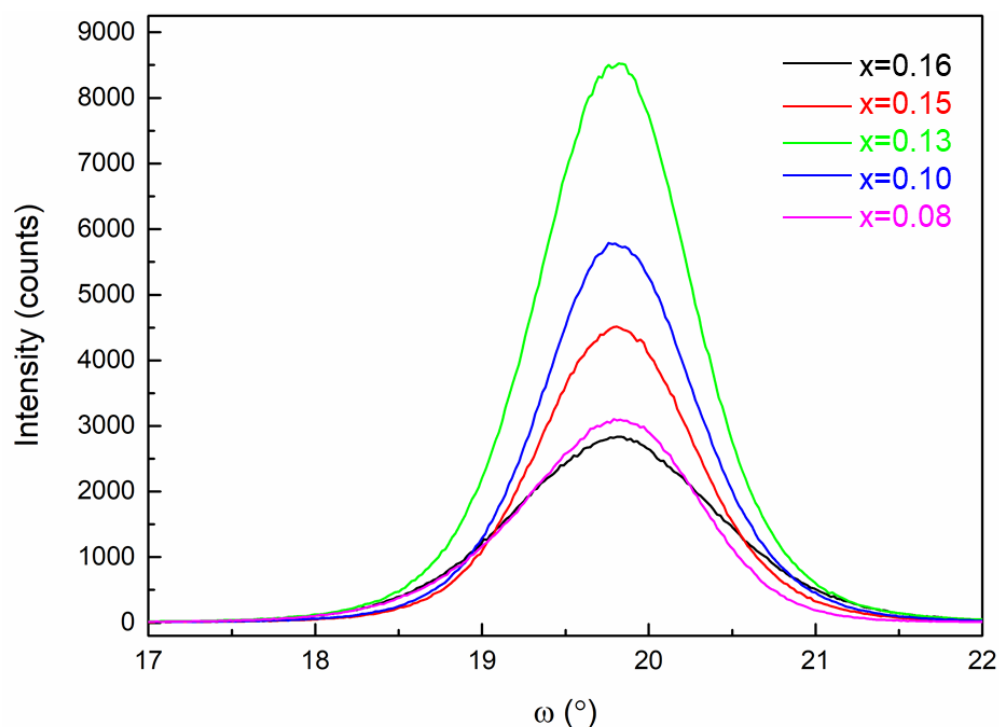
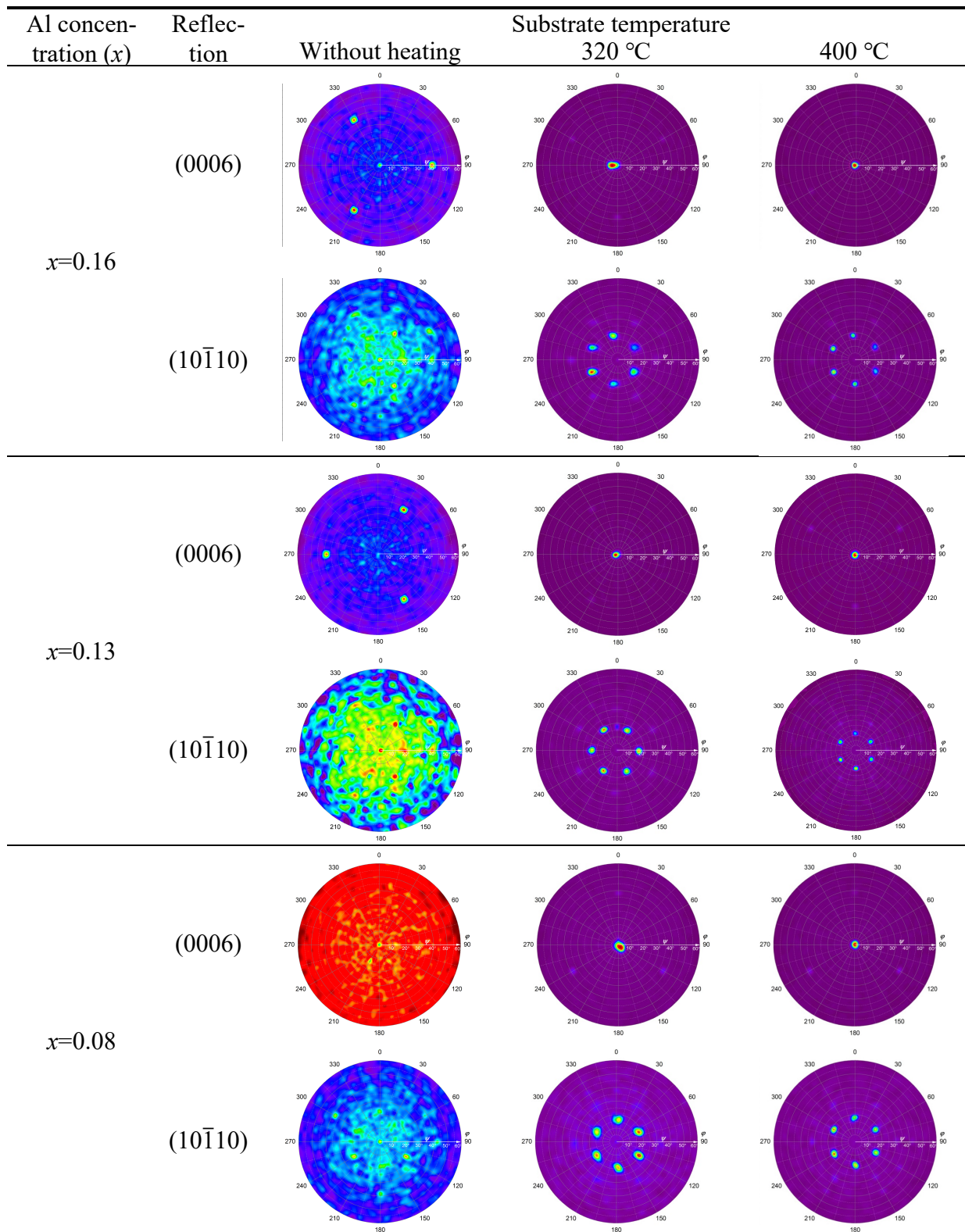


Fig. 79 XRD rocking curves ( $\omega$ -scans) of the (0006) reflections of the  $\alpha\text{-(Cr}_{1-x}\text{Al}_x\text{)}_2\text{O}_3$  films with  $x = 0.08, 0.10, 0.13, 0.15$  and  $0.16$  deposited on the  $\alpha\text{-Al}_2\text{O}_3$  substrates at 400°C. The FWHM values of these mosaic spreading reflections are 1.23°, 1.08°, 1.07°, 1.10° and 1.43°, respectively.

Detailed observations of the microstructure of the films and the relationship between the films and the substrates were done by TEM analyses as shown in Fig. 80. Two different films with different Al concentration are considered here: the first one is a film with highest Al concentration ( $x = 0.16$ ), and it is described in Fig. 80 (a) (c) and (e); the other one is a film with Al concentration of  $x = 0.13$  which has been grown on substrates placed

below the center of the target during the deposition process, and this film is described in Fig. 80 (b) (d) and (f). Fig. 80 (a) and (b) show cross-section BF TEM images of the  $\alpha$ -(Cr<sub>1-x</sub>Al<sub>x</sub>)<sub>2</sub>O<sub>3</sub> films deposited on the  $\alpha$ -Al<sub>2</sub>O<sub>3</sub> substrates, indicating individual columnar grains in the films grown in *c*-axis direction of the substrates. The surfaces of the films show a long period corrugation because of the tops of the individual crystals. The grain size of the film with Al concentration  $x = 0.16$  is about 10.5 nm, while that of the film with Al concentration  $x = 0.13$  is about 17.2 nm. This is in good agreement with the results from XRD described above, where the FWHM of the (0006) reflection of the film with  $x = 0.13$  is smaller than that of the film with  $x = 0.16$  (i.e. its grain size is larger). There is a slight tilt of about 3° of the crystals (and not of the orientation) with respect to the *c*-axis of the substrate for the film with  $x = 0.16$  (i.e. deposited at Pos. 1), while there is almost no tilt for the film with  $x = 0.13$  (i.e. deposited at Pos. 3). This crystal tilting is attributed to the position of the samples in relation to the target during deposition (major influence) rather than to the different materials constituting the segmented target (please note that there is a relatively small composition difference of the two parts of the target, i.e. only 20 at. % Al<sub>2</sub>O<sub>3</sub>). The SAED patterns dominated by both the films and the substrates are shown in Fig. 80 (c) and (d). The lattice planes have been identified in the SAED patterns, revealing the epitaxial relationships between the films and the substrates are  $(0001)_{film} // (0001)_{substrate}$  and  $(10\bar{1}0)_{film} // (10\bar{1}0)_{substrate}$ . The reflections of the (0002) and (0004) lattice planes which should be forbidden are observed and thus come from multiple excitation diffraction. The diffracted beam acts in the second crystal as a primary beam resulting in the same symmetry and diffraction direction as the primary beam [52,245]. The HRTEM images of the films are shown in Fig. 80 (e) and (f), which approve the crystal grain size again. The grain boundary between two individual crystals can be clearly observed. Small areas of the HRTEM images are enlarged to show more details of grain boundaries which are shown in black squares in Fig. 80 (e) and (f), and found that the lattice planes continue between the neighboring crystals. It seems that the oxygen layers between neighboring crystals are continuous, but the cation change the stacking layer type. The insets shown in Fig. 80 (e) and (f) are the FFT images of the HRTEM images which provide identical results on the lattice plane distances as obtained from the SAED patterns shown in Fig. 80 (c) and (d).

Table 16 Texture evolution of the  $\alpha$ -(Cr<sub>1-x</sub>Al<sub>x</sub>)<sub>2</sub>O<sub>3</sub> films with different Al concentration ( $x=0.16, 0.13$  and  $0.08$ ) grown on the  $\alpha$ -Al<sub>2</sub>O<sub>3</sub> substrates after plasma-etching at different substrate temperatures.



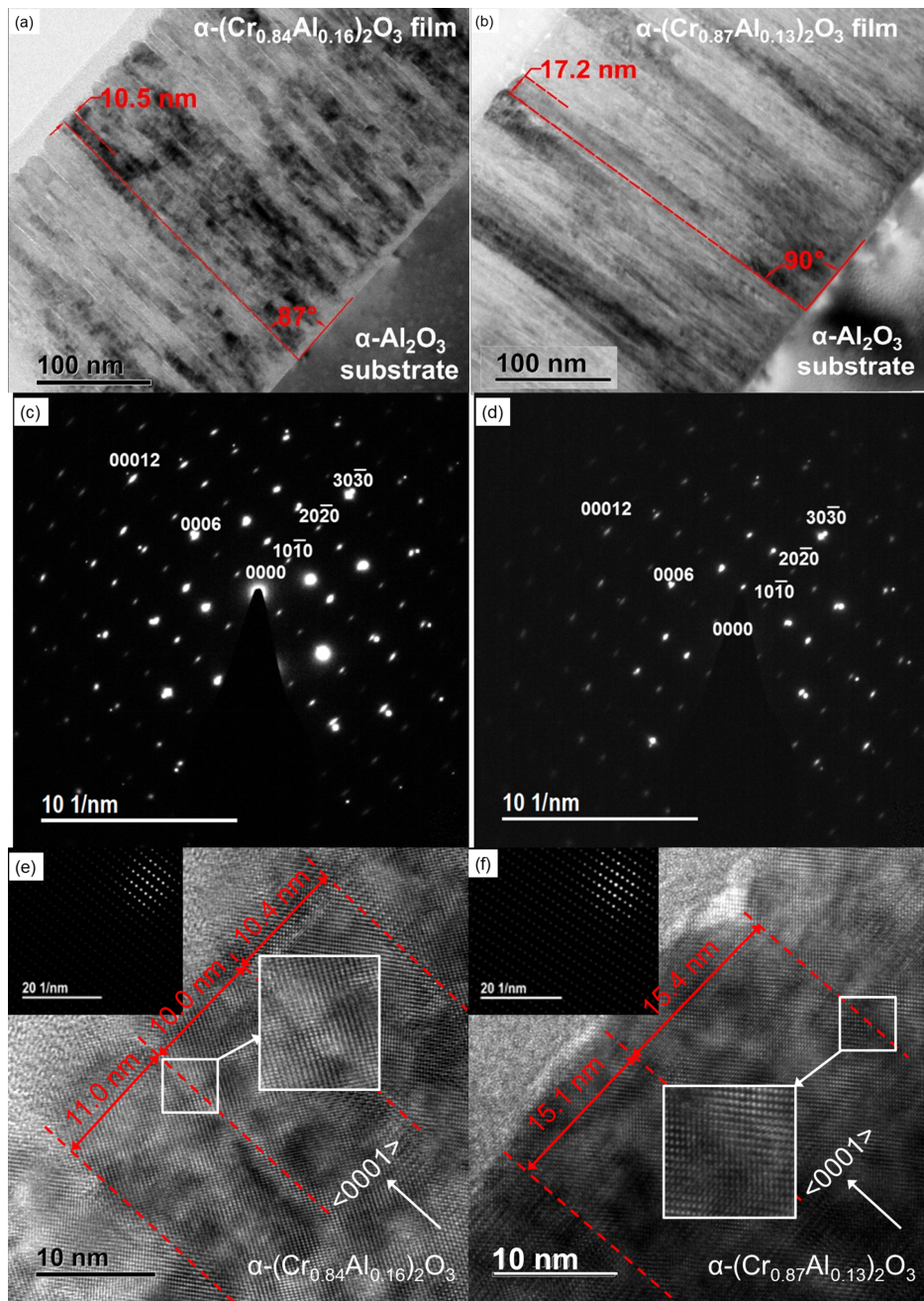


Fig. 80 TEM images of the  $\alpha\text{-(Cr}_{1-x}\text{Al}_x\text{)}_2\text{O}_3$  films with (a) (c) (e):  $x = 0.16$  and (b) (d) (f):  $x = 0.13$  deposited at  $400\text{ }^\circ\text{C}$  on the  $\alpha\text{-Al}_2\text{O}_3$  substrates. (a) and (b): BF image showing a cross sectional view of the films grown on the  $\alpha\text{-Al}_2\text{O}_3$  substrates. (c) and (d): SAED patterns revealing a partially epitaxial orientation relationship between the films and the substrates. (e) and (f): HRTEM images of the films, with the insets showing the FFT images of the HRTEM images, indicating the same lattice planes as shown in (c) and (d). The dashed lines indicate the boundaries of the individual grains. The arrows in (e) and (f) show the film growth direction of  $\langle 0001 \rangle$ .

### 4.3.3 Raman spectroscopy analysis

Raman spectroscopy analysis was performed to confirm the phase composition and crystal quality of the films indirectly in the following. Fig. 81 shows the Raman spectra of the films with different composition deposited at different substrate temperatures.

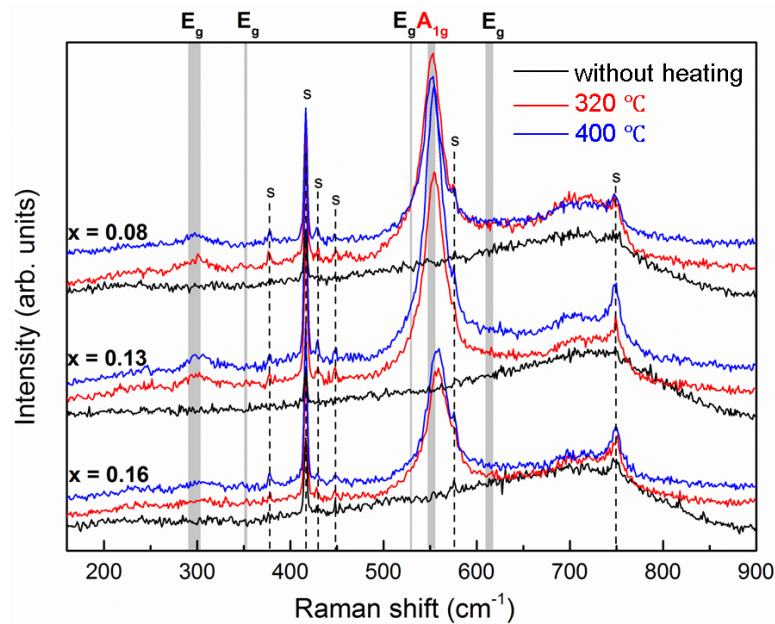


Fig. 81 Raman spectra of the  $\alpha$ - $(\text{Cr}_{1-x}\text{Al}_x)_2\text{O}_3$  films with different Al concentration of  $x = 0.08$  (curves in the upper part),  $0.13$  (curves in the middle part), and  $0.16$  (curves in the bottom part) deposited on the  $\alpha$ - $\text{Al}_2\text{O}_3$  substrates at different temperatures. “s” indicates the reflexes corresponding to the substrates. The gray areas refer to the Raman active modes of pure  $\text{Cr}_2\text{O}_3$  cited from ref. [230,242–244].

Two different features are shown in these Raman spectra: the peaks marked with “s” are attributed to the  $\alpha$ - $\text{Al}_2\text{O}_3$  substrates (these are visible with regard to the film thickness); the others are assigned to the films. Different Raman modes of pure  $\text{Cr}_2\text{O}_3$  according to literature data ([230,242–244]) are marked as gray areas in Fig. 81. The black curves in Fig. 81 show the Raman spectra of the films deposited without substrate heating. These show no Raman active features of the films, only the characteristic substrate lines are observed, confirming again that the films deposited without substrate heating should be amorphous and not have long-range ordering. The films deposited at  $320\text{ }^\circ\text{C}$  and  $400\text{ }^\circ\text{C}$  show the strongest feature of the  $A_{1g}$  vibrational mode occurring in the range of  $552.4\text{ cm}^{-1} - 560.0\text{ cm}^{-1}$ , which fits very well with the pure  $\text{Cr}_2\text{O}_3$  line shown as gray area

in Fig. 81. This indicates clearly the crystalline quality of the films. The films deposited at 400 °C show higher intensity and smaller width of the  $A_{1g}$  mode than those deposited at 320 °C, which indicates a better crystal quality with increasing substrate temperature. These observations confirm the results and conclusions made on basis of XRD analyses.

The peak position of  $A_{1g}$  mode shifts not only with the film composition but also with the substrate temperature (or crystal quality). Fig. 82 shows the Raman shift of the  $A_{1g}$  mode of the films deposited at 320 °C and 400 °C dependent on the Al concentration  $x$ . The  $A_{1g}$  band of all  $\alpha$ - $(Cr_{1-x}Al_x)_2O_3$  films with crystalline structure are observed at larger frequency positions compared to the  $Cr_2O_3$  single crystal ( $552\text{ cm}^{-1}$ ) which was supplied by EVOCHEM Advanced Materials GmbH and used as a reference. The  $A_{1g}$  band shifts to the larger frequency side with increasing the Al concentration which is independent of the substrate temperature because the lattice distance  $d_{0006}$  decreases with increasing the Al concentration as discussed in RSM, which is in agreement with the Raman results of  $Cr_2O_3$  films (see in section 4.1.2). This result is similar to the results of a Raman spectroscopy study of  $Fe_{2-x}Cr_xO_3$  bulk materials in the Fe-Cr-O system [243]. The phonon frequency varies due to the contraction of the unit cell by incorporation of Al [243].

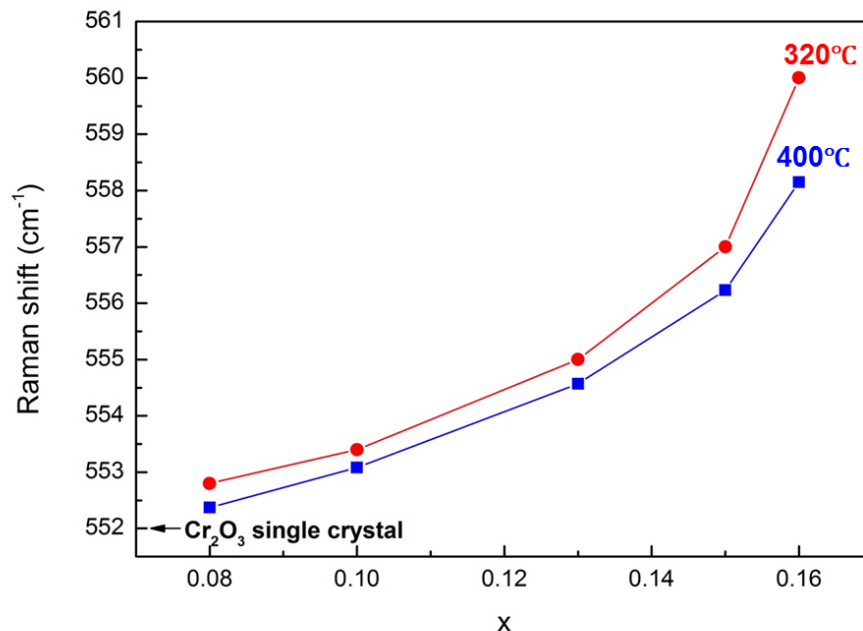


Fig. 82 Dependence of the Raman shift of the  $A_{1g}$  mode on the Al concentration  $x$  ( $0.08 \leq x \leq 0.16$ ) of the  $\alpha$ - $(Cr_{1-x}Al_x)_2O_3$  films deposited at 320 °C and 400 °C. The  $A_{1g}$  mode of the  $Cr_2O_3$  single crystal is located at  $552.0\text{ cm}^{-1}$ .

Considering simultaneously the results of Raman spectroscopy and XRD analyses, it can be said that the variation of the peak position of the  $A_{1g}$  mode in different films with different Al concentration is obviously dependent on the lattice parameter  $c$  (shown in Fig. 83). The substitution of Al for Cr in the films initially causes a reduction in the lattice parameter  $c$  which was also concluded from the  $\theta - 2\theta$  XRD analyses. The variation of the  $A_{1g}$  mode position for  $\alpha\text{-(Cr}_{1-x}\text{Al}_x)_2\text{O}_3$  towards higher frequency in comparison to the analyses of pure  $\text{Cr}_2\text{O}_3$  is caused by the contraction of the unit cell. This lattice parameter  $c$  reduction with increasing Al concentration causes the increasing of the Raman frequency of the  $A_{1g}$  mode.

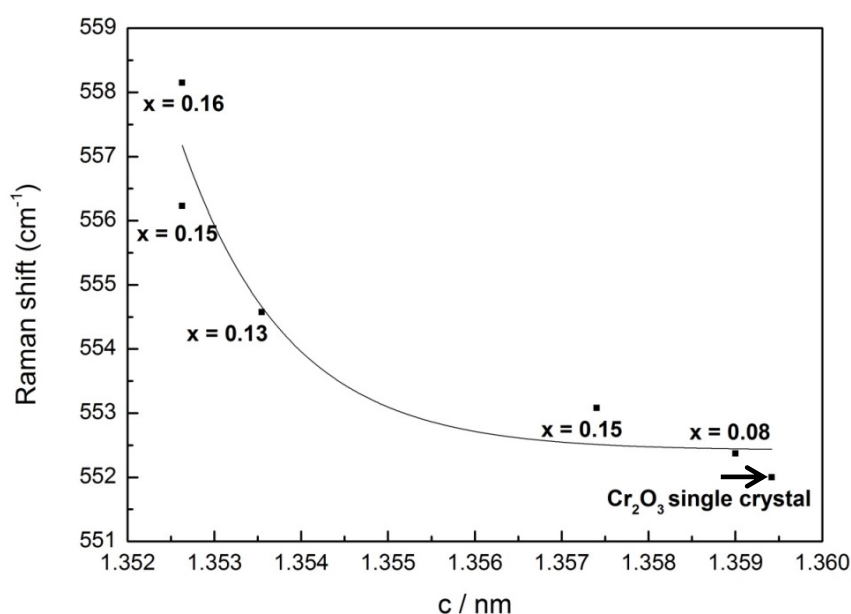


Fig. 83 Correlation of the Raman shift of the  $A_{1g}$  mode of  $\alpha\text{-(Cr}_{1-x}\text{Al}_x)_2\text{O}_3$  films with various Al concentration ( $x = 0.16, 0.15, 0.13, 0.10, 0.08$ ) and deposited at  $400\text{ }^\circ\text{C}$  with the corresponding lattice constant  $c$  of the films ( $c$  has been calculated from results of  $\theta - 2\theta$  XRD measurements). The black curve is fitted by an exponential function.

#### 4.3.4 Infrared absorption spectroscopy analysis

Fig. 84 shows the IRRAS spectra of  $\text{Cr}_2\text{O}_3$  and  $\alpha\text{-(Cr}_{1-x}\text{Al}_x)_2\text{O}_3$  films ( $0.08 \leq x \leq 0.16$ ) deposited at  $400\text{ }^\circ\text{C}$ , and Table 17 lists the band assignments of each film in this study compared to the data of bulk  $\text{Cr}_2\text{O}_3$  from the literatures. The absorbance band is observed in a wavenumber range between  $726\text{ cm}^{-1}$  and  $749\text{ cm}^{-1}$  and it varies with the Al concentration, which is assigned to a longitudinal optical phonon mode of the films [207,256].

The absorbance bands of the films exhibit slightly asymmetric features which can be explained by an overlap of the  $A_{2u}$  and  $E_u$  modes. According to the infrared reflectivity measurements of bulk  $\text{Cr}_2\text{O}_3$  by Lucovsky and Zeidler et al. [207,257], the longitudinal optical phonon with an amplitude parallel to the  $c$ -axis lies at  $726\text{ cm}^{-1}$  ( $A_{2u}$  mode) and the phonon with an amplitude perpendicular to the  $c$ -axis lies at  $734\text{ cm}^{-1}$  ( $E_u$  mode), which has been marked as dashed red lines in Fig. 84. The absorbance bands of the films are fitted into two bands by Gaussian functions, in which one is  $A_{2u}$  mode and the other is  $E_u$  mode shown as the blue curves in Fig. 84. When the Al concentration decreases to 0, i.e. pure  $\text{Cr}_2\text{O}_3$  film, the band shows narrower and more symmetric shape, due to the fact that the  $A_{2u}$  feature becomes weaker with decreasing the Al content.

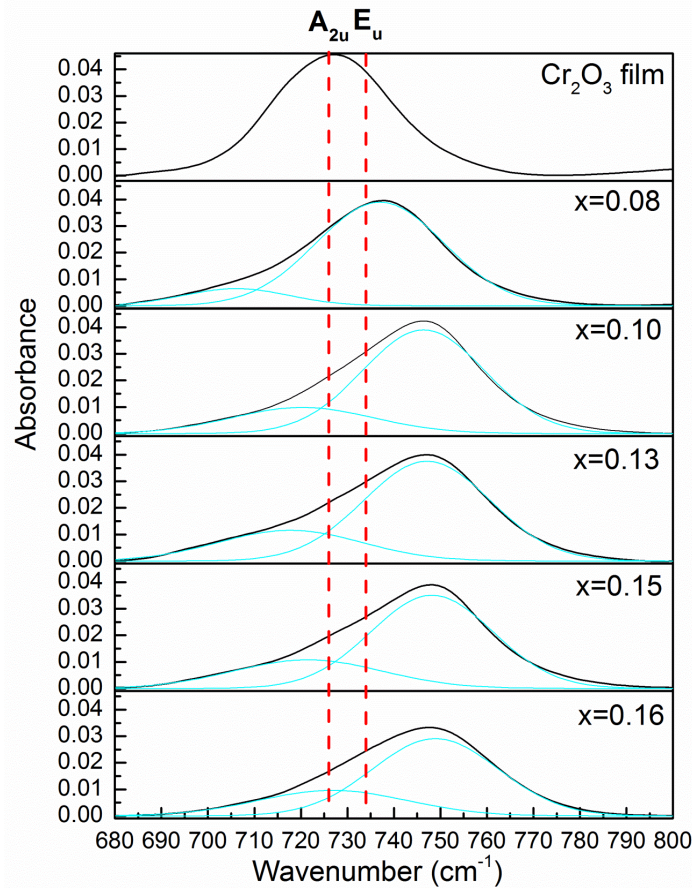


Fig. 84 The IRRAS spectra of the  $\text{Cr}_2\text{O}_3$  and  $\alpha\text{-(Cr}_{1-x}\text{Al}_x)_2\text{O}_3$  films with different composition ( $x = 0.08, 0.10, 0.13, 0.15,$  and  $0.16$ ) deposited on  $\alpha\text{-Al}_2\text{O}_3$  substrates at  $400\text{ }^\circ\text{C}$ . The spectra of  $\alpha\text{-(Cr}_{1-x}\text{Al}_x)_2\text{O}_3$  films can be fitted to two peaks ( $A_{2u}$  mode and  $E_u$  mode) by Gaussian functions. The red dashed lines represent the longitudinal optical phonon frequency of the  $A_{2u}$  and  $E_u$  mode of single crystal  $\text{Cr}_2\text{O}_3$  according to ref. [207].

Table 17 Infrared band assignments of the  $\text{Cr}_2\text{O}_3$  and  $\alpha\text{-(Cr}_{1-x}\text{Al}_x)_2\text{O}_3$  ( $x = 0.08, 0.10, 0.13, 0.15,$  and  $0.16$ ) films deposited on  $\alpha\text{-Al}_2\text{O}_3$  substrates at  $400\text{ }^\circ\text{C}$  in this study, and the reference of the bulk  $\text{Cr}_2\text{O}_3$  cited from ref. [207].

	Film	Band Position / $\text{cm}^{-1}$	Assignment	Band Position / $\text{cm}^{-1}$	Assignment
	$\text{Cr}_2\text{O}_3$	727	$A_{2u}$ mode		
PRESENT WORK	$\alpha\text{-(Cr}_{0.92}\text{Al}_{0.08})_2\text{O}_3$	706	$A_{2u}$ mode	737	$E_u$ mode
	$\alpha\text{-(Cr}_{0.90}\text{Al}_{0.10})_2\text{O}_3$	720	$A_{2u}$ mode	746	$E_u$ mode
	$\alpha\text{-(Cr}_{0.87}\text{Al}_{0.13})_2\text{O}_3$	718	$A_{2u}$ mode	747	$E_u$ mode
	$\alpha\text{-(Cr}_{0.85}\text{Al}_{0.15})_2\text{O}_3$	721	$A_{2u}$ mode	748	$E_u$ mode
	$\alpha\text{-(Cr}_{0.84}\text{Al}_{0.16})_2\text{O}_3$	727	$A_{2u}$ mode	749	$E_u$ mode
REFERENCE [207]		726	$A_{2u}$ mode	734	$E_u$ mode

Fig. 85 shows that the  $E_u$  mode band position shifts towards lower wavenumbers (longer wavelengths) from  $748.9\text{ cm}^{-1}$  to  $726.9\text{ cm}^{-1}$  with decreasing the Al concentration from  $x = 0.16$  to  $0$  (i.e. increasing the lattice constant  $c$ ), which is in agreement with the results in ref. [258] where a decreasing IR-frequency was found with increasing Cr-O distance.

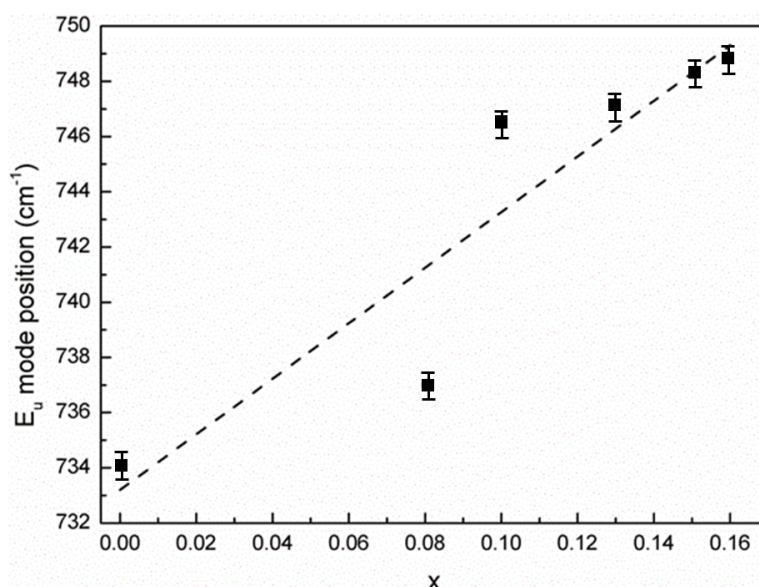


Fig. 85 Dependence of the band position of the  $E_u$  mode of the  $\alpha\text{-(Cr}_{1-x}\text{Al}_x)_2\text{O}_3$  ( $0.08 \leq x \leq 0.16$ ) films deposited at  $400\text{ }^\circ\text{C}$  and the pure  $\text{Cr}_2\text{O}_3$  ( $x = 0$ ) cited from ref. [207] on Al concentration.

Further, the IRRAS spectra of the  $\alpha$ -(Cr<sub>1-x</sub>Al<sub>x</sub>)<sub>2</sub>O<sub>3</sub> films deposited at different substrate temperatures are shown in Fig. 86.

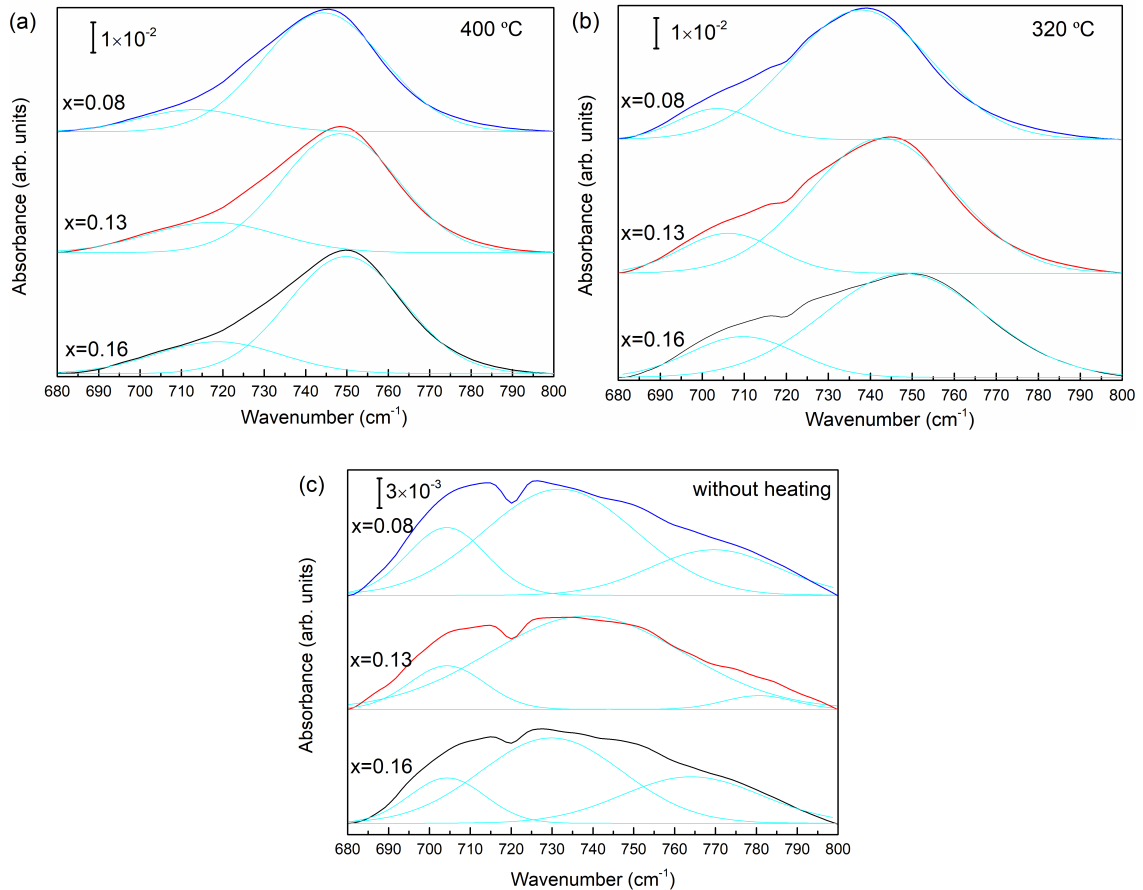


Fig. 86 The IRRAS spectra of the  $\alpha$ -(Cr<sub>1-x</sub>Al<sub>x</sub>)<sub>2</sub>O<sub>3</sub> films with different concentration ( $x = 0.08$ , blue curves;  $x = 0.13$ , red curves;  $x = 0.16$ , black curves) deposited at different substrate temperatures. The absolute length of the vertical axis in (a) (b) and (c) are the same. The blue curves are fitted by Gaussian function.

The absorbance band position, the width and the intensity of the bands vary dependent on the substrate temperature. The high intensity of the bands of the films deposited at 320 °C and 400 °C indicates the good crystalline nature of these materials [259]. The intensity of the absorbance bands increases and the band width becomes narrower with increasing substrate temperature (Fig. 86 (a) and (b)), indicating the crystal quality is better when the films deposited at higher temperature of 400 °C than 320 °C. The films deposited without substrate heating are amorphous according to  $\theta - 2\theta$  XRD and Raman spectroscopy.

copy analyses, which results in the very low infrared absorbance of these films in comparison to the crystalline ones. The absorbance bands of these amorphous films are fitted into different vibrational modes as shown in Fig. 86 (c). The IRRAS spectra of these films show extremely irregular shapes, and an additional weak band in the range of  $760\text{ cm}^{-1}$  -  $780\text{ cm}^{-1}$  which might be related with the amorphous structure with no long range order or imperfect polarization [257]. In case of the crystalline films deposited at  $320\text{ }^{\circ}\text{C}$  and  $400\text{ }^{\circ}\text{C}$ , the absorbance bands can be characterized by fitted features that can be attributed to  $A_{2u}$  and  $E_u$  like vibrational modes. The distance between two mode positions decreases from  $38\text{ cm}^{-1}$  to  $30\text{ cm}^{-1}$  with increasing the deposition temperature from  $320\text{ }^{\circ}\text{C}$  to  $400\text{ }^{\circ}\text{C}$  (increasing the crystal quality) and increases from  $38.3\text{ cm}^{-1}$  to  $34.2\text{ cm}^{-1}$  with decreasing the Al concentration from  $x = 0.16$  to  $x = 0.08$ . These two features seem to merge when the Al concentration decreases to 0 (i.e. pure  $\text{Cr}_2\text{O}_3$  films), which supports the observation of a more symmetric absorbance band in case of pure  $\text{Cr}_2\text{O}_3$  films as shown in Fig. 84. Fig. 87 shows the  $E_u$  mode position dependent on the film composition for the crystalline films, indicating that the  $E_u$  mode band tends to shift towards larger wavenumber with increasing the Al concentration (decreasing the lattice constant  $c$ ) independent of the deposition temperature. Additionally, the frequency of the  $E_u$  mode of the films deposited at  $400\text{ }^{\circ}\text{C}$  is higher than the films with the same composition deposited at  $320\text{ }^{\circ}\text{C}$ , which confirms the conclusion that the smaller the lattice constant  $c$  the larger the frequency of the  $E_u$  mode.

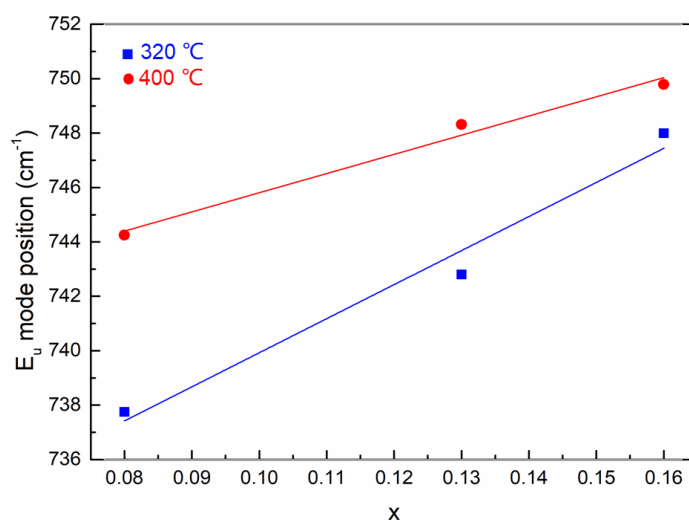


Fig. 87 Dependence of the  $E_u$  mode position of the  $\alpha\text{-(Cr}_{1-x}\text{Al}_x\text{)}_2\text{O}_3$  ( $0.08 \leq x \leq 0.16$ ) films deposited at  $320\text{ }^{\circ}\text{C}$  and  $400\text{ }^{\circ}\text{C}$  on the Al concentration.

### 4.3.5 Optical properties characterization

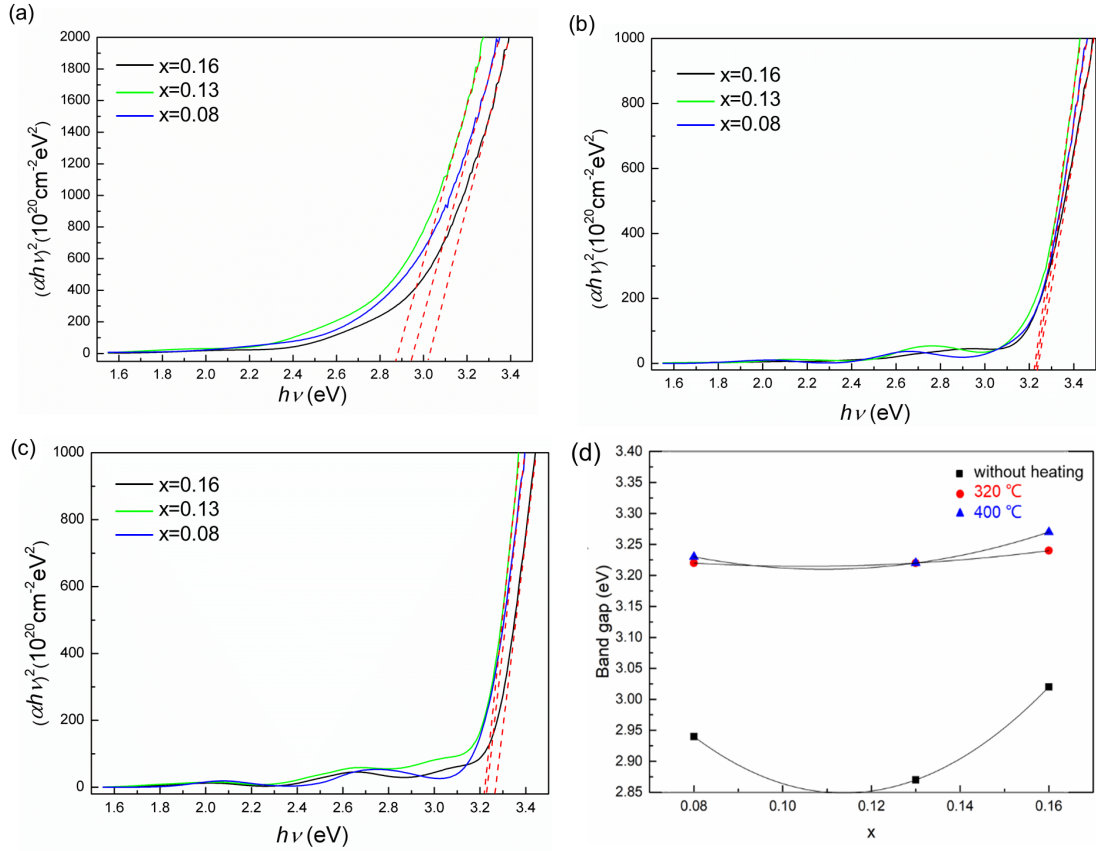


Fig. 88 Plots of  $(ah\nu)^2$  vs.  $h\nu$  for the  $\alpha$ -(Cr<sub>1-x</sub>Al<sub>x</sub>)<sub>2</sub>O<sub>3</sub> ( $x = 0.16, 0.13, 0.08$ ) deposited at (a) without substrate heating (135 °C) (b) 320 °C and (c) 400 °C. (d) Dependence of the experimental band gap of  $\alpha$ -(Cr<sub>1-x</sub>Al<sub>x</sub>)<sub>2</sub>O<sub>3</sub> films on the Al concentration  $x$  and substrate temperature.

Plots of  $(ah\nu)^2$  as a function of photon energy for the  $\alpha$ -(Cr<sub>1-x</sub>Al<sub>x</sub>)<sub>2</sub>O<sub>3</sub> with different Al concentration and deposited at different temperatures are shown in Fig. 88. The extrapolation of the photon energy by a straight line (dashed red lines in Fig. 88 (a) - (c)) to the horizontal ordinate gives the band gap  $E_g$  value.  $E_g$  and  $B$  values in Tauc's equation (Eq. (18)) are shown in Table 18. The trend of the  $E_g$  value show in Fig. 88 (d). The direct band gap of  $\alpha$ -Al<sub>2</sub>O<sub>3</sub> and Cr<sub>2</sub>O<sub>3</sub> was found to be 8.8 eV and 3.07 eV, respectively [62,200]. For the alloys, the  $E_g$  values of the Cr-Al-O films in amorphous state are from 2.87 eV to 3.02 eV, and the  $E_g$  values of the Cr-Al-O films in crystalline state are from 3.22 eV to 3.27 eV, which are close to the reported results of the value for pure Cr<sub>2</sub>O<sub>3</sub> by other authors [105,237,246]. The intensity of the absorbance band in the visible light range is

higher with increasing crystalline quality. The band gap of the crystalline films is larger than that of the amorphous films. The films exhibit a minimum  $E_g$  value when  $x = 0.13$  due to the best crystal quality nearly without tilting and with largest grain size.

Table 18 Optical parameters of the  $\alpha$ -( $\text{Cr}_{1-x}\text{Al}_x$ ) $_2\text{O}_3$  films ( $x$  is the Al concentration;  $E_g$  is the band gap;  $B$  is a constant in Eq. (18)).

Deposition temperature	$x$	$E_g$ (eV)	$B$ ( $10^{23} \text{ cm}^{-1}\text{eV}^{-1}$ )
Without heating	0.16	3.02	5.8
	0.13	2.87	5.9
	0.08	2.94	5.5
320 °C	0.16	3.24	4.0
	0.13	3.22	4.9
	0.08	3.22	4.2
400 °C	0.16	3.27	5.8
	0.13	3.22	6.9
	0.08	3.23	6.1

#### 4.4 $\alpha$ -( $\text{V}_{1-x}\text{Al}_x$ ) $_2\text{O}_3$ solid solution thin films grown on $c$ -plane $\alpha$ - $\text{Al}_2\text{O}_3$ substrates

In this chapter, The growth of V-Al-O thin films synthesized on  $c$ -plane  $\alpha$ - $\text{Al}_2\text{O}_3$  substrates by using another segmented target is described. Researchers are interested in the optical and magnetic properties of solid solution in  $\text{Al}_2\text{O}_3$  -  $\text{V}_2\text{O}_3$  system [180], but the films with Al-rich systems are difficult to be obtained at low temperature. In this case, one half plate is made of an  $\text{Al}_2\text{O}_3$  (20 at. %)- $\text{V}_2\text{O}_3$  (80 at. %) mixture; the other half plate is made of pure  $\text{V}_2\text{O}_3$ . In section 4.1.4 and 4.2.4, it is proved that the etching process on the substrates before deposition badly effects on the film epitaxial growth. Therefore, the substrates are without plasma-etching before deposition in this chapter. All V-Al-O films were deposited at 400 °C and were thoroughly analyzed. The samples were placed under the sputter target as shown in Fig. 17 (d). Films with a thickness of 1.2  $\mu\text{m}$  were prepared for EPMA analysis, and films with thickness of 120 nm were used for all other measurements.

#### 4.4.1 Chemical composition

The chemical composition of the films was determined by EPMA, and the results are displayed in Table 19. The composition of the films is dependent on the position where the substrates were placed during the deposition. A gradient variation of the Al, V and O concentration of the films from Pos. 1 to Pos. 5 is observed as presented in Fig. 89. Similar to the films discussed in the previous chapters, impurities i.e. C, N, and Ar were detected and can be ignored as their total concentration is clearly below 2 at. % (and mostly even much lower).

The relative concentration of Al is defined as  $x$ :

$$x = \frac{\omega(\text{Al})}{\omega(\text{Al}) + \omega(\text{V})} \quad (23)$$

And the deviation from the ideal metal to oxygen stoichiometry  $\delta$  is given by:

$$\delta = 3 \cdot \frac{\omega(\text{Al}) + \omega(\text{V})}{\omega(\text{O})} - 2 \quad (24)$$

where  $\omega(\text{Al})$  and  $\omega(\text{V})$  are the atomic concentrations of Al and Cr in the films, respectively.

Table 19 The chemical composition of the V-Al-O films deposited on the substrates in different positions related to the target:  $x$  and  $\delta$  describe the relative Al concentration and the deviation from a perfect theoretical stoichiometry in Eq. (23) and (24) respectively (standards used for calibrating see section 3.2.1).

Pos.	Al (at. %)	V (at. %)	O (at. %)	C (at. %)	N (at. %)	Ar (at. %)	$x$	$\delta$
1	5.7 ± 0.07	30.1 ± 0.16	63.1 ± 0.32	0.7 ± 0.24	0.4 ± 0.02	0.0	0.16	-0.30
2	4.4 ± 0.01	28.3 ± 0.14	66.0 ± 0.17	0.5 ± 0.08	0.4 ± 0.02	0.0	0.14	-0.51
3	3.6 ± 0.04	28.2 ± 0.19	67.1 ± 0.25	0.5 ± 0.06	0.4 ± 0.02	0.0	0.11	-0.58
4	2.9 ± 0.04	29.6 ± 0.17	66.3 ± 0.16	0.6 ± 0.07	0.4 ± 0.02	0.0	0.09	-0.53
5	2.5 ± 0.06	32.8 ± 0.27	62.9 ± 0.39	1.5 ± 0.23	0.4 ± 0.02	0.0	0.07	-0.32

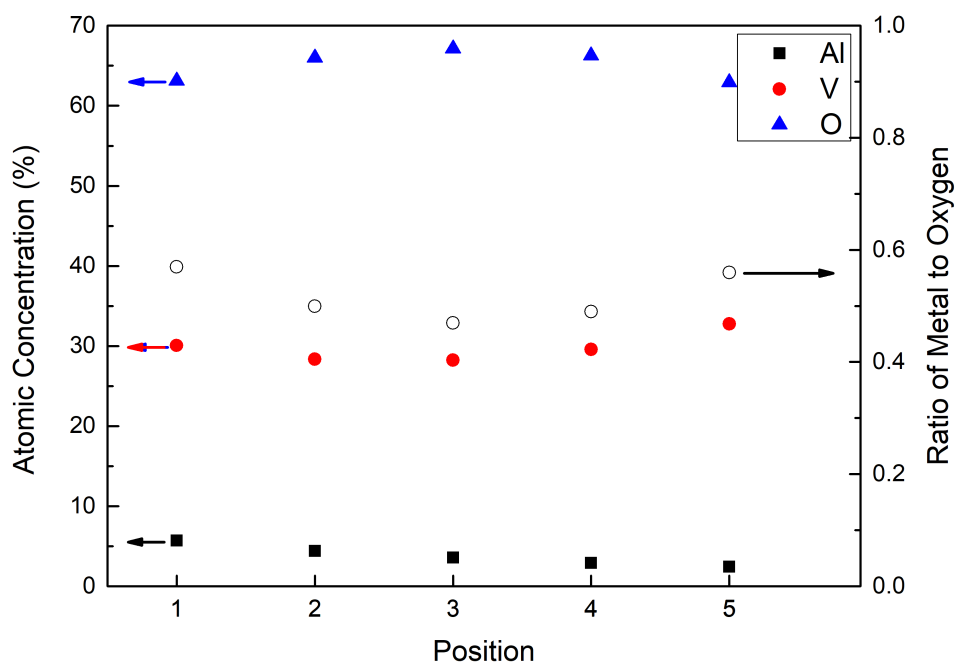


Fig. 89 The atomic concentration of the elements in the V-Al-O films (left-sided Y-axis) and the atomic concentration ratio of metal to oxygen concentration (right-sided Y-axis, data shown in hollow circles) dependent on different sample positions in relation to the target.

These values are shown in Table 19. In case of the V-Al-O films, the deviation of the concentration from the ideal metal to oxygen stoichiometry  $\delta$  is relatively large and cannot be ignored. All calculated metal to oxygen concentration ratios of the films are smaller than  $2/3$ , and has the lowest value in Pos. 3. In Fig. 89, the Al concentration decreases with a slight gradient from Pos. 1 to Pos. 5. The sum of the metal concentrations remains more or less constant, independent of the position but is significantly below the theoretically expected value of 40 at. %. The atomic concentration of O in all the films is larger than the ideal value of 60 at. %, which could indicate a small amount of other phases except  $Me_2O_3$  were synthesized. The film deposited in Pos. 3 possesses highest O and lowest V concentration. It has been reported that the elemental content is dependent on the energy of ions bombarding the target, the target - substrate configurations (e.g. the separation, the size of the target and the substrates and the position of the samples related to the target), the sputtering yield, and the magnetic field configuration [15]. So the explanation of the concentration of V in each position is complicated and need to be further discussed.

#### 4.4.2 Structural analysis

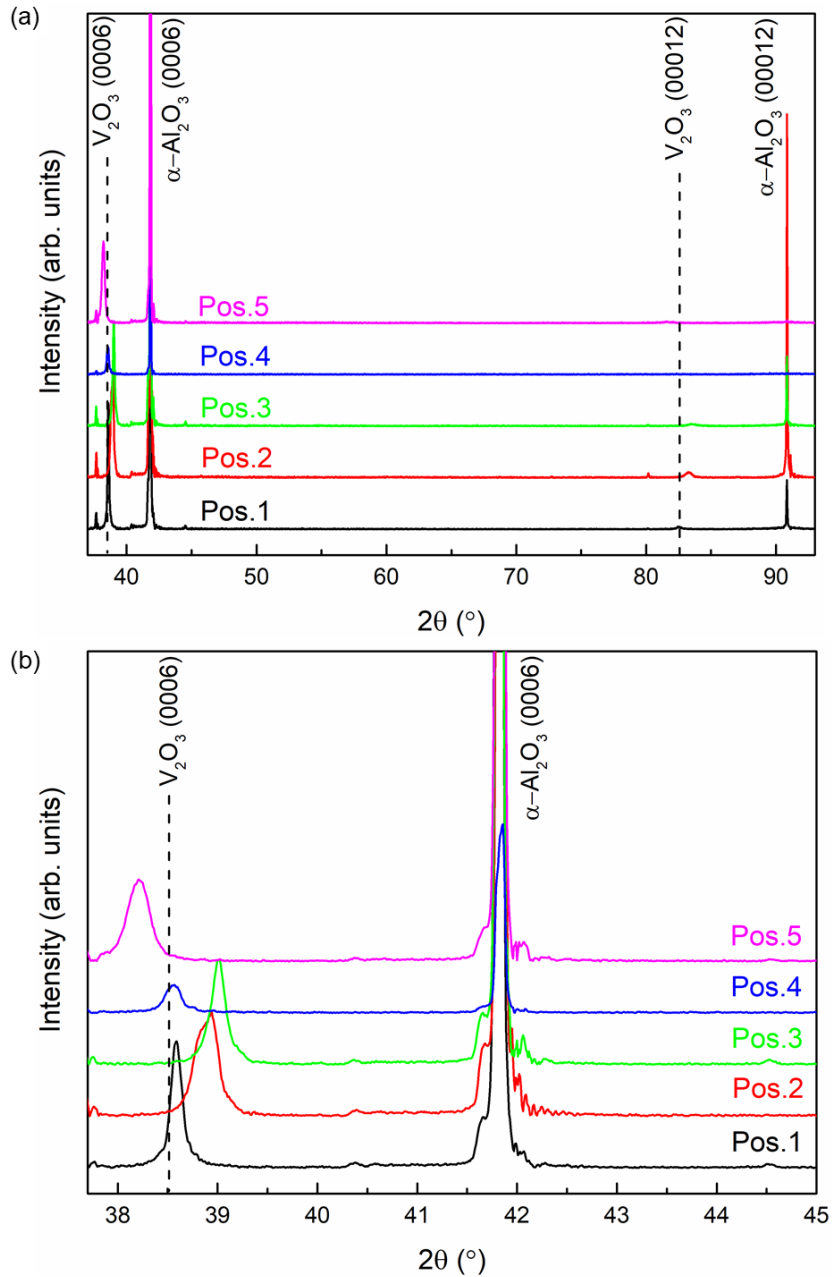


Fig. 90  $\theta - 2\theta$  XRD patterns of  $\alpha-(V_{1-x}Al_x)_2O_3$  thin films deposited on the  $\alpha-Al_2O_3$  substrates at different positions as shown in Fig. 17 (d). The reflections of the films are observed at lower  $2\theta$  positions in relation to the substrates. The dashed line indicates the theoretical position of the (0006) reflection of  $V_2O_3$  according to the PDF card No. 34-187 from the ICDD-database. (a)  $\theta - 2\theta$  XRD patterns in large range of the diffraction angle. (b) the (0006) reflections of the films and the substrates in more detail for a narrow range of the diffraction angle.

$\theta - 2\theta$  XRD analysis was used to determine the crystallinity, phase composition and crystallographic lattice constant  $c$  of the films with different composition. Fig. 90 shows  $\theta - 2\theta$  XRD patterns of the films with different composition deposited on the  $\alpha$ -Al<sub>2</sub>O<sub>3</sub> substrates at 400 °C. Only (0006) and (00012) reflections of the films and the substrates are observed in XRD in Bragg-Brentano geometry, indicating a single-phase solid solution in corundum-type structure (with strong deviation from the perfect stoichiometry). The diffraction patterns with the most intense peaks at the position of  $2\theta = 41.69^\circ$  correspond to the (0006) lattice plane of the  $\alpha$ -Al<sub>2</sub>O<sub>3</sub> substrate. The (0006) reflections of the films are shown next to the  $\alpha$ -Al<sub>2</sub>O<sub>3</sub> reflections, and their positions are dependent on the film composition. The theoretical (0006) reflection of the V<sub>2</sub>O<sub>3</sub> is at  $2\theta = 38.514^\circ$  according to the PDF card No. 34-187 from the ICDD-database and is shown as the vertical dashed line in Fig. 90. The (0006) reflections of the films shift dependent not only on the Al concentration of  $x$  but also the deposition sample positions.

Fig. 91 and Fig. 92 show the lattice plane distance  $d_{0006}$  value of the thin films is dependent on the sample positions and the atomic concentration of the Al in the films, respectively. On one hand, the value of  $d_{0006}$  (or lattice constant  $c$ ) should decrease with increasing Al content of the films when the V atoms are substituted by the Al atoms in the solid solution, mainly as a consequence of the ionic radius of V<sup>3+</sup> (0.064 nm) which is larger than Al<sup>3+</sup> (0.057 nm) [182]. On the other hand, the value of  $d_{0006}$  (or lattice constant  $c$ ) is influenced by the sample positions during the deposition (i.e. the films forming from the species coming with different angle to the substrate surface). The film deposited in the sample Pos. 3 possesses the smallest (0006) lattice plane distance  $d_{0006}$  (or lattice constant  $c$ ), due to the film possesses the best epitaxial quality among these five samples. The lattice parameters can usually be related to the crystalline quality, strain, and composition of the films. Except for the film deposited in the Pos. 5, the  $d_{0006}$  values of all the films are smaller than the theoretical  $d_{0006}$  value of the V<sub>2</sub>O<sub>3</sub>. Such anomalies in the film deposited in the sample Pos. 5 could be caused by the disturbance (or cation disorder) in the crystals.

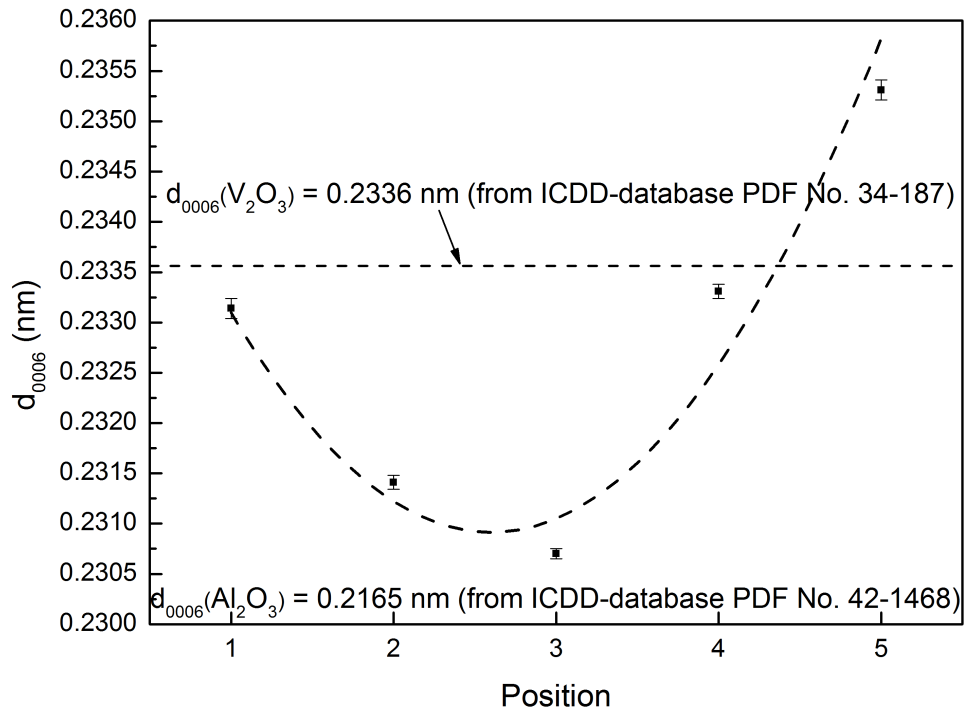


Fig. 91 Dependence of the (0006) lattice plane distance ( $d_{0006}$ ) on the sample position during deposition. The theoretical  $d_{0006}$  values of the  $V_2O_3$  and  $Al_2O_3$  are marked in this graph. The dashed line is a fitting curve.

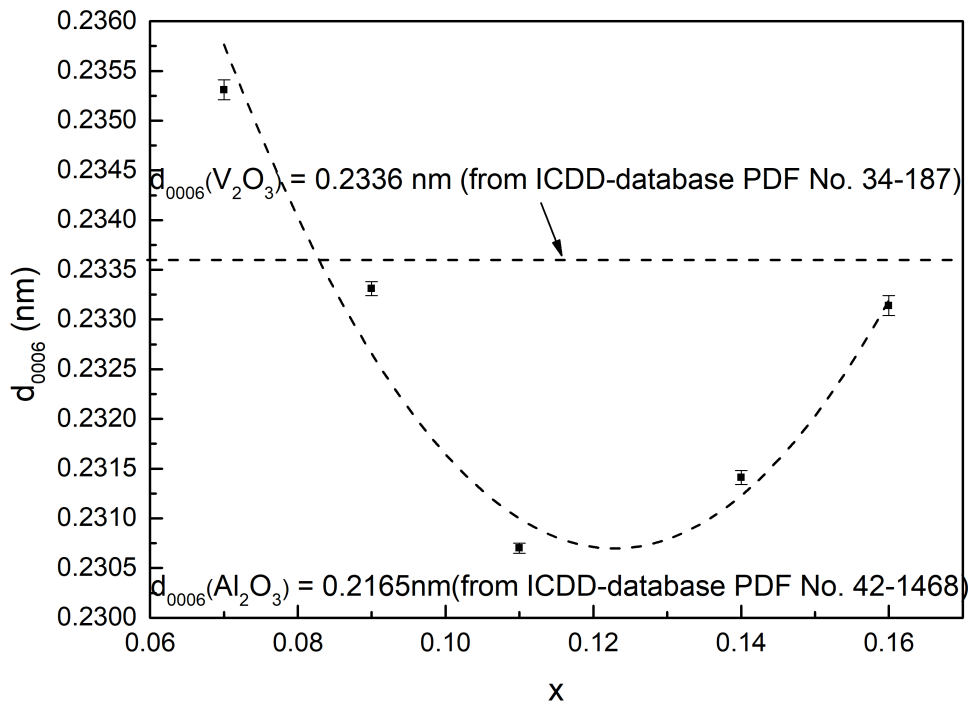


Fig. 92 Dependence of the (0006) lattice plane distance ( $d_{0006}$ ) on the concentration of Al. The dashed line is a fitting curve.

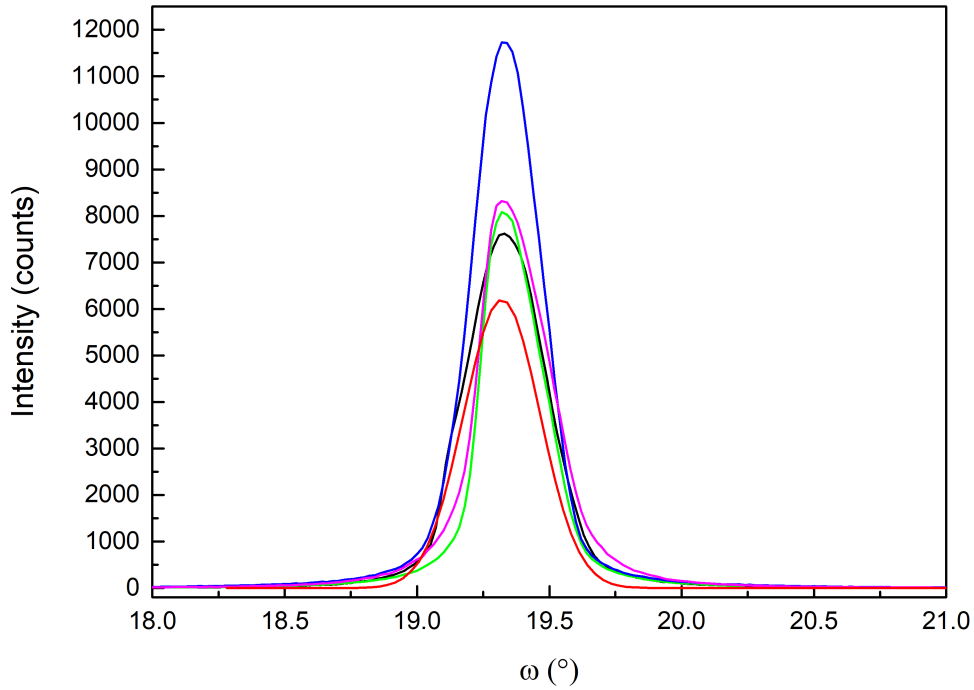


Fig. 93 The XRD rocking curves ( $\omega$ -scans) of the (0006) reflections of the V-Al-O films deposited at different positions, from Pos. 1 to Pos. 5 (in black, red, green, blue, and magenta color, respectively).

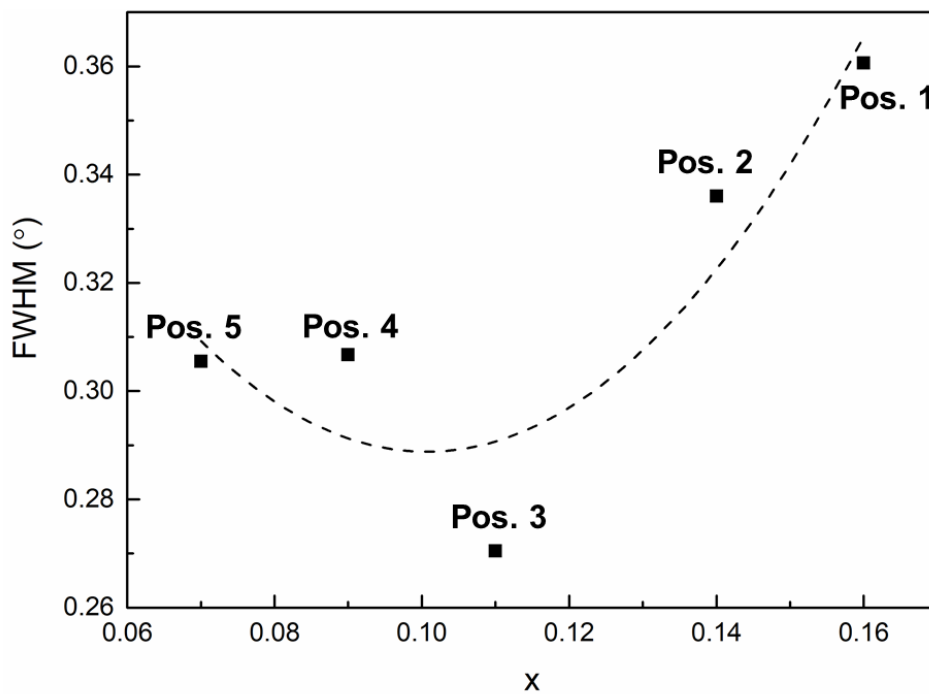


Fig. 94 Dependence of the FWHM values of the mosaic spreadings of the (0006) reflections on the Al concentration (From Pos. 1 to Pos. 5:  $0.36^\circ$ ,  $0.34^\circ$ ,  $0.27^\circ$ ,  $0.31^\circ$  and  $0.31^\circ$ , respectively).

Fig. 93 shows the mosaic spreading of the (0006) reflections of the films with different composition to determine the epitaxial quality of the films with respect to the substrates. The FWHM values of these reflections are between  $0.27^\circ$  and  $0.36^\circ$ . This indicates that the films exhibit nice epitaxial growth on the  $\alpha\text{-Al}_2\text{O}_3$  substrates. Fig. 94 shows the FWHM values of the mosaic spreading reflections in Fig. 93 dependent on the sample positions and the Al concentration of  $x$ , respectively. The FWHM values are  $0.36^\circ$ ,  $0.34^\circ$ ,  $0.27^\circ$ ,  $0.31^\circ$  and  $0.31^\circ$  for the films deposited in the Pos. 1 to Pos. 5, respectively. The epitaxial quality of the film which is in the Pos. 3 is the best. It is in agreement with the Al-Cr-O solid solution films. The tilt of the crystals which were grown under the center of the segmented target (i.e. Pos. 3) is smaller than that of the films deposited in other positions.

The symmetric (0006) and asymmetric ( $10\bar{1}10$ ) RSM were performed to obtain the in-plane and out-of-plane lattice parameters and to determine the epitaxial quality of the films, which are shown in Fig. 95. In the symmetric (0006) reflections,  $q_{//}$  of the center of these films is close to 0, indicating a strong  $c$ -axis texture.  $q_{//}$  of the center of the film deposited in Pos. 3 (shown in Fig. 95 (c)) is exactly equal to 0, while the films deposited in other positions are not (shown in Fig. 95 (a) and (e)), indicating a very small tilt of the (0006) planes when the films are deposited not below the center of the segmented target. In the asymmetric ( $10\bar{1}10$ ) reflections, the lines connecting the reflections from the substrates to the origins (which is the line of the unstrained (fully relaxed) lattice parameter) does not run through the reflections from the films, suggesting that partially epitaxial films are grown on the substrate. Then, the lattice parameters  $a$  and  $c$  of the films were calculated from the RSM results, and the theoretical values are calculated according to the Vegard's law as following:

$$a_{relaxed} = x \cdot a_{\text{Al}_2\text{O}_3} + (1-x) \cdot a_{\text{V}_2\text{O}_3} \quad (25)$$

$$c_{relaxed} = x \cdot c_{\text{Al}_2\text{O}_3} + (1-x) \cdot c_{\text{V}_2\text{O}_3} \quad (26)$$

where  $a_{\text{Al}_2\text{O}_3} = 0.47588$  nm,  $c_{\text{Al}_2\text{O}_3} = 1.2992$  nm according to the PDF card No. 42-1468 from the ICDD-database,  $a_{\text{V}_2\text{O}_3} = 0.49540$  nm,  $c_{\text{V}_2\text{O}_3} = 1.40083$  nm according to the PDF card No. 34-187 from the ICDD-database.  $x$  is “ $x$ ” in  $\alpha\text{-(V}_{1-x}\text{Al}_x)_2\text{O}_3$ ,  $a_{relaxed}$  and  $c_{relaxed}$  are the lattice parameters  $a$  and  $c$  in the films in the relaxed state of the films.

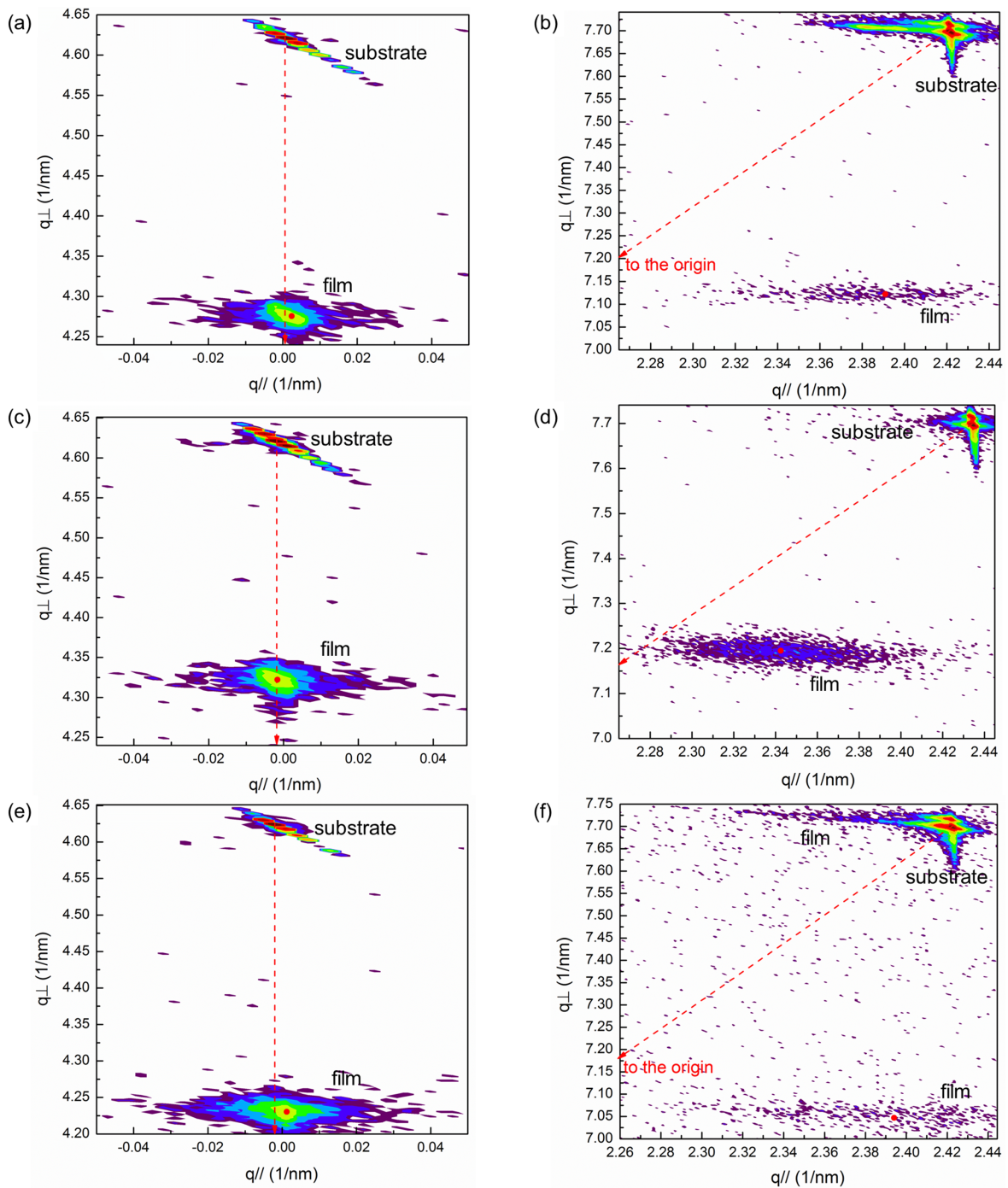


Fig. 95 RSM results of the  $\alpha$ - $(V_{1-x}Al_x)_{\delta+2}O_3$  films deposited on  $\alpha$ - $Al_2O_3$  substrates in different positions related to the target: (a) and (b) in Pos. 1; (c) and (d) in Pos. 3; (e) and (f) in Pos. 5. (a), (c) and (e) are the symmetric (0006) reflections and (b), (d) and (f) are the asymmetric  $(10\bar{1}10)$  reflections.

Both the lattice parameters  $a$  and  $c$  values derived from the RSM data and the theoretically calculated ones are shown in Fig. 96. The deviation of the lattice parameters  $a$  and  $c$

between the real and the theoretical values is smallest for the film deposited in Pos. 3 (which is the position under the center of the segmented target). All the real lattice parameters  $a$  are smaller than the theoretical values, suggesting a good locally epitaxial quality and some stress in the films. The strain of the in-plane interface between the films and the substrates is 0.8% - 2.4%, which indicates good epitaxial quality.

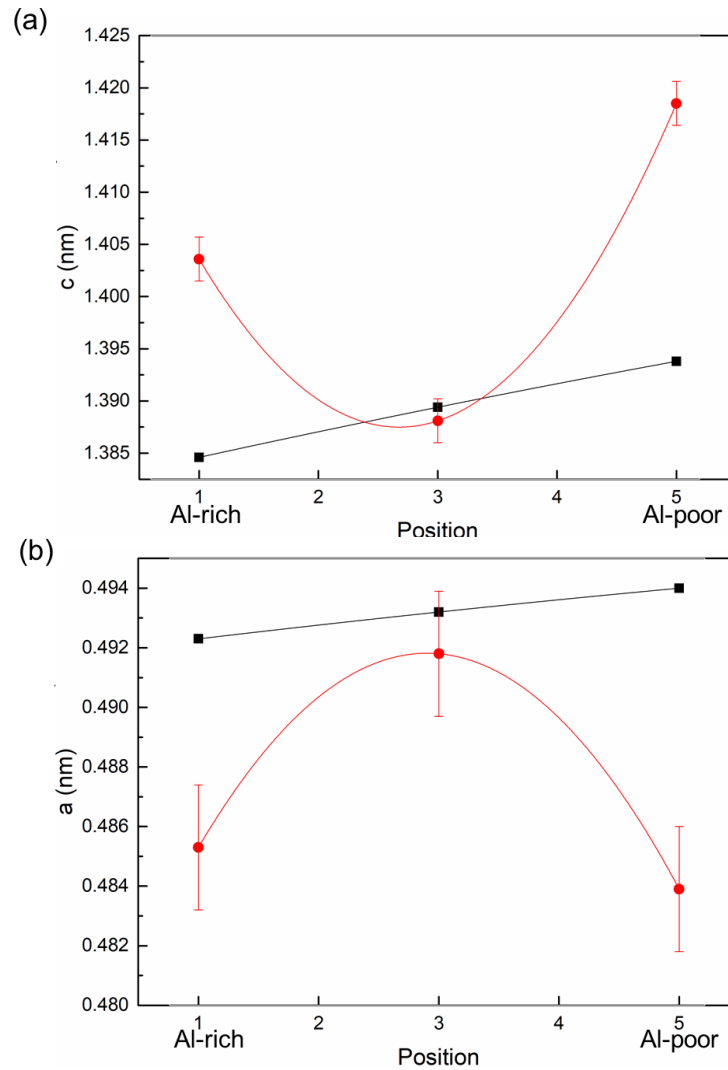


Fig. 96 The lattice constants  $a$  (below) and  $c$  (above) versus the sample positions during deposition. ● (red solid circles) show the real lattice constants calculated from RSM; ■ (black solid squares) show the theoretical lattice constants calculated using data from PDF card No. 34-187 and No. 42-1468 (the ICDD-database) according to Vegard's law.

Texture evolution of the films is independent of the film composition. Here, X-ray pole figures taken from the (0006) and (10 $\bar{1}$ 10) reflections of the film deposited in Pos.3 are

shown in Fig. 97. A strong fiber texture grows in the  $c$ -axis which is observed from the (0006) reflection, and 3-fold symmetry ( $10\bar{1}10$ ) reflections of the films illustrate no or few stacking faults in the films, which is similar to the results shown for pure  $V_2O_3$  films grown on the substrates without plasma-etching before deposition (described in section 4.2). This should be related to the fact that the V-Al-O films were also deposited on the substrate without plasma-etching.

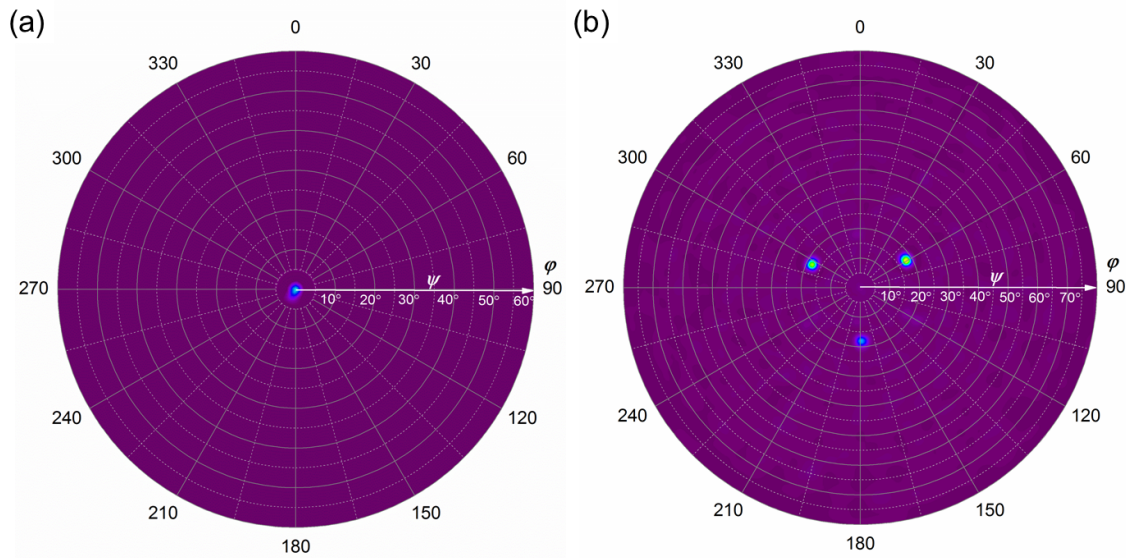


Fig. 97 X-ray pole figures taken from (a) the (0006) reflections and (b) the ( $10\bar{1}10$ ) reflections of the  $\alpha$ - $(V_{1-x}Al_x)_2O_3$  film deposited on the substrate without plasma-etching process.

More information on the microstructure of the film deposited in Pos. 3 is obtained from TEM analyses as shown in Fig. 98. Fig. 98 (a) shows a cross-section BF TEM image of the  $\alpha$ - $(V_{1-x}Al_x)_2O_3$  film with a very flat surface, deposited on the  $\alpha$ - $Al_2O_3$  substrate, indicating the film was grown in a layer by layer mode. The SAED patterns dominated by both the film and the substrate are shown in Fig. 98 (b), indicating the epitaxial relationships between the film and the substrate are  $(0001)_{film} // (0001)_{substrate}$  and  $(10\bar{1}0)_{film} // (10\bar{1}0)_{substrate}$ . The (0006) reflections were observed which should be forbidden, due to the second diffraction as discussed in the previous chapters. The lattice plane distances of the film near the interface and the surface were obtained from HRTEM images shown in Fig. 98 (c) and (d), respectively. The lattice plane distances of the film near

the interface were  $d_{0006} = 0.222$  nm and  $d_{11\bar{2}0} = 0.233$  nm, which are smaller in both direction than that of the film near the surface (i.e. far away from the interface,  $d_{0006} = 0.233$  nm and  $d_{11\bar{2}0} = 0.244$  nm). This indicates that the layers grow in strained state at the beginning with an epitaxial relationship to the substrate, and then (after a certain thickness) the layers gradually tend to grow in a relaxed state.

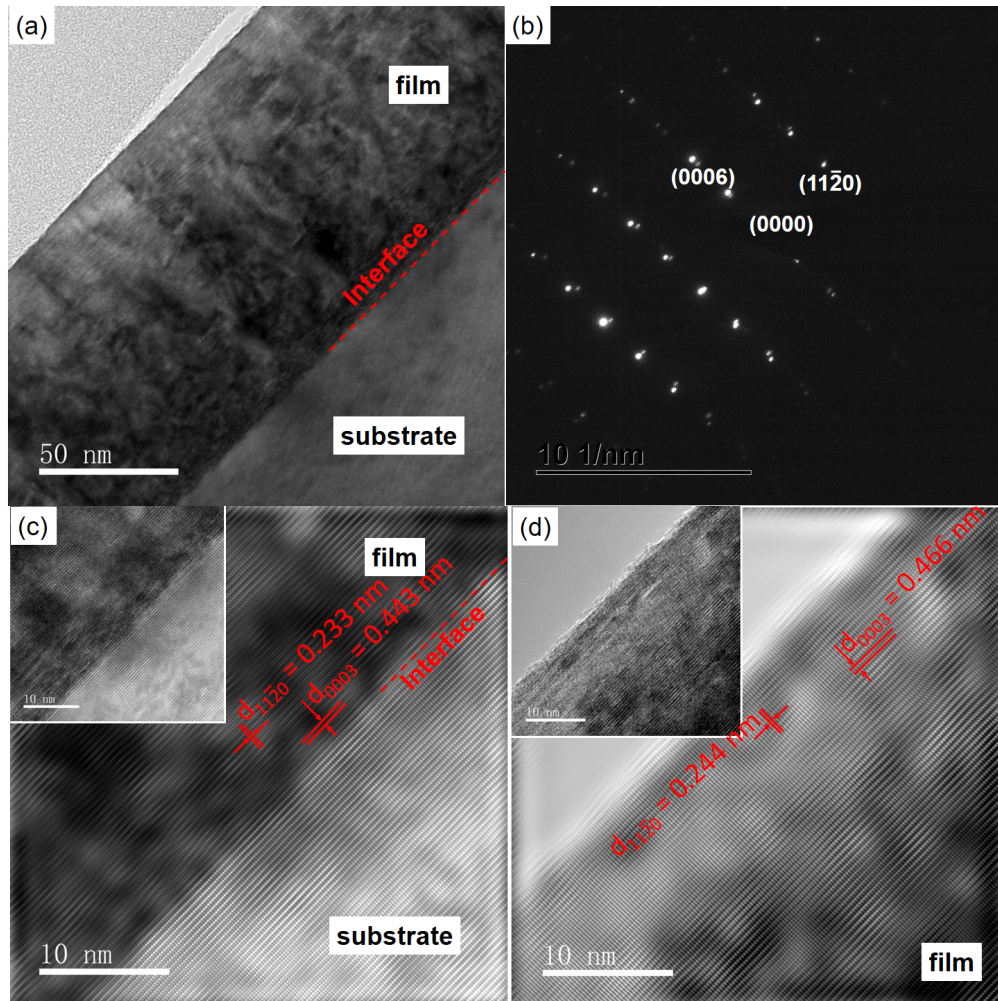


Fig. 98 TEM images of the  $\alpha$ -( $V_{1-x}Al_x$ ) $_2O_3$  film deposited in Pos. 3. (a) BF image showing a cross sectional view of the film grown on the  $\alpha$ - $Al_2O_3$  substrate. (b) SAED patterns revealing a partially epitaxial orientation relationship between the film and the substrate. (c) IFFT image of the HRTEM image shown in the inset which shows the interface between the substrate and the film. (d) IFFT image of the HRTEM image shown in the inset which shows the film.

### 4.4.3 Raman spectroscopy analysis

The Raman spectra of the  $\alpha$ -( $V_{1-x}Al_x$ ) $_2O_3$  thin films with different composition are shown in Fig. 99. Two different features are shown in these Raman spectra: the peaks marked with “s” are attributed to the  $\alpha$ - $Al_2O_3$  substrates; the others are assigned to the films. The referenced Raman active modes of the pure  $V_2O_3$  cited from ref. [247–249,251] are shown in the gray areas in Fig. 99. The spectra of the samples in the Pos. 1, 2, 4 and 5 show two strong bands in the range from 150  $cm^{-1}$  to 300  $cm^{-1}$ . The spectrum of the sample in Pos. 3 is different from others. The first  $E_g$  and  $A_{1g}$  modes merge into one band at around 229  $cm^{-1}$  in case of the film deposited in Pos. 3. The Raman spectra are fitted by Gaussian curves in Origin. Then, the dependence of the two  $A_{1g}$  modes on the sample position during deposition are shown in Fig. 100. The Raman shifts of the  $A_{1g}$  modes around 245  $cm^{-1}$  and 535  $cm^{-1}$  dependent on the sample positions show the same trend. The  $A_{1g}$  modes of the film with less V concentration shift towards the lower frequency, because of the variation of the atom distances changes the phonon frequency.

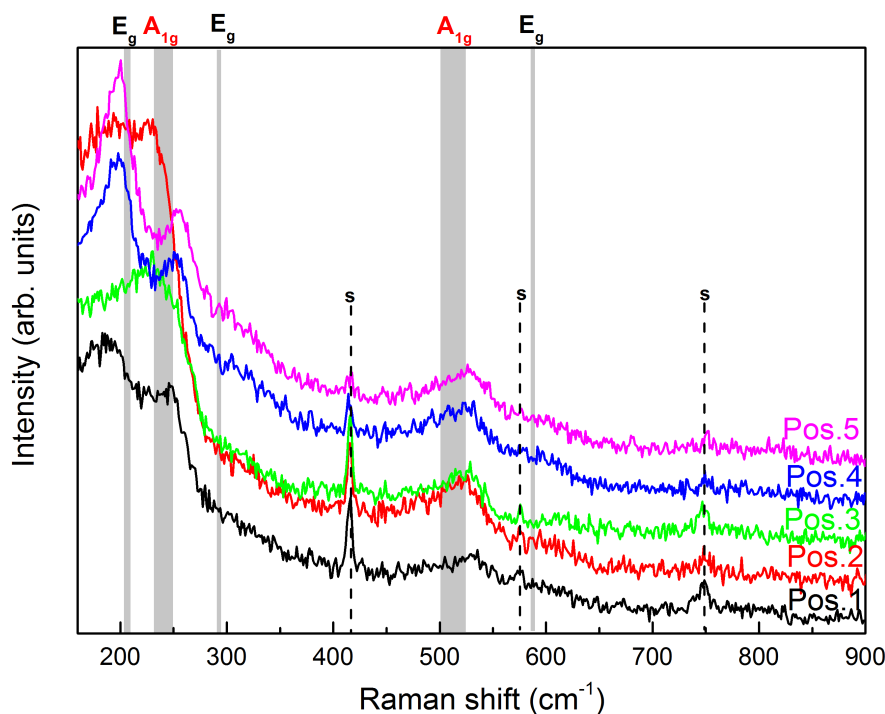


Fig. 99 Raman spectra of the  $\alpha$ -( $V_{1-x}Al_x$ ) $_2O_3$  thin films deposited on the  $\alpha$ - $Al_2O_3$  substrates in different positions related to the target. “s” indicates the reflexes corresponding to the substrates. The gray areas refer to the Raman active modes of pure  $V_2O_3$  measured at room temperature according to ref. [247–249,251].

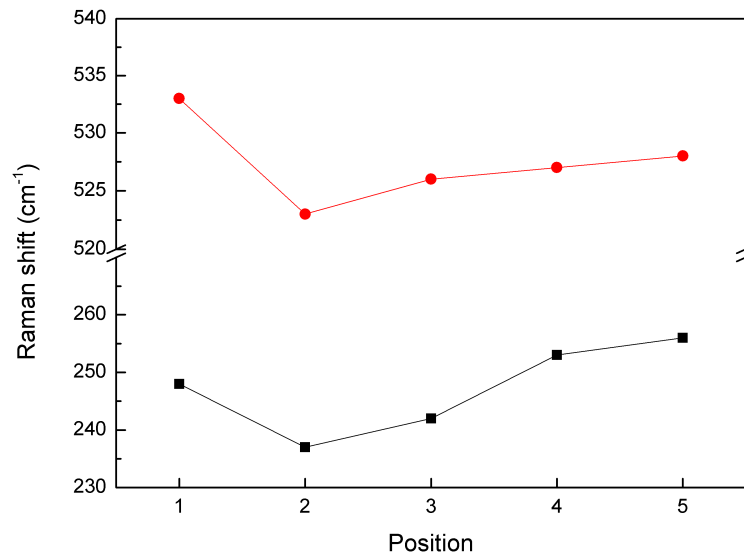


Fig. 100 Dependence of Raman shift of the two  $A_{1g}$  modes on the sample position. The black curve indicates the Raman shift of the first  $A_{1g}$  mode dependent on the sample position. The red curve indicates the Raman shift of the second  $A_{1g}$  mode dependent on the sample position.

#### 4.4.4 Infrared absorption spectroscopy analysis

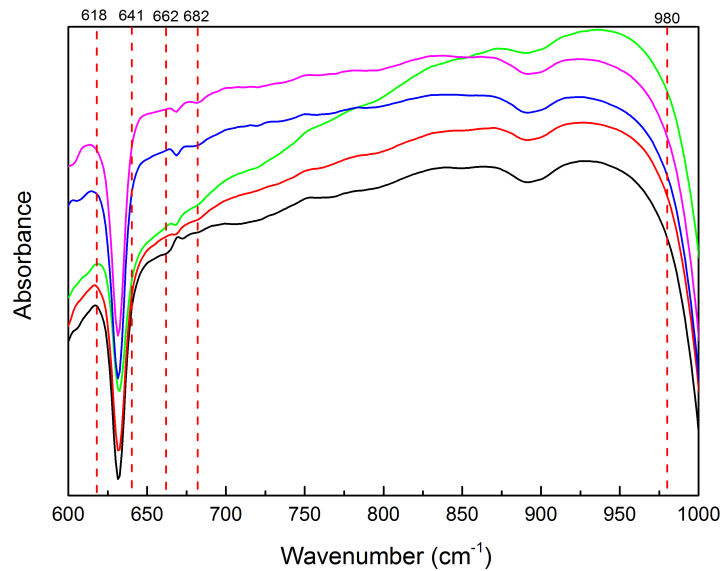


Fig. 101 The IRRAS spectra of the  $\alpha$ - $(V_{1-x}Al_x)_2O_3$  thin films with different composition deposited on  $\alpha$ - $Al_2O_3$  substrates. The red dashed lines give the IR bands cited from ref. [139]. The curves with different colors indicate the films deposited in different positions (black, red, green, blue, and magenta represent the samples deposited in Pos. 1 to Pos. 5 respectively).

Further, the IRRAS spectra of the  $\alpha$ -(V<sub>1-x</sub>Al<sub>x</sub>)<sub>2</sub>O<sub>3</sub> thin films deposited in different sample positions are shown in Fig. 101. Except for the film with the lowest V content which was deposited in Pos. 3, the absorbance band position, the width and the intensity of the bands are nearly independent of the film composition. In general, the absorbance of the film with the lowest V increases in the range of 600 cm<sup>-1</sup> to 950 cm<sup>-1</sup>.

#### 4.4.5 Optical properties characterization

Plots of  $(ah\nu)^2$  as a function of the photon energy are shown in Fig. 102 for the  $\alpha$ -(V<sub>1-x</sub>Al<sub>x</sub>)<sub>2</sub>O<sub>3</sub> thin films with different composition. The extrapolation of the photon energy by straight dashed lines to the horizontal ordinate gives the  $E_g$  values.  $E_g$  and  $B$  values in Tauc's equation (Eq.(18)) are shown in Table 20. The direct band gap of  $\alpha$ -Al<sub>2</sub>O<sub>3</sub> is 8.8 eV in ref. [62], that of V<sub>2</sub>O<sub>3</sub> is about 1.9 eV from our experiments and 1 eV cited from [184]. In case of the V-Al-O films of this study, the  $E_g$  values are from 3.82 eV to 4.83 eV. The  $E_g$  value of Al<sub>2</sub>O<sub>3</sub> is larger than that of V<sub>2</sub>O<sub>3</sub>, so the  $E_g$  value increases with substitution of Al for V. On the other hand, the  $E_g$  value is also influenced by the crystal quality. The better crystal quality, the lower  $E_g$  value. The dependence of the band gap on the sample deposited position is shown in Fig. 103. The films deposited at the sample Pos. 3 reach the minimum  $E_g$  value because the crystal quality is the best among five samples.

Table 20 Optical parameters of the  $\alpha$ -(V<sub>1-x</sub>Al<sub>x</sub>)<sub>2</sub>O<sub>3</sub> thin films ( $E_g$  is the band gap;  $B$  is a constant in Eq.(18)).

Pos.	$E_g$ (eV)	$B$ (10 <sup>24</sup> cm <sup>-1</sup> eV <sup>-1</sup> )
1	4.83	11.3
2	4.58	53.9
3	3.82	2.1
4	4.11	24.5
5	4.53	54.2

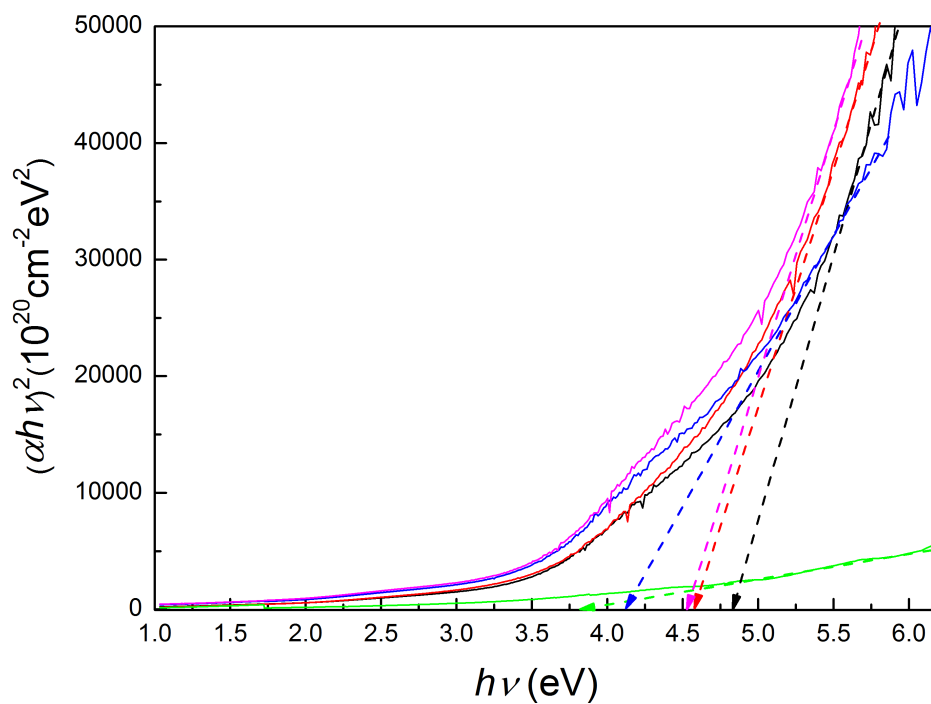


Fig. 102 Plots of  $(\alpha h\nu)^2$  vs.  $h\nu$  for the  $\alpha$ - $(V_{1-x}Al_x)_2O_3$  thin films with different composition, deposited on  $\alpha$ - $Al_2O_3$  substrates. The curves with different colors indicate the films deposited in different positions (black, red, green, blue, and magenta for the Pos. 1 to Pos. 5 respectively).

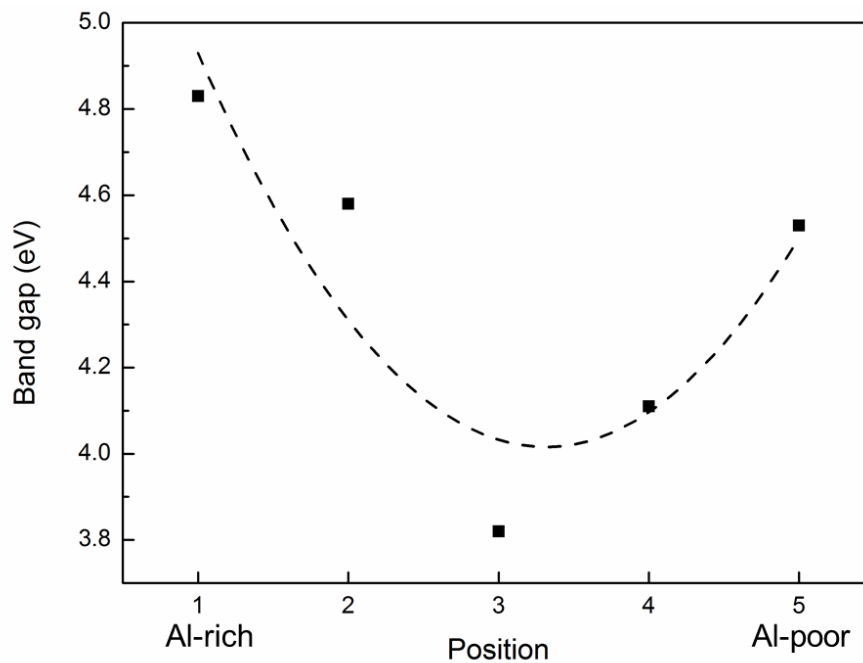


Fig. 103 Dependence of the band gap of the films on the sample positions.

## 4.5 $\alpha$ -(V<sub>1-x</sub>Cr<sub>x</sub>)<sub>2</sub>O<sub>3</sub> solid solution thin films grown on *c*-plane $\alpha$ -Al<sub>2</sub>O<sub>3</sub> substrates

In this chapter, The V-Cr-O thin films synthesized on *c*-plane  $\alpha$ -Al<sub>2</sub>O<sub>3</sub> substrates by a segmented target (one half is the Cr<sub>2</sub>O<sub>3</sub> (100 at. %); the other half is V<sub>2</sub>O<sub>3</sub> (100 at. %)) at 400 °C were analyzed. The samples were placed as shown in Fig. 17 (e). In section 4.1.4 and 4.2.4, it is proved that the etching process on the substrates before deposition negatively effects on the film epitaxial growth. Therefore, plasma-etching is not applied to the substrates before deposition in this chapter. Films with a thickness of 1.4  $\mu$ m were prepared for the EPMA analysis, and films with thickness of 308 nm for the structural and optical measurements.

### 4.5.1 Chemical composition

The chemical composition of the films is displayed in Table 21. The composition is dependent on the position of the substrates during the deposition. A gradient variation of the Cr and V concentration from Pos. 1 (Cr-rich side) to Pos. 5 (V-rich side) can be observed.

The relative concentration of Cr is defined as  $x$ :

$$x = \frac{\omega(\text{Cr})}{\omega(\text{Cr}) + \omega(\text{V})} \quad (27)$$

And the deviation from the ideal metal to oxygen stoichiometry  $\delta$  is given by:

$$\delta = 3 \cdot \frac{\omega(\text{Cr}) + \omega(\text{V})}{\omega(\text{O})} - 2 \quad (28)$$

where  $\omega(\text{Cr})$  and  $\omega(\text{V})$  are the atomic percentage of Al and Cr in the films, respectively.

However, all films are V-rich, due to the higher deposition rate of V<sub>2</sub>O<sub>3</sub> compared to Cr<sub>2</sub>O<sub>3</sub>. The deviation from the ideal metal to oxygen stoichiometry  $\delta$  is very small (near zero) and can be ignored in the following discussions. The metal/oxygen stoichiometry of these films is very close to the ideal value of 2/3. The concentration of contaminations (C, N and Ar) is between 1.1 at. % and 1.2 at. %, which can be ignored.

Table 21 The chemical composition of the V-Cr-O films deposited on the substrates in different positions related to the target:  $x$  and  $\delta$  describe the relative Cr concentration and the deviation from a perfect theoretical stoichiometry in Eq. (27) and (28) respectively (standards used for calibrating see section 3.2.1).

Pos.	Cr (at. %)	V (at. %)	O (at. %)	C (at. %)	N (at. %)	Ar (at. %)	$x$	$\delta$
1	$4.5 \pm 0.29$	$35.1 \pm 0.11$	$59.2 \pm 0.35$	$0.8 \pm 0.04$	$0.4 \pm 0.01$	0.0	0.12	0.01
2	$3.7 \pm 0.19$	$35.3 \pm 0.26$	$59.9 \pm 0.42$	$0.7 \pm 0.01$	$0.4 \pm 0.03$	0.0	0.10	-0.05
3	$3.5 \pm 0.10$	$35.7 \pm 0.22$	$59.7 \pm 0.27$	$0.7 \pm 0.03$	$0.4 \pm 0.02$	0.0	0.09	-0.04
4	$3.4 \pm 0.06$	$36.0 \pm 0.13$	$59.5 \pm 0.17$	$0.7 \pm 0.04$	$0.4 \pm 0.02$	0.0	0.08	-0.01
5	$2.9 \pm 0.15$	$35.8 \pm 0.28$	$60.2 \pm 0.47$	$0.7 \pm 0.05$	$0.4 \pm 0.02$	0.0	0.07	-0.07

#### 4.5.2 Structural analysis

Fig. 104 shows the XRD  $\theta - 2\theta$  patterns of the V-Cr-O thin films with different composition deposited on the  $\alpha$ -Al<sub>2</sub>O<sub>3</sub> substrates in different sample positions. These XRD analysis indicated a single crystalline corundum-type phase for all deposited films. Only (0006) and (00012) reflections of the films and the  $\alpha$ -Al<sub>2</sub>O<sub>3</sub> substrates were observed in the XRD Bragg-Brentano geometry as shown in Fig. 104 (a). Since the intensities of the (00012) reflections are very weak and the reflections are broad compared to the (0006) reflections, only the (0006) reflections are shown in Fig. 104 (b). The (0006) reflections attributed to the films are observed next to the  $\alpha$ -Al<sub>2</sub>O<sub>3</sub> reflections. The FWHM values of the (0006) reflections of the films are between 0.07° to 0.13°, which indicates good crystal quality of the films. The theoretical (0006) reflection of the Cr<sub>2</sub>O<sub>3</sub> and V<sub>2</sub>O<sub>3</sub> at  $2\theta = 39.749^\circ$  and  $38.514^\circ$  according to the PDF card No. 38-1479 and No. 34-187 from the ICDD-database, respectively, are marked as vertical dashed lines in Fig. 104. The (0006) reflections of the films shift from the side of theoretical Cr<sub>2</sub>O<sub>3</sub> to V<sub>2</sub>O<sub>3</sub> from the film deposited in Pos. 1 to Pos. 5, suggesting the increasing of the lattice plane distance  $d_{0006}$  value with decreasing Cr concentration (or increasing V concentration) as shown in Fig. 105. The lattice plane distance  $d_{0006}$  (or lattice constant  $c$ ) of all the films are larger than that the pure Cr<sub>2</sub>O<sub>3</sub> and for most of the films they are smaller than for pure V<sub>2</sub>O<sub>3</sub>, resulting from the ionic radius of V<sup>3+</sup> which is larger than the one of Cr<sup>3+</sup> [182]. However, the lattice plane distance  $d_{0006}$  of the film deposited in the sample Pos. 5 are larger than the pure V<sub>2</sub>O<sub>3</sub> which could be caused by the defects in the crystals.

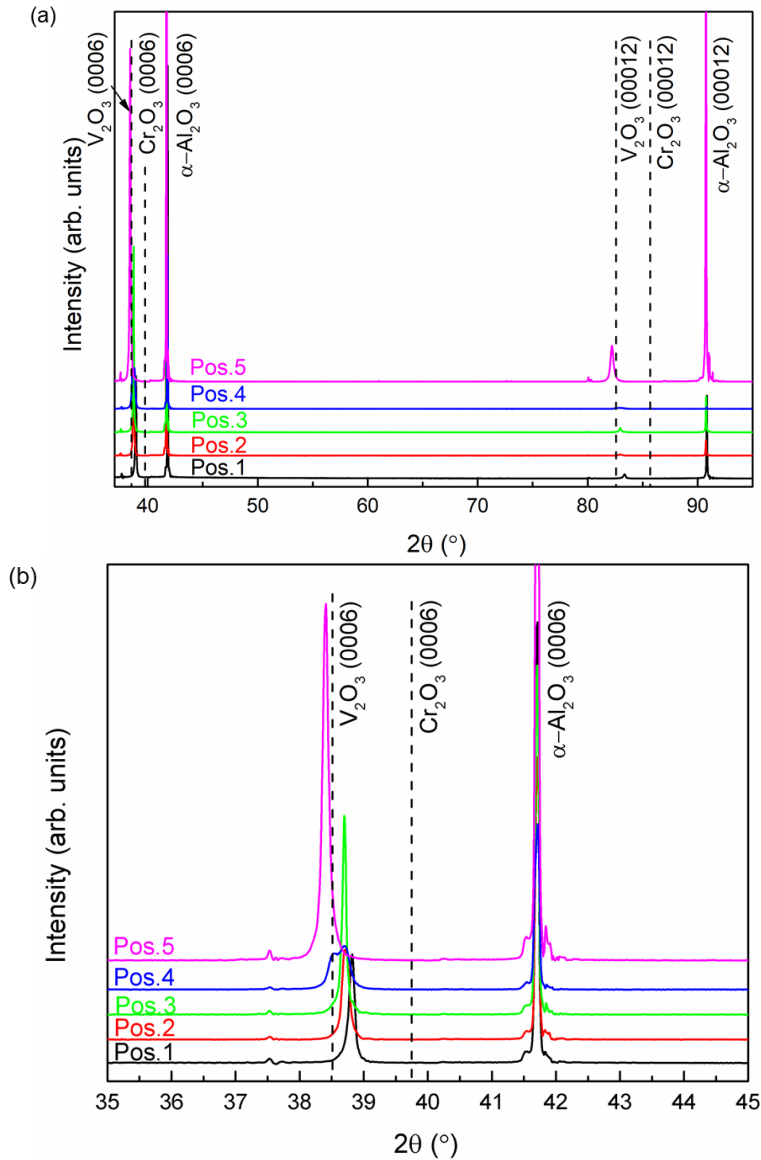


Fig. 104  $\theta - 2\theta$  XRD patterns of the  $\alpha-(V_{1-x}Cr_x)_2O_3$  films with different composition ( $x = 0.115, 0.094, 0.088, 0.087$  and  $0.078$ ) deposited on the  $\alpha-Al_2O_3$  substrates in the sample Pos. 1 to 5, respectively. The (0006) reflections of the films are observed at lower diffraction angle compared to the substrates. The dashed lines indicate the theoretical (0006) reflection positions of  $Cr_2O_3$  and  $V_2O_3$  according to the PDF card No. 38-1479 and No. 34-187 from the ICDD-database. (a)  $\theta - 2\theta$  XRD patterns in large range of the diffraction angle. (b) the (0006) reflections of the films and the substrates in more detail for a narrow range of the diffraction angle.

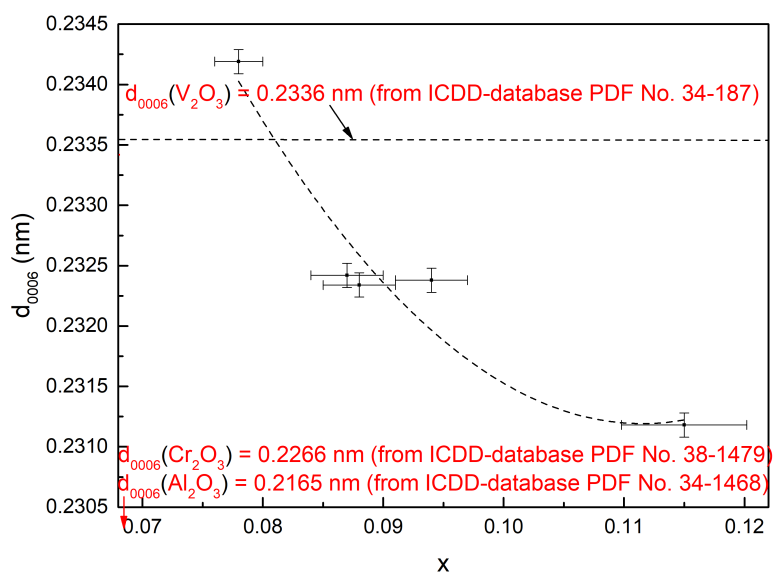


Fig. 105 Dependence of the lattice plane distance  $d_{0006}$  on the Cr concentration of the films (the abscissa is the coefficient  $x$  in  $\alpha\text{-(V}_{1-x}\text{Cr}_x\text{)}_2\text{O}_3$ ). The dashed horizontal line represents the theoretical  $d_{0006}$  value of  $\text{V}_2\text{O}_3$ ,  $\text{Cr}_2\text{O}_3$  and  $\text{Al}_2\text{O}_3$  according to the PDF card No. 34-187, No. 38-1479, and No. 42-1468 from the ICDD-database, respectively. ( $d_{0006}(\text{V}_2\text{O}_3) = 0.2336$  nm,  $d_{0006}(\text{Cr}_2\text{O}_3) = 0.2266$  nm, and  $d_{0006}(\text{Al}_2\text{O}_3) = 0.2165$  nm) .

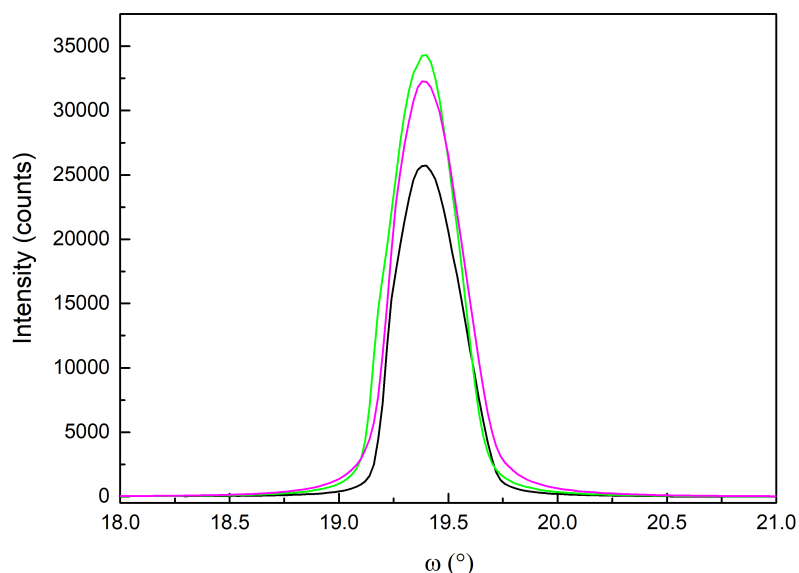


Fig. 106 XRD rocking curves ( $\omega$ -scans) of the (0006) reflections of the  $\alpha\text{-(V}_{1-x}\text{Cr}_x\text{)}_2\text{O}_3$  films with  $x = 0.12$ ,  $0.09$ , and  $0.07$  deposited in Pos. 1 (black), Pos. 3 (green) and Pos. 5 (magenta). The FWHM values of these mosaic spreading reflections are  $0.358^\circ$ ,  $0.366^\circ$  and  $0.365^\circ$ , respectively.

Fig. 106 shows the mosaic spreading of the (0006) reflections of the films of different

composition. The FWHM values of these reflections are between  $0.36^\circ$  and  $0.37^\circ$ , indicating the good epitaxial quality of the films with respect to the substrates. It is difficult to compare the epitaxial quality of the films from the mosaic spreading because of the similar FWHM. Thus, RSM analysis was carried out.

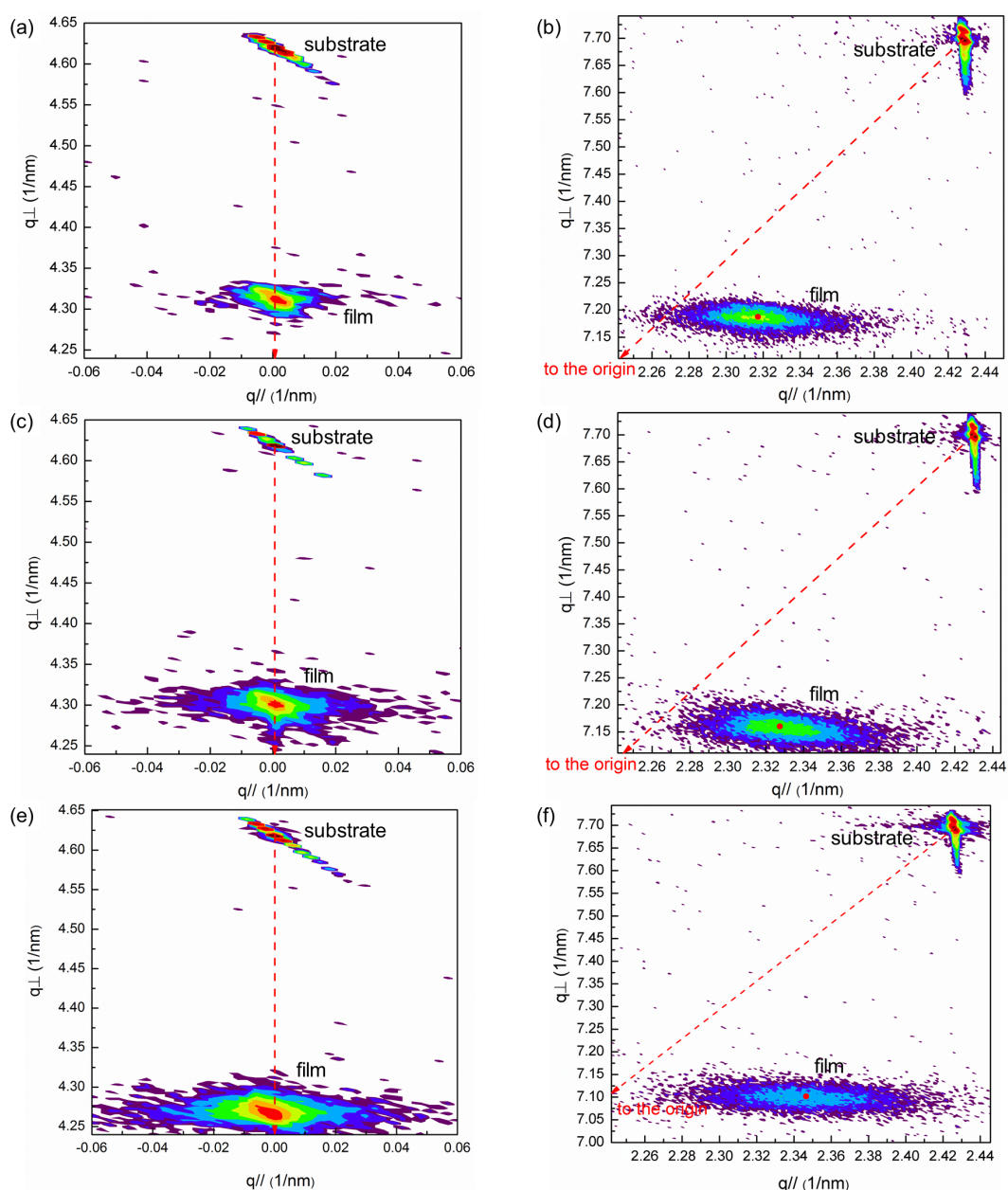


Fig. 107 RSM results of the V-Cr-O films deposited on  $\alpha$ -Al<sub>2</sub>O<sub>3</sub> substrates in different positions related to the target: (a) and (b) are in Pos. 1; (c) and (d) are in Pos. 3; (e) and (f) are in Pos. 5. (a), (c) and (e) are the symmetric (0006) reflections, and (b), (d) and (f) are the asymmetric (10 $\bar{1}$ 10) reflections.

Fig. 107 shows the symmetric (0006) and asymmetric (10 $\bar{1}$ 10) RSM of the  $\alpha$ -(V<sub>1-x</sub>Cr<sub>x</sub>)<sub>2</sub>O<sub>3</sub> films of different composition grown on the  $\alpha$ -Al<sub>2</sub>O<sub>3</sub> substrates. From the (0006) reciprocal lattice points of all the films it can be seen that  $q_{//}$  is nearly zero, suggesting a strong  $c$ -axis texture. Only  $q_{//}$  of the film deposited in the sample Pos. 3 is exactly equal to 0 as shown in Fig. 107 (c), which indicates there is almost no tilt of the (0006) lattice planes against the substrates when the films are deposited under the center of the segmented target. From the (10 $\bar{1}$ 10) reciprocal lattice points it can be seen that the lines connecting the reflections of the substrates and the origins do not through the reflections of the films, indicating partially epitaxial films are grown on the substrate. The  $q_{//}$  values of the center of the (10 $\bar{1}$ 10) reflections of the films deposited in the sample Pos. 1, Pos. 3 and Pos. 5 are 2.316 1/nm, 2.327 1/nm, and 2.346 1/nm, respectively, which shows a trend of the films shifting to the substrates where  $q_{//} = 2.428$  1/nm. The lattice parameter  $a$  of the films is more close to the  $a$  value of the substrate with increasing V concentration (or decreasing Cr concentration), indicating the epitaxial quality of the films with respect to the substrate is better. On one hand, the lattice mismatch between V<sub>2</sub>O<sub>3</sub> and Al<sub>2</sub>O<sub>3</sub> is larger than the mismatch between Cr<sub>2</sub>O<sub>3</sub> and Al<sub>2</sub>O<sub>3</sub> which has adverse effect on the epitaxial growth of V-Cr-O films of higher V concentration on the Al<sub>2</sub>O<sub>3</sub> substrate. On the other hand, the growth of V-rich films in crystalline state is much easier to reach at low temperatures. However, the larger the V concentration in the films, the better the epitaxial quality of the films. The theoretical and experimental lattice parameters  $a$  and  $c$  are calculated from the reciprocal lattice points and are shown in Fig. 108. The theoretical lattice parameters  $a$  and  $c$  are inversely linear with respect to the relative Cr concentration  $x$ , due to the ionic radius of Cr<sup>3+</sup> (0.0615 nm) which is smaller than that of V<sup>3+</sup> (0.064 nm) [182]. The experimental lattice parameters  $a$  decreases and  $c$  increases with decreasing Cr concentration (or increasing V concentration) of the films. The variation tendency of the experimental lattice parameter  $c$  is same as that of the theoretical values, while the tendency of the  $a$  value is inverse. This suggests a straining in the interface between the films and the substrates, maybe caused by the locally epitaxial growth. The deviation between the experimental values and the theoretical values is the smallest when the film is deposited in the sample Pos. 3. The misfit of the in-plane interface between the film and the substrate are 4.8 %, 4.3 %, and 3.4 %, respectively, which indicates the films with higher V content

possess higher epitaxial quality.

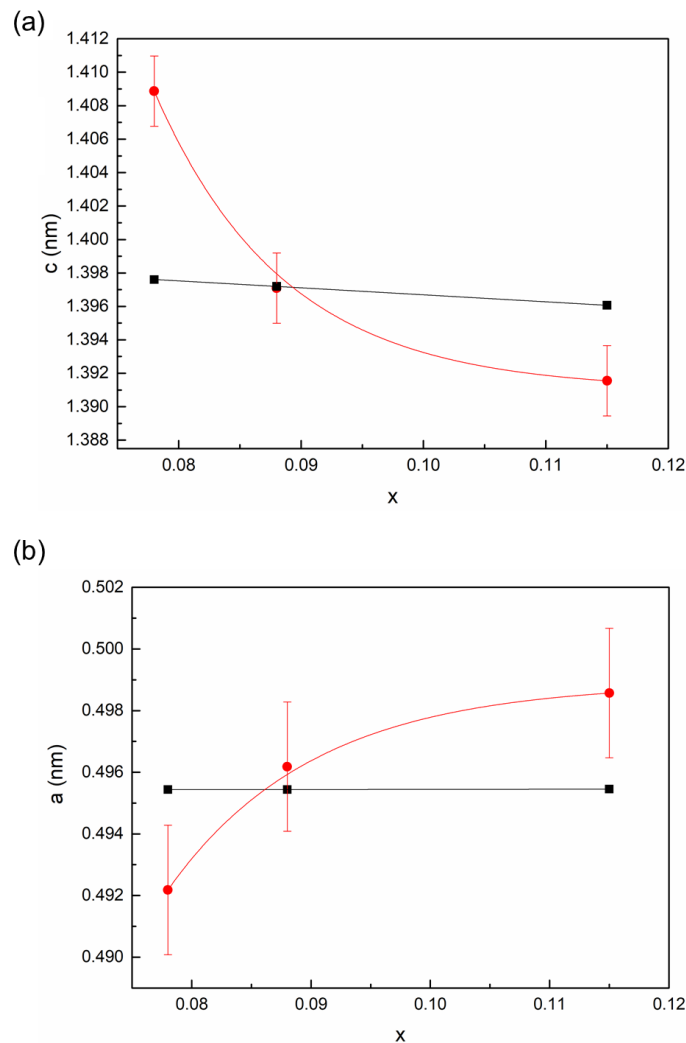


Fig. 108 The lattice constants (a)  $c$  and (b)  $a$  versus Cr concentration  $x$ . ● (red solid circles) show the real lattice constants calculated from RSM data; ■ (black solid squares) show the theoretical lattice constants calculated using data from PDF card No. 34-187 and No. 38-1479 (the ICDD-database) according to Vegard's law.

Texture evolution of the  $\alpha$ - $(V_{1-x}Cr_x)_2O_3$  films is independent of the film composition. X-ray pole figures taken from the (0006) and  $(10\bar{1}10)$  reflections of the V-Cr-O film which is deposited in the sample Pos. 3 are shown in Fig. 109 representative of all films. A strong fiber texture grows in the  $c$ -axis which is observed from the (0006) reflections. 3-fold symmetry from  $(10\bar{1}10)$  reflections of the films as  $\alpha$ - $Al_2O_3$  substrate are observed in Fig. 109 (b), which illustrates there are almost no stacking faults in the films. Only

3-fold symmetry from  $(10\bar{1}10)$  reflections is observed which may be explained by the thought that there is no plasma-etching process on the pure substrate before deposition and the substrate surface is perfect.

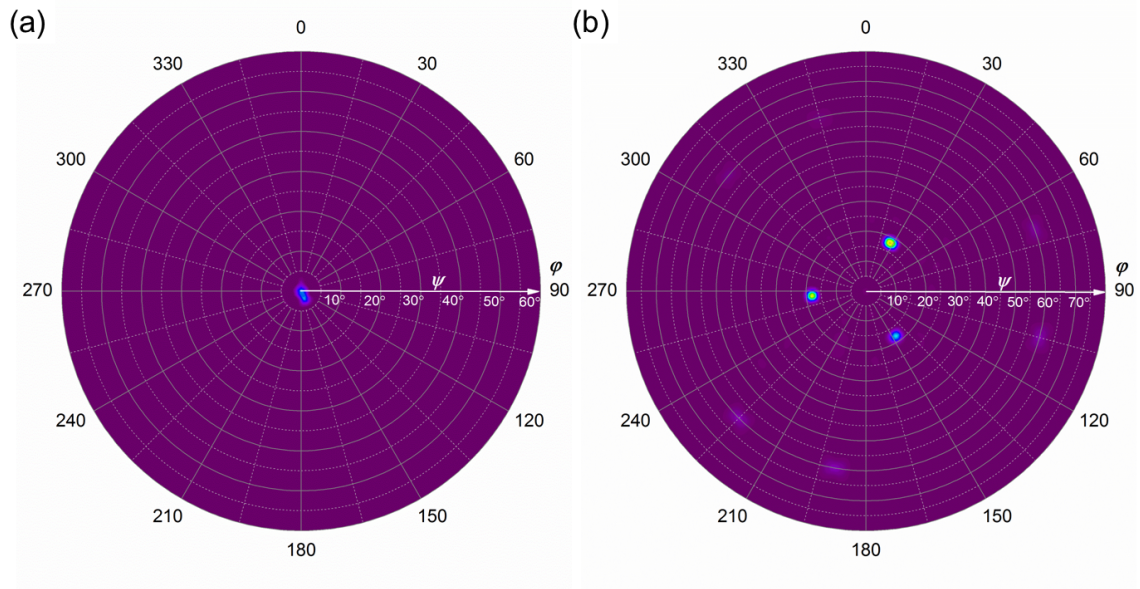


Fig. 109 X-ray pole figures taken from (a) the  $(0006)$  reflection and (b) the  $(10\bar{1}10)$  reflection of the  $\alpha\text{-}(\text{V}_{1-x}\text{Cr}_x)_2\text{O}_3$  film deposited on the substrate without plasma etching process.

Detailed information on the microstructure of the film deposited in Pos. 3 is obtained from TEM analysis as shown in Fig. 110. (a) shows the cross-section BF TEM image of the  $\alpha\text{-}(\text{V}_{1-x}\text{Cr}_x)_2\text{O}_3$  film with a very flat surface, deposited on the  $\alpha\text{-Al}_2\text{O}_3$  substrate, from which dislocation lines are visible. Fig. 110 (b) shows the SAED patterns dominated by both the film and the substrate, indicating the epitaxial relationships between the film and the substrate are  $(0001)_{\text{film}} // (0001)_{\text{substrate}}$  and  $(11\bar{2}0)_{\text{film}} // (11\bar{2}0)_{\text{substrate}}$ . The inner spots are from the film and the outer ones are from the substrate. The spots of the film in the SAED are circular shaped which is similar to the perfect single crystal substrate, indicating the perfect crystal quality of the film. Fig. 110 (c) shows the HRTEM image of the interface between the substrate and the film, which shows a fully epitaxial growth over the complete film in the thickness and laterally. The lattice planes are running through the interface between the substrate and the film. Only little disturbance caused by dislocations are present in or near the interface between the substrate and the film. The

HRTEM image of the film is shown in Fig. 110 (d). No faceted grains are present. The lattice plane distances of the film are  $d_{0006} = 0.227$  nm and  $d_{11\bar{2}0} = 0.232$  nm. The  $(11\bar{2}0)$  lattice plane distance of the substrate is 0.238 nm. The strain between the film and the substrate is only 2.5 %, indicating the film were grown near fully epitaxial on the substrate.

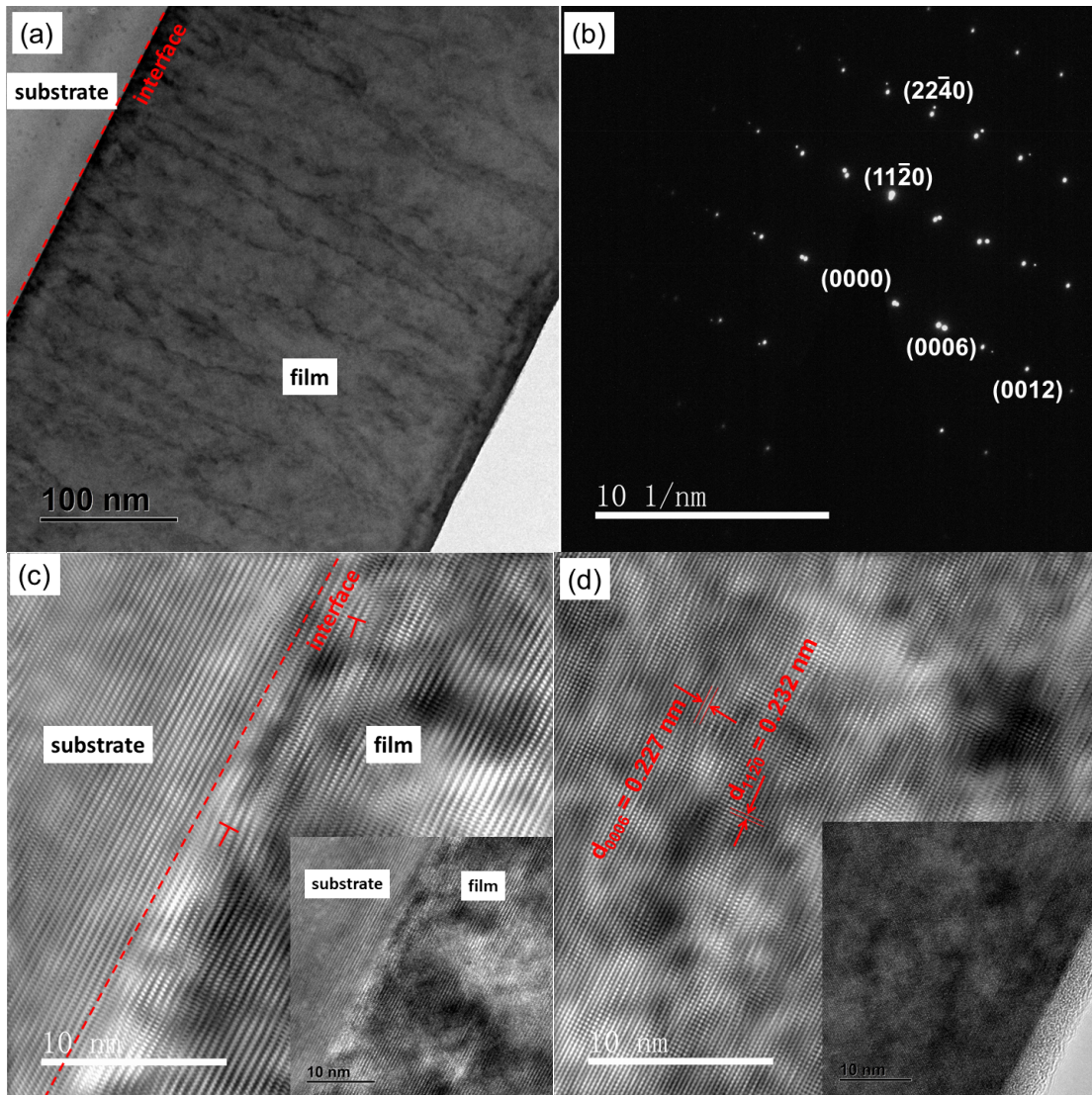


Fig. 110 TEM images of the  $\alpha$ -(V<sub>1-x</sub>Cr<sub>x</sub>)<sub>2</sub>O<sub>3</sub> film deposited in Pos. 3. (a) BF image showing a cross sectional view of the film grown on the  $\alpha$ -Al<sub>2</sub>O<sub>3</sub> substrate. (b) SAED patterns revealing an epitaxial orientation relationship between the film and the substrate. (c) IFFT image of the HRTEM image shown in the inset, pointing to the interface between the substrate and the film. (d) IFFT image of the HRTEM image shown in the inset, describing the film.

### 4.5.3 Raman spectroscopy analysis

The Raman spectra of the V-Cr-O thin films of different composition deposited in different sample positions are shown in Fig. 111. Only the features which are assigned to the films are shown in these Raman spectra. The referenced Raman active modes of the pure  $V_2O_3$  cited from ref. [247–249,251] are marked by the gray areas and those of the pure  $Cr_2O_3$  cited from ref. [230,242–244] are marked by the cyan areas in Fig. 111. The  $A_{1g}$  modes with the highest intensity shift from  $255\text{ cm}^{-1}$  for the Cr-rich side film deposited in Pos. 1 to  $209\text{ cm}^{-1}$  for the V-rich side film deposited in Pos. 5. The second  $A_{1g}$  modes shift from  $519\text{ cm}^{-1}$  for the Cr-rich side film deposited in Pos. 1 to  $511\text{ cm}^{-1}$  for the V-rich side film deposited in Pos. 5. The Raman spectra show a significant shift of phonon frequency with the  $(000l)$  lattice plane distance. The Raman  $A_{1g}$  mode shifts to the smaller wavenumber value side with increasing the  $(000l)$  lattice plane distance (or lattice parameter  $c$ ). The Cr-rich films deposited in the sample Pos. 1 and Pos. 2 show a band at  $307\text{ cm}^{-1}$  which is close to the  $E_g$  mode of the  $Cr_2O_3$ , and the V-rich films show a band at  $298\text{ cm}^{-1}$  which is close to the  $E_g$  mode of the  $V_2O_3$  deposited at the sample Pos. 5. The lattice parameter  $c$  increases with increasing V (or decreasing Cr) concentration which could cause a decreasing of the Raman frequency of the  $A_{1g}$  mode.

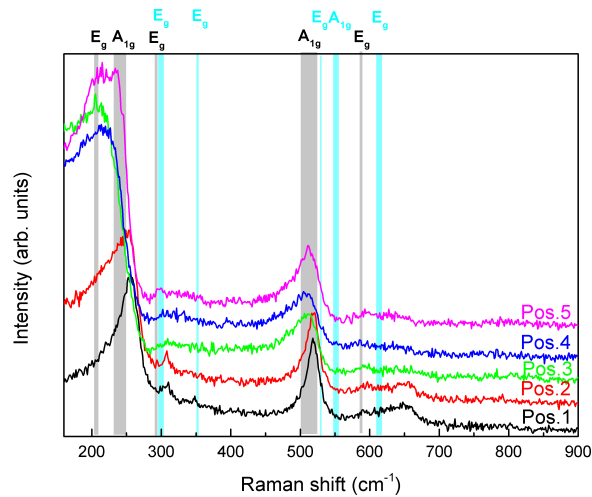


Fig. 111. Raman spectra of the V-Cr-O films of different composition deposited on  $\alpha\text{-Al}_2\text{O}_3$  substrates. The films vary from the Cr-rich side to Cr-poor side from Pos. 1 to Pos. 5. The cyan areas refer to the Raman active modes of pure  $Cr_2O_3$  cited from ref. [230,242–244]. The gray areas refer to the Raman active modes of pure  $V_2O_3$  cited from ref. [247–249,251].

#### 4.5.4 Infrared absorption spectroscopy analysis

Further, the IRRAS spectra of the V-Cr-O thin films of different composition deposited in different sample positions are shown in Fig. 112. In general, the absorbance of the films with the higher Cr concentration of  $x = 0.12$  and  $0.10$  increases in the range from  $600\text{ cm}^{-1}$  to  $935\text{ cm}^{-1}$ , and the absorbance of the films with the lower Cr concentration of  $x = 0.07 - 0.09$  is steady. There is an absorbance band near  $935\text{ cm}^{-1}$  for the films with the highest Cr concentration deposited in Pos. 1.

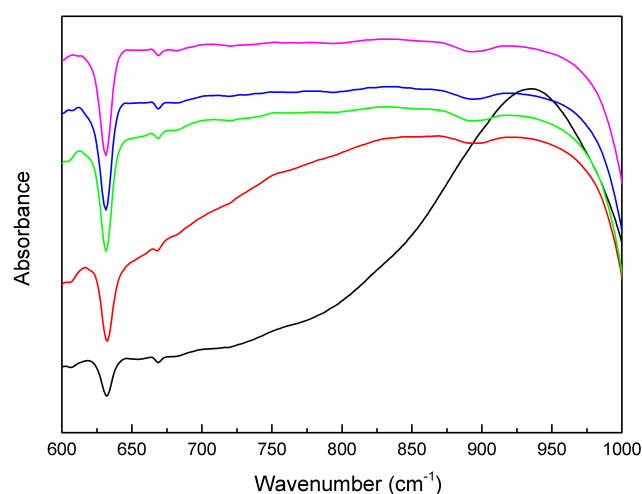


Fig. 112 The IRRAS spectra of the V-Cr-O thin films with different composition deposited on  $\alpha\text{-Al}_2\text{O}_3$  substrates. The curves with different colors indicate the films deposited in different positions (black, red, green, blue, and magenta represent the samples deposited in Pos. 1, Pos. 2, Pos. 3, Pos. 4 and Pos. 5 respectively).

#### 4.5.5 Optical properties characterization

The colors of the binary  $\text{V}_2\text{O}_3$  and  $\text{Cr}_2\text{O}_3$  thin films were black and light green, respectively, while that of the solid solution Cr-V-O films became more and more greenish with increasing Cr concentration. Plots of  $(ah\nu)^2$  as a function of the photon energy are shown in Fig. 113 for the V-Cr-O thin films of different composition. The extrapolation of the photon energy by straight dashed lines to the horizontal ordinate gives the  $E_g$  values.  $E_g$  and  $B$  values determined by Tauc's equation (Eq.(18)) are shown in Table 22. The direct band gap of  $\text{V}_2\text{O}_3$  and  $\text{Cr}_2\text{O}_3$  is 1 eV and 3.07 eV, respectively [184,200]. For V-Cr-O solid solution, the  $E_g$  values are between 1.21 eV and 2.06 eV. The dependence of the band gap on the film composition (Cr concentration) is shown in Fig. 114. The band gap

of the films increases with increasing Cr concentration, which is in agreement with the fact that the band gap of  $\text{Cr}_2\text{O}_3$  is larger than  $\text{V}_2\text{O}_5$ .

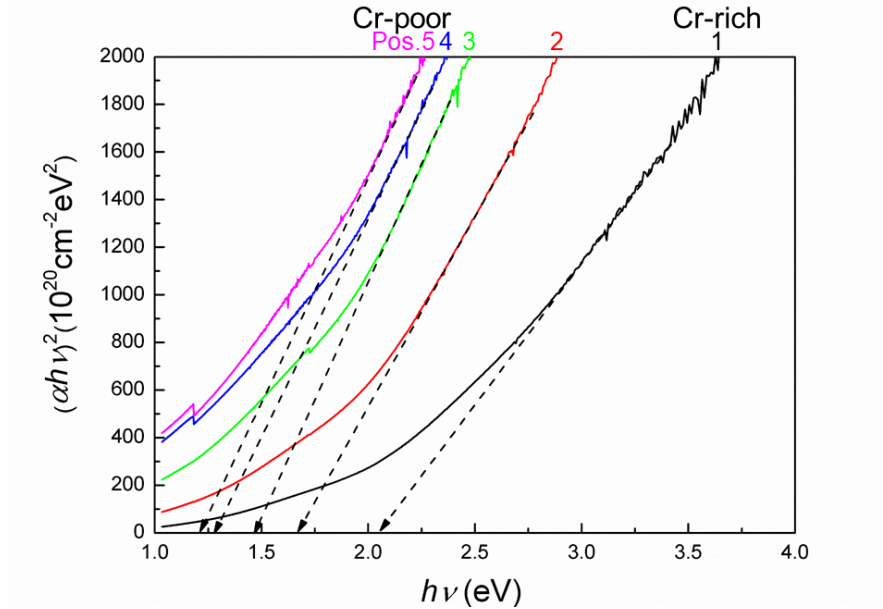


Fig. 113 Plots of  $(\alpha h\nu)^2$  vs.  $h\nu$  for the V-Cr-O thin films of different composition deposited on  $\alpha\text{-Al}_2\text{O}_3$  substrates. The sample positions are marked in the graph correspondingly.

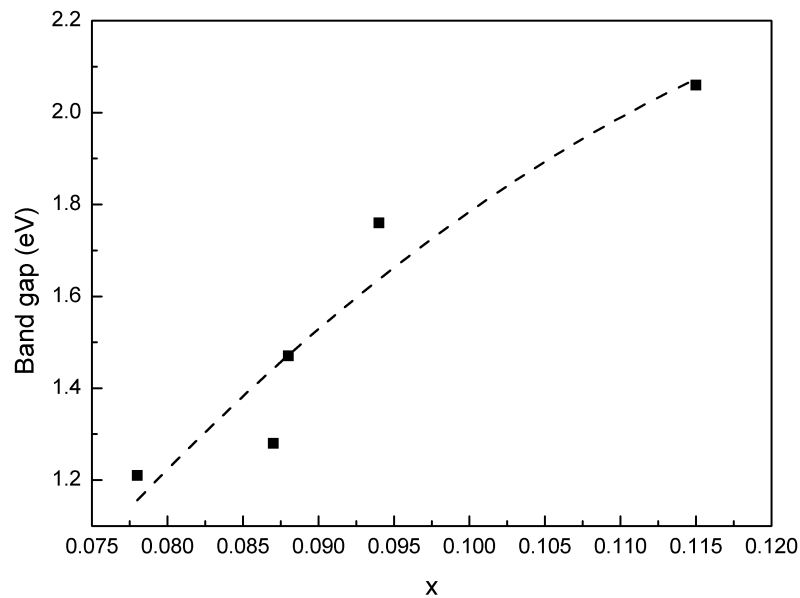


Fig. 114 Dependence of the band gap of the films on the relative Cr concentration  $x$ .

Table 22 Optical parameters of the V-Cr-O thin films ( $E_g$  is the band gap;  $B$  is a constant in Eq. (18)).

Pos.	x	$E_g$ (eV)	$B$ ( $10^{23} \text{ cm}^{-1} \text{ eV}^{-1}$ )
1	0.12	2.06	1.2
2	0.10	1.76	1.8
3	0.09	1.47	2.0
4	0.08	1.28	1.9
5	0.07	1.21	2.0

## 5 Summary discussion

Corundum-type structured (0001)-oriented stoichiometric binary ( $\text{Cr}_2\text{O}_3$  and  $\text{V}_2\text{O}_3$ ) and ternary (Al-Cr-O, V-Al-O, and V-Cr-O) thin films were locally epitaxially grown on (0001)  $\alpha\text{-Al}_2\text{O}_3$  substrates with a relationship of  $(0001)_{\text{film}} // (0001)_{\text{substrate}}$  and  $(10\bar{1}10)_{\text{film}} // (10\bar{1}10)_{\text{substrate}}$  at relatively low temperature ( $\leq 400$  °C) by non-reactive RF magnetron sputtering from ceramic targets.

There are many publications about the  $\text{Cr}_2\text{O}_3$  films growth as introduced in section 2.3. Polycrystalline  $\text{Cr}_2\text{O}_3$  thin films were grown on other substrates such as Si, Pt, or steel at low temperature below 500 °C but with post-treatment or only very thin films were obtained [99,129,132–134]. In this work, epitaxial  $\text{Cr}_2\text{O}_3$  (0001) films with strong texture were successfully and for the first time grown using  $\alpha\text{-Al}_2\text{O}_3$  (0001) substrates at 320 °C. Epitaxial  $\text{V}_2\text{O}_3$  films were grown on  $\alpha\text{-Al}_2\text{O}_3$  substrates at the temperature above 500 °C by electron-beam evaporation, PLD or reactive sputtering with metal target [31,143,154,156]. In this work, crystalline  $\text{V}_2\text{O}_3$  films were synthesized on  $\alpha\text{-Al}_2\text{O}_3$  substrates even at 150 °C by non-reactive RF magnetron sputtering from  $\text{V}_2\text{O}_3$  targets and the epitaxial quality increases with increasing the substrate temperature. Corundum-type  $(\text{Al}_x\text{Cr}_{1-x})_2\text{O}_3$  solid solution thin films were deposited on other non-isostructural substrates (e.g. cemented carbide, Si, WC and so on) at the temperature above 500 °C [162,168–171]. While locally epitaxial  $(\text{Al,Cr})_2\text{O}_3$  films were also for the first time grown on the iso-structural  $\alpha\text{-Al}_2\text{O}_3$  substrates at 320 °C. No much works on the  $(\text{V,Cr})_2\text{O}_3$  and  $(\text{V,Al})_2\text{O}_3$  thin films have been published. Corundum-type V-Cr-O thin films were deposited on the cemented carbide substrates by reactive RF magnetron sputtering of a segmented Cr-V target in an Ar/ $\text{O}_2$  atmosphere at the temperature of 350 °C, which was a previous work in our group [188]. In this work, corundum-type V-Cr-O thin films were developed to epitaxial  $(\text{V}_{1-x}\text{Cr}_x)_2\text{O}_3$  thin films grown on iso-structural  $\alpha\text{-Al}_2\text{O}_3$  substrates using a segmented ceramic target. For V-Al-O system, only V-Al-O bulks were published. In this work, epitaxial corundum structured  $(\text{V}_{1-x}\text{Al}_x)_2\text{O}_3$  films were obtained at 400 °C. Epitaxial corundum structured films were grown at lower temperature by using

the iso-structured substrates ( $\alpha$ -Al<sub>2</sub>O<sub>3</sub>) and stoichiometric composition was obtained by using the ceramic targets.

All these corundum-type films in crystalline structure show strong fiber texture in the *c*-axis. The crystal quality and lattice parameters are dependent on the substrate temperature and the film thickness. There is an effective way to increase the epitaxial quality of the crystalline films: by increasing the substrate temperature so that the adatoms have sufficient surface diffusion to remove the effects of atomic shadowing. The diffusion coefficients of the atoms are given by Arrhenius equation:

$$D = D_0 \exp(-Q/RT) \quad (29)$$

where  $D$  is diffusion coefficient;  $D_0$  is temperature-independent preexponential (m<sup>2</sup>/s);  $Q$  is the activation energy for diffusion (J/mol);  $R$  is Boltzmann's constant (8.31 J/mol·K);  $T$  is the absolute temperature (K) [260]. The diffusion coefficients of the atoms increase with increasing the substrate temperature. For example, the diffusion coefficients of O in Al<sub>2</sub>O<sub>3</sub> are  $2 \times 10^{-84}$  m<sup>2</sup>/s and  $5 \times 10^{-51}$  m<sup>2</sup>/s at the substrate without heating and 400 °C, respectively, which is calculated from Eq. (29) [260]. The diffusion coefficients of Al in Al<sub>2</sub>O<sub>3</sub> are  $10^{-66}$  m<sup>2</sup>/s and  $1.6 \times 10^{-41}$  m<sup>2</sup>/s at the substrate without heating and 400 °C, respectively. Oxygen diffusion coefficients are greater than metal in these Me<sub>2</sub>O<sub>3</sub> [261]. Increasing the substrate temperature will allow the arriving atoms to travel further and faster to search the lowest energy nucleation site. Thus, increasing the substrate temperature will lead to fewer nucleation sites and to larger crystals in the final thin film, so that the crystal grain size is larger with increasing the substrate temperature during deposition. The diffusion coefficients of the metals are  $D(V) > D(Cr) > D(Al)$  at the same temperature ( $D(V) = 10^{-10}$  m<sup>2</sup>/s,  $D(Cr) = 10^{-15}$  m<sup>2</sup>/s,  $D(Al) = 10^{-22}$  m<sup>2</sup>/s, at 1000 °C) [262,263]. This is one of reasons that the film surface of V<sub>2</sub>O<sub>3</sub> is more flat. The lattice plane distance  $d_{0006}$  (or lattice constant  $c$ ) decreases with increasing the substrate temperature during deposition.

Films have higher crystal quality including the larger grain size with higher deposition temperature and larger film thickness. The lattice plane distance  $d_{0006}$  (or lattice constant  $c$ ) decreases with increasing the substrate temperature during deposition and increasing the

film thickness. Thinner films grow in strained state with respect to the expected equilibrium state as expressed in the PDF cards, while the thicker films grow in nearly fully relaxed state.

First, stoichiometric binary films  $\text{Me}_2\text{O}_3$  (i.e.  $\text{Cr}_2\text{O}_3$  and  $\text{V}_2\text{O}_3$ ) were synthesized and epitaxially grown on (0001)  $\alpha\text{-Al}_2\text{O}_3$  substrates by non-reactive RF magnetron sputtering using  $\text{Me}_2\text{O}_3$  targets. Crystalline  $\alpha\text{-Al}_2\text{O}_3$  is difficult to be obtained at such low temperature by magnetron sputtering which is introduced in section 2.2.2.  $\text{V}_2\text{O}_3$  is obviously crystallizing at lower temperature than  $\text{Cr}_2\text{O}_3$ . Crystalline  $\text{V}_2\text{O}_3$  films were obtained at the substrate temperature of 150 °C, but  $\text{Cr}_2\text{O}_3$  films could not be obtained at such low temperature in this study. Two films with similar film thickness deposited at 400 °C are compared here. The FWHM values of the (0006) reflections in XRD Bragg-Brentano mode of the  $\text{Cr}_2\text{O}_3$  films are around 0.5° (shown in Fig. 34), which is larger than that of the  $\text{V}_2\text{O}_3$  films are around 0.1° (shown in Fig. 53). This relatively sharper XRD reflex of the  $\text{V}_2\text{O}_3$  films compared to the  $\text{Cr}_2\text{O}_3$  films indicates  $\text{V}_2\text{O}_3$  films possess larger crystal grain size than  $\text{Cr}_2\text{O}_3$  films. The FWHM values of the (0006) reflections from the  $\omega$  scans of the  $\text{Cr}_2\text{O}_3$  films is 1.32°, which is larger than that of the  $\text{V}_2\text{O}_3$  films (0.75°). The mosaic spreading of the  $\text{V}_2\text{O}_3$  films is larger than that of  $\text{Cr}_2\text{O}_3$  films, indicating the tilt of (0006) planes of the  $\text{V}_2\text{O}_3$  films is smaller. This is possibly due to the different film growth mode which will be discussed in the following. The misfit of the in-plane interface between the  $\text{Cr}_2\text{O}_3$  film in the fully relaxed state and the  $\text{Al}_2\text{O}_3$  substrate is 4.2 %, and the misfit of the in-plane interface between the  $\text{V}_2\text{O}_3$  film in the fully relaxed state and the  $\text{Al}_2\text{O}_3$  substrate is 4.1 %. As we known, it is easier to get the epitaxial films with less in-plane misfit with respect to the substrate. As the mismatch gets larger, the film material may strain to accommodate the lattice structure of the substrate, which is the case during the early stages of film formation. The in-plane strain of  $\text{V}_2\text{O}_3$  films is calculated by Eq. (13) and the value is around 1.1 %, which is larger than that of  $\text{Cr}_2\text{O}_3$  films (< 0.5 %) as shown in Fig. 116. Larger in-plane strain means the film with an in-plane parameter is closer to that of the substrate. This supports the conclusion that the epitaxial crystal quality of  $\text{V}_2\text{O}_3$  films is better. The microstructure of  $\text{V}_2\text{O}_3$  films and  $\text{Cr}_2\text{O}_3$  films (as characterized by TEM analyses) are compared to identify differences in the growth of both types of films.  $\text{Cr}_2\text{O}_3$  films show many individual faceted grains grown in the  $c$ -axis direction, while

$V_2O_3$  films show no grain boundaries and a flat surface which indicates a layer by layer growth which has been introduced in section 2.1.1.2. Obviously, the epitaxial growth mode of the  $Cr_2O_3$  films is similar to the VW growth mode (i.e. 3D morphology, island growth) or to the SK growth mode. For SK growth mode, the initial layer is strained to match the substrate, and then the strain is relaxed after a few layers. The film strain for  $Cr_2O_3$  films becomes from strained to relaxed with increasing the film thickness which has been discussed in section 4.1. The growth mode of the  $V_2O_3$  films is very similar to the FM mode in which the films grow layer by layer [264]. The films with slow diffusion tend to grow in VW mode. The film growth modes can be influenced by the substrate (growth) temperature, deposition rate, and surface energy difference between the substrate and the film wets the surface to lower surface energy [265]. The surface energy of the (0001)  $\alpha$ - $Al_2O_3$ ,  $Cr_2O_3$  and  $V_2O_3$  are  $1.9 \text{ J/m}^2$ ,  $3.0 \text{ J/m}^2$  and  $16 \text{ J/m}^2$ , respectively [266,267]. The surface energy is  $V_2O_3 > Cr_2O_3 > Al_2O_3$ . Normally epitaxial layers are grown on substrates that have higher surface energy [268]. Substrates with lower surface energy are more difficult for adatoms to be attached to due to the lower number of dangling bonds [268]. In this study, films with higher surface energy were grown on the substrates with lower surface energy. Both the lattice strain and surface energy of the system play an important role in determining which film growth mode is. Deposition rate of the  $Cr_2O_3$  and  $V_2O_3$  films deposited at the same conditions ( $400 \text{ }^\circ\text{C}$ ,  $0.6 \text{ Pa}$  in Ar,  $100\text{W}$  RF power) are  $9.7 \text{ nm/min}$  and  $11.3 \text{ nm/min}$ , respectively (i.e. the deposition rate of  $V_2O_3$  films is higher than that of  $Cr_2O_3$  films). The deposition rate is higher with higher surface energy [37]. The films with higher surface energy are much easier to be grown in crystalline and possess better epitaxial quality. Thermodynamic approach leads to the definition of the growth modes. These modes refer to the morphology taken on by a system grown close to thermodynamic equilibrium. Films are grown far away from equilibrium during PVD process and their morphology is determined by kinetics.

With regard of the TEM results, the  $Cr_2O_3$  films consist of columns with continuous grain boundaries between them according to the structure zone 2 as shown in Fig. 12. Random clustering of atoms at initial stages of the growth can lead to a wide range of island sizes followed by side-wall growth of these clusters at low surface diffusion rates. The  $V_2O_3$  film surface is relatively flat and no faceted grains are present, and thus, this structure is

more similar to that of the zone 3 (or the transition structure from zone 2 to zone 3) in Fig. 12. This interpretation based on the structure zone model gives an explanation of the observation that the films possess larger grain size and better crystal quality with increasing substrate temperature. According to the structure-zone-model which is shown in Fig. 12, the film morphology is influenced by substrate temperature ( $T$ ), film melting point ( $T_m$ ) and Ar pressure during deposition ( $p = 0.6$  Pa in this study). When the substrate temperature is low (i.e.  $T/T_m$  is low), little surface diffusion happens and small diameter columns with poor crystallinity or amorphous structure could be obtained. With increasing the substrate temperature (i.e. increasing  $T/T_m$ ), the surface and volume diffusion increases and the films undergo from zone 1, zone T, zone 2 to zone 3, during which process surface diffusion becomes more important, fewer defects and smoother surface can be observed, grain size is larger. The melting points of  $\text{Cr}_2\text{O}_3$  and  $\text{V}_2\text{O}_3$  are 2675 K and 2759 K, respectively.  $T/T_m$  is 0.25 and 0.24 for the  $\text{Cr}_2\text{O}_3$  and  $\text{V}_2\text{O}_3$  films, respectively, when the substrate temperature is 400 °C in this study. According to the structure-zone-model in Fig. 12, both  $\text{Cr}_2\text{O}_3$  and  $\text{V}_2\text{O}_3$  films are in zone T. However, it is not in agreement with the TEM results. This is due to the film morphology is influenced not only by the deposition condition, but also the deposition rate, diffusion and so on. In this study, the iso-structure substrates are used which makes the film crystal quality better and easier. Therefore, there is some deviation between the experiments and the theoretical knowledge.

On one hand, plasma-etching could clean the substrate surface (i.e. remove the contaminants). On the other hand, cleaning the substrate surface by ion bombardment has side effects on the substrate or the film growth. The influence of the plasma-etching before deposition in  $\text{Cr}_2\text{O}_3$  and  $\text{V}_2\text{O}_3$  films was observed. The films deposited on the substrate with plasma-etching show 6-fold symmetry. There are two different in-plane  $(10\bar{1}10)$  orientations rotated by  $60^\circ$  domain variants which is caused by stacking faults. However, the films deposited on the substrate without plasma-etching show only 3-fold symmetry which indicates no stacking faults in the interface between the substrates and the films or in the films during growth. Ion bombardment sets atoms in the surface region in motion and thus leads to a wide range of changes in the arrangement of atoms at the surface and can eventually induce strong variations in surface topography and defects like vacancies

and interstitials [84]. In general, the nucleation will be in a random pattern. This can be modified by the substrate. If the substrate is structured this can be transferred to the growing film. This is the reason why (0001)  $\alpha$ -Al<sub>2</sub>O<sub>3</sub> single crystals were chosen as substrates. Hence, defects in the surface can generate defects in the subsequent film. The films deposited on the substrate without plasma-etching process possess higher lattice constant  $c$  and smaller lattice constant  $a$ , which indicated better epitaxial quality of films. Furthermore, plasma-etching process can increase the in-plane misfit between the substrate and the film. The plasma-etching will destroy the original ordered atomic substrate surface. The depth of the disordered area in the substrate near the interface is around 2-5 nm which can be observed from TEM analyses. This distorted area is the result of the ion bombardment of the substrate during the plasma-etching which usually causes a rough surface due to the difference in sputter rates for different grain orientations (or different bombard directions). Further, the damage to the substrate induced by the ion bombardment will contribute to enhance the misfit and strain between the substrate and the film, so worse epitaxial quality occurs.

Then ternary oxides in various systems with the same corundum-type structures were extended from the binary systems. In the ternary systems, the influence of a substitution of the metal cation in single-phase solid solution crystallized thin films on the microstructure and the properties of the films were investigated. The conclusion in the previous text for the binary systems is also valid for the ternary systems. Except of the (V,Al)<sub>2</sub>O<sub>3</sub> solid solution, the metal/oxygen stoichiometry of other ternary films is very close to the ideal value of 2/3 using the stoichiometric segmented ceramic targets. In case of the V-Al-O films, the deviation of the concentration from the ideal metal to oxygen stoichiometry  $\delta$  is relatively large. The Ellingham-Richardson diagram [269] which is for metals reacting to form oxides could explain this. The lower the position of a metal's line in the Ellingham diagram, the greater is the stability of its oxide. The line for Al (oxidation of aluminum) is found to be below that for V (formation of V<sub>2</sub>O<sub>3</sub>). During the magnetron sputter deposition, metal and oxygen atoms with the concentration ratio of 2:3 are emitted from the targets. As discussed in previous text, the deposition coefficient of O is larger than that of the metals. V<sub>2</sub>O<sub>5</sub> could be formed if the oxygen offer is high enough. Therefore, extra oxygen was observed in the films by EPMA.

The growth of the Cr-rich Al-Cr-O films is similar to the growth of  $\text{Cr}_2\text{O}_3$  films, and the growth of the V-rich V-Al-O and V-rich V-Cr-O films is similar to the growth of  $\text{V}_2\text{O}_3$  films. The FWHM values of the (0006) reflections in XRD Bragg-Brentano mode of Cr-rich  $(\text{Cr}_{1-x}\text{Al}_x)_2\text{O}_3$  films are  $0.15^\circ - 0.35^\circ$  (shown in Fig. 76), which is smaller than that of the  $\text{Cr}_2\text{O}_3$  films. This indicates that the grain size of Cr-rich  $(\text{Cr}_{1-x}\text{Al}_x)_2\text{O}_3$  is larger than that of  $\text{Cr}_2\text{O}_3$  films which could be attributed to the fact that the misfit between the  $(\text{Cr}_{1-x}\text{Al}_x)_2\text{O}_3$  films and the  $\text{Al}_2\text{O}_3$  substrates is smaller by substitution of Al in  $\text{Cr}_2\text{O}_3$ . The FWHM values of the (0006) reflections from the  $\omega$  scans of the Cr-rich  $(\text{Cr}_{1-x}\text{Al}_x)_2\text{O}_3$  films is  $1.01^\circ - 1.43^\circ$ , which is similar to that of the  $\text{Cr}_2\text{O}_3$  films ( $1.32^\circ$ ). The FWHM values of the (0006) reflections in XRD Bragg-Brentano mode of V-rich  $(\text{V}_{1-x}\text{Al}_x)_2\text{O}_3$  and  $(\text{V}_{1-x}\text{Cr}_x)_2\text{O}_3$  films are  $0.13^\circ - 0.27^\circ$  and  $0.07^\circ - 0.13^\circ$ , respectively. The FWHM values of the (0006) reflections from the  $\omega$  scans of V-rich  $(\text{V}_{1-x}\text{Al}_x)_2\text{O}_3$  films and  $(\text{V}_{1-x}\text{Cr}_x)_2\text{O}_3$  films are  $0.27^\circ - 0.36^\circ$  and  $0.35^\circ - 0.37^\circ$ , respectively, which is much smaller than that of  $\text{V}_2\text{O}_3$  films. This indicates V-rich ternary thin films possess better epitaxial quality than  $\text{V}_2\text{O}_3$ . Substitution of Al or Cr in  $\text{V}_2\text{O}_3$  increases the film epitaxial quality due to the decreased lattice mismatch. The misfit of the in-plane interface between the films and the substrates in the  $\text{Cr}_2\text{O}_3$ ,  $\text{V}_2\text{O}_3$ , Al-Cr-O, V-Al-O, and V-Cr-O films is 3.6 % - 4.2 %, 4.3 % - 5.2 %, 1.3 % - 4.5 %, 1.2 % - 3.3 %, and 3.4 % - 4.8 %, respectively. The in-plane misfit is larger with increasing the V content because the epitaxial quality is better. Therefore, the in-plane misfit in the  $\text{V}_2\text{O}_3$  films is larger than  $\text{Cr}_2\text{O}_3$  films in the binary systems and the in-plane misfit is larger with less Al content in Al-Cr-O system and larger V content in V-Al-O and V-Cr-O systems. On one hand, increasing the Al content in the ternary systems makes the epitaxial film grown at the low temperature more difficult; on the other hand, increasing the Al content decreases the misfit between the films and the substrates which is advantageous to the film growth. In ternary systems, the crystalline structure possesses poorer quality with higher Al content and higher quality with higher V content. The higher the Al content, the higher the tendency to build extremely nanocrystalline or even amorphous structures.

Lattice parameters change along with the film composition as shown in Fig. 115. For Cr-Al-O films, lattice parameter  $c$  decreases and the epitaxial quality increases with lower Al content; For V-Al-O and V-Cr-O films, lattice parameter  $c$  increases and the epitaxial

quality increases with higher V content. In this thesis, theoretical lattice parameters of the ternary solid solutions were calculated according to Vegard's law however the measured lattice parameters deviated from Vegard's law. Vegard's law states that, in a solid solution system, the lattice parameters of the unit cell should change linearly with composition [270]. In substitutional solid solutions, the lattice parameter usually increases or decreases when cations of larger or smaller radii are substituted into the matrix. Rossi et al. [254] investigated the linearity of the lattice parameters in bulk solid solutions of  $\text{Al}_2\text{O}_3\text{-Cr}_2\text{O}_3$ . The lattice parameters should vary linearly with composition, but the measured values do not. Because the cations in the corundum structure lie in pairs along the *c*-axis and the nearest neighbor distances are unequal. For all the ternary films, the deviation of the measured lattice parameter from Vegard's law is the smallest in the films with the best epitaxial quality (including the largest grain size and almost no tilt of the lattice planes) which were deposited in Pos. 3. The crystal quality of the Cr-Al-O films is the worst among these ternary systems, so the deviations from the theoretical values are the largest. The deviations are due to the imperfect crystal with defects and large strain in the film.

In this study, some design rules could be derived to grow hard coatings in a corundum structure according to Fig. 118. Fig. 118 shows the film growth and properties of the  $\text{Al}_2\text{O}_3\text{-Cr}_2\text{O}_3\text{-V}_2\text{O}_3$  system deposited at 400 °C. The films show amorphous at the  $\text{Al}_2\text{O}_3$  side, and change to the polycrystalline films when the films' composition trends to  $\text{Cr}_2\text{O}_3$  or  $\text{V}_2\text{O}_3$  sides. The structure-zone-model is from zone 1 to zone 3 with the films from  $\text{Al}_2\text{O}_3$  to  $\text{Cr}_2\text{O}_3$ . The film growth modes change from island growth mode to layer by layer growth mode and the in-plane lattice misfit increases with the composition changing from  $\text{Cr}_2\text{O}_3$  and  $\text{Al}_2\text{O}_3$  sides to  $\text{V}_2\text{O}_3$  side. The crystal quality is better and the grain size is larger with varying the film composition from  $\text{Cr}_2\text{O}_3$  and  $\text{Al}_2\text{O}_3$  sides to  $\text{V}_2\text{O}_3$  side, and the grain size is smaller and the crystal quality is worse with substitution of Al for Cr in  $(\text{Al,Cr})_2\text{O}_3$ . With increasing the V content in  $(\text{V,Cr})_2\text{O}_3$  and  $(\text{V,Al})_2\text{O}_3$ , the epitaxial quality of the films is better. Further, the band gap of the  $\text{Cr}_2\text{O}_3$ ,  $\text{V}_2\text{O}_3$ , Cr-rich Al-Cr-O, V-rich V-Al-O, and V-rich V-Cr-O films is 3.01 eV - 3.14 eV, 1.84 eV - 1.92 eV, 3.22 eV - 3.27 eV, 3.82 eV - 4.83 eV, and 1.21 eV - 2.06 eV, respectively, which indicates the relationship of the band gap of these films is  $\text{Al}_2\text{O}_3 > \text{V-rich V-Al-O} > \text{Cr-rich}$

Cr-Al-O > Cr<sub>2</sub>O<sub>3</sub> > V-rich V-Cr-O / V<sub>2</sub>O<sub>3</sub>, as shown in Fig. 117. It is in agreement with the band gap of these materials in the literatures [79,105,184,237,246,271]. But there is no information about the band gap of V-Al-O and V-Cr-O systems. There is a trend that the films with better epitaxial crystal quality possess lower band gap value. The amorphous area is larger and epitaxial area is smaller with decreasing the substrate temperature.

The systematics can be applied to even higher systems like Al-Cr-V-O. New multi-principal elemental oxides in corundum structure are developed to apply into different areas. For example, if a coating with maximum Al content is desired and the substrate temperature should be as low as possible for tool applications, a certain content of V could be substituted for Al.

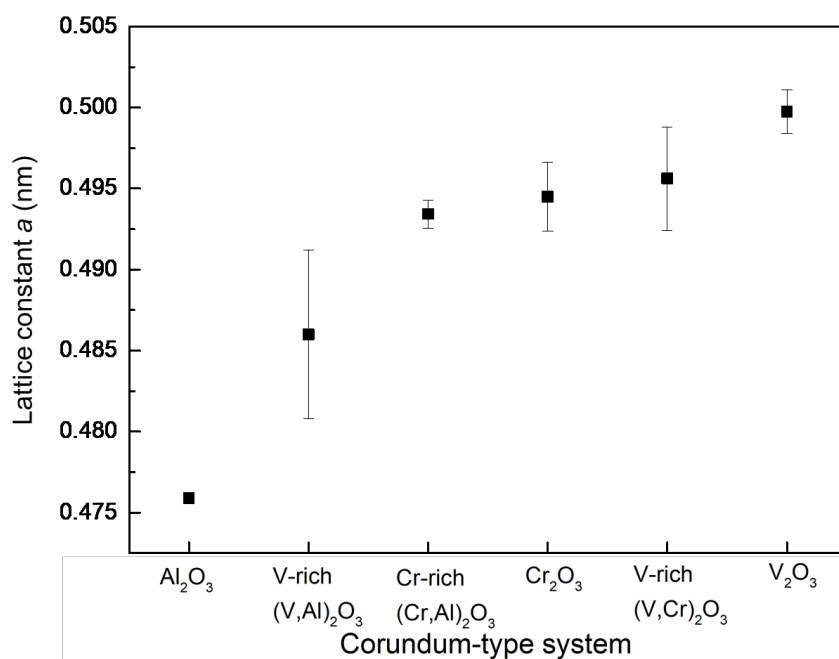


Fig. 115 The lattice constant *a* of the different corundum-type systems including Al<sub>2</sub>O<sub>3</sub>, Cr<sub>2</sub>O<sub>3</sub>, V<sub>2</sub>O<sub>3</sub>, V-rich (V,Al)<sub>2</sub>O<sub>3</sub>, Cr-rich (Cr,Al)<sub>2</sub>O<sub>3</sub>, and V-rich (V,Cr)<sub>2</sub>O<sub>3</sub>.

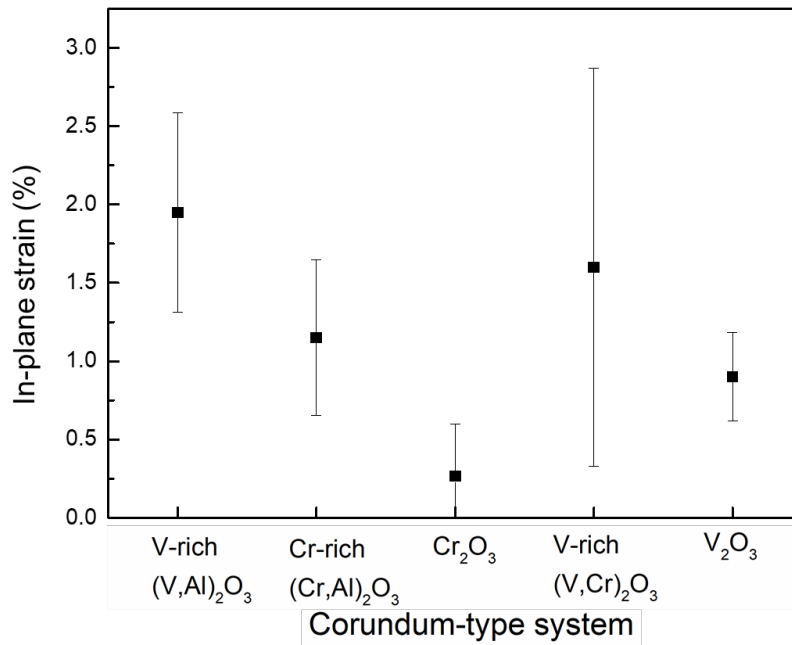


Fig. 116 The in-plane strain of the different corundum-type systems including Al<sub>2</sub>O<sub>3</sub>, Cr<sub>2</sub>O<sub>3</sub>, V<sub>2</sub>O<sub>3</sub>, V-rich (V,Al)<sub>2</sub>O<sub>3</sub>, Cr-rich (Cr,Al)<sub>2</sub>O<sub>3</sub>, and V-rich (V,Cr)<sub>2</sub>O<sub>3</sub>.

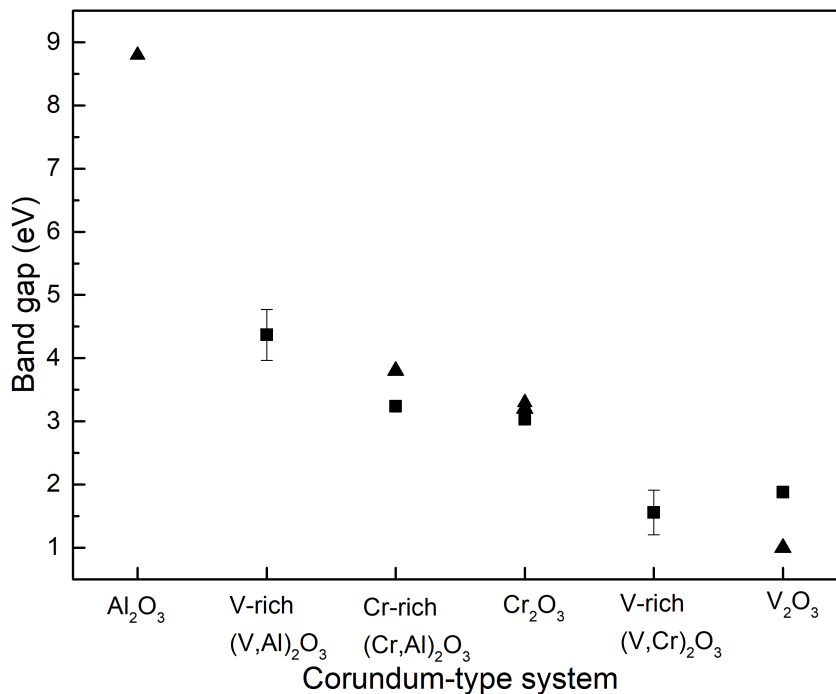


Fig. 117 The band gap of the different corundum-type systems including Al<sub>2</sub>O<sub>3</sub>, Cr<sub>2</sub>O<sub>3</sub>, V<sub>2</sub>O<sub>3</sub>, V-rich (V,Al)<sub>2</sub>O<sub>3</sub>, Cr-rich (Cr,Al)<sub>2</sub>O<sub>3</sub>, and V-rich (V,Cr)<sub>2</sub>O<sub>3</sub>. ■ indicates the experimental data, and ▲ indicates the cited data from ref. [79,105,184,237,246,271].

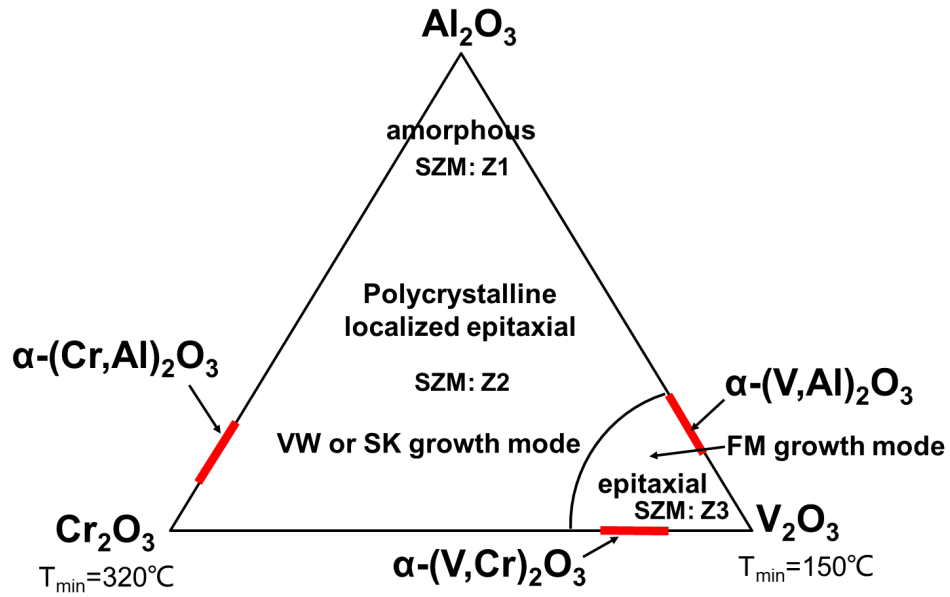


Fig. 118 Film growth, structure and crystallized substrate temperature of  $\text{Al}_2\text{O}_3$ - $\text{Cr}_2\text{O}_3$ - $\text{V}_2\text{O}_3$  system. SZM indicates the structure-zone-model which is described in Fig. 12 (Z1, Z2 and Z3 are zone 1, zone 2 and zone 3, respectively). The red regions are the composition of the ternary films studied in this work.  $T_{\min}$  indicate the minimum temperature to crystallize, respectively.



## 6 Summary

The goal of this work is to synthesize the iso-structured films on the  $\alpha$ -Al<sub>2</sub>O<sub>3</sub> substrates with locally epitaxial growth at the low temperature less than 400 °C by RF magnetron sputtering from ceramic oxide targets. The growth of the film on the iso-structured substrate was studied. This work is to help to decide deposition parameters according to the films quality that we want to get and predict the microstructure or the properties of the films. In this work, the factors influencing the microstructure, epitaxial quality etc. of the films are successfully investigated.

### 1. Deposition temperature

It is clear that all the films have higher crystal quality with higher deposition temperature. Only amorphous films are synthesized on the substrates without heating during the deposition for the Cr<sub>2</sub>O<sub>3</sub> films. Even there are crystalline in the V<sub>2</sub>O<sub>3</sub> films on the substrates at 150 °C, the crystal quality is very poor. The grain size is larger and the lattice constant  $c$  is smaller with higher deposition temperature.

### 2. Film thickness

The grain size is larger and the lattice parameter  $c$  decreases with increasing the film thickness until a critical thickness in order of  $\mu\text{m}$  is reached. The films change from strained to relaxed gradually with increasing the film thickness.

### 3. Surface condition of the substrates

The influence of the plasma-etching process on the crystal growth of the Cr<sub>2</sub>O<sub>3</sub> and V<sub>2</sub>O<sub>3</sub> films are studied. The films deposited on the substrates without plasma-etching before coating possess larger grain size and better crystal quality. The plasma-etching process on the substrate will destroy the original ordered atomic substrate surface, which causes stacking faults in the interface between the substrates and the films and worse epitaxial crystal quality of the film.

#### 4. Composition

Different films such as  $\text{Cr}_2\text{O}_3$ ,  $\text{V}_2\text{O}_3$ , Cr-Al-O, V-Al-O, and V-Cr-O are investigated in this work. The films with different composition were grown in different modes. The  $\text{Cr}_2\text{O}_3$  and  $\alpha\text{-(Cr}_{1-x}\text{Al}_x)_2\text{O}_3$  films show many individual grains and their surface shows long period corrugation, which were grown in the Volmer-Weber (VW) or Stranski-Krastanov (SK) mode. The  $\text{V}_2\text{O}_3$  and V-rich ternary systems such as  $\alpha\text{-(V}_{1-x}\text{Al}_x)_2\text{O}_3$ ,  $\alpha\text{-(V}_{1-x}\text{Cr}_x)_2\text{O}_3$  show very flat surface and no faceted grains, which were grown in layer by layer mode. In binary systems, because of the higher surface energy of  $\text{V}_2\text{O}_3$ ,  $\text{V}_2\text{O}_3$  is much easier to be grown in crystalline and epitaxially on the substrate than  $\text{Cr}_2\text{O}_3$ . In ternary system, the growth is easier and the epitaxial quality is better at the same condition with decreasing the Al content and increasing the V content. Further, the films with less Al in Al-Cr-O system or more V in V-Al-O and V-Cr-O systems possess larger lattice constant  $c$ .

What's more, lattice vibration, electronic and optical properties are basic properties of a crystal, which are influenced by the microstructure, lattice parameters etc.. Raman spectra show a significant shift of phonon frequency with the lattice constant which is varied by the film thickness, the deposition temperature and the composition. The Raman  $A_{1g}$  mode shifts to the smaller wavenumber value side with increasing the (000 $l$ ) lattice plane distance and the  $E_g$  modes shift to the larger wavenumber side with decreasing the (000 $l$ ) lattice plane distance. The band gap of these films is  $\text{Al}_2\text{O}_3 > \text{V-rich V-Al-O} > \text{Cr-rich Cr-Al-O} > \text{Cr}_2\text{O}_3 > \text{V-rich V-Cr-O} / \text{V}_2\text{O}_3$ . It is the first time to investigate the band gap of V-Al-O and V-Cr-O systems. There is a trend that the films with better epitaxial crystal quality possess lower band gap value.

Material properties depend on the microstructure. Understanding the microstructure dependent on the deposition condition and the composition of the film is very important, which gives a guidance to control the film crystal quality and the properties which is benefited for applications. This work develops the iso-structure system for epitaxial film growth from binary to ternary, and the systematics can be applied to even higher systems like Al-Cr-V-O.

## References

- [1] M. Froment, ed., *Materials Science and Engineering*, Elsevier, New York, 1984.
- [2] K. Wasa, M. Kitabatake, H. Adachi, *Thin Film Materials Technology: Sputtering of Compound Materials*, William Andrew, Springer, USA, 2004.
- [3] K. R. Dixit, Epitaxial growth of thin films, *Proc. Indian Acad. Sci., Sect. A*, 48 (1958), 330–335, doi:10.1007/BF03052917.
- [4] T. C. Kaspar, S. E. Chamberlin, M. E. Bowden, R. Colby, V. Shutthanandan, S. Manandhar, et al., Impact of lattice mismatch and stoichiometry on the structure and bandgap of  $(\text{Fe,Cr})_2\text{O}_3$  epitaxial thin films, *J. Phys. Condens. Matter.*, 26 (2014), 135005, doi:10.1088/0953-8984/26/13/135005.
- [5] J. Wang, A. Gupta, T. M. Klein, Plasma enhanced chemical vapor deposition of  $\text{Cr}_2\text{O}_3$  thin films using chromium hexacarbonyl ( $\text{Cr}(\text{CO})_6$ ) precursor, *Thin Solid Films*, 516 (2008), 7366–7372, doi:10.1016/j.tsf.2008.02.027.
- [6] K. Sarakinos, J. Alami, S. Konstantinidis, High power pulsed magnetron sputtering: A review on scientific and engineering state of the art, *Surf. Coat. Technol.*, 204 (2010), 1661–1684, doi:10.1016/j.surfcoat.2009.11.013.
- [7] P. B. Barna, M. Adamik, Fundamental structure forming phenomena of polycrystalline films and the structure zone models, *Thin Solid Films*, 317 (1998), 27–33.
- [8] A. Anders, S. Anders, I. G. Brown, I. C. Ivanov, Low Energy Ion Implantation / Deposition as a Film Synthesis and Bonding Tool, in: *Mater. Res. Soc. Symp. Proceeding*, 1994, 833–844.
- [9] Milton Ohring, *Materials Science of Thin Films*, Second Edi, Academic Press, San Diego, 1992.

- [10] K. Wasa, S. Hayakawa, Handbook of Sputter Deposition Technology Fundamentals and Applications for Functional Thin Films, Nanomaterials, and MEMS, Second Edi, Elsevier Inc., Waltham, USA and Oxford, UK, 2012. doi:10.1016/B978-1-4377-3483-6.00006-1.
- [11] P. J. Kelly, R. D. Arnell, Magnetron sputtering: a review of recent developments and applications, *Vacuum*, 56 (2000), 159–172, doi:10.1016/S0042-207X(99)00189-X.
- [12] X. Tan, J. Liu, J. Niu, J. Liu, J. Tian, Recent Progress in Magnetron Sputtering Technology Used on Fabrics, *Materials (Basel)*, 11 (2018), doi:10.3390/ma11101953.
- [13] P. Jin, G. Xu, M. Tazawa, K. Yoshimura, D. Music, J. Alami, et al., Low temperature deposition of  $\alpha$ -Al<sub>2</sub>O<sub>3</sub> thin films by sputtering using a Cr<sub>2</sub>O<sub>3</sub> template, *J. Vac. Sci. Technol., A Vacuum, Surfaces, Film*, 20 (2002), 2134, doi:10.1116/1.1513641.
- [14] S. Rупpi, Deposition, microstructure and properties of texture-controlled CVD  $\alpha$ -Al<sub>2</sub>O<sub>3</sub> coatings, *Int. J. Refract. Met. Hard Mater.*, 23 (2005), 306–316, doi:10.1016/j.ijrmhm.2005.05.004.
- [15] E. Serra, G. Benamati, O. Ogorodnikova, Hydrogen isotopes transport parameters in fusion reactor materials, *J. Nucl. Mater.*, 255 (1998), 105–115, doi:10.1016/S0022-3115(98)00038-5.
- [16] B. Lux, C. Colombier, H. Altena, K. Stjernberg, Preparation of Alumina Coatings by Chemical Vapour Deposition, *Thin Solid Films*, 138 (1986), 49–64.
- [17] J. Mu, M. Schierling, E. Zimmermann, D. Neuschu, Chemical vapor deposition of smooth  $\alpha$ -Al<sub>2</sub>O<sub>3</sub> films on nickel base superalloys as diffusion barriers, *Surf. Coat. Technol.*, 121 (1999), 16–21.
- [18] M. Karadge, X. Zhao, M. Preuss, P. Xiao, Microtexture of the thermally grown alumina in commercial thermal barrier coatings, *Scr. Mater.*, 54 (2006), 639–644, doi:10.1016/j.scriptamat.2005.10.043.

- [19] R. Brill, F. Koch, J. Mazurelle, D. Levchuk, M. Balden, Y. Yamada-Takamura, et al., Crystal structure characterisation of filtered arc deposited alumina coatings: temperature and bias voltage, *Surf. Coatings Technol.*, 174–175 (2003), 606–610, doi:10.1016/S0257-8972(03)00539-5.
- [20] P. D. Ye, B. Yang, K. K. Ng, J. Bude, G. D. Wilk, S. Halder, et al., GaN metal-oxide-semiconductor high-electron-mobility-transistor with atomic layer deposited Al<sub>2</sub>O<sub>3</sub> as gate dielectric, *Appl. Phys. Lett.*, 86 (2005), 63501, doi:10.1063/1.1861122.
- [21] Sanghun Jeon, Hyundoek Yang, Dae-Gyu Park, Hyunsang Hwang, Electrical and Structural Properties of Nanolaminate (Al<sub>2</sub>O<sub>3</sub>/ZrO<sub>2</sub>/Al<sub>2</sub>O<sub>3</sub>) for Metal Oxide Semiconductor Gate Dielectric Applications, *Jpn. J. Appl. Phys.*, 41 (2002), 2390–2393, doi:10.1143/JJAP.41.2390.
- [22] C. Deshpandey, L. Holland, Preparation and properties of Al<sub>2</sub>O<sub>3</sub> films by D. C. and R. F. magnetron sputtering, *Thin Solid Films*, 96 (1982), 265–270.
- [23] B. Hirschauer, S. Söderholm, U. O. Karlsson, Highly oriented  $\alpha$ -alumina films grown by pulsed laser deposition, *Thin Solid Films*, 305 (1997), 243–247.
- [24] Carl M. Lampert, Advanced optical materials for energy efficiency and solar conversion, *Sol. Wind Technol.*, 4 (1987), 347–379, doi:10.1016/0741-983X(87)90067-1.
- [25] G. V. Samsonov, *The Oxide Handbook*, Second Edition, IFI/PLENUM, New York, 1973.
- [26] P. Hones, F. Levy, Influence of deposition parameters on mechanical properties of sputter-deposited Cr<sub>2</sub>O<sub>3</sub> thin films, *J. Mater. Res.*, 14 (1999), 3623–3629.
- [27] H. Cao, X. Qiu, Y. Liang, M. Zhao, Q. Zhu, Sol-gel synthesis and photoluminescence of p-type semiconductor Cr<sub>2</sub>O<sub>3</sub> nanowires, *Appl. Phys. Lett.*, 88 (2006), 1–4, doi:10.1063/1.2213204.

- [28] J. Robertson, High density constant oxides, *Eur. Phys. J. Appl. Phys.*, 28 (2004), 265–291, doi:10.1051/epjap.
- [29] S. D. Yim, I. S. Nam, Characteristics of chromium oxides supported on TiO<sub>2</sub> and Al<sub>2</sub>O<sub>3</sub> for the decomposition of perchloroethylene, *J. Catal.*, 221 (2004), 601–611, doi:10.1016/j.jcat.2003.09.026.
- [30] Bert M. Weckhuysen, Israel E. Wachs, Robert A. Schoonheydt, Surface Chemistry and Spectroscopy of Chromium in Inorganic Oxides, *Chem. Rev.*, 96 (1996), 3327–3349, doi:10.1016/S0167-2991(08)63630-7.
- [31] B. S. Allimi, S. P. Alpay, D. Goberman, T. Huang, J. I. Budnick, D. M. Pease, et al., Growth of V<sub>2</sub>O<sub>3</sub> thin films on a-plane (110) and c-plane (001) sapphire via pulsed-laser deposition, *J. Mater. Res.*, 22 (2007), 2825–2831, doi:10.1557/JMR.2007.0378.
- [32] K. Dumbuya, K. Christmann, S.L. M. Schroeder, Epitaxial growth of single-crystalline Al<sub>2</sub>O<sub>3</sub> films on Cr<sub>2</sub>O<sub>3</sub> (0001), *Langmuir*, 23 (2007), 5386–5393, doi:10.1021/la061434w.
- [33] Sang-Yong Jeong, Jin-Bok Lee, Hyunseok Na, Tae-Yeon Seong, Epitaxial growth of Cr<sub>2</sub>O<sub>3</sub> thin film on Al<sub>2</sub>O<sub>3</sub> (0001) substrate by radio frequency magnetron sputtering combined with rapid-thermal annealing, *Thin Solid Films*, 518 (2010), 4813–4816.
- [34] T. Maeda, M. Yoshimoto, T. Ohnishi, G. H. Lee, H. K., Orientation-defined molecular layer epitaxy of  $\alpha$ -Al<sub>2</sub>O<sub>3</sub> thin films, *J. Cryst. Growth*, 8 (1997), 95–101.
- [35] H. Holleck, Basic principles of specific applications of ceramic materials as protective layers, *Surf. Coatings Technol.*, 43–44 (1990), 245–258, doi:10.1016/0257-8972(90)90078-Q.
- [36] H. Holleck, Design of Nanostructured Thin Films for Tribological Applications, in: Ashok Kumar, Yip-Wah Chung, John J. Moore, Gary L. Doll, Kyoshi Yatsui, D. S. Misra (Eds.), *Surf. Eng. Sci. Technol. II*, Warrendale, Pennsylvania, 1999, 207-218.

- [37] Richard Myers, *The Basics of Chemistry*, Greenwood Press, London, 2005, doi:10.1007/0-387-28390-0.
- [38] Yu-Ran Luo, *Comprehensive Handbook of Chemical Bond Energies*, CRC Press, 2007.
- [39] I. J. Lee, J.-Y. Kim, C. Yu, C.-H. Chang, M.-K. Joo, Y. P. Lee, et al., Morphological and structural characterization of epitaxial  $\alpha$ -Fe<sub>2</sub>O<sub>3</sub> (0001) deposited on Al<sub>2</sub>O<sub>3</sub> (0001) by dc sputter deposition, *J. Vac. Sci. Technol., A Vacuum, Surfaces, Film*, 23 (2005), 1450, doi:10.1116/1.2013321.
- [40] Wang-ping Wu, Zhao-feng Chen, *Iridium Coating: Processes, Properties and Application*, *Johnson Matthey Technol. Rev.*, 61 (2017), 93–110.
- [41] RF Bunshah, *Handbook of deposition technologies for films and coatings: science, technology and applications*, 1994.
- [42] Donald E. Sands, *Introduction to Crystallography*, New York, 1975.
- [43] J. Kepler, *De nive sexangula [The Six-sided Snowflake]*, Oxford: Clarendon Press, 1966.
- [44] Robert Hooke, *Micrographia*, Courier Dover Publications, London, 1664.
- [45] Steno Nicolaus, *De Solido intra solidum naturaliter contento dissertations prodromus*, Florentiae, 1669.
- [46] Rome de L' Isle, *Crystallographie*, Paris, 1783.
- [47] G. F. Kunz, The life and work of Haüy, *Am. Mineral.*, 3 (1918), 60–89.
- [48] Christopher Hammond, *The Basics of Crystallography and Diffraction*, Third Edit, Oxford University Press, Oxford, New York, 2009.
- [49] V. M. Goldschmidt, *Geochemische Verteilungsgesetze der Elemente VIII: Untersuchungen über Bau und Eigenschaften von Krystallen*, *Skrifter Norske Videnskap-Akademi Oslo Mat. Naturv. Klasse*, 1926.

- [50] Jenny Pickworth Glusker, Kenneth N. Trueblood, *Crystal Structure Analysis: A Primer*, Third Edit, Oxford University Press, Oxford, 1998.
- [51] Ruili Wang, Eric Habib, X. X. Zhu, Application of close-packed structures in dental resin composites, *Dent. Mater.*, 33 (2017), 288–293, doi:10.1016/j.dental.2016.12.006.
- [52] W. E. Lee, K. P. D. Lagerlof, Structural and Electron Diffraction Data for Sapphire ( $\alpha$ -Al<sub>2</sub>O<sub>3</sub>), *J. Electron Microsc. Tech.*, 2 (1985), 247–258.
- [53] A. G. Jackson, *Handbook of Crystallography: For Electron Microscopists and Others*, Springer-Verlag, New York, 1991.
- [54] Larry W. Finger, Robert M. Hazen, Crystal structure and isothermal compression of Fe<sub>2</sub>O<sub>3</sub>, Cr<sub>2</sub>O<sub>3</sub>, and V<sub>2</sub>O<sub>3</sub> to 50 kbars, *J. Appl. Phys.*, 51 (1980), 5362–5367, doi:10.1063/1.327451.
- [55] Joseph R. Symyth, Steven D. Jacobsen, Robert M. Hazen, Comparative Crystal Chemistry of Orthosilicate Minerals, *Rev. Mineral. Geochemistry*, 41 (2000), 187-209, doi:10.2138/rmg.2000.41.7.
- [56] L. J. Eckert, R. C. Bradt, Thermal Expansion of Corundum Structure Rh<sub>2</sub>O<sub>3</sub>, *Mater. Res. Bull.*, 8 (1973), 375–378.
- [57] G. E. Gurr, P. W. Montgomery, C. D. Knutson, B. T. Gorres, The crystal structure of trigonal diboron trioxide, *Acta Crystallogr., Sect. B, Struct. Crystallogr. Cryst. Chem.*, 26 (1970), 906–915, doi:10.1107/S0567740870003369.
- [58] J A Sans, R Vilaplana, D Errandonea, V P Cuenca-Gotor, B García-Domene, C Popescu, et al., Structural and vibrational properties of corundum-type In<sub>2</sub>O<sub>3</sub> nanocrystals under compression, *Nanotechnology*, 28 (2017), 205701.
- [59] Y. B. He, A. Stierle, W. X. Li, A. Farkas, N. Kasper, H. Over, Oxidation of Ir (111): From O-Ir-O Trilayer to Bulk Oxide Formation, *J. Phys. Chem. C.*, 112 (2008), 11946–11953.

- [60] M. L. Kronberg, Plastic deformation of single crystals of sapphire basal slip and twinning, *Acta Metall.*, 5 (1957), 507–524.
- [61] Igor Levin, David Brandon, Metastable Alumina Polymorphs: Crystal Structures and Transition Sequences, *J. Am. Ceram. Soc.*, 81 (1998), 1995–2012.
- [62] W. Y. Ching, Y. N. Xu, First-Principles Calculation of Electronic, Optical, and Structural Properties of  $\alpha$ -Al<sub>2</sub>O<sub>3</sub>, *J. Am. Ceram. Soc.*, 77 (1994), 404–411, doi:10.1111/j.1151-2916.1994.tb07008.x.
- [63] J. Lewis, D. Schwarzenbach, H. D. Flack, Electric Field Gradients and Charge Density in Corundum,  $\alpha$ -Al<sub>2</sub>O<sub>3</sub>, *Acta Crystallogr.*, (1982), 733–739.
- [64] Z. Lodziana, K. Parlinski, Dynamical stability of the  $\alpha$  and  $\theta$  phases of alumina, *Phys. Rev. B.*, 67 (2003), 174106, doi:10.1103/PhysRevB.67.174106.
- [65] M. Halvarsson, S. Vuorinen, Influence of the nucleation surface on the growth of CVD  $\alpha$ -Al<sub>2</sub>O<sub>3</sub> and  $\kappa$ -Al<sub>2</sub>O<sub>3</sub>, *Surf. Coatings Technol.*, 76–77 (1995), 287–296, doi:10.1016/0257-8972(95)02584-7.
- [66] S. Vuorinen, L. Karlsson, Phase transformation in chemically vapour-deposited  $\kappa$ -alumina, *Thin Solid Films*, 214 (1992), 132–143, doi:10.1016/0040-6090(92)90761-Y.
- [67] H. C. Stumpf, Allen S. Russel, J. W. Newsome, C. M. Tucker, Thermal Transformations of Aluminas and Alumina Hydrates, *Ind. Eng. Chem.*, 42 (1950), 1398–1403. doi:10.1021/ie50487a039.
- [68] K. A. Matori, L. C. Wah, M. Hashim, I. Ismail, M. H. Mohd Zaid, Phase transformations of  $\alpha$ -alumina made from waste aluminum via a precipitation technique, *Int. J. Mol. Sci.*, 13 (2012), 16812–16821, doi:10.3390/ijms131216812.
- [69] V. A. Pustovarov, V. S. Aliev, T. V. Perevalov, V. A. Gritsenko, A. P. Eliseev, Electronic structure of an oxygen vacancy in Al<sub>2</sub>O<sub>3</sub> from the results of Ab Initio quantum-chemical calculations and photoluminescence experiments, *J. Exp. Theor. Phys.*, 111 (2010), 989–995, doi:10.1134/S1063776110120113.

- [70] Stuart Ansell, Shankar Krishnan, J. K. Richard Weber, John J. Felten, Paul C. Nordine, Mark A. Beno, et al., Structure of Liquid Aluminum Oxide, *Phys. Rev. Lett.*, 78 (1997), 464–466, doi:10.1103/PhysRevLett.78.464.
- [71] S. J. Schneider, C. L. Mcdaniel, Effect of Environment Upon the Melting Point of  $\text{Al}_2\text{O}_3$ , *J. Res. Natl. Bur. Stand. - A. Phys. Chem.*, 71 (1967), 317–333.
- [72] P. Jin, S. X. Wang, L. M. Wang, Localized epitaxial growth of  $\alpha\text{-Al}_2\text{O}_3$  thin films on  $\text{Cr}_2\text{O}_3$  template by sputter deposition at low substrate temperature, *Appl. Phys. Lett.*, 82 (2003), 1024, doi:10.1063/1.1544442.
- [73] A. L. Drago, J. J. Diamond, Transitions in Vapor-Deposited Alumina from 300 to 1200 °C, *J. Am. Ceram. Soc.*, 50 (1967), 568–574.
- [74] T. M. Besmann, N. S. Kulkarni, K. E. Spear, Thermochemical Analysis and Modeling of the  $\text{Al}_2\text{O}_3\text{-Cr}_2\text{O}_3$ ,  $\text{Cr}_2\text{O}_3\text{-SiO}_2$ , and  $\text{Al}_2\text{O}_3\text{-Cr}_2\text{O}_3\text{-SiO}_2$  Systems Relevant to Refractories, *J. Am. Ceram. Soc.*, 89 (2006), 638–644, doi:10.1111/j.1551-2916.2005.00719.x.
- [75] Tetsuya K. Kaneko, Jingxi Zhu, Hugh Thomas, James P. Bennett, Seetharaman Sridhar, Influence of Oxygen Partial Pressure on Synthetic Coal Slag Infiltration into Porous  $\text{Al}_2\text{O}_3$  Refractory, *J. Am. Ceram. Soc.*, 95 (2012), 1764–1773, doi:10.1111/j.1551-2916.2012.05175.x.
- [76] Mineralogy Database, (n.d.). [Online]. Available: <http://webmineral.com/>.
- [77] A. B. Sinani, N. K. Dynkin, L. A. Lytvinov, P. V. Konevsky, E. P. Andreev, Sapphire hardness in different crystallographic directions, *Bull. Russ. Acad. Sci. Phys.*, 73 (2009), 1380–1382, doi:10.3103/S1062873809100177.
- [78] Corundum Mineral Data, (n.d.). [Online]. Available: [http://www.webmineral.com/data/Corundum.shtml#.Wzs4\\_vnOkZQ](http://www.webmineral.com/data/Corundum.shtml#.Wzs4_vnOkZQ).
- [79] Roger H. French, Electronic Band Structure of  $\text{Al}_2\text{O}_3$ , with Comparison to AlON and AlN, *J. Am. Ceram. Soc.*, 73 (1990), 477–489.

- [80] Scott A. Chambers, Epitaxial growth and properties of thin film oxides, *Surf. Sci. Rep.*, 39 (2000), 105–180.
- [81] L. R. Carley, J. A. Bain, G. K. Fedder, D. W. Greve, D. F. Guillou, M. S. C. Lu, et al., Single-chip computers with microelectromechanical systems-based magnetic memory ( invited ), *J. Appl. Phys.*, 87 (2000), 6680–6685, doi:10.1063/1.372807.
- [82] B. Bhushan, *Mechanics and Reliability of Flexible Magnetic Media*, Springer, New York, 1992.
- [83] TDnucl - ThermoData Nuclear Phase Diagrams, (n.d.). [Online]. Available: [http://www.crct.polymtl.ca/fact/Documentation/TDnucl/TDnucl\\_Figs.htm](http://www.crct.polymtl.ca/fact/Documentation/TDnucl/TDnucl_Figs.htm).
- [84] H. A. Wierdt, The Al-O (Aluminum-Oxygen) System, *Bull. Alloy Phase Diagrams*, 6 (1985), 548–550. [Online]. Available: <https://link.springer.com/article/10.1007/BF02887157?no-access=true>.
- [85] Aluminium Oxide, ILO-ICSC, (n.d.). [Online]. Available: [http://www.ilo.org/dyn/icsc/showcard.display?p\\_version=2&p\\_card\\_id=0351](http://www.ilo.org/dyn/icsc/showcard.display?p_version=2&p_card_id=0351).
- [86] X. Liu, S. H. Chan, F. Wu, Y. Li, S. Keller, J. S. Speck, et al., Metalorganic chemical vapor deposition of Al<sub>2</sub>O<sub>3</sub> using trimethylaluminum and O<sub>2</sub> precursors: Growth mechanism and crystallinity, *J. Cryst. Growth*, 408 (2014), 78–84, doi:10.1016/j.jcrysgro.2014.09.029.
- [87] O. Kyrylov, D. Kurapov, J. M. Schneider, Effect of ion irradiation during deposition on the structure of alumina thin films grown by plasma assisted chemical vapour deposition, *Appl. Phys. A.*, 80 (2005), 1657–1660, doi:10.1007/s00339-004-2998-y.
- [88] L. Hiesinger, H. Koenig, Optics and Structure of Cathodic Sputtered Layers with Special Consideration of the Reaction with the Residual Gas, in: A. Ruthardt (Ed.), *Festschr. 100 Jährigen Jubil. W. C. Heraeus GmbH*, 1951: pp. 376–392.

- [89] O. Zywitzki, G. Hoetzsch, F. Fietzke, K. Goedicke, Effect of the substrate temperature on the structure and properties of  $\text{Al}_2\text{O}_3$  layers reactively deposited by pulsed magnetron sputtering, *Surf. Coatings Technol.*, 82 (1996), 169–175.
- [90] J. M. Andersson, E. Wallin, U. Helmersson, U. Kreissig, E. P. Munger, Phase control of  $\text{Al}_2\text{O}_3$  thin films grown at low temperatures, *Thin Solid Films*, 513 (2006), 57–59, doi:10.1016/j.tsf.2006.01.016.
- [91] P. Eklund, M. Sridharan, M. Sillassen, J. Bottiger,  $\alpha\text{-Cr}_2\text{O}_3$  template-texture effect on  $\alpha\text{-Al}_2\text{O}_3$  thin-film growth, *Thin Solid Films*, 516 (2008), 7447–7450, doi:10.1016/j.tsf.2008.03.038.
- [92] D. E. Ashenford, F. Long, W. E. Hagston, B. Lunn, A. Matthews, Experimental and theoretical studies of the low-temperature growth of chromia and alumina, *Surf. Coatings Technol.*, 116–119 (1999), 699–704, doi:10.1016/S0257-8972(99)00181-4.
- [93] Y. Gao, H. Leiste, S. Ulrich, M. Stueber, Synthesis of local epitaxial  $\alpha\text{-}(\text{Cr}_{1-x}\text{Al}_x)_2\text{O}_3$  thin films ( $0.08 \leq x \leq 0.16$ ) on  $\alpha\text{-Al}_2\text{O}_3$  substrates by r.f. magnetron sputtering, *Thin Solid Films*, 644 (2017), 129–137, doi:10.1016/j.tsf.2017.05.054.
- [94] A. Kawabata, M. Yoshinaka, K. Hirota, O. Yamaguchi, Hot Isostatic Pressing and Characterization of Sol-Gel-Derived Chromium (III) Oxide, *J. Am. Ceram. Soc.*, 78 (1995), 2271–2273.
- [95] Arnulf Muan, Shigeyuki Somiya, Phase Equilibrium Studies in the System Iron Oxide- $\text{Al}_2\text{O}_3$ - $\text{Cr}_2\text{O}_3$ , *J. Am. Ceram. Soc.*, 42 (1959), 603–613, doi:10.1111/j.1151-2916.1959.tb13581.x.
- [96] SGnucl - SGTE nuclear database, (2004). [Online]. Available: [http://www.crct.polymtl.ca/fact/phase\\_diagram.php?file=Cr-O.jpg&dir=SGnucl](http://www.crct.polymtl.ca/fact/phase_diagram.php?file=Cr-O.jpg&dir=SGnucl).
- [97] R. N. McNally, F. I. Peters, P. H. Ribbe, Laboratory Furnace for Studies in Controlled Atmospheres; Melting Points of  $\text{MgO}$  in a  $\text{N}_2$  Atmosphere and of  $\text{Cr}_2\text{O}_3$  in  $\text{N}_2$  and in Air Atmospheres, *J. Am. Ceram. Soc.*, 44 (1961), 491–493.

- [98] H. V. Wartenberg, H. J. Reusch, E. Saran, Schmelzpunktsdiagramme höchstfeuerfester Oxyde. VII. Systeme mit CaO und BeO, *Zeitschrift Für Anorg. Und Allg. Chemie.*, 230 (1937), 257–276, doi:10.1002/zaac.19372300309.
- [99] P. S. Robbert, H. Geisler, J. C. A. Ventrice, J. Ek, S. Chaturvedi, J. A. Rodriguez, et al., Novel electronic and magnetic properties of ultrathin chromium oxide films grown on Pt (111), *J. Vac. Sci. Technol. A*, 16 (1998), 990, doi:10.1116/1.581283.
- [100] R. Cheng, T. Komesu, H. K. Jeong, L. Yuan, S. H. Liou, B. Doudin, et al., Temperature dependent induced spin polarization in Cr<sub>2</sub>O<sub>3</sub> overlayers on epitaxial CrO<sub>2</sub> films, *Phys. Lett., Sect. A Gen. At. Solid State Phys.*, 302 (2002), 211–216, doi:10.1016/S0375-9601(02)01050-2.
- [101] A. Sokolov, C. S. Yang, L. Yuan, S. H. Liou, Ruihua Cheng, H. K. Jeong, Zero-bias anomaly in CrO<sub>2</sub> junctions, *Europhys. Lett.*, 58 (2002), 448.
- [102] J. M. D. Coey, A. E. Berkowitz, Ll. Balcells, F. F. Putris, A. Barry, Magnetoresistance of Chromium Dioxide Powder Compacts, *Phys. Rev. Lett.*, 80 (1998), 3815–3818, doi:10.1103/PhysRevLett.80.3815.
- [103] R. Cheng, B. Xu, C. N. Borca, A. Sokolov, C. S. Yang, L. Yuan, et al., Characterization of the native Cr<sub>2</sub>O<sub>3</sub> oxide surface of CrO<sub>2</sub>, *Appl. Phys. Lett.*, 79 (2001), 3122–3124, doi:10.1063/1.1416474.
- [104] R. H. Misho, W. A. Murad, G. H. Fattahallah, Preparation and Optical Properties of Thin Films of CrO<sub>3</sub> and Cr<sub>2</sub>O<sub>3</sub> Prepared by The Method of Chemical Spray Pyrolysis, *Thin Solid Films*, 169 (1989), 235–239.
- [105] M. M. Abdullah, Fahd M. Rajab, Saleh M. Al-Abbas, Structural and optical characterization of Cr<sub>2</sub>O<sub>3</sub> nanostructures : Evaluation of its dielectric properties, *AIP Adv.*, 4 (2014), 27121, doi:10.1063/1.4867012.
- [106] Harish C. Barshilia, K. S. Rajam, Growth and characterization of chromium oxide coatings prepared by pulsed-direct current reactive unbalanced magnetron sputtering, *Appl. Surf. Sci.*, 255 (2008), 2925–2931, doi:10.1016/j.apsusc.2008.08.057.

- [107] H. Mändar, T. Uustare, J. Aarik, A. Tarre, A. Rosental, Characterization of asymmetric rhombohedral twin in epitaxial  $\alpha$ -Cr<sub>2</sub>O<sub>3</sub> thin films by X-ray and electron diffraction, *Thin Solid Films*, 515 (2007), 4570–4579, doi:10.1016/j.tsf.2006.11.037.
- [108] A. S. Kao, M. F. Doerner, V. J. Novotny, Processing effects on the tribological characteristics of reactively sputtered chromium oxide (Cr<sub>2</sub>O<sub>3</sub>) overcoat films, *J. Appl. Phys.*, 66 (1989), 5315–5321, doi:10.1063/1.343722.
- [109] Bharat Bhushan, Gerard S. A. M. Theunissen, Xiaodong Li, Tribological studies of chromium oxide films for magnetic recording applications, *Thin Solid Films*, 311 (1997), 67–80, doi:10.1016/S0040-6090(97)00453-7.
- [110] V. Zieren, M. De Jongh, J. B. A. Van Zon, P. Lasinski, G. S. A. M. Theunissen, A. B. van Groenou, Ultrathin Wear-Resistant Coatings For The Tape Bearing Surface Of Thin-Film Magnetic Heads For Digital Compact Cassette, *IEEE Trans. Magn.*, 30 (1994), 340–345, doi:10.1109/20.312284.
- [111] Carl M. Lampert, Optical Films for Solar Energy Applications, *Technol. Stratif. Media.*, 36 (1983), 36–54, doi:10.1117/12.934982.
- [112] Atul Tiwari, Anthony Galanis, Mark D. Soucek, eds., *Biobased and Environmentally Benign Coatings*, Wiley, 2016.
- [113] M. G. Hutchins, Selective thin film coatings for the conversion of solar radiation, *Surf. Technol.*, 20 (1983), 301–320, doi:10.1016/0376-4583(83)90111-5.
- [114] P. H. Holloway, K. Shanker, G. A. Alexander, L. De Sedas, Oxidation and diffusion in black chrome selective solar absorber coatings, *Thin Solid Films*, 177 (1989), 95–105, doi:10.1016/0040-6090(89)90559-2.
- [115] Toshiro Maruyama, Hisao Akagi, Chromium Oxide Thin Films Prepared by Chemical Vapor Deposition from Chromium Acetylacetonate and Chromium Hexacarbonyl, *J. Electrochem. Soc.*, 143 (1996), 1955–1958.

- [116] John C. C. Fan, Steven A. Spura, Selective black absorbers using rf-sputtered Cr<sub>2</sub>O<sub>3</sub>/Cr cermet films, *Appl. Phys. Lett.*, 30 (1977), 511–513.
- [117] M. Cherian, M. S. Rao, W. T. Yang, J. M. Jehng, A. M. Hirt, G. Deo, Oxidative dehydrogenation of propane over Cr<sub>2</sub>O<sub>3</sub>/Al<sub>2</sub>O<sub>3</sub> and Cr<sub>2</sub>O<sub>3</sub> catalysts: Effects of loading, precursor and surface area, *Appl. Catal. A Gen.*, 233 (2002), 21–33, doi:10.1016/S0926-860X(02)00132-1.
- [118] J. S. Park, S. K. Hong, T. Minegishi, I. H. Im, S. H. Park, T. Hanada, et al., The high quality ZnO growth on c-Al<sub>2</sub>O<sub>3</sub> substrate with Cr<sub>2</sub>O<sub>3</sub> buffer layer using plasma-assisted molecular beam epitaxy, *Appl. Surf. Sci.*, 254 (2008), 7786–7789, doi:10.1016/j.apsusc.2008.02.031.
- [119] P. Hones, M. Diserens, F. Levy, Characterization of sputter-deposited chromium oxide thin films, *Surf. Coatings Technol.*, 120–121 (1999), 277–283.
- [120] Chromic Acid, Chromium Salt, Pubchem Open Chem. Database, (n.d.). [Online]. Available: <https://pubchem.ncbi.nlm.nih.gov/compound/165971#section=Top>.
- [121] Chromium Oxide Powder (Cr<sub>2</sub>O<sub>3</sub>), (n.d.). [Online]. Available: <https://www.reade.com/products/chromium-oxide-powder-cr2o3>.
- [122] Eskolaite, *Handb. Mineral*, (n.d.), doi:10.3746/jfn.2005.10.2.187.
- [123] P. H. Fang, W. S. Brower, Dielectric Constant of Cr<sub>2</sub>O<sub>3</sub> Crystals, *Phys. Rev.*, 129 (1951), 1561–1561, doi:10.1103/PhysRev.129.1561.
- [124] J. C. Nable, S. L. Suib, F. S. Galasso, Metal organic chemical vapor deposition of Al<sub>2</sub>O<sub>3</sub> and Cr<sub>2</sub>O<sub>3</sub> on nickel as oxidation barriers, *Surf. Coatings Technol.*, 186 (2004), 423–430, doi:10.1016/j.surfcoat.2003.11.022.
- [125] R. Chaim, S. Almaleh-Rockman, L. Gal-Or, H. Bestgen, Electrochemical Chromium(III) Oxide Coatings on Non-oxide Ceramic Substrates, *J. Am. Ceram. Soc.*, 77 (1994), 3202–3208, doi:10.1111/j.1151-2916.1994.tb04570.x.

- [126] V. M. Bermudez, W. J. DeSisto, Study of chromium oxide film growth by chemical vapor deposition using infrared reflection absorption spectroscopy, *J. Vac. Sci. Technol. A.*, 19 (2001), 576, doi:10.1116/1.1339008.
- [127] M. F. Al-Kuhaili, S. M. A. Durrani, Optical properties of chromium oxide thin films deposited by electron-beam evaporation, *Opt. Mater.*, 29 (2007), 709–713, doi:10.1016/j.optmat.2005.11.020.
- [128] S. Hong, E. Kim, D.-W. Kim, T.-H. Sung, K. No, On measurement of optical band gap of chromium oxide films containing both amorphous and crystalline phases, *J. Non. Cryst. Solids.*, 221 (1997), 245–254, doi:10.1016/S0022-3093(97)00367-0.
- [129] X. Pang, K. Gao, F. Luo, H. Yang, L. Qiao, Y. Wang, et al., Annealing effects on microstructure and mechanical properties of chromium oxide coatings, *Thin Solid Films*, 516 (2008), 4685–4689, doi:10.1016/j.tsf.2007.08.083.
- [130] K. Pedersen, J. Bøttiger, M. Sridharan, M. Sillassen, P. Eklund, Texture and microstructure of  $\text{Cr}_2\text{O}_3$  and  $(\text{Cr,Al})_2\text{O}_3$  thin films deposited by reactive inductively coupled plasma magnetron sputtering, *Thin Solid Films*, 518 (2010), 4294–4298, doi:10.1016/j.tsf.2010.01.008.
- [131] A. Stierle, P. Boedeker, H. Zabel, Epitaxial oxide formation on Cr (110) films, *Surf. Sci.*, 327 (1995), 9–16.
- [132] L. Zhang, M. Kuhn, U. Diebold, Growth, structure and thermal properties of chromium oxide films on Pt (111), *Surf. Sci.*, 375 (1997), 1–12.
- [133] L. Zhang, Epitaxial growth of ultrathin films of chromium and its oxides on Pt(111), *J. Vac. Sci. Technol., A Vacuum, Surface, Film*, 15 (1997), 1576, doi:10.1116/1.580635.
- [134] S. A. Chambers, Y. Liang, Y. Gao, Noncommutative band offset at  $\alpha\text{-Cr}_2\text{O}_3/\alpha\text{-Fe}_2\text{O}_3$  (0001) heterojunctions, *Phys. Rev. B.*, 61 (2000), 223–229.

- [135] Y. Ito, K. Kushida, H. Takeuchi, Role of chromium sublayers in the growth of highly crystalline (111)-oriented gold films on sapphire, *J. Cryst. Growth*, 112 (1991), 427–436, doi: 10.1016/0022-0248(91)90319-Z.
- [136] H. A. Wriedt, The O-V (Oxygen-Vanadium) system, *Bull. Alloy Phase Diagrams*, 10 (1989), 271–277, doi:10.1007/BF02877512.
- [137] O’Neil, *The Merck Index - An Encyclopedia of Chemicals, Drugs, and Biologicals*, UK: Royal Society of Chemistry, Cambridge, 2013.
- [138] A. Mukherjee, An investigation of the structure and the stability of phases in the V-O system, *J. Less Common Met.*, 107 (1985), 89–97.
- [139] I. L. Botto, M. B. Vassallo, E. J. Baran, G. Minelli, IR spectra of VO<sub>2</sub> and V<sub>2</sub>O<sub>3</sub>, *Mater. Chem. Phys.*, 50 (1997), 267–270.
- [140] C. Wessel, C. Reimann, A. Müller, D. Weber, M. Lerch, T. Ressler, et al., Electronic structure and thermodynamics of V<sub>2</sub>O<sub>3</sub> polymorphs., *J. Comput. Chem.*, 33 (2012), 2102–7, doi:10.1002/jcc.23046.
- [141] M. M. Qazilbash, A. A. Schafgans, K. S. Burch, S. J. Yun, B. G. Chae, B. J. Kim, et al., Electrodynamics of the vanadium oxides VO<sub>2</sub> and V<sub>2</sub>O<sub>3</sub>, *Phys. Rev. B.*, 77 (2008), 115121, doi:10.1103/PhysRevB.77.115121.
- [142] C. Lamsal, N. M. Ravindra, Optical properties of vanadium oxides-an analysis, *J. Mater. Sci.*, 48 (2013), 6341–6351, doi:10.1007/s10853-013-7433-3.
- [143] B. Sass, C. Tusche, W. Felsch, N. Quaas, A. Weismann, M. Wenderoth, Structural and electronic properties of epitaxial V<sub>2</sub>O<sub>3</sub> thin films, *J. Phys. Condens. Matter.*, 16 (2004), 77–87, doi:10.1088/0953-8984/16/1/008.
- [144] L. Baldassarre, A. Perucchi, D. Nicoletti, A. Toschi, G. Sangiovanni, K. Held, et al., Quasiparticle evolution and pseudogap formation in V<sub>2</sub>O<sub>3</sub>: An infrared spectroscopy study, *Phys. Rev. B.*, 77 (2008), 113107, doi:10.1103/PhysRevB.77.113107.

- [145] R. S. Rana, D. D. Nolte, F. A. Chudnovski, Optical bistability from a thermodynamic phase transition in vanadium dioxide, *Opt. Lett.*, 17 (1992), 1385, doi:10.1364/OL.17.001385.
- [146] Michael S. Thomas, Jeff F. Denatale, Patrick J. Hood, High Temperature Optical Properties of Thin Film Vanadium Oxides VO<sub>2</sub> and V<sub>2</sub>O<sub>3</sub>, *Mater. Res. Soc.*, 479 (1997), 161, doi: 10.1557/PROC-479-161.
- [147] Divanadium Trioxide, Pubchem Open Chem. Database, (n.d.). [Online]. Available: <https://pubchem.ncbi.nlm.nih.gov/compound/518710#section=Top>.
- [148] Maryadele J. O'Neil, ed., *The Merck Index - An Encyclopedia of Chemicals, Drugs, and Biologicals*, Royal Society of Chemistry, Cambridge, 2013.
- [149] W. M. Haynes, *CRC Handbook of Chemistry and Physics*, 95th Edition, CRC Press LLC, Boca Raton.
- [150] Pubchem Open Chemistry Database, (n.d.). [Online]. Available: <https://pubchem.ncbi.nlm.nih.gov/compound/518710>.
- [151] A. A. Valeeva, D. A. Davydov, S. V. Rempel, A. A. Rempel, Microstructure and Microhardness of Vanadium Oxides in the Range VO<sub>0.57</sub>-VO<sub>1.29</sub>, *Inorg. Mater.*, 45 (2009), 905–909, doi:10.1134/S0020168509080159.
- [152] J. Piao, S. Takahashi, S. Kohiki, Preparation and characterization of V<sub>2</sub>O<sub>3</sub> powder and film, *Japanese J. Appl. Physics, Part 1 Regul. Pap. Short Notes Rev. Pap.*, 37 (1998), 6519–6523.
- [153] D. P. Partlow, S. R. Gurkovich, K. C. Radford, L. J. Denes, Switchable vanadium oxide films by a sol-gel process, (1991), 443–452.
- [154] H. Schuler, S. Klimm, G. Weissmann, C. Renner, S. Horn, Influence of strain on the electronic properties of epitaxial V<sub>2</sub>O<sub>3</sub> thin films, *Thin Solid Films*, 299 (1997), 119–124, doi:10.1016/S0040-6090(96)09399-6.
- [155] K. D. Rogers, J. A. Coath, M. C. Lovell, Characterization of epitaxially grown films of vanadium oxides, *J. Appl. Phys.*, 70 (1991), 1412–1415, doi:10.1063/1.349550.

- [156] B. S. Allimi, S. P. Alpay, C. K. Xie, B. O. Wells, J. I. Budnick, D. M. Pease, Resistivity of  $V_2O_3$  thin films deposited on a-plane (110) and c-plane (001) sapphire by pulsed laser deposition, *Appl. Phys. Lett.*, 92 (2008), 202105, doi:10.1063/1.2921787.
- [157] D. Levchuk, H. Bolt, M. Döbeli, S. Eggenberger, B. Widrig, J. Ramm, Al-Cr-O thin films as an efficient hydrogen barrier, *Surf. Coatings Technol.*, 202 (2008), 5043–5047, doi:10.1016/j.surfcoat.2008.05.012.
- [158] Sung S. Kim, Thomas H. Sanders, Thermodynamic Modeling of the Isomorphous Phase Diagrams in the  $Al_2O_3$ – $Cr_2O_3$  and  $V_2O_3$ – $Cr_2O_3$  Systems, *J. Am. Ceram. Soc.*, 84 (2001), 1881–1884.
- [159] F. Bondioli, A. M. Ferrari, C. Leonelli, T. Manfredini, L. Linati, P. Mustarelli, Reaction mechanism in alumina/chromia ( $Al_2O_3$ - $Cr_2O_3$ ) solid solutions obtained by coprecipitation, *J. Am. Ceram. Soc.*, 83 (2000), 2036–2040, doi:10.1111/j.1151-2916.2000.tb01508.x.
- [160] T. Hirata, T. Morimoto, A. Deguchi, N. Uchida, Corrosion Resistance of Alumina-Chromia Ceramic Materials Against Molten Slag, *Mater. Trans.*, 43 (2002), 2561–2567.
- [161] T. Hirata, T. Morimoto, S. Ohta, N. Uchida, Improvement of the corrosion resistance of alumina-chromia ceramic materials in molten slag, *J. Eur. Ceram. Soc.*, 23 (2003), 2089–2096, doi:10.1016/S0955-2219(03)00023-2.
- [162] D. Diechle, M. Stueber, H. Leiste, S. Ulrich, V. Schier, Combinatorial approach to the growth of  $\alpha$ - $(Al_{1-x},Cr_x)_2O_3$  solid solution strengthened thin films by reactive r.f. magnetron sputtering, *Surf. Coatings Technol.*, 204 (2010), 3258–3264, doi:10.1016/j.surfcoat.2010.03.029.
- [163] A. Khatibi, Deposition and Phase Transformations of Ternary Al-Cr-O Thin Films, Linköping University, 2011.
- [164] J. Ramm, M. Ante, T. Bachmann, B. Widrig, H. Brändle, M. Döbeli, Pulse enhanced electron emission ( $P3e^{TM}$ ) arc evaporation and the synthesis of wear

- resistant Al-Cr-O coatings in corundum structure, *Surf. Coatings Technol.*, 202 (2007), 876–883, doi:10.1016/j.surfcoat.2007.05.044.
- [165] C. M. Koller, R. Hahn, B. Widrig, J. Ramm, S. Kolozsvári, J. Paulitsch, et al., Triggering the Phase Evolution Within (Al,Cr)<sub>2</sub>O<sub>3</sub>-based Coatings by Alloying and Microstructural Concepts, *BHM Berg- Und Hüttenmännische Monatshefte*, 161 (2016), 325–329, doi:10.1007/s00501-016-0506-2.
- [166] C. M. Koller, J. Ramm, S. Kolozsvári, F. Munnik, J. Paulitsch, P. H. Mayrhofer, Corundum-type Fe-doped cathodic arc evaporated Al-Cr-O coatings, *Scr. Mater.*, 97 (2015), 49–52, doi:10.1016/j.scriptamat.2014.10.037.
- [167] M. Witthaut, R. Cremer, K. Reichert, D. Neuschuetz, Preparation of Cr<sub>2</sub>O<sub>3</sub>-Al<sub>2</sub>O<sub>3</sub> Solid Solutions by Reactive Magnetron Sputtering, *Microchim. Acta.*, 133 (2000), 191–196, doi:10.1007/s006040070092.
- [168] M. Pohler, R. Franz, J. Ramm, P. Polcik, C. Mitterer, Seed layer stimulated growth of crystalline high Al containing (Al,Cr)<sub>2</sub>O<sub>3</sub> coatings deposited by cathodic arc evaporation, *Thin Solid Films*, 550 (2014), 95–104, doi:10.1016/j.tsf.2013.10.125.
- [169] M. Pohler, R. Franz, J. Ramm, P. Polcik, C. Mitterer, Cathodic arc deposition of (Al,Cr)<sub>2</sub>O<sub>3</sub>: Macroparticles and cathode surface modifications, *Surf. Coatings Technol.*, 206 (2011), 1454–1460, doi:10.1016/j.surfcoat.2011.09.028.
- [170] J. Ramm, M. Ante, H. Brändle, A. Neels, A. Dommann, M. Döbeli, Thermal Stability of Thin Film Corundum-Type Solid Solutions of (Al<sub>1-x</sub>Cr<sub>x</sub>)<sub>2</sub>O<sub>3</sub> Synthesized Under Low-Temperature Non-Equilibrium Conditions, *Adv. Eng. Mater.*, 9 (2007), 604–608, doi:10.1002/adem.200700081.
- [171] Dominic Diechle, Herstellung und Charakterisierung oxid- basierter PVD-Hartstoffschichten in den Stoffsystemen Al-Cr-O und Al-Cr-O-N, Karlsruhe Institute of Technology, 2012.
- [172] H. Najafi, A. Karimi, P. Dessarzin, M. Morstein, Formation of cubic structured (Al<sub>1-x</sub>Cr<sub>x</sub>)<sub>2+δ</sub>O<sub>3</sub> and its dynamic transition to corundum phase during cathodic arc

- evaporation, *Surf. Coatings Technol.*, 214 (2013), 46–52, doi:10.1016/j.surfcoat.2012.10.062.
- [173] A. Khatibi, J. Palisaitis, C. Höglund, A. Eriksson, P. O. Å. Persson, J. Jensen, et al., Face-centered cubic  $(Al_{1-x}Cr_x)_2O_3$ , *Thin Solid Films*, 519 (2011), 2426–2429, doi:10.1016/j.tsf.2010.11.052.
- [174] A. Callaghan, M. J. Rossiter, F. S. Stone, Magnetic Properties of  $V_2O_3$ - $Al_2O_3$  Solid Solutions, *Trans. Faraday Soc.* 62 (1966) 3463–3469.
- [175] M. H. L. Pryce, W. A. Runciman, The absorption spectrum of vanadium corundum, *Discuss. Faraday Soc.*, 26 (1958), 34–42, doi:10.1039/df9582600034.
- [176] Zeng Li, Study on Phase Diagram of  $FeO$ - $V_2O_3$ - $SiO_2$ - $Al_2O_3$  System, Chongqing University, China, 2013.
- [177] Arnulf Muan, Mitri S. Najjar, Compositions involving  $V_2O_3$ - $Al_2O_3$ - $CaO$ , Texaco Inc., White Plains, N.Y.: U.S., 1991.
- [178] Nitri S. Najjar, Arnulf Muan, Compositions involving  $V_2O_3$ - $Al_2O_3$ - $TiO_2$ , Texaco Inc., White Plains, N.Y.: U.S., 1990.
- [179] M. Foex, C. Martinez, Etude des Proprietes Semi-Conductrices des Ceramiques Formees Par Le Sesquioxyde de Vanadium Avec Lalumine, *Bull. Soc. Chim.*, 17 (1950), 1301.
- [180] V. V. Viktorov, Magnetic properties and structure of  $(V_xAl_{1-x})_2O_3$ , *Phys. Status Solidi.*, 179 (1993), 531–537.
- [181] D. B. McWhan, T. M. Rice, J. P. Remeika, Mott transition in Cr-Doped  $V_2O_3$ , *Phys. Rev. Lett.*, 23 (1969), 1384–1387, doi:10.1103/PhysRevLett.23.1384.
- [182] R. D. Shannon, Revised Effective Ionic Radii and Systematic Studies of Interatomic Distances in Halides and Chalcogenides, *Acta Cryst. A*, 32 (1976), 751–767.
- [183] P. A. Metcalf, S. Guha, L. P. Gonzalez, J. O. Barnes, E. B. Slamovich, J. M. Honig, Electrical, structural, and optical properties of Cr-doped and non-stoichiometric

- V<sub>2</sub>O<sub>3</sub> thin films, *Thin Solid Films*, 515 (2007), 3421–3425, doi:10.1016/j.tsf.2006.10.003.
- [184] A. Perucchi, L. Baldassarre, P. Postorino, S. Lupi, Optical properties across the insulator to metal transitions in vanadium oxide compounds, *J. Phys. Condens. Matter.*, 21 (2009), 323202, doi:10.1088/0953-8984/21/32/323202.
- [185] P. Homm, L. Dillemans, M. Menghini, B. Van Bilzen, P. Bakalov, C. Y. Su, et al., Collapse of the low temperature insulating state in Cr-doped V<sub>2</sub>O<sub>3</sub> thin films, *Appl. Phys. Lett.*, 107 (2015), 1–5, doi:10.1063/1.4931372.
- [186] H. Kuwamoto, J. M. Honig, J. Appel, Electrical properties of the (V<sub>1-x</sub>Cr<sub>x</sub>)<sub>2</sub>O<sub>3</sub> system, *Phys. Rev. B*, 22 (1980), 2626–2636, doi:10.1103/PhysRevB.22.2626.
- [187] T. Oyama, Y. Iimura, K. Takeuchi, Synthesis of (Cr<sub>x</sub>V<sub>1-x</sub>)<sub>2</sub>O<sub>3</sub> fine particles by a laser-induced vapor-phase reaction and their crystal structure, *J. Mater. Sci.*, 4 (1999), 439–444, doi:10.1023/A:1004517906572.
- [188] S. Spitz, M. Stüber, H. Leiste, S. Ulrich, H. J. Seifert, Microstructure and hardness of reactively r.f. magnetron sputtered Cr-V-O thin films in dependence on composition and substrate bias, *Surf. Coatings Technol.*, 257 (2014), 355–362, doi:10.1016/j.surfcoat.2014.07.040.
- [189] Scott A. Chambers, Epitaxial growth and properties of doped transition metal and complex oxide films, *Adv. Mater.*, 22 (2010), 219–248, doi:10.1002/adma.200901867.
- [190] S. Spitz, M. Stueber, H. Leiste, S. Ulrich, H. J. Seifert, Microstructure evolution of radio-frequency magnetron sputtered oxide thin films in the Cr–Zr–O system, *Thin Solid Films*, 548 (2013), 143–149, doi:10.1016/j.tsf.2013.09.038.
- [191] H. Mashiko, T. Oshima, A. Ohtomo, Epitaxial Structures of Band-Gap-Engineered  $\alpha$ -(Cr<sub>x</sub>Fe<sub>1-x</sub>)<sub>2</sub>O<sub>3</sub> (0 ≤ x ≤ 1) Grown on C-Plane Sapphire, *Jpn. J. Appl. Phys.*, 51 (2012), 1–5.

- [192] S. E. Chamberlin, T. C. Kaspar, M. E. Bowden, V. Shutthanandan, B. Kabius, S. Heald, et al., Structural perturbations of epitaxial  $\alpha$ -(Fe<sub>1-x</sub>V<sub>x</sub>)<sub>2</sub>O<sub>3</sub> thin films driven by excess oxygen near the surface, *J. Appl. Phys.*, 116 (2014), 233702.
- [193] L. A. Tietz, S. R. Summerfelt, C. B. Carter, The effect of substrate orientation on the chemical vapor deposition growth of  $\alpha$ -Fe<sub>2</sub>O<sub>3</sub> on  $\alpha$ -Al<sub>2</sub>O<sub>3</sub>, *Philos. Mag. A*, 65 (1992), 439–460, doi:10.1080/01418619208201532.
- [194] C. Wang, S. Thevuthasan, F. Gao, D. E. Mccready, S. A. Chambers, The characteristics of interface misfit dislocations for epitaxial  $\alpha$ -Fe<sub>2</sub>O<sub>3</sub> on  $\alpha$ -Al<sub>2</sub>O<sub>3</sub> (0001), *Thin Solid Films*, 414 (2002), 31–38.
- [195] S. A. Chambers, T. Droubay, Role of oxide ionicity in electronic screening at oxide/metal interfaces, *Phys. Rev. B*, 64 (2001), 1–6, doi:10.1103/PhysRevB.64.075410.
- [196] T. Fujii, M. Takano, R. Kakano, Y. Isozumi, Y. Bando, Spin-flip anomalies in epitaxial  $\alpha$ -Fe<sub>2</sub>O<sub>3</sub> films by Moessbauer spectroscopy, *J. Magn. Magn. Mater.*, 135 (1994), 231–236.
- [197] S. -H. Park, H. Jang, J. -Y. Kim, B. -G. Park, T. -Y. Koo, J. -H. Park, Strain control of Morin temperature in epitaxial  $\alpha$ -Fe<sub>2</sub>O<sub>3</sub> (0001) film, *Europhys. Lett.*, 103 (2013), 27007, doi:10.1209/0295-5075/103/27007.
- [198] H. W. Holleck, Advanced concepts of PVD hard coatings, *Vacuum*, 41 (1990), 2220–2222, doi:10.1016/0042-207X(90)94229-J.
- [199] Hisanori Mashiko, Takayoshi Oshima, Akira Ohtomo, Band-gap narrowing in  $\alpha$ -(Cr<sub>x</sub>Fe<sub>1-x</sub>)<sub>2</sub>O<sub>3</sub> solid-solution films, *Appl. Phys. Lett.*, 99 (2011), 241904.
- [200] Sara E Chamberlin, Yong Wang, Kenneth Lopata, Tiffany C Kasper, Alicia W Cohn, Daniel R Gamelin, et al., Optical absorption and spectral photoconductivity in  $\alpha$ -(Fe<sub>1-x</sub>Cr<sub>x</sub>)<sub>2</sub>O<sub>3</sub> solid-solution thin films, *J. Physics. Condens. Matter.*, 25 (2013), 392002.

- [201] Donald M. Mattox, Handbook of Physical Vapor Deposition (PVD) Processing: Film Formation, Adhesion, Surface Preparation and Contamination Control, Noyes Publications, Westwood, New Jersey, U.S.A., 1998, doi:10.1080/10426919908907566.
- [202] S. Swann, Magnetron sputtering, Phys. Technol., 19 (1988), 67–75.
- [203] Alexander Piel, Plasma Physics: An Introduction to Laboratory, Space, and Fusion Plasma, Springer-Verlag, Berlin Heidelberg, 2010.
- [204] W. D. Münz, F. J. M. Hauzer, D. Schulze, B. Buil, A new concept for physical vapor deposition coating combining the methods of arc evaporation and unbalanced-magnetron sputtering, Surf. Coatings Technol., 49 (1991), 161–167, doi:10.1016/0257-8972(91)90049-3.
- [205] Orlando Auciello, Juergen Engemann, eds., Multicomponent and Multilayered Thin Films for Advanced Micro-technologies : Techniques, Fundamentals and Devices, Springer Science + Business Media, B. V., 1992, doi:10.1007/978-94-011-1727-2.
- [206] Mitsuharu Konuma, Film Deposition by Plasma Techniques, Springer-Verlag, 1992.
- [207] G. Lucovsky, R. J. Sladek, J. W. Allen, Infrared-active phonons in Cr<sub>2</sub>O<sub>3</sub>, Phys. Rev. B, 16 (1977), 4716–4718.
- [208] J. A. Thornton, Influence of apparatus geometry and deposition conditions on the structure and topography of thick sputtered coatings, J. Vac. Sci. Technol., 11 (1974), 666–670, doi:10.1116/1.1312732.
- [209] Charles A. Bishop, Nucleation, Coalescence, and Film Growth, in: Vac. Depos. onto Webs, Film. Foils, First Edit, ELSEVIER, Oxford, UK, 2007: pp. 205–224, doi:10.1016/b978-081551535-7.50011-2.
- [210] T. Nakano, Study of particle transport in high pressure sputter deposition process, University of Tokyo, 2001.

- [211] Atomic Radius of the elements, Mathematica's ElementData, Wolfram Research, Inc., (n.d.). [Online]. Available: <http://periodictable.com/Properties/A/AtomicRadius.v.html>.
- [212] LENNTECH, Molecular Weight Calculator, Lenntech B.V., (n.d.). [Online]. Available: <https://www.lenntech.com/calculators/molecular/molecular-weight-calculator.html>.
- [213] Ronald A. Powell, Stephen M. Rossnagel, PVD for Microelectronics: Sputter Deposition Applied to Semiconductor Manufacturing, ACADEMIC PRESS, 1999, doi:10.1016/S1079-4050(99)80012-X.
- [214] W. Reuter, Electron probe microanalysis, *Surf. Sci.*, 25 (1971), 80–119, doi:10.1016/0039-6028(71)90211-1.
- [215] W. Abel, P.D. W. Eschrich, R. G. H. A. Uihli, U. L. J. B. Passioura, *Microautoradiography and Electron Probe Analysis*, Springer-Verlag, Berlin, Heidelberg, New York, 1972.
- [216] Peter Duncumb, Quantitative analysis with the electron microprobe. The first 50 years and beyond, *J. Anal. At. Spectrom.*, 14 (1999), 357–366.
- [217] A. I. Kirkland, P. D. Nellist, R. Reichelt, G. Botton, W. E. King, F. M. Ross, et al., *Science of Microscopy*, Springer, New York, USA, 2007.
- [218] John F. Watts, John Wolstenholme, *An Introduction to Surface Analysis by XPS and AES*, Wiley, Chichester, 2003.
- [219] Armin Segmueller, I. C. Noyan, V. S. Speriosu, X-Ray Diffraction Studies of Thin Films and Multilayer Structures, *Prog. Cryst. Growth Charact.*, 18 (1988), 21–66.
- [220] W. H. Bragg, W. L. Bragg, The Reflection of X-rays by Crystals, *Proc. R. Soc. London. Ser. A*, (1913), 428–438, doi:10.1126/science.58.1507.400.
- [221] E. Prince, ed., *International Tables for Crystallography Volume C, Third Edit*, Klumer Academic Publisher, Dordrecht/Boston/London, 2004.

- [222] International Tables for X-ray Crystallography, Volume I, 1972.
- [223] Harold P. Klug, Leroy E. Alexander, X-Ray Diffraction Procedures: For Polycrystalline and Amorphous Materials, Second Edi, Wiley-VCH, 1974, doi:10.1016/0001-6160(56)90124-9.
- [224] M. A. Moram, M. E. Vickers, X-ray diffraction of III-nitrides, Reports Prog. Phys., 72 (2009), 36502, doi:10.1088/0034-4885/72/3/036502.
- [225] Olutayo I. Olubiyi, Fa-Ke Lu, David Calligaris, Ferenc A. Jolesz, Nathalie Y. Agar, Advances in Molecular Imaging for Surgery, in: Alexandra J. Golby (Ed.), Image-Guided Neurosurg., Academic Press, 2015: pp. 407–439, doi:10.1016/B978-0-12-800870-6.00017-0.
- [226] H. J. Bowley, D. J. Gardiner, D. L. Gerrard, P. R. Graves, J. D. Loudon, G. Turrell, Practical Raman Spectroscopy, Springer-Verlag, 1989, doi:10.1007/978-3-642-74040-4.
- [227] Ian R. Lewis, Howell G. M. Edwards, eds., Handbook of Raman Spectroscopy, Taylor and Francis Group, LLC, New York, Basel, 2001.
- [228] S. Bhagavantam, T. Venkataryudu, Raman effect in relation to crystallographic structure, Proc. Ind. Acad. Sci. A, 9 (1939), 224, [Online]. Available: <https://doi.org/PISAA7>.
- [229] Y. Repelin, E. Husson, C. Proust, Relation between valence force constants and elastic constants in  $\alpha$ -Alumina: Evolution at high temperature, J. Solid State Chem., 116 (1995), 378–384.
- [230] J. Mougín, T. Le Bihan, G. Lucazeau, High-pressure study of Cr<sub>2</sub>O<sub>3</sub> obtained by high-temperature oxidation by X-ray diffraction and Raman spectroscopy, J. Phys. Chem. Solids., 62 (2001), 553–563, doi:10.1016/S0022-3697(00)00215-8.
- [231] B. Schrader, ed., Infrared and Raman Spectroscopy, VCH Publishers, New York, 1995.

- [232] Valeri A. Skryshevsky, Irina V. Chernyshova, Valeri A. Skryshevsky, Handbook of Infrared Spectroscopy of Ultrathin Films, John Wiley & Sons, Inc., Hoboken, New Jersey, 2003.
- [233] K. Yamamoto, H. Ishida, Kramers-Kronig analysis applied to reflection-absorption spectroscopy, *Vib. Spectrosc.*, 15 (1997), 27–36, doi:10.1016/S0924-2031(97)00017-9.
- [234] F. Hoffmann, Infrared reflection-absorption spectroscopy of adsorbed molecules, *Surf. Sci. Rep.*, 3 (1983), 107, doi:10.1016/0167-5729(83)90001-8.
- [235] Heinz Helmut Perkampus, ed., UV-VIS Spectroscopy and Its Applications, Springer-Verlag, Berlin, 1992, doi:10.1007/b94239.
- [236] A. Jamal, M. M. Rahman, S. B. Khan, P. Khan, K. Akhtar, Simple Growth and Characterization of  $\alpha$ - $\text{Sb}_2\text{O}_4$  : Evaluation of their Photo-catalytic and Chemical Sensing Applications, *J. Ceram. Soc., Pakistan*, 35 (2013), 570–576.
- [237] C.-S. Cheng, H. Gomi, H. Sakata, Electrical and Optical Properties of  $\text{Cr}_2\text{O}_3$  Films Prepared by Chemical Vapour Deposition, *Phys. Status Solidi.*, 417 (1996), 417–425.
- [238] B. Fultz, J. Howe, Transmission Electron Microscopy and Diffractometry of Materials 3rd Edition, Springer-Verlag, New York, 2008.
- [239] Havi Singh Nalwa, Handbook of Surfaces and Interfaces of Materials, 2001.
- [240] D. Magnfält, Fundamental processes in thin film growth, 2014. [Online]. Available: <http://liu.diva-portal.org/smash/get/diva2:710286/FULLTEXT01.pdf>.
- [241] Ludwig Reimer, Transmission Electron Microscopy, Springer-Verlag Berlin Heidelberg GmbH, New York and Tokyo, 1984.
- [242] S.-H. Shim, T. Duffy, R. Jeanloz, C.-S. Yoo, V. Iota, Raman spectroscopy and x-ray diffraction of phase transitions in  $\text{Cr}_2\text{O}_3$  to 61 GPa, *Phys. Rev. B*, 69 (2004), 1–12, doi:10.1103/PhysRevB.69.144107.

- [243] K. F. Mccarty, D. R. Boehme, A Raman study of the systems  $\text{Fe}_{3-x}\text{Cr}_x\text{O}_4$  and  $\text{Fe}_{2-x}\text{Cr}_x\text{O}_3$ , *J. Solid State Chem.*, 79 (1989), 19–27, doi:10.1016/0022-4596(89)90245-4.
- [244] T. R. Hart, R. L. Aggarwal, B. Lax, in *Proceedings of the Second International Conference on Light Scattering in Solids*, Flammarion Sciences, Paris, 1971.
- [245] Yin Gao, Harald Leiste, Michael Stueber, S. Ulrich, The process of growing  $\text{Cr}_2\text{O}_3$  thin films on  $\alpha\text{-Al}_2\text{O}_3$  substrates at low temperature by r.f. magnetron sputtering, *J. Cryst. Growth*, 457 (2017), 158–163, doi:10.1016/j.jcrysgro.2016.08.009.
- [246] M. D. Julkarnain, J. Hossain, K. S. Sharif, K. A. Khan, Temperature effect on the electrical properties of chromium oxide ( $\text{Cr}_2\text{O}_3$ ) thin films, *J. Optoelectron. Adv. Mater.*, 13 (2011), 485–490.
- [247] Atsushi Okamoto, Yoshitaka Fujita, Chieji Tatsuyama, Raman study on the high temperature transition in  $\text{V}_2\text{O}_3$ , *J. Phys. Soc. Japan*, 52 (1983), 312–317, doi:10.1143/JPSJ.52.312.
- [248] X. Chen, J. Shin, H. Kim, Y. Lim, Raman analyses of co-phasing and hysteresis behaviors in  $\text{V}_2\text{O}_3$  thin film, *Raman Spectrosc.*, 43 (2012), 2025–2028, doi:10.1002/jrs.4112.
- [249] N. Kuroda, H. Y. Fan, Raman scattering and phase transition of  $\text{V}_2\text{O}_3$ , *Phys. Rev. B*, 16 (1977), 5003–5008.
- [250] M. J. Rozenberg, G. Kotliar, H. Kajueter, G. A. Thomas, D. H. Rapkine, J. M. Honig, et al., Optical Conductivity in Mott-Hubbard Systems, *Phys. Rev. Lett.*, 75 (1995), 105–108.
- [251] Xiang-Bai Chen, Meng-Hong Kong, Jeong-Yong Choi, Hyun-Tak Kim, Raman spectroscopy studies of spin-wave in  $\text{V}_2\text{O}_3$  thin films, *J. Phys. D. Appl. Phys.*, 49 (2016), 465304, doi:10.1088/0022-3727/49/46/465304.

- [252] Lorenzo Fallarino, Christian Binek, Andreas Berger, Boundary magnetization properties of epitaxial  $\text{Cr}_{2-x}\text{Al}_x\text{O}_3$  thin films, *Phys. Rev. B*, 91 (2015), 214403. [Online]. Available: <http://link.aps.org/doi/10.1103/PhysRevB.91.205132>.
- [253] Thomas F. Kuech, Handbook of Crystal Growth Thin Films and Epitaxy : Basic Techniques Handbook of Crystal Growth, Second, Elsevier, 2015.
- [254] Louis R. Rossi, Willis G. Lawrence, Elastic Properties of Oxide Solid Solutions: The System  $\text{Al}_2\text{O}_3\text{-Cr}_2\text{O}_3$ , *J. Am. Ceram. Soc.*, 53 (1970), 604–608.
- [255] Tiffany C. Kaspar, Peter V. Sushko, Mark E. Bowden, Steve M. Heald, Alexandra Papadogianni, Carsten Tschammer, et al., Defect compensation by Cr vacancies and oxygen interstitials in  $\text{Ti}^{4+}$ -doped  $\text{Cr}_2\text{O}_3$  epitaxial thin films, *Phys. Rev. B*, 94 (2016), 54509, doi:10.1103/PhysRevB.94.054509.
- [256] H. Hagiwara, S. Koya, M. Wilde, M. Matsumoto, T. Okano, K. Fukutani, Growth and vibrational properties of ultra-thin  $\text{Cr}_2\text{O}_3$  films grown on Cr (110) studied by RAIRS, *Surf. Sci.*, 600 (2006), 3252–3257, doi:10.1016/j.susc.2006.06.013.
- [257] S. Zeidler, T. Posch, H. Mutschke, Optical constants of refractory oxides at high temperatures, *Astron. Astrophys.*, 553 (2013), A81, doi:10.1051/0004-6361/201220459.
- [258] K. Xiang, R. Pandey, J. M. Recio, E. Francisco, J. M. Newsam, A Theoretical Study of the Cluster Vibrations in  $\text{Cr}_2\text{O}_2$ ,  $\text{Cr}_2\text{O}_3$ , and  $\text{Cr}_2\text{O}_4$ , (2000), 990–994.
- [259] S. Musi, M. Maljkovi, S. Popovi, Formation of Chromia from Amorphous Chromium Hydroxide, *Croat. Chem. ACTA.*, 72 (1999), 789–802.
- [260] A. H. Heuer, Oxygen and aluminum diffusion in  $\alpha\text{-Al}_2\text{O}_3$  : How much do we really understand ?, *J. Eur. Ceram. Soc.*, 28 (2008), 1495–1507, doi:10.1016/j.jeurceramsoc.2007.12.020.
- [261] A. C. S. Sabioni, B. Lesage, A. M. Huntz, J. C. Pivin, C. Monty, Self-diffusion in  $\text{Cr}_2\text{O}_3$  I. Chromium diffusion in single crystals, *Philos. Mag. A Phys. Condens.*

- Matter, Struct. Defects Mech. Prop., 66 (1992), 333–350, doi:10.1080/01418619208201560.
- [262] Harold J. Frost, Michael F. Ashby, Oxides with the  $\alpha$ -Alumina Structure:  $\text{Al}_2\text{O}_3$ ,  $\text{Cr}_2\text{O}_3$  and  $\text{Fe}_2\text{O}_3$ , (n.d.). [Online]. Available: [http://engineering.dartmouth.edu/defmech/chapter\\_14.htm](http://engineering.dartmouth.edu/defmech/chapter_14.htm).
- [263] Z. Jiang, K. Klyukin, V. Alexandrov, Structure, hydrolysis, and diffusion of aqueous vanadium ions from Car-Parrinello molecular dynamics, *J. Chem. Phys.*, 145 (2016), 1–21, doi:10.1063/1.4962748.
- [264] Harald Brune, Epitaxial Growth of Thin Films, in: Klaus Wandelt (Ed.), *Surf. Interface Science Solid-Solid Interfaces Thin Film.*, Wiley-VCH Verlag GmbH & Co. KGaA, 2014: p. 432, doi:10.1080/01418619208247997.
- [265] Y. Han, D. Kim, J. S. Cho, Y. W. Beag, S. K. Koh, V. S. Chernysh, Effects of substrate treatment on the initial growth mode of indium-tin-oxide films, *J. Appl. Phys.*, 97 (2005), 24910, doi:10.1063/1.1835003.
- [266] J. Sun, T. Stirner, A. Matthews, Structure and surface energy of low-index surfaces of stoichiometric  $\alpha$ - $\text{Al}_2\text{O}_3$  and  $\alpha$ - $\text{Cr}_2\text{O}_3$ , *Surf. Coatings Technol.*, 201 (2006), 4205–4208, doi:10.1016/j.surfcoat.2006.08.061.
- [267] G. Kresse, S. Surnev, J. Schoiswohl, F. P. Netzer,  $\text{V}_2\text{O}_3$  (0001) surface terminations: A density functional study, *Surf. Sci.*, 555 (2004), 118–134, doi:10.1016/j.susc.2004.02.009.
- [268] H. Y. Xu, Y. N. Guo, Y. Wang, J. Zou, J. H. Kang, Q. Gao, et al., Effects of annealing and substrate orientation on epitaxial growth of GaAs on Si, *J. Appl. Phys.*, 106 (2009), doi:10.1063/1.3248372.
- [269] H. J. T. Ellingham, Reductibility of Oxides and Sulphides in Metallurgical Processes, *J. Soc. Chem. Ind.*, 63 (1944), 125–160, doi:10.1002/jctb.5000630201.

- [270] Maria Castellanos, Anthony R. West, Deviations from Vegard's law in oxide solid solutions. The systems  $\text{Li}_2\text{TiO}_3\text{-MgO}$  and  $\text{Li}_2\text{TiO}_3\text{-Na}_2\text{TiO}_3$ , J. Chem. Soc. Faraday Trans. I, Phys. Chem. Condens. Phases, 35 (2000), 289–296.
- [271] Eunah Kim, Zhong-Tao Jiang, Kwangsoo No, Measurement and Calculation of Optical Band Gap of Chromium Aluminum Oxide Films, Japan Soc. Appl. Phys., 39 (2000), 4820–4825.



# Publications and Conferences

1. Yin Gao, Harald Leiste, Michael Stueber, Sven Ulrich. The process of growing  $\text{Cr}_2\text{O}_3$  thin films on  $\alpha\text{-Al}_2\text{O}_3$  substrates at low temperature by RF magnetron sputtering. *Journal of Crystal Growth*. 457 (2017) 158-163.
2. Yin Gao, Harald Leiste, Sven Ulrich, Michael Stueber. Synthesis of local epitaxial  $\alpha\text{-(Cr}_{1-x}\text{Al}_x)_2\text{O}_3$  thin films ( $0.08 \leq x \leq 0.16$ ) on  $\alpha\text{-Al}_2\text{O}_3$  substrates by RF magnetron sputtering. *Thin Solid Films*. Available on line (2017). <https://doi.org/10.1016/j.tsf.2017.05.054>.
3. Yin Gao, Harald Leiste, Stefan Heissler, Sven Ulrich, Michael Stueber, Optical properties of radio-frequency magnetron sputtered  $\alpha\text{-(Cr}_{1-x}\text{Al}_x)_2\text{O}_3$  thin films grown on  $\alpha\text{-Al}_2\text{O}_3$  substrates at different temperatures. *Thin Solid Films*. 660 (2018) 439-446. <https://doi.org/10.1016/j.tsf.2018.06.053>.
4. Yin Gao, Harald Leiste, Michael Stueber, Sven Ulrich. Growth of  $\alpha\text{-Cr}_2\text{O}_3$  thin films on  $\alpha\text{-Al}_2\text{O}_3$  substrate at low temperature by RF magnetron sputtering. The Fifth European Conference on Crystal Growth (ECCG5). Poster presentation. Bologna, Italy. September 09-11, 2015.
5. Yin Gao, Harald Leiste, Michael Stueber, Sven Ulrich. Locally epitaxial growth of  $\alpha\text{-(Cr}_{1-x}\text{Al}_x)_2\text{O}_3$  thin films with different composition on  $\alpha\text{-Al}_2\text{O}_3$  substrates at low temperature by RF magnetron sputtering. Junior Euromat 2016. Oral presentation. Lausanne, Switzerland. July 10-14, 2016.
6. Yin Gao, Harald Leiste, Michael Stueber, Sven Ulrich. Locally epitaxial growth and characterization of  $\text{Cr}_2\text{O}_3$  thin films on  $\alpha\text{-Al}_2\text{O}_3$  substrates with different thickness by RF magnetron sputtering at 320 °C. Materials Science Engineering (MSE) 2016. Poster presentation. Darmstadt, Germany. September 27-29, 2016.